Modelling of Hollow Fibre Membrane Contactors: Application to Post-combustion Carbon Dioxide Capture

David Ricardo Albarracin Zaidiza

▶ **To cite this version:**

David Ricardo Albarracin Zaidiza. Modelling of Hollow Fibre Membrane Contactors: Application to Post-combustion Carbon Dioxide Capture. Food and Nutrition. Université de Lorraine, 2016. English. NNT : 2016LORR0035 . tel-01752215

HAL Id: tel-01752215

https://hal.univ-lorraine.fr/tel-01752215v1

Submitted on 29 Mar 2018

HAL is a multi-disciplinary open access archive for the deposit and dissemination of scientific research documents, whether they are published or not. The documents may come from teaching and research institutions in France or abroad, or from public or private research centers.

L'archive ouverte pluridisciplinaire **HAL**, est destinée au dépôt et à la diffusion de documents scientifiques de niveau recherche, publiés ou non, émanant des établissements d'enseignement et de recherche français ou étrangers, des laboratoires publics ou privés.

AVERTISSEMENT

Ce document est le fruit d'un long travail approuvé par le jury de soutenance et mis à disposition de l'ensemble de la communauté universitaire élargie.

Il est soumis à la propriété intellectuelle de l'auteur. Ceci implique une obligation de citation et de référencement lors de l'utilisation de ce document.

D'autre part, toute contrefaçon, plagiat, reproduction illicite encourt une poursuite pénale.

Contact : ddoc-theses-contact@univ-lorraine.fr

LIENS

Code de la Propriété Intellectuelle. articles L 122. 4
Code de la Propriété Intellectuelle. articles L 335.2- L 335.10
http://www.cfcopies.com/V2/leg/leg_droi.php
http://www.culture.gouv.fr/culture/infos-pratiques/droits/protection.htm

Doctoral dissertation

Thesis submitted and defended on February 2nd, 2016, in Nancy, France, in a partial fulfilment of the requirement of the degree of

Docteur de l'Université de Lorraine

PhD of the Univeristy of Lorraine

Specialité : Génie des Procédés et des Produits

Field: Chemical Engineering

Modelling of Hollow Fibre Membrane Contactors: Application to Post-combustion Carbon Dioxide Capture

---

David Ricardo ALBARRACIN ZAIDIZA

Chemical Engineer

Supervised by: Pr. Sabine Rode (director)
Bouchra Belaissaoui, PhD (co-director)

Composition of jury:

President	Eric FAVRE	Professor at University of Lorraine (ENSIC)
Rapporteurs	Ewan MCADAM	Lecturer at University of Cranfield
	Kitty NIJMEIJER	Professor at University of Twente
Reviewer	Arnaud BAUDOT	PhD Engr. at IFP Energies nouvelles
	Sabine RODE	Professor at University of Lorraine (ENSIC)
	Bouchra BELAISSAOUI	Associate professor University of Lorraine

Acknowledgments

Writing this part of your manuscript means that you have finished the last correction, modification or upgrading of it. Despite of being the last thing you do for the manuscript, it is placed almost on the top of it, as if it were your letter of presentation. This is to say, you'd better finish everything you do as well as you have started it, so your effort will be appreciated from the very beginning. At this time, a long journey has been accomplished but time has gone by quickly, requiring to step back and take stock. In the vast forest of knowledge, a very tiny bush leaf has grown due to all your (not negligible) efforts. However, this minuscule contribution represents all a sea of personal progress, which is the result of constant challenges. It is difficult to sort all the developments that result of such experience, however, I would like to synthesise two aspects that have marked me the most. From a professional perspective, all the challenges have lead you to develop a critical and argumentative thinking (you'll never read a scientific paper in the same way). From a personal point of view, you have a valuable experience allowing you to identify (and sometimes acquire) the strengths of your partners and how to deal with their (and your) weaknesses, in order to be a better human being. You've might conclude that in both perspectives, it is all a matter of equilibrium. All things considered, I would like to dedicate this last blank page to express my gratitude to all those who have allowed me to be in this very moment, writing this very message.

First and foremost I express my deepest gratitude to the members of the jury, who have kindly accepted to review this work, and whose reflections have enhanced and expanded the perspectives of my research. I also take the opportunity to thank my supervisors Sabine and Bouchra. Sabine, you are my mentor, you have spent a lot of time guiding me and cultivating in me an argumentative and critic spirit. I've learned from you the meaning of being precise. Bouchra, your organisational skills and your ability to address to the point of each paper and presentation, have valuably enriched this research. It has been a pleasure to be one of the first doctoral students at your charge. Both of you have always treated me as a peer, we have shared very good moments, not to say *industrially relevant* moments, thus giving me, beyond a professional relation, a friendship.

I would like to thank Christophe, Denis and Eric, who always enabled an open discussion, thus allowing me to learn from their invaluable expertise. Precious advices and remarks for the progression of my research have been made by them. I also express a special appreciation to *Thibaut et al.* who has enabled me to better understand critical aspects and

to enhance modelling skills. Special thanks to Seth G., Junjie and Stéphanie with whom I was fortunate to work, very talented and proactive. I also express my gratitude to Christine, Danielle and Hervé for their kindness and their caring.

Since every good laboratory is composed of good people, at the LRGP I have had the opportunity to meet excellent human beings who have filled this three-year experience of many *convivial* and unforgettable moments. *BFF*, Marco-Polo, David, Mr. Key, Tita, Etienne, Amandine, Clément, Valentin, Olivier, Mahbub, Assia… thanks to you all for having shared countless brainstorming, breaks, coffee breaks, *beer breaks* and also for having motivated me to accomplish this manuscript in the tough moments. I have been fortunate to meet people to whom I owe the kindness and the pleasure of working in this laboratory. Of course, the list is not exhaustive but thanks to *our -D.G.*, the BJC[1], Nadia, Billy, la Paisa, Lau, Carlos, Karine, Sofian, Ivana and to all that I have met but I could not include in this list.

One of the best things of living in France (without mentioning food, museums, les Alpes,…) is the diversity of people, nationalities, cultures and religions. This mixture allows you to enrich and to put every aspect of your life into several perspectives, resulting in an enormous personal progress. This paragraph is dedicated to all these people, because the thing is that after all that, I've learnt to see them with other eyes. Julia, Nathalie, Aurélie, Julie, Arnaud, Flo and Chiara, thank you for being always open to share with me your personal lives. Nico, Fabio, Torrado and Felipe, brothers of mine, thank you for being always there when I needed. *"All"* our conversations and dissertations have contributed to this accomplishment.

To my family, mom and dad, you have given me all the tools necessary to set out on this journey. I recognise all your teachings and I am very grateful for the education and the values I have learnt from you. The more I go through this experience, the better I realize your wisdom. Erika, Jorge and Cesar, as my brothers and sister, I admire all the determination you put in everything you do. I have always been supported by the union that characterises you and I could not be more proud of being part of you.

I would like to dedicate this last paragraph to the person that has been by my side the last three years. Dariny, you are simply the most beautiful person I have ever met. You have given me the courage, the peace and the spiritual nourishment that I needed and of which I will be forever grateful. I hope we will share more and more adventures as we have been doing from the day we met.

[1] Miriam, Alice, François and Jérémy, it has been a pleasure becoming convivial®

Résumé

L'augmentation de l'effet de serre est attribuée à la hausse des concentrations des gaz à effet de serre d'origine anthropique, principalement le CO_2. Les centrales thermiques à charbon sont responsables d'environ 30% des émissions fixes de CO_2. Afin de limiter l'effet de serre, la capture du CO_2 par absorption réactive en postcombustion est une solution intéressante car elle peut être implémentée dans les centrales thermiques existantes. La technologie mature associée à cette capture est la colonne à garnissage. Toutefois, afin de rendre le procédé plus attractif, il convient de réduire le volume des équipements et le coût énergétique associé, ou, en d'autres termes, il convient de l'intensifier.

Une technologie intéressante permettant d'atteindre cette intensification est le contacteur membranaire à fibres creuses. En effet, ce type de contacteur permet de développer d'importantes aires spécifiques et des coefficients de transfert élevés, conduisant potentiellement à une intensification des transferts gaz-liquide. Ainsi l'utilisation des contacteurs membranaires pourrait permettre de réduire la taille des installations dans l'étape d'absorption réactive du CO_2, mais aussi de réduire la consommation énergétique dans l'étape de régénération du solvant par la diminution de la quantité de vapeur de stripage.

Cependant, l'utilisation des contacteurs membranaires dans les deux étapes de capture du CO_2 en postcombustion a été peu étudiée pour l'instant. L'objectif de mon travail de doctorat est de combler cette lacune. Pour ce faire, des modèles à différents niveaux de complexité : monodimensionnel, bidimensionnel, isotherme et adiabatique ont été développés, comparés et validés. Ceci afin d'identifier le niveau de complexité approprié. Cette modélisation a été accompagnée d'une description rigoureuse de la thermodynamique du système car les conditions industrielles l'imposent. Le phénomène de mouillage associé aux membranes microporeuses a été pris en compte dans le modèle et son impact sur le transfert de matière simulé. Les résultats de simulation mettent en évidence le potentiel d'intensification de cette technologie dans l'étape d'absorption et aussi de stripage. Ceci se traduit par une réduction en volume de 4 à 10 fois par rapport aux colonnes à garnissage. Néanmoins, les contacteurs membranaires peuvent difficilement réduire le coût énergétique de l'ensemble de l'opération étant donné que celui-ci provient principalement de l'étape de stripage, qui fonctionne dans des conditions très proches de la limite thermodynamique. Finalement et de façon plus générale, la clé du succès des contacteurs membranaires réside dans le contrôle du mouillage des membranes, qui affecte significativement la performance du dispositif. Une compréhension fondamentale des mécanismes de mouillage dans des

conditions industrielles est nécessaire, afin de développer des modèles fiables et simples qui pourraient s'implémenter dans un modèle de module membranaire.

Abstract

This work addressed modelling of Post-combustion CO_2 Capture (PCC) using aqueous solutions of monoethanolamine by means of Hollow Fibre Membrane Contactors (HFMC). The absorption and stripping steps were studied under laboratory and industrial operating conditions.

A comprehensive thermodynamic model was implemented and accurate predictions of thermodynamic properties, such as CO_2 solubility, were obtained over a large domain. Fundamental aspects of mass-transfer through micro-porous membranes were investigated, i.e. convection inside membrane pores and membrane wetting. It has been determined that convection through the porous medium can be neglected while membrane wetting needs to be taken into account as it is more likely to occur under PCC conditions, significantly decreasing membrane mass-transfer coefficients.

Transfer models with different levels of complexity were developed for the absorption step using HFMC, ranging from one-dimensional isothermal single-component to two-dimensional adiabatic multi-component. Counter-current flow with liquid flowing through the fibre lumen was considered. Under laboratory conditions, i.e. high reactant excess, isothermal and adiabatic models led to comparable simulation results. However, under relevant industrial operating conditions, i.e. high reactant conversions and high CO_2 capture ratios, differences of roughly 60% in terms of CO_2 specific absorbed flux were obtained. After comparing the simulation results from both one- and two- dimensional models, a relative difference of less than 3% was found in the CO_2 specific absorbed flux, regardless of whether laboratory or industrial conditions were applied. Membrane wetting could be simulated conveniently, using an average membrane mass-transfer coefficient, representative of partially wetted membranes.

Under industrial conditions, significant axial temperature variations, up to 30 °C, as well as transmembrane reversal flux of the solvent, corresponding to solvent condensation and evaporation, were predicted. At this stage, membrane wetting due to capillary condensation was found likely to occur. Provided that the membrane mass-transfer coefficient is higher than $5{\cdot}10^{-3}$ ms^{-1}, CO_2 specific absorbed fluxes from 2 to 10 $molm^{-3}s^{-1}$ could be attained, for fibre external radius varying between 400 and 100 µm, and fibre thickness between 80 and 20 µm, respectively. This corresponds roughly to volumetric contactor reduction factors comprised between 2 and 10, compared to traditional packed columns. Alternative flow arrangements, such as co-current flow and liquid in shell, were simulated and their applicability was analysed.

Three techniques for liquid absorbent regeneration were addressed: High-Temperature Stripping (HTS) using packed columns and high- and Low-Temperature Stripping (LTS) using HFMC. Compared to HTS using packed columns, simulations revealed that HTS by means of HFMC, which to our knowledge have to date not been investigated, were shown to potentially reduce the stripper volume by a factor of 10, provided that the membranes are resistant to high temperatures and wetting. Finally, LTS proved to be more energy consuming and offered lower volumetric reductions.

Nomenclature

Uppercase Latin Symbols

Symbol	Meaning	Unit
A	Membrane surface area	[m^2]
$AARD$	Average absolute relative deviation, $AARD = \frac{1}{n}\sum_{i=1}^{n}\frac{\lvert f_i^{exp} - f_i^{est}\rvert}{f_i^{exp}}$	[--]
C	Molar concentration	[mol m^{-3}]
C_{LM}	Log-mean average concentration between gas and liquid	[molm^{-3}]
Cp	Specific heat	[J $mol^{-1}K^{-1}$]
CFD	Computational fluid dynamics	
D_i	Diffusion coefficient	[$m^{-2}s^{-1}$]
E	Enhancement factor	[--]
Fr	Froude number	[--]
G	Gas molar flux	[mol $m^{-2}s^{-1}$]
Gz	Graetz number, $Gz_i = \frac{v_F {d_h}^2}{D_{i,F}\, z}$	[--]
ΔH^o_{abs}	Enthalpy of absorption	[J mol^{-1}]
ΔH^o_j	Enthalpy of reaction	[J mol^{-1}]
ΔH^o_{vap}	Latent heat	[J mol^{-1}]
IF	Intensification factor $IF = \frac{Packed\ column\ volume}{HFMC\ volume}$	[--]
K	Overall mass-transfer coefficient or Equilibrium constant	[m s^{-1}] or (molar scale)
K_{koz}	Kozeny constant for pressure drop	[m^{-2}]
L	Liquid molar flux	[mol $m^{-2}s^{-1}$]
M	Molar mass	[kg mol^{-1}]
N_i	Molar flux	[mol m^{-2} s^{-1}]
Nu	Nusselt number	[--]

P	Pressure	[Pa]
P_i^{sat}	Saturation pressure of component i	[Pa]
$\Delta P_{L\text{-}G}$	Transmembrane pressure [Pa]	[Pa]
ΔP_{break}	Liquid breakthrough pressure [Pa]	[Pa]
Pr	Prandtl number	[--]
Q	Heat flow of fluid volumetric flow rate	[W]or[$m^{-3}s^{-1}$]
R	Gas constant	[$Jmol^{-1}K^{-1}$]
Re	Reynolds number	[--]
RE	Regeneration factor, $RF = 1 - \frac{lean\ liquid\ loading}{rich\ liquid\ loading}$	[--]
S	Oversaturation in gas phase	[--]
Sc	Schmith number	[--]
Sh	Sherwood number	[--]
T	Temperature	[K]
U	Overall heat transfer coefficient	[$W \cdot m^{-2}K^{-1}$]
V	Molar volume	[m^3mol^{-1}]
V_i^{∞}	Brelvi-O'Connell partial molar volume for CO_2 at infinite dilution in H_2O	[m^3mol^{-1}]
W	Electric work	[W]
We	Weber number	[--]
Z	Contactor length	[m]

Lowercase Latin Symbols

Symbol	Meaning	Unit
a_M	Log-mean membrane specific area per unit volume of contactor	[m^2m^{-3}]
a_{ext}	External specific area per unit volume of contactor	[m^2m^{-3}]
a_{int}	Internal specific area per unit volume of contactor	[m^2m^{-3}]
a_d	Dry specific area per unit volume of packed column	[m^2m^{-3}]
a_i	Activity of component i	[$molm^{-3}$]

c	Parameter of equilibrium constant correlations	[--]
d_h	Hydraulic diameter, $d_h = 4\frac{flow\ volume}{fluid-membrane\ interfacial\ area}$	[m]
d_p	Membrane pore diameter	[m}
g	Gas molar flow rate	[mol s^{-1}]
h	Heat transfer coefficient	[W $m^{-2}K^{-1}$]
k	Local mass-transfer coefficient	[m s^{-1}]
k_r	kinetic constant	(molar scale)
$k_{M,CO2}^{eq}$	Equivalent membrane mass-transfer coefficient of CO_2 at 40°C and 1 bar	[m s^{-1}]
l	Liquid molar flow rate	[mol s^{-1}]
Δn_j	Variation of the moles from an initial state to the chemical equilibrium	[mol]
m	Partition coefficient $m_i = \frac{RT}{\mathcal{H}_i}$ or $m_i = \frac{RTC_{T,L}}{P_i^{sat}}$	[--]
q	Heat flux	[$W \cdot m^{-2}$]
r_e	Outer fibre radius	[m]
r_i	Inner fibre radius	[m]
r_s	Happel free-surface shell radius	[m]
r_{CO2}	Reaction rate relative to CO_2	[$mol \cdot m^{-3} \cdot s^{-1}$]
u	Superficial fluid velocity	[ms^{-1}]
v	Interstitial fluid velocity	[ms^{-1}]
w	Component mass fraction	[--]
w_M	Volumetric membrane wetting fraction	[--]
x_i	True molar fraction in liquid	[--]
y_i	True molar fraction in gas	[--]
z	Dimensionless contactor length	[--]

Greek Symbols

Symbol	Meaning	Unit
α	CO_2 solvent loading	[$mol_{CO2}mol_{amine}^{-1}$]
β	Geometric factor for non-cylindrical pores	[--]
δ	Fibre thickness	[--]
ε_p	Membrane porosity	[--]
φ	Fibre volume fraction	[--]
ϕ_i	Fugacity coefficient of the gas phase for component *i*	[--]
γ	Liquid surface tension	[Nm^{-1}]
$\mathcal{H}_i$	Herny constant for component *i*	[Pa m^3mol^{-1}]
$\mathcal{K}$	GLE, VLE or MS constant	[--]
κ	Hydrodynamic permeability of the porous medium	[m^{-2}]
γ_i^{∞}	Infinite dilution activity coefficient for gas species in water	[--]
λ	Thermal conductivity	[$Wm^{-1}K^{-1}$]
μ	Viscosity	[$Pa \cdot s^{-1}$]
ν_{ij}	Stoichiometric coefficient of the compound *i* in the reaction *j*	[--]
ρ	Density	[kgm^{-3}]
τ	Membrane tortuosity	[--]
Θ	CO_2 capture ratio	[--]
θ	Liquid-membrane contact angle	[gradients]
ξ	MEA conversion or *extent of reaction*	

Abbreviations

Abbrev.	Meaning
AMP	2-amino-2- methyl-1-propanol
CFD	Computational fluid dynamics
CO_2	Carbone dioxide
CO^{3-}	Carbonate

DEA	Ethanolamine
DIPA	n,n-Diisopropylamine
elec-NRTL	Non-random two liquid for electrolytes activity model
HCO^{3-}	Bicarbonate
HFMC	Hollow fibre membrane contactor
MEA	Monoethanolamine
$MEAH^{+}$	Protonated ethanolamine
$MEACOO^{-}$	Carbamate ion of ethanolamine
PCC	Post-combustion CO_2 capture
PG	Propylene glycol
PP	Polypropylene
PDMS	Polydimethylsiloxane
PVDF	Polyvinylidene fluoride
PTFE	Polytetrafluoroethylene
PZ	Piperazine
UNIQUAC	UNIversal QUAsiChemical activity model

Subscripts and Superscripts

Script	Meaning
i	Compound
j	Reaction
G	Relative to gas
F	Relative to fluid
L	Relative to liquid
M	Relative to the membrane
W	Relative to water
abs	Absorption
$cond$	Relative to condensation

int	Internal surface of the fibers
ext	External surface of the fibres
vap	Vaporisation
In	Inlet
LEAN	Lean liquid absorbent
RICH	Rich liquid absorbent
L	At the liquid inlet or gas outlet
Out	Outlet
0	Initial or gas inlet

Contents

Introduction

Carbon dioxide, or CO_2, acts as Earth's principal temperature regulator. An absence of CO_2 within the atmosphere would cause excessively cold temperatures on Earth and an excess would cause average global temperature to rise. The latter is known as the greenhouse effect. In the short-term, the scientific community has warned that the increase of current average global temperatures in a few kelvins (e.g. 2K) would lead to the loss of many ecosystems as well as to an increased occurrence of extreme climate events. In the long-term, the temperature change would increase other greenhouse gas emissions, such as water or methane, which ultimately would lead to a chaotic greenhouse effect.

Since the industrial revolution, anthropogenic CO_2 emissions have increased exponentially. Representing about 77% of total greenhouse gas emissions, atmospheric CO_2 reached a concentration of 400 ppm in 2013, roughly 60% higher than the associated level before the industrial revolution. There is unequivocal evidence of climate changes caused by these emissions; hotter and drier summers and colder winters have been reported in various parts of the world for the past decade.

To combat climate change, the Kyoto Protocol established in 1997 set out a series of specific commitments to reduce greenhouse gas emissions for developed countries between 2008 and 2012. Since then, the Conference of Parties (COP), the supreme decision-making body of the United Nations Framework Convention on Climate Change formed by the adherent countries of this protocol, meets every year with the objective of defining action plans and making political and economic decisions to attain Kyoto protocol policies. For instance, the COP21[2] held on December 2015, addressed the commitment of developed countries to raise one hundred billion dollars annually to help developing countries cope with climate change. In order to establish realistic goals, it is important to quantify current advancements in technology solutions to reduce CO_2 emissions. Hence, the agents would have solution portfolios to support their decisions.

Today, coal power plants are responsible for an estimated 8.5 Gt of CO_2 emissions per year, which is approximately 30% of total CO_2 emissions. Among proposed strategies aimed at mitigating CO_2 emissions from this source, post-combustion CO_2 capture (PCC) based on the absorption of CO_2 by chemical solvents is a practical solution as it can be retrofitted to existing coal power plants and can integrated into new plants relatively

[2] http://www.cop21.gouv.fr/

easily. Absorption using aqueous solutions of monoethanolamine (MEA) as liquid absorbent in packed columns is considered to be the most promising technology available today. However, the following two major challenges must be addressed to achieve the technical and economic targets: decreasing process energy requirements (or operating costs) using novel solvents and heat-integration approaches, and reducing equipment size (or capital costs), through process intensification.

Over the past three decades, membrane contactors have been considered as an innovative alternative to conventional gas-liquid contactors such as packed columns. In this technology, a membrane separates the gas and the liquid streams, leading to a non-dispersive and modular character, thus avoiding liquid entrainment or flooding. A technology commonly proposed is the use of hollow fibre membrane contactor (HFMC), consisting of a fibre bundle with an outer diameter of between 0.1 and 1 mm. The small diameter allows this contactor to develop sizeable interfacial areas, which could potentially lead to significant reduction in equipment volume.

HFMC technology has been widely investigated for its use in CO_2 absorption with chemical solvents under laboratory conditions. However, despite the potential advantages of membrane contactors, very few investigations have studied implementing this technology for CO_2 post-combustion capture within an industrial framework. The performance of CO_2 absorption and liquid absorbent regeneration using this technology under industrial conditions is still unknown. Indeed, there is currently a lack of rigorous models and experiments that consider these conditions.

Objectives and Methodology

This thesis addresses the feasibility of CO_2 capture using hollow fibre membrane contactors through modelling and process simulation. To do this, the following objectives needed to be met to allow for both the absorption and desorption steps:

- Identify the optimal modelling approach. The ideal model is simple but robust enough to predict HFMC performance in both laboratory and industrial conditions.
- Estimate the intensification potential of HFMC in industrial conditions.

In order to identify the optimal modelling strategy, several approaches were developed, each with differing degrees of complexity: one-dimensional (1D), two-dimensional (2D), isothermal single-component and adiabatic multi-component. Their predictions were compared and validated using available experimental data. HFMC performance in industrial conditions was estimated by simulating the process for different module and membrane characteristics. Within this framework, the manuscript is structured as follows:

In **Chapter 1**, CO_2 emissions and carbon capture is presented together with the reference process, i.e. detailed description of post-combustion capture using chemical solvents. Furthermore, membrane contactor technology is described. The advantages and drawbacks related to conventional gas-liquid contactor technology (i.e. packed columns) are presented and laboratory and pilot plant investigations are discussed. Particular emphasis is given to here to summarizing the specific modelling strategies and operating conditions used for studying HFMC.

Chapter 2 presents the thermodynamic and kinetic aspects which are indispensable for modelling gas-liquid contactors. Since the thermodynamic and reaction kinetic models play a fundamental role, selecting an appropriate modelling approach was crucial at this stage. These models are described here and their predictions validated against available data documented in the literature related to both laboratory and industrial conditions.

In **Chapter 3**, the phenomenological aspects related to mass-transfer though microporous membranes, i.e. convection through a porous medium and membrane wetting, are described and their role in the CO_2 post-combustion capture is highlighted. Isothermal modelling of hollow fibre membrane contactors is then addressed at two levels of complexity, i.e. 1D and 2D modelling approaches are compared.

Moving forward to modelling with greater complexity, **Chapter 4** details the adiabatic multi-component approach of CO_2 absorption in HFMC. Thermal effects, such as temperature variations associated with solvent evaporation and condensation fluxes, are quantified and their impact on the contactor functioning is discussed. HFMC performance under industrial conditions are compared to that of packed columns. The latter are modelled, simulated and validated to ensure an accurate comparison. The development of several modelling complexities, such as for 1D and 2D approaches, are described and a comparison is made between corresponding model predictions under industrial conditions. At this point, an optimal modelling approach is identified followed by simulations for different flow configurations of HFMC, such as co- and counter-current, and an analysis of results for the CO_2 absorption operation.

The modelling and simulation of CO_2 stripping using HFMC is studied in **Chapter 5**. Three techniques are investigated: high-temperature stripping using packed columns and high- and low- temperature stripping using HFMC. The intensification potential of membrane contactor technology over the packed column under industrial operating conditions is calculated here for the first time. Lastly, the pertinence of the low-temperature technique is discussed.

This thesis has been financially supported by a grant of the French Government, in the Laboratory of Reactions and Chemical Engineering (known by its French acronym LRGP) in Nancy, France. Three scientific papers and one book chapter have been written based

on this work. Two of the papers were published in the *Journal of Membrane Science* and are integrated in **Chapter 3** and **Chapter 4**. The third paper has recently been submitted for publication in the journal *Chemical Engineering Science*. The book chapter is a part of the "*Process Design"* section of the book "*Absorption-Based Post-Combustion Capture of Carbon Dioxide",* currently in press with the *Elsevier* publishing house.

Chapter 1. General Context

1.1. CO_2 Emissions, Capture and Storage

1.1.1. CO_2 Emissions

An increase in the global human population correlates with an increase in total energy demand (see Figure 1.1). This is due to both the increase of the average standard of living per habitant and to economic growth. Among all industrial waste generated from energy production, carbon dioxide emission represents a significant part. Over the last decade, CO_2 emissions have increased by 2.3% per year and, in 2014, power generation contributed to as much as 40% (see Figure 1.2). Scientific consensus has revealed that the main contribution to climate change corresponds to an increase in atmospheric concentrations of greenhouse gases, of which CO_2 represents 77% [1], [2].

In order to reduce CO_2 emissions, energy policies need to be adapted to establish energy production methods aimed at mitigating CO_2 emissions while responding to energy demands. The International Energy Agency suggests two scenarios related to climate change, energy production and related CO_2 emissions. The first considers the Intended Nationally Determined Contributions (INDC), in which international pledges have a positive impact towards slowing growth of global energy-related emissions but in which they will continue to rise from 2013 to 2030. And the second, the *450 Scenario*, in which a goal of a maximum temperature increase of 2°C is targeted for 2040, corresponding to a significant decrease in CO_2 emissions.

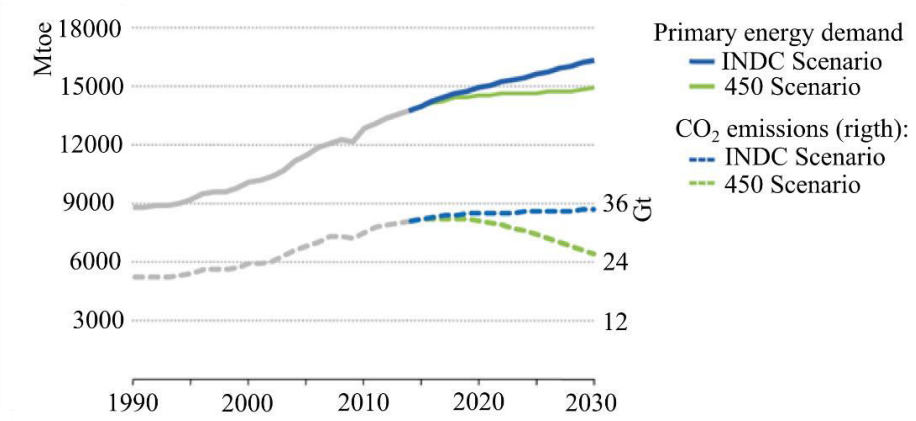

Figure 1.1 Global primary energy demand and related CO_2 emissions by scenario. Source World Energy Outlook [3].

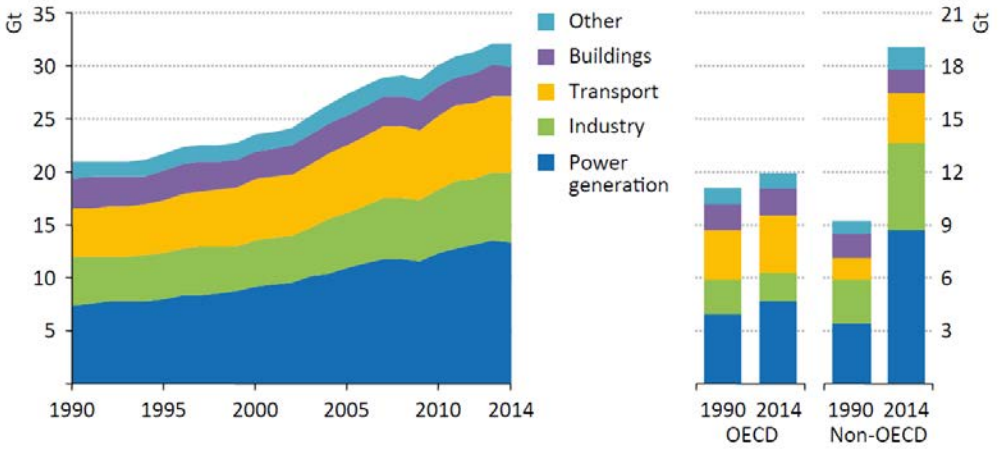

Notes: "Other" includes agriculture, non-energy use (except petrochemical feedstock), oil and gas extraction and energy transformation. International bunkers are included in the transport sector at the global level but excluded from the regional data.

Figure 1.2 Global energy-related CO_2 emissions by sector and region. Figure taken from [3]

To make a transition between the two scenarios possible, the following measures have been proposed [3]:

- Increasing energy efficiency in industry, construction and transportation sectors.
- Progressively reducing the use of the least-efficient coal-fired power generating plants and banning new construction.
- Increasing investment in renewable energies in the power sector.
- Gradually phasing out fossil-fuel subsidies to most end-users by 2030.
- Reducing methane emissions in upstream oil and gas production.

In the 450 Scenario, illustrated in Figure 1.3, the reduction of CO_2 emissions is achieved by the improvement of the end-use energy efficiency (39%), the shift to renewables (23%), Carbon Capture and Storage (17%), end-use fuel switching (12%), nuclear energy (8%) and improving power generation efficiency and fuel switching (1%). CCS would be increasingly adopted beginning in the mid-2020s, with deployment accelerating in the 2030s to capture roughly 5.1 Gt of CO_2 emissions per year by 2040. CCS is therefore a key technology in this scenario and, in order to ensure that it is available at the required scale by the early 2020s, furthering advancement of research, development and deployment will be essential [3], [4].

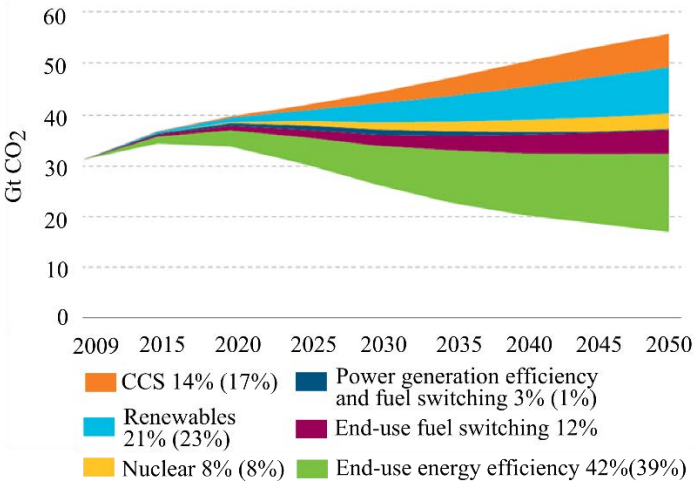

Note: Percentages indicate cumulative values. Parenthesis indicate values in 2050

Figure 1.3 Global energy-related CO_2 emissions abatement in the 450 scenario relative to INDC. Source World Energy Outlook [4].

1.1.2. CO_2 Capture and Storage

Carbon capture and storage separates and captures CO_2 from stationary, concentrated and large tonnage sources (i.e. power and industrial sources), then compresses the CO_2 in a dense supercritical phase, to finally transport it to a suitable site for injection into deep underground formations for permanent storage. Since emissions from power plants account for about 40% of the total emissions, the implementation of CCS for these sources would lead to a significant reduction of energy-related CO_2 emissions.

The first commercial power plant to incorporate CCS was introduced in 2014, in Canada, with a capacity of 40 Mt per year of CO_2 capture and 120 MW. This represents a milestone in CCS.

The challenge lies in identifying the most performant CCS process for use by power plants. The following strategies were proposed by the IPCC in 2005 [5]: oxy-fuel combustion, pre-combustion and post-combustion.

The oxy-fuel process is based on combustion in an atmosphere of almost pure oxygen, wherein a stream of essentially water and CO_2 is obtained and can be easily separated by condensation. The cryogenic distillation required to produce the oxygen stream consumes the most energy in this process.

Pre-combustion consists in burning an already carbon-free carburant, i.e. H_2, which has an elevated heating value. The CO_2 produced during the process of reforming carbon-hydrogenated sources (e.g. natural gas, biomass), required to produce the hydrogen, is then separated at high temperatures and pressures. The energy penalty of this process is shared between CO_2/H_2 separation and carbon monoxide conversion.

Finally, post-combustion consists of capturing diluted CO_2 in N_2, following combustion of the fossil energy source. The CO_2 concentration of the flue gases varies between 4% and 15%, depending of the combustible. Given such concentrations, several processes are considered: chemical or physical absorption, cryogenic separation, selective adsorption and membrane separation.

Geological storage sites compatible with long-term CO_2 retention are comprised of tail-end oil production sites or gas fields and saline aquifers. A first stage involves identifying and characterizing appropriate sites which are then subjected to CO_2 injection, and finally prepared for closure. The stages of carbon injection and closure are monitored closely to detect any risk of carbon leakage [6].

1.1.3. CO_2 Post-combustion Capture by Chemical Absorption

Among multiple strategies for CO_2 capture, post-combustion capture is particularly advantageous as it can be retrofitted and adapted to existing power plants, and integrated into new systems. The low CO_2 partial pressures of power plant flue gases makes the chemical absorption process the most interesting for its robust and high performing nature. In addition, this process has been well documented as it has been widely used in natural gas treatment and in ammonia production processes.

Figure 1.4 illustrates the CO_2 capture process by chemical absorption. The already solid and sulfur free[3] flue gases are cooled to the temperature of the absorption step. Then, the gases enter to the absorber where the liquid absorbent[4] captures the CO_2, rendering it *rich absorbent*. A washing section placed on the top of the absorber allows for component recovery, otherwise lost by evaporation and/or aerosol formation [7]. The rich absorbent is pumped to a heating section and then to the desorber, in which CO_2 is stripped from the absorbent. In order to separate de CO_2 from the absorbent liquid, the later comes in contact with water vapor, which is obtained through partial evaporation of the liquid absorbent in the reboiler. The heat applied to the reboiler is provided by the condensation of a steam stream taken directly from the furnace of the power plant. A pre-condenser is added to this section in order to increase enthalpy and solvent recovery. The relatively warm *lean absorbent* is then sent to the economizer, in which it is cooled by the rich absorbent, to finally enter to the absorber to close the loop. Once the CO_2 is separated from water in the condenser, it is ready to be carried to the compression section, in which the CO_2 is carried up to supercritical conditions, suited to its transport.

[3] The purification of flue gases from SO_x and NO_x is performed in order to avoid the solvent degeneration [7]

[4] *Liquid absorbent* are referred to solvents in several publications. Instead of solvent, *liquid absorbent* is preferred here to avoid any confusion due to the use of solvent (water) in the thermodynamic model.

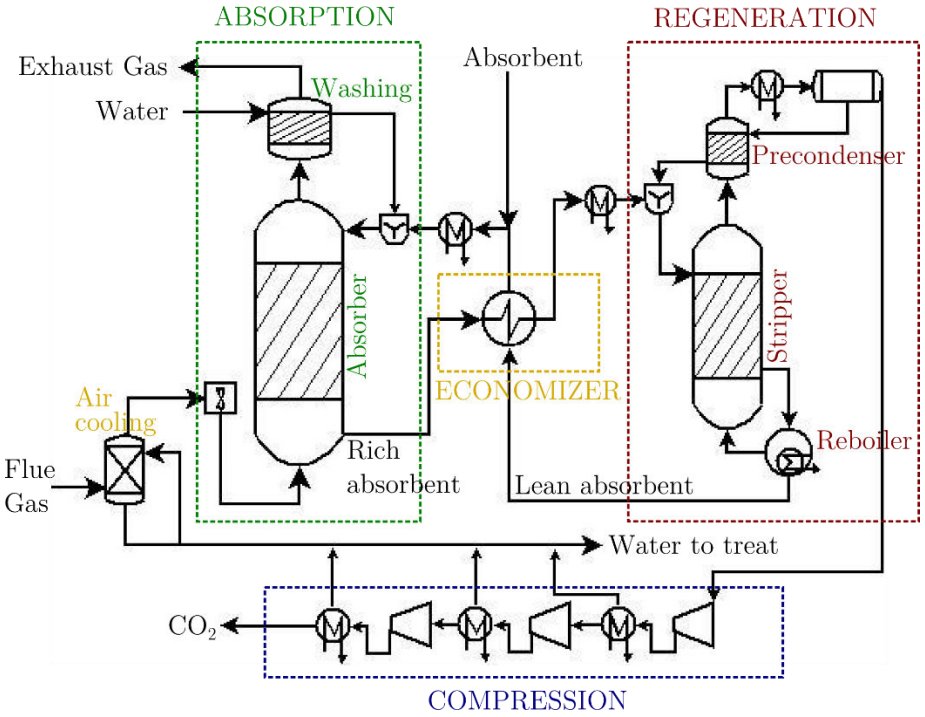

Figure 1.4 Schematic representation of the CO_2 capture by chemical absorption

Aqueous amine solutions are commonly used liquid absorbents due to their high affinity towards CO_2, high absorption loading (moles of CO_2 per mole of active amine) and elevated reaction rates. The monoethanolamine (MEA, C_2H_7NO), a primary amine, is the reference amine for this type of liquid absorbent. This amine is known to have high reaction rates but, likewise, high CO_2 heat of absorption. This allows for the utilization of smaller units, however it makes the stripping high energy consuming, respectively. Others amines such as the methyldiethanolamine (MDEA, secondary amine), triethanolamine (TEA, tertiary amine), 2-amino-2-methyl-propanol (AMP), Piperazine and their blends, as well as the addition of additives (such as enzymes) are still being investigated [8]. The goal is to find the best trade-off between reaction rates, heat of absorption and loading capacity.

For the case of the MEA, the operating conditions are fixed such as to minimize the heat duty of the reboiler. These conditions correspond to high MEA conversions as well as relatively loaded lean absorbent.

The reference technology for performing absorption and desorption is the packed column, due to its high flow capacity and robustness. However, due to high quantities of flue gases which require treatment, large sized equipment is required. In order to render this process sufficiently attractive to ensure the accomplishment of the 450 Scenario, increased treatment capacity per unit volume and reduced energy consumption are necessary. In other words, the process needs to be intensified.

For the last decade, an innovative technology involving membrane contactors, has been widely studied due to their intensification potential. This technology is presented in the Section 1.2.

1.2. Membrane Contactors for Post-combustion Carbon Capture

Membrane contactors are considered as one of the most promising strategies for intensified gas–liquid absorption processes. The key concept of a membrane contactors lies in making use of a permeable, hydrophobic membrane material that separates the gas and the liquid streams in a gas absorption process. Due to the membrane, a supplementary mass-transfer resistance needs to be considered, when compared to a classical gas–liquid absorption situation in which there is direct contact between the two phases. However, possible development of much higher interfacial areas per unit volume than current reference technologies, i.e., gravity-driven tray- or packed columns, is expected to significantly counterbalance the increase of the mass-transfer resistance, making significant process intensification possible. For instance, in acid gas scrubbing, significant reduction factors of equipment size, ranging from 10 to 30, have been estimated [9], [10].

Among the various potential utilizations of membrane contactors for gas–liquid absorption processes that have already been explored, post-combustion carbon dioxide capture by absorption in a chemical liquid absorbent are currently the most intensively investigated application [11]–[13]. For this process, the major development targets are decreasing equipment capital cost and size, and minimizing the energy requirement in order to meet technical and economic constraints.

Most investigations to date have focused on the absorption section of the process [11], [14]. Indeed, this step is characterized by mild operating conditions, i.e. near ambient temperatures and almost atmospheric pressure, suitable for membrane use. For the regeneration step by means of vapour stripping, higher temperatures are required. Hence, polymeric membranes contactors are difficult to implement as available choices of suitable membrane materials able to withstand such conditions are limited [15]–[17]. In order to reduce the operating temperature, regeneration through membrane vacuum processes has been studied [18]–[20]. More recently, using membrane contactors has been suggested as an additional step in the absorption/desorption loop, dedicated to process enthalpy recovery by means of water evaporation or condensation [21], [22].

Various liquid formulations have been used in membrane contactors, mainly aimed at minimizing the process energy requirement. However, in the selection process, membrane compatibility issues pose an additional constraint [23]–[27].

1.2.1. Module and Fibre Characteristics

The membrane may be implemented in the contactor as either a flat or a spiral wound sheet, or as a bundle of hollow fibres. The latter arrangement is preferred for gas-liquid contacting, as it allows for developing the highest interfacial areas per unit volume.

Hollow fibre membrane contactors (HFMC, Figure 1.5) are made up of a bundle of hollow fibres arranged in a geometrical array inserted in a shell. The bundle is supported by a sealing ring. One of the fluids flows through the lumen of the hollow fibres, whereas the other flows through the shell surrounding the fibres. Analogous to shell and tube heat exchangers, the flow in the shell of HFMC can be orientated in different directions with respect to the direction of the flow through the fibre lumen. In Co- and counter-current parallel flow, both crossflow and multipass arrangements are encountered. In the latter, the fluid passing through the lumen is fed to an adjacent fibre bundle (e.g. two passes, as shown in Figure 1.5.b).

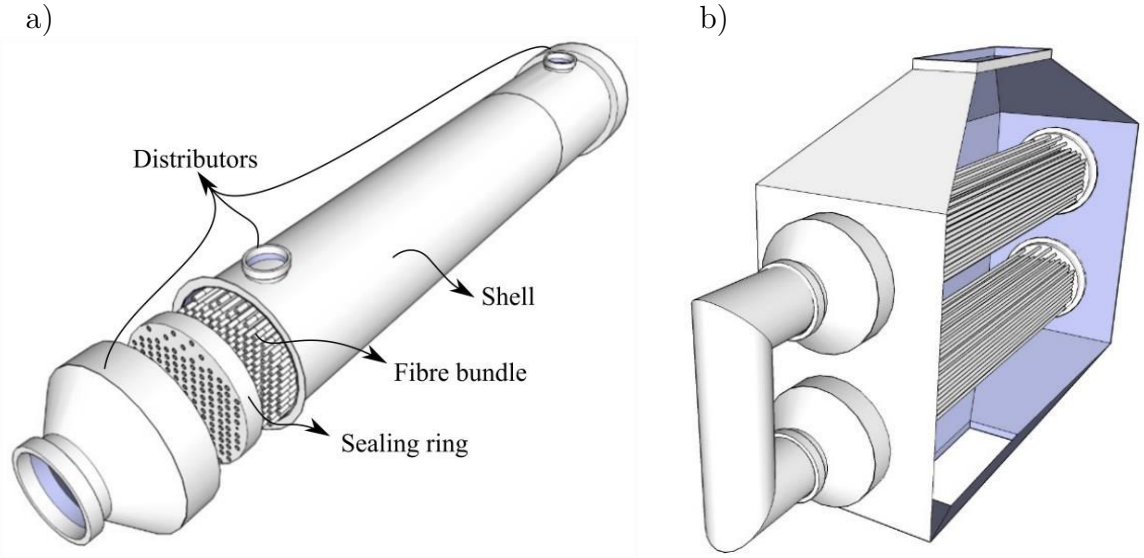

Figure 1.5 Exploded representation of hollow fibre membrane contactors. a) Parallel flow. b) Cross flow.

In a laboratory environment, the fibre bundle can stand by itself. However, an industrial membrane contactor for post-combustion carbon capture would contain thousands of fibres grouped in the same bundle. Therefore, a grid must be included in order to support the entire bundle during sealing, which also maintains the bundle structure [28].

Typical values of HFMC key geometrical characteristics used in industry are presented in Table 1-1.

Table 1-1 Key geometrical characteristics of commercial size HFMC

	Symbol	Value	Units
External fibre radius	r_e	100 - 500	µm
Relative fibre thickness	δ/r_e	0.2 - 0.6	--
Packing volume fraction	ϕ	0.4 - 0.7	--
Resulting specific membrane area (based on log-mean fibre radius)	a_M	2500 – 12000	m^{-1}
Fibre array arrangement	triangular, square or random		

1.2.2. Membrane Characteristics

Three types of membranes can be used in HFMC for carbon capture: microporous, self-standing dense and composite. SEM photographs of fibres made using the different membranes are shown in Figure 1.6.

The microporous membranes are commonly made of a hydrophobic polymeric matrix, which is able to permeate the gas phase while blocking the liquid phase at the surface pore. The major commercially available microporous membrane materials and geometrical characteristics are shown in Table 1-2. The most common polymers are polypropylene (PP), polyvinylidene fluoride (PVDF) and polytetrafluoroethylene (PTFE). The wide range of both pore-size and pore-shaped polymers, render values of the average tortuosity and average pore size unreliable. The microporous membranes do not offer any selectivity for a particular species, but act as a barrier between the phases. Moreover, their porous nature makes them subject to both liquid breakthrough and gas bubbling.

Table 1-2 Microporous hollow fibre membrane commonly cited for PCC: main suppliers and range of membrane characteristics [29]–[31]

Membrane material	Suppliers	Average pore size, d_p (µm)	Porosity ε (-)	Tortuosity τ (-)	Membrane thickness, δ (µm)
PP	GE Water, Membrana				
PVDF	Pall, Millipore, Pall Gelman	0.01 – 0.45	0.2 – 0.6	2 – 10	30 – 400
PTFE	Millipore, GE Water, Sartorius				

Previous studies have investigated dense, self-supporting polymeric membranes with thicknesses between 50 and 100 µm for the fact that they prevent breakthrough [32], [33]. For instance, polydimethylsiloxane (PDMS) was studied as it exhibits the largest CO_2

permeability among rubbery polymers. However, calculations and experimental investigations revealed that these membranes lead to prohibitively low mass transfer coefficients.

Composite membranes make use of a thin, dense polymer skin coated on a microporous support to avoid fluid breakthrough. Dense skins based on PDMS, PMP (polymethylpentene), PPO (Poly(*p*-phenylene oxide)) , PTMSP (poly(1-trimethylsilyl-1-propyne) or Teflon AF are cited in literature studies for CO_2 absorption using HFM contactors [12]. The thickness of the dense skin is comprised, for instance, between 2 and 10 µm for PDMS and 0.1 and 1 µm for PMP. Due the thinness of the dense film, the overall mass-transfer coefficient of these membranes is reasonably close to that measured for microporous membranes. However, manufacturing these membranes is an arduous process [12], [34], [35].

Modification of the membrane pore size and shape distribution [30], [35], [36] or the selection of new polymers (e.g. polyether ether ketone, PEEK) [37] can lead to super hydrophobic membranes which are resistant to both wetting and aging. However, producing such materials is expensive and is currently still under development. Given that the PCC process presents certain economic constraints, use of these materials is to date not a viable option.

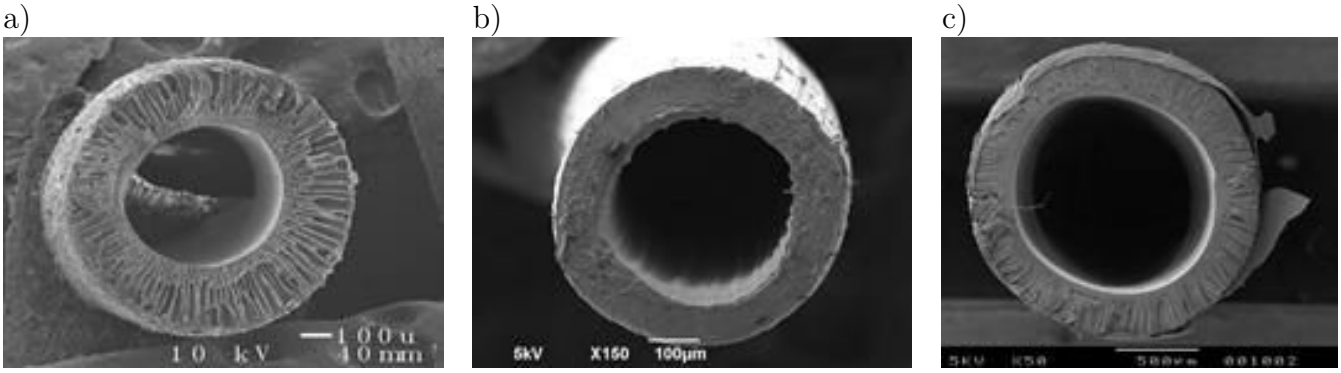

Figure 1.6 SEM pictures of three different types of hollow fibre membrane a) Microporous hydrophobic (b) Dense self-standing (c) Dense skin composite or asymmetric

1.2.3. Advantages and Drawbacks of Membrane Contactors

The principal advantages and drawbacks of HFMC technology in post-combustion carbon capture are summarized in Table 1-3. The intensification potential of this technology resides essentially in the large interfacial area per unit volume, roughly 20 times higher than that attained in packed columns, which would eventually lead to equipment size reduction. This confers important advantages, particularly in offshore applications where weight and volume considerations play a key role. Another interesting feature of hollow fibre membrane contactors lies in the physical separation of the gas and liquid phases,

thereby avoiding the flooding and liquid entrainment that limits the operational range of packed columns. The main issue that has to be addressed in order to develop the technology is the stability of the membrane mass-transfer resistance under severe operating conditions and over long-term operation times. Indeed, the membrane mass-transfer resistance can be tremendously enhanced through membrane aging, wetting or solid plugging.

The scale-up of the HFMC is an a priori straightforward numbering-up procedure. However, the significantly high throughputs involved in post-combustion carbon dioxide capture lead to important distribution issues. But this is also the case in conventional technology, i.e. packed columns. As a result, the scale-up problematic is not a discriminating feature between technologies.

Table 1-3 Membrane contactor main advantages and drawbacks compared to packed column technology

Main Advantages	Main Drawbacks

• Intensification potential due to higher interfacial areas per unit volume
• Larger operating range of gas and liquid velocities:
  ○ No liquid entrainment or flooding
  ○ No partial wetting of packing
  ○ No foaming
  ○ Independent pressure profiles of the gas and the liquid flow
• Special interest in offshore and zero gravity applications due to:
  ○ Low equipment weight
  ○ No gravity-driven flow
	• Additional transfer resistances due to the membrane
	• Disadvantages specific to porous membranes:
	  ○ Membrane wetting due to liquid breakthrough
	  ○ Gas bubbling
	  ○ Capillary condensation
	• Membrane and module aging (i.e. structural change) due to chemical and physical attack:
	  ○ Exposure to liquid absorbents
	  ○ Temperature and pressure variations
	• Fibre plugging due to solid particles (e.g. fly ash)

1.2.4. Membrane Wetting

Over the last decade, membrane wetting has been identified as the principal issue determining membrane contactor performance [38]. The possible states with respect to wetting are illustrated in Figure 1.7 for a microporous membrane. Ideally, the membrane is non-wetted (Figure 1.7 a), i.e. the membrane pores are totally gas filled. In this state, the membrane resistance is relatively low, e.g. only one order of magnitude lower than that of the gas-side.

For important liquid-gas pressure differences, the liquid can penetrate the membrane pores. This phenomenon is known as liquid breakthrough. Another cause for membrane wetting, albeit less studied, is capillary condensation. Indeed, as water vapour passes

through the membrane pores, it may condensate within the membrane structure. Both liquid breakthrough and capillary condensation lead to partial or even complete membrane wetting (Figure 1.7 b and c respectively). When liquid fills the membrane pores, the mass transfer rate drops dramatically as the species are forced to diffuse through the liquid.

For composite membranes, the thin coating which is placed on the liquid-side of the membrane avoids liquid breakthrough. However, membrane wetting due to capillary condensation may occur as a result of the porous support.

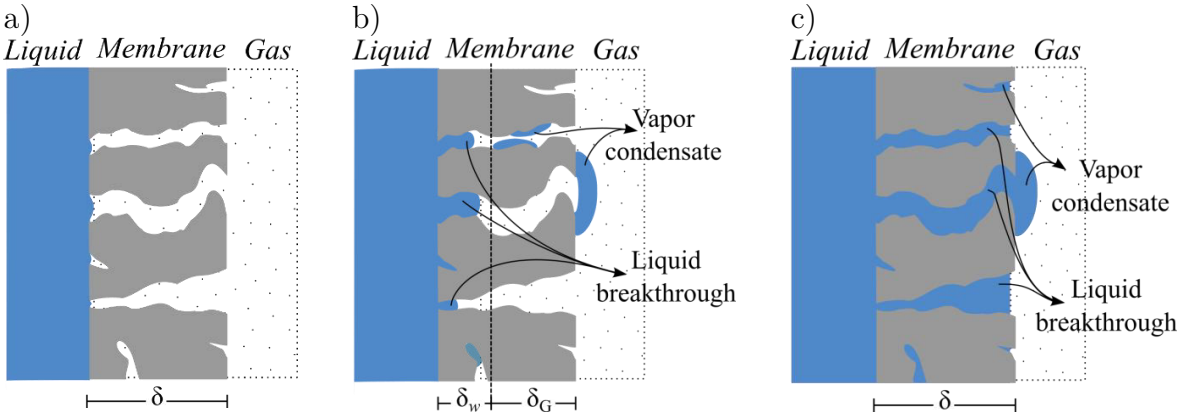

Figure 1.7 States of microporous membrane wetting: a) Gas filled pores, b) partially wetted and c) totally wetted

The breakthrough pressure, ΔP_{break}, is defined as the pressures difference between the gas and the liquid phase at which point the liquid can penetrate the membrane pores. This is estimated using the Laplace (Cantor) equation [39]:

$$\Delta P_{break} = -\frac{4\,\beta\,\gamma\cos(\theta)}{d_p{}^{max}} \tag{1.1}$$

where γ stands for the liquid surface tension, θ is the liquid-membrane contact angle, $d_p{}^{max}$ is the largest pore size, which is the most vulnerable to wetting. The coefficient β is a geometric factor used for non-cylindrical pores. Pore wetting occurs when the transmembrane pressure, $\Delta P_{L\text{-}G}$, is higher than ΔP_{break}. Consequently, the choice of a suitable combination of absorption liquid and membrane characteristics is crucial. An ideal combination would be a absorption liquid with high surface tension, e.g. $\gamma > 7\text{x}10^{-2}$ Nm^{-1} [23]–[27], and a membrane with both a high contact angle towards the liquid, e.g. $\theta >> 90°$ [37], as well as an optimal pore size, which would avoid breakthrough while maintaining sufficiently elevated mass transfer coefficients [40]. For the case of aqueous MEA solutions, depending on the CO_2 loading and temperature, the surface tension may vary from 5 to $7\text{x}10^{-2}$ Nm^{-1}, and the contact angle with PP membranes vary from 120 to 91°. As a result,

the combination of aqueous MEA with PP membranes is likely to suffer of membrane wetting by liquid breakthrough.

The critical water oversaturation, S_{crit}, is defined as the oversaturation at which water vapour condensates in a porous medium. This is estimated using the Kelvin equation [41]:

$$S_{crit} = \exp\left(-\frac{4\,\gamma_w \cos(\theta)\,V_w}{d_p\,RT_M}\right) \tag{1.2}$$

where γ_w stands for the water surface tension, d_p is the average membrane pore size and V_w is the water molar volume. Capillary condensation occurs when $S_w > S_{crit}$, where S_w stands for the oversaturation of water defined as the molar fraction of water in the membrane divided by the dew point water molar fraction calculated at the membrane temperature.

Pore wetting may occur more easily in an aged membrane contactor, as the structural change of the membrane due to aging generally corresponds to a modified pore shape, an increase in the average pore size and a decrease in the contact-angle [38]. Nowadays, there are not robust correlations to predict membrane aging due to chemical and physical attack.

1.2.5. Investigations on the Laboratory Scale

Various literature reviews of the utilisation of membrane contactors are available [11], [12], [14], [42]. An overview of the investigations in the PCC context performed on the laboratory scale is presented in this section and is divided in four parts, each in chronological order, as follows:

- Experimental investigations without modelling, presented in Table 1-4.
- One-dimensional modelling studies for the absorption step, presented in Table 1-5.
- Two-dimensional modelling studies for the absorption step, presented in Table 1-6.
- CO_2 stripping investigations, presented in Table 1-7.

In general, the laboratory scale consists of membrane contactors for which the membrane surface does not exceed the 0.1 m^2. For the investigations cited in this section, the fibre packing fractions vary from 0.15 to 0.6, the average being 0.3. As such, flow distribution issues related to contactors of a higher scale were not addressed in these works. The laboratory scale is characterized by mild operating conditions, corresponding to lab-gases (e.g. no ashes), short-term operation (e.g. no absorbent degradation), low reagent concentrations and conversions, i.e. high liquid-to-gas flowrate ratio and unloaded liquid absorbents. These conditions do not apply to industrial interests. In terms of modelling, isothermal single-component models supported by experimental results and counter-current flow arrangement were similar in most of the approaches.

Experimental investigations of the carbon absorption step (Table 1-4), addressed compatibility between liquid absorbent and membrane materials. It can be concluded that PP and PVDF membranes suffered wetting problems very likely attributed to altered surface properties of the membrane in contact with the solvent. PTFE membranes, on the other hand, showed relative stability over time.

The isothermal two-dimensional approach, shown in Table 1-5 and Table 1-6, not considering gas and liquid pressure drops, is the most common (two in five investigations employ a 1D approach). However, both the one- and two-dimensional approaches show good agreement between experimental data and simulation results, under the conditions in which they were compared. Complementing this further, only three published studies consider thermal effects and water transfer. From all investigations studying absorption using HFMC, it can be concluded that wetting occurred when PP or PVDF membranes were used and that using additives, such as NaCl, did not appear to help prevent wetting, which significantly decreases the contactor performance. Moreover, the CO_2 absorption flux per unit volume of HFMC is on average 4.43 $molm^{-3}s^{-1}$. Naturally, it depends on the nature of the solvent and the fibre packing, as well as on operating conditions, but it is a reliable performance indicator. To date, no long-term study has been performed under severe conditions, i.e. low liquid-to-gas flow rate ratio and preloaded liquid absorbents, and as such, the process of membrane aging remains poorly understood.

An overview of the stripping step investigations is presented in Table 1-7. In these investigations, unlike the conventional stripping process, low temperature stripping was studied, a process which requires water vapour and vacuum or nitrogen as the sweep gas. The results show that the CO_2 desorption specific flux to be almost two times smaller than the flux in absorption using HFMC. Moreover, when operating at 48 kPa of vacuum, energy consumption of regeneration using HFMC is lower than that for high temperature regeneration[5]. However, long-term running of membrane vacuum regeneration increases the risk of membrane wetting due to the increase of membrane pore size. It has been concluded that the increase of liquid flow rate, as well as increased temperatures and concentrations of the rich liquid absorbent, result in a significant increase of CO_2 stripping flux. Nevertheless, it is likely that these variables may not be modified in an absorption-desorption loop operation, since they are already constrained by CO_2 capture ratio specifications. Finally, while high temperature stripping is the reference process, its implementation by means of membrane contactors has not been addressed in literature. This is attributed to the fact that no economical membrane material can withstand such temperatures, i.e. around 120°C.

[5] Conventional stripping process as illustrated in Section 1.1.3.

Table 1-4 Experimental investigations of CO_2 absorption using HFMC

Membrane *Furnisher*	Gas mixture	Liquid abs. [Molarity]	u_L/u_G	Wetting [%]	Performance	Main remarks	Ref.
PP, PTFE *In house*	6.8-14.9% CO_2 in air	MEA[1-3M]; AMP [2 M] α^{LEAN} =0.02-0.3	[0.0043-0.017]	NA	K_{ov} ≈ [0.59 - 1.5]x10^{-3} ms^{-1}	PP membranes show a decline in performance over time when used with aqueous alkanolamine solutions; PTFE membranes maintain their initial level of performance. The counter-current mode of operation produced results that were 20% higher than results obtained under a co-current flow arrangement.	deMontigni et al 2006 [25]
PP	No gas	MEA [5M] MDEA[3M]	--	--	Hydrophobicity loss of PP after 60 days of immersion	Absorbent molecules diffuse into PP during immersion, resulting in membrane swelling. The interaction between the membrane and the absorbent alters the surface properties and reduces the hydrophobicity of the membrane. No chemical reaction occurs between PP and the solvent.	Lv et al. 2010 [43]
PP, PTFE, PMPc, AFc	15% CO2 in N2	MEA [5M]	NA	K_{ov} drops 50% after 25 days for PP	K_{ov} ≈ [0.6-3.3]x10-4 ms-1	After 25 days exposure to MEA, a drop in the mass transfer rate by 18 (PTFE) and 20% (plasma-treated) is observed. PTFE fibres show a relatively good resistance to wetting effects. But, they are more expensive. PTFE does not allow small diameter fibres to be produced	Chabanon et al. 2011 [44]

Table 1-5 1D-modelling with (unless specified) experimental investigations of CO_2 absorption using HFMC

Membrane *Furnisher*	Gas mixture	Liquid abs. [Molarity]	u_L/u_G	Wetting [%]	Performance	Main remarks *(unless otherwise indicated, the studies are **isothermal, counter-current** and have **experimental data**)*	Ref.
PP *In house*	CO_2 pure	Water; Propylene Carbonate (PC)	Semi-batch u_L= [0.03-0.8] ms^{-1}	Flux CO_2 drops from up to 50% after 2 weeks	$k_{M,CO2}^{eq} \approx$ [10^{-3} - 10^{-2}] ms^{-1}	The wetting problem in long-term application can be avoided by applying over-pressure on the gas-side. However, in such case, the liquid pressure drops over the fibre length and becomes a critical design parameter to ensure a non-wetted mode of operation. The overall mass transfer coefficient is found to be independent of the system pressure	Dindore et al 2004 [45]
PVDF, PP Celgard	20 % CO_2 in N_2	DEA [2M] α^{LEAN} ~0	[1.3-4]	[0-10]	PP: Flux $CO_2 \approx$ [1.7 - 5.8] $molm^{-3}s^{-1}$ PDFV: Flux $CO_2 \approx$ [1.8 - 5.7] $molm^{-3}s^{-1}$	Both the PP and PVDF modules were found to be wetted. The mass transfer in the wetted membrane phase is the rate-controlling step. CO_2 absorption performance cannot be effectively improved by adjusting the liquid velocity or the gas velocity unless the wetting could be mitigated.	Zhang et al. 2008 [46]
PP, PVDF Memcar ®	20 % CO_2 in N_2	MEA, DEA, AMP, MEA+ NaCl, MEA + SG [0 - 0.1M]	[2-5]	K_{ov} drops 75% after 12 days	Flux $CO_2 \approx$ [0.1-0.4] $molm^{-3}s^{-1}$ $K_{OV} \approx$ [1-8]x10-7 ms^{-1}	The use of MEA solution and SG as absorbents gave highest CO_2 flux. The use of mixed amine solutions and the addition of NaCl did not help protect the membrane wetting but the addition of SG in to MEA solution can improve flux and prevent from membrane wetting.	Rongwong et al. 2009 [47]
PP	15% CO2 rest N2	MEA [1.2M] α^{LEAN}= 0.24 α^{RICH}= 0.48	4.79 * 10-3	No wetted condition	Flux $CO_2 \approx$ [1-25] $molm^{-3}s^{-1}$	*Simulations* Reducing the external radius of the fibres leads to a process intensification. Liquid flow around the fibres that proceeds with gas flowing through the lumen of the fibres is shown to be particularly effective.	Rode et al. 2012 [48]
PTFE PVDF	15% CO2 in N2	MEA [3 M] α^{LEAN}= 0-0.3	Varying	0-50	Flux $CO_2 \approx$ 0.6 $molm^{-3}s^{-1}$	*Adiabatic* PTFE are modelled without wetting. Fitting of PVDF experimental data required 50% of membrane wetting.	Rongwong et al. 2013 [49]

Table 1-6 2D-modelling with (unless specified) experimental investigations of CO_2 absorption using HFMC

Membrane *Furnisher*	Gas mixture	Liquid abs. [Molarity]	u_L/u_G	Wetting [%]	Performance	Main remarks *(unless otherwise indicated, the studies are **isothermal, counter-current** and have **experimental data**)*	Ref.
PTFE *W.L.Gore ®*	0.5-10% CO_2 in N_2	MEA [5 M] MDEA [1M] α^{LEAN}= 0-0.4	[2-8]x10^{-3}	No-wetting	Flux CO_2 ≈ [0.4-1.9] molm^{-3} s^{-1} $k_{M,CO2}^{eq}$ ≈ 3x10^{-2} ms^{-1}	*Adiabatic* The diffusion of the ionic reaction products is the rate limiting factor. Models of membrane contactors for diffusion-reaction systems must discretize the liquid film.	Hoff et al. 2004 [50]
PP *Celgard*	20 % CO_2 in N_2	DEA [1M] α^{LEAN} ~0	[1.3-4]	[0-5]	Flux CO_2 ≈ [2.3- 4.6] molm^{-3}s^{-1}	The reduction of overall mass transfer coefficient may reach 20% even if the membrane pores are 5% wetted.	Wang et al. 2005 [51]
PP *Celgard*	20 % CO_2 in N_2	DEA [2M]; α^{LEAN} ~0	[0.8-2.3]	No-wetted condition	Flux CO_2 ≈ [1.6 - 5.6] molm^{-3}s^{-1}	*Co-current flow* Gas phase CO_2 concentration serves as the rate-determining factor for the reaction between CO_2 and DEA. The increase of the module length is not a useful approach to enhance CO_2 absorption when the module length is longer than L_{eff}.	Zhang et al. 2006 [52]
PP	20 % CO_2 in N_2	DEA [2M] α^{LEAN} = 0	[1.3-4]	[0-85]	Flux CO_2 ≈ [2.3- 4.6] molm^{-3}s^{-1}	Flux CO_2 drops from up to 30% after 6 days. The chemical reactions inside the wetted pores have considerable positive effects on the prediction of membrane wetting fraction.	Keshavarz et al. 2008 [53]
PP	CO_2 pure	DEA [0.01-10M] AMP [0.01-10M] DIPA [0.01-10M] For all: α^{LEAN} = 0	v_L: [0.01-0.1] ms^{-1}	No-wetted condition	Capture ratio ≈ 0.95	*Simulations* A two-step carbamate formation mechanism is proposed. The AMP presents a higher absorption capacity and better selectivity than the other two amines	Boucif et al. 2008 [54]

PP, PVDF *Pall Co.*	1-15 % CO_2 in N_2	AMP+PZ; [1M]α^{LEAN}=0 MDEA+PZ ; [1M]α^{LEAN}=0	[0.6 - 2.5]	[0.07-0.4] (PP) [0.04-0.4] (PVDF)	$k_{M,CO2}^{eq}$ ≈ [1.09 - 8.34]x10^{-3} ms^{-1}	The wetting of membrane is only important in the system using an absorbent with a high reaction rate.	Lin et al. 2009 [26]
PTFE	0.8-20% CO_2 in N_2	PG [0.5-3 M] α^{LEAN}= 0	[0.9-5]	No-wetted condition	Flux CO_2 ≈ [0.1-1] $molm^{-3}$ s^{-1}	*Simulations* CO_2 mass transfer rate and removal efficiency were favored by concentration of PG, liquid flow rate and liquid temperature. The gas temperature has no influence on the removal efficiency	Eslami et al. 2011 [55]
Non-specified	0.5-50% CO_2 in N_2	MEA [5M] α^{LEAN}= 0	0.6-2	10%	Flux CO_2 ≈ [1-20] $molm^{-3}$ s^{-1}	The decrease in gas velocity, due to the CO_2 absorption, becomes significant for the higher CO_2 content.	Faiz et al. 2011 [56]
PP, PDMS	12% CO_2 rest N_2	MEA [1.2M] α^{LEAN}= 0	[1.6* 10^{-2} - 1.04]	No-wetted condition	Capture ratio < 0.75	*Simulations* Describing the shell domain gas velocity by plugflow, Happel free surface and Navier-Stokes models reveals that the latter fits better the experimental results.	Boucif et al. 2012 [57]
PTFE, PMP	0.5-15 % CO_2 in N_2	MEA [3-5 M] α^{LEAN}= 0-0.242	[0.5-1]x10^{-2}	No-wetting	$k_{M,CO2}^{eq}$ ≈ [0.8-1.3]x10^{-3} ms^{-1}	Different models lead to comparable predictions of the experimental results, with slightly similar membrane mass transfer coefficient values.	Chabanon et al. 2013 [58]

Table 1-7 CO_2 stripping investigations using HFMC

Membrane *Furnisher*	Gas mixture	Liquid abs. [Molarity]	u_L/u_G	Wetting [%]	Performance	Main remarks *(unless otherwise indicated, the studies are **isothermal, counter-current** and involve **experimental data and modelling**)*	Ref.
PTFE	N_2 as sweep gas	MEA [3-7M] $\alpha^{RICH} = 0.45$	[0.05-0.2]	CO_2 desorption flux drop of 50% after 8	$k_{M,CO2}^{eq} \approx 5x10^{-3}$ ms^{-1} Flux $CO_2 \approx$ [0.3-1.6] molm^{-3}s^{-1}	*1D Modelling & Experiments* The stripping gas velocity had a minor effect on the CO_2 desorption flux. A high membrane porosity showed a superior desorption performance, but the long term performance deteriorated due to the membrane wetting	Khaisri et al. 2011 [59]
PVDF	CO2 pure	Water	[5-45]	High wetting resistance. No wetting	Absorption flux CO_2 ≈[0.1-1.2] molm^{-3}s^{-1} Stripping flux CO_2< 0.1 molm^{-3}s^{-1}	*Only experiments* Absorption & stripping The CO_2 absorption flux was approximately 10 times higher than the CO_2 stripping flux at the same operating condition due to high solubility of CO2 in water.	Mansourizadeh et al. 2012 [60]
PP *Zheda Kaihua®*	H_2O in vacuum (48 kPa)	MEA [3M] $\alpha^{RICH} = 0.5$	0.02	Occurs after 480h	CO_2 desorption flux ≈ 0.2 molm^{-3} s^{-1}	*1D Modelling & Experiments* When operating at 48 kPa of vacuum, the energy consumption of the regeneration using HFMC is lower than that of thermal regeneration. Long-term running of membrane vacuum regeneration increases the risk of membrane wetting due to an increase of membrane pore size.	Fang et al. 2012 [19]
PVDF *In house*	N_2 pure	DEA [1-3 M] $\alpha^{RICH} =$ NA		No wetted condition	CO_2 desorption flux ≈ [0.2-1.4] molm^{-3} s^{-1}	*1D Modelling & Experiments* Increasing the liquid flow rate, as well as the temperature and concentration of the rich solvent, results in a significant increase of CO_2 stripping flux.	Rahbari-Sisakht et al. 2013 [61]
PVDF PEI *In house*	N_2 pure	DEA [1 M] $\alpha^{RICH} = 0.4$	1.2 - 7	NA	CO_2 desorption flux ≈ [0.4-3.8] molm^{-3} s^{-1}	*Only experiments* Despite having smaller pore size, the PEI experienced membrane wetting In addition, the desorbed CO_2 flux were lower than those observed for PVDF.	Naim et al. 2014 [17]
Non-specified	H_2O in vacuum (20 kPa)	MEA [3M] $\alpha^{RICH} = 0.5$	Varying	0-100	CO_2 desorption flux ≈ [0.02-0.1] molm^{-3} s^{-1}	*Simulation 2D modelling. Co-current flow arrangement* Increasing membrane's length will improve CO_2 stripping performance, but not infinitely due to the thermodynamic limitation. Membrane wetting significantly deteriorates CO_2 membrane desorption performance.	Wang et al. 2013 [62]

1.2.6. Investigations on the Pilot-Plant Scale

In the context of industrial application, hollow fibre membrane contactors have been in use for the past decade in various pilot plant tests performed in the Netherlands, France, China and Australia. Available operating conditions together with the most important results of pilot plant tests are summarized in Table 1-8. Mainly commercial contactors were used for these tests (Liqui-cell ® and Celgard ® for PP and Polymem contactor for PTFE). The operation mode was consistently counter-current, while the local flow was either transversal or parallel, depending on the technology used. The total membrane surface varied between 0.27 and 24 m^2, as much as 200 times higher than that used on the laboratory scale.

Most of the investigations were performed using aqueous solutions of pure MEA or reactant mixtures containing MEA. However, Scholes et al. [33] used a commercial absorption liquid formulation and Feron et al.[23] used a patented formulation. Lab-gases as well as flue-gases were used. The investigations were performed by setting lower liquid-to-gas flow rate ratios than those found in the laboratory scale investigations, with some of them using partially loaded liquid absorbents. These conditions combined with high membrane areas correspond to more severe conditions than those applied on the laboratory scale, but were not as severe as would be found in industrial application.

Earlier work conducted in a pilot plant focused on economic membrane material, i.e. PP and PVDF, and diluted solutions in order to reduce investment costs while preventing wetting [23], [27]. Despite this fact membrane wetting was frequently observed. As discussed in Section 1.2.5, laboratory experiments showed that the more expensive PTFE fibres can prevent wetting when operating with low liquid reactant concentrations [38]. However, low concentrations are not relevant from an economical point of view. More recent pilot investigations were performed using PTFE membrane contactors together with high reactant concentrations. Again, membrane wetting was reported. Further still, Scholes et al. [33] and Chabanon et al.[63] noticed liquid droplets in the outflowing gas.

Another issue addressed by the different investigators is pertinent to shell-side distribution, whether or not the liquid or the gas-phase flows through this compartment. Axial dispersion, channelling, as well as dead-zones appear to reduce mass-transfer performances.

In most of the investigations, the average overall mass-transfer coefficient is not reported. However, its value seems to be relatively low which is likely linked to membrane wetting. The average CO_2 absorbed flux per unit volume is comprised between 0.6 and 4 $molm^{-3}s^{-1}$ which is still higher than that reached in industrial packed columns operation [64]. This information should be considered with some reserve, as lean liquid loading as well as liquid and gas reagent conversions attained in HFMC pilot plants are low in general when compared to industrial scale packed-column operations.

Table 1-8 Pilot plant test of membrane contactors for post-combustion CO_2 chemical absorption

Parameter	Feron et al. 2002 [23]	Yeon et al. 2005 [65]	Yang et al. 2008 [66]	Vogt et al. 2011 [27]	Scholes et al. 2014 [33]	Chabanon et al. 2014 [63]	EnergieCapt 2014 [67]
Contactor							
Contactor type and operation mode	In-house Counter-current Transversal flow	Commercial Counter-current Parallel flow	Commercial Counter-current Parallel flow	Commercial Counter-current Parallel flow	Commercial & in-house Counter-current Transversal & Parallel flow	Commercial Counter-current Parallel flow	Commercial Counter-current Parallel flow
Liquid exchange surface (m^2)	0.27	2.8	3.02	24	0.017 – 7.01	10.2	10.2
Contactor length(m)	0.2	0.52	0.8	Non reported	0.14 – 0.25	0.8	0.8
Packing fraction	~ 0.3	0.4	0.1	Not reported	0.03 – 0.37	0.59	0.59
Membrane type	microporous PP	microporous PVDF	microporous PP	microporous PP	microporous PP microporous PTFE dense PDMS	Micro-porous PTFE	Micro-porous PTFE
External fibre radius (m)	5×10^{-4}	5.3×10^{-4}	2.23×10^{-4}	Not reported	$(1 – 1.5) \times 10^{-4}$	4.35×10^{-4}	4.35×10^{-4}
Fibre thickness (µm)	100	116	50	Not reported	20 – 54	217	217
Contactor diameter (m)	Not reported	7.6×10^{-2}	8×10^{-2}	Not reported	$(4.5 – 8.5) \times 10^{-2}$	0.108	0.108
Gas							
Gas type	CO_2-air mixture	Flue gas	Lab gases	Flue gases	Flue gases	Lab gases	Flue gases
Flow rate (Nm^3h^{-1})	0.5 – 4	1.2 – 2.5	4.42 – 12.13	< 2.5	Not reported	0.3 – 1.8	11 – 18
Temperature (K)	313	313	293 – 323	Not reported	~ 313	298	~325
Pressure (kPa)	Atmospheric pressure	Not reported	106	Not reported	Fluctuating	Not reported	100
Inlet CO_2 mole-frac	4×10^{-4} – 0.4	0.11	0.14	0.14	0.12	0.15	0.105
Liquid							
Absorbent type	CORAL	MEA–TEA mixture	MEA	MEA-DGA-K-glycerine blend	PuraTreat™ F	MEA	MEA

Reactant content (Molarity or wt.)	2 M	0.1 wt.	0.06 wt.	< 0.1 wt.	0.3 wt. suggested	0.3 wt.	0.3 wt.
Flow rate (L h^{-1})	0.520	36 – 108	50 - 200	< 2	Not reported	30 – 198	30 – 80
Temperature (K)	303 – 313	313	293 – 323	Not reported	~ 313	298	288
Pressure (kPa)	Not reported	Not reported	>106	Not reported	50 over gas pressure	110	105
Lean CO_2 loading	0.05 – 0.4	Not reported	0 – 0.06	Not reported	0.17	Partially loaded	0 – 0.16
Results							
Gas-liquid flow configuration	Liquid in lumen	Liquid in lumen	Liquid in lumen	Liquid in shell	Liquid in shell	Liquid in lumen	Liquid in lumen
L/G ratio ($m^3_L m^{-3}_G$)	$7.5x10^{-3}$ – 2.4	(1.4– 9) $x10^{-2}$	$4.1x10^{-3}$- $4x10^{-2}$	$8x10^{-4}$ -$4.7x10^{-3}$	Not reported	1 $x10^{-2}$ – 0.7	(1.6– 7.2) $x10^{-3}$
Average CO_2 absorbed flux per unit volume (mol $m^3 s^{-1}$)	1 – 4	0.6 – 1.3	1.6 – 2.16	Not reported	Not reported	Not reported	1.45 – 2.33
Overall mass transfer coefficient (m s^{-1})	1.6 $x10^{-3}$	No value	3.6 – 4.9 $x10^{-4}$	No value	PP: $9x10^{-4}$ – $1.3x10^{-3}$ PTFE: 1.5 $x10^{-3}$ PDMS: 3 $x10^{-6}$ – $7x10^{-6}$	~$5x10^{-5}$	~$5x10^{-4}$
Remarks/comments	No membrane wetting observed in experiments performed intermittently over 4 months.	CO_2 absorption rate 2.7 times higher than in packed columns. Membrane wetting observed after 80h of operation, for the MEA-PVDF combination. For hybrid absorption liquid (i.e. MEA-TEA), no wetting occurred.	The operation was performed over a short time period (no additional details available) No wetting was observed.	The liquid mixture is formulated in order to maintain high surface tensions. Membrane wetting was observed after a few hours of operation. Hence, no intensification was obtained.	Wetting observed for PP and PTFE membranes, and attributed to the fluctuating flue gas pressure. No significant ash build up and no influence of minor components as SO_x on the contactor performance. Increase of the *in-shell* fluid *Reynolds* number enhanced the overall mass transfer for transversal flow.	Low overall mass transfer coefficients were measured, reflecting wetting and/or channelling issues.	Low overall mass transfer coefficient reflecting wetting and/or channelling issues.

1.3. Summary and Conclusions

Post-combustion carbon dioxide capture represents an important strategy for mitigating energy-related CO_2 emissions. The most advantageous PCC process is chemical absorption, performed by using packed column technology. The treatment of large quantities of flue gases requires large-size equipment.

Hollow fibre membrane contactors (HFMC) are attractive in that they allow for considerable reduction in equipment size due to their high interfacial area. Laboratory scale and pilot plant investigations have produced promising results in terms of intensification potential, represented by the CO_2 absorption flux per unit volume, which has been found to be from 2 to 8 times higher than that observed in packed columns. Nevertheless, no investigation to date has addressed absorption or the stripping step using HFMC under relevant industrial operating conditions, i.e. high reactant conversions and partially loaded lean liquid absorbents. Moreover, HFMC technology is subject to membrane wetting which is a principal concern of membrane contactor performance.

The actual selection of an adequate model approach for HFMC remains slightly ambiguous since both the one- two- dimensional approaches used by several authors have produced acceptable predictive results. Moreover, the thermal effects and water transfer have been scarcely taken into account.

1.4. Résumé et conclusions

Dans l'objectif de limiter les émissions de CO_2 liées à la production d'énergie (issue des ressources carbonées), le captage du CO_2 contenu dans les fumées de postcombustion est une stratégie indispensable/incontournable. Le procédé de captage de référence est l'absorption réactive, suivie d'une étape de stripage, toutes deux mises en œuvre dans des colonnes à garnissage. L'importante quantité de gaz à traiter impose cependant des équipements de grande taille.

Une technologie intéressante permettant d'atteindre une réduction de la taille des installations est le contacteur membranaire à fibres creuses (CFMC), puisqu'il permet de développer d'importantes surfaces spécifiques. Des travaux de la littérature à l'échelle du laboratoire et à l'échelle pilote ont montré des résultats prometteurs en termes d'intensification, par comparaison du flux de CO_2 absorbé par unité de volume. En effet, les valeurs relevées sont de 2 à 8 fois plus grandes en CMFC qu'en colonnes à garnissage. Cependant, l'opération d'absorption et de stripage en utilisant des contacteurs membranaires dans des conditions d'intérêt industriel, (i.e. en imposant des conversions élevées de réactifs et en utilisant des absorbants liquides partiellement chargés), n'a pas encore été étudiée. Par

ailleurs, les CMFC sont soumis à un phénomène de mouillage des membranes, ce qui est un problème majeur de la performance de cette technologie.

Le choix d'une stratégie de modélisation adéquate pour ce procédé de captage en CMFC est ambigu, puisque les approches monodimensionnelles et bidimensionnelles, publiées par plusieurs auteurs, ont fourni des résultats prédictifs acceptables. Par ailleurs, les effets thermiques et le transfert d'eau associé n'ont guère été pris en compte.

Chapter 2. Thermodynamics and reaction kinetics of carbon dioxide absorption in aqueous amine solutions

The principle mechanism of carbon dioxide capture by chemical absorption resides in the affinity of CO_2 with the liquid absorbent, which is higher than that of other compounds present in the gas to treat. Once the CO_2 is physically absorbed by the liquid, it reacts chemically with the reactant component of the liquid, e.g. amines, and becomes chemically-bounded in an ionic form. Since ionic species are non-volatile, the solubility of CO_2 *increases* relative to physical absorption.

The thermodynamics substantially influence the separation process because it determines the driving force as well as the reaction rates. Therefore, an accurate description of the thermodynamic equilibria is essential for predicting performance of the separation units. The chemical reactions involved in this type of system are known to be kinetically controlled, thus description of the reaction kinetics is likewise essential for predicting performance of the separation unit. This chapter outlines modelling of the thermodynamics, the reaction kinetics, and modelling of auxiliary operations used in the absorption-desorption process.

2.1. Thermodynamic Models of CO_2 Solubility

The thermodynamic equilibria of the CO_2-N_2-MEA-H_2O system is illustrated in Figure 2.1. The molecular species in a gaseous state are absorbed or condensate at the vapour-liquid interface, at which point they react in the liquid phase until reaching chemical equilibrium. Therefore, thermodynamic models consist in the description of both vapour-liquid and chemical equilibrium.

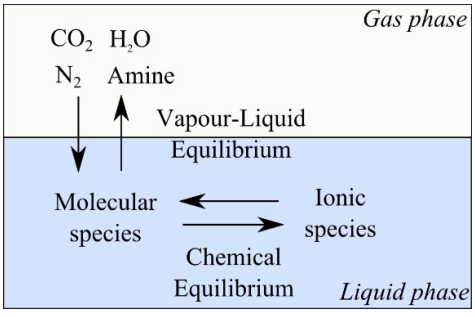

Figure 2.1 Schematic representation of the CO_2 solubility in aqueous amine solutions

Optimal modelling strategies require simplicity and accuracy at every stage, including the thermodynamic description of the system. Models with too many parameters are complex, time consuming and cumbersome. That said, models which are too simple in form can provide less accurate results. Thus, there is a trade-off between complexity and accuracy.

The simplest model links gaseous CO_2 concentrations proportionally to liquid concentrations solely by means of a solubility constant (Henry's law), which is estimated using empirical correlations [68]. This approach cannot be applied to kinetically controlled systems, since chemical reactions make concentrations near the interface different to those of the bulk liquid. In addition, these models cannot estimate further properties such as amine volatility, heat of absorption or the distribution of chemical composition in the liquid phase. The latter is known as true liquid speciation and is necessary to compute reaction rates.

The true speciation can only be estimated by thermodynamic models of these systems. It can be computed by simultaneously solving the equations corresponding to the molar balances of each species, the electric charge balance and the chemical equilibrium associated with each chemical reaction [69]. Thus the problem resides in the estimation of the chemical equilibrium, which can be described using chemical equilibrium constants [70]. The equilibrium constants available in literature, usually expressed in polynomial form as a function of temperature, correspond to those of diluted species, relating the concentrations (e.g. molar concentration or molar fraction) of the reactants and products [71]. True speciation calculation using these equilibrium constants leads to significant deviations from the experimental data, within the interval of interest for concentrations [72].

Thermodynamic models based on activity coefficients take into account mixture interaction effects, thus correcting deviations that occurred using expressions for diluted species. Indeed, these models are based on the excess Gibbs free energy formulations [71], [73]–[75]. The mixture interactions may be classified by local (combinatorial and/or residual)[6] and long-range contributions (Debye-Hückel ion-ion interactions). The simplest of the excess Gibbs free energy thermodynamic approaches which has been used successfully for systems such as amine[7]-CO_2-H_2O, is based on the specific ion interaction theory (SIT), which only takes into account long-range contributions. However, this approach has not yet been used within rate-based transfer models for CO_2 absorption, where a physically meaningful representation of the mixture interactions is believed to be crucial. Moreover, prediction of additional properties, such as heat of absorption, is not clear and has not been proved to be suitable. Adding to their complexity, electrolyte-NRTL and UNIQUAC models, which

[6] It depends whether it is within the frame of UNIQUAC or elcNRTL formulations.

[7] MEA, AMP, Piperazine and AMP-PZ mixtures at high concentrations [73]

take into account the group of interactions mentioned above, are able to predict the true speciation as well as all thermodynamic properties with physical meaning, and thus are reliable means for extrapolating. Moreover, application of both approaches within rate-based transfer models has been proved to be suitable [64], [76], [77]. Nevertheless, fitting for a large number of parameters required for these models has been found to be complicated. Further, the results are strongly dependent on the experimental methods used to obtain the required data.

Despite the different formulations, the excess Gibbs free energy models have the following points in common: 1) iterations are required since the activity coefficients depend on true speciation, which itself depends on these coefficients, 2) equations of molar balances, electric charge balance and chemical equilibrium associated with each chemical reaction need to be solved and their convergence is strongly sensitive to the initial point, and 3) in addition to the interaction parameters, it has been found that the equilibrium constants have also been fitted . In order to prevent iterations and thus reducing calculation time of the CO_2 absorption model with amine aqueous solutions by means of membrane contactors, Hoff et al. [50], [78] have stated that, with an adequate formulation, speciation can be solved in a straightforward manner. In addition, they introduced activity coefficients in the form of polynomials in order to tune the thermodynamic model, fitting experimental data. By contrast, Aboudheir et al. [69] introduced apparent equilibrium constants to take into account the nonidealities of the system and rigorously solved the system of equations corresponding to speciation. Similarly, Puxty et al. [73] adjusted the diluted species equilibrium constant but included computation of long-term interactions. The models of Hoff et al., Aboudheir et al. as well as Puxty et al. have shown excellent agreement between the experimental data and the model predictions, with significantly fewer parameters to fit than more complex models while maintaining a physical representation.

The approach implemented in this present work is an adaptation of the three investigations previously mentioned. Indeed, the formulation to solve the chemical speciation without iterations is employed, and the equilibrium constants are fitted to lump the nonidealities of the system. The introduction of long-term interactions had no positive effect on the accuracy of the model. The approach is detailed in the following sections.

2.1. Vapour-Liquid Equilibria

The phase equilibria are described through the equality of liquid and vapour chemical potentials for each compound. Since the gas contains vapour or non-supercritical species, i.e. H_2O and MEA, and gas or supercritical species, i.e. CO_2 and N_2, formulation for the chemical potential is carried out heterogeneously. That is, the water is treated as the solvent and the other species as the solutes.

For the vapour species:

$$y_i \phi_i P = x_i \gamma_i P_i^{sat} exp\left(\frac{V_i^l (P - P_i^{sat})}{RT}\right) \tag{2.1}$$

For the gas species:

$$y_i \phi_i P = x_i \gamma_i \frac{\mathcal{H}_i C_l^{tot}}{\gamma_i{}^{\infty}} exp\left(\frac{V_i^{\infty}(P - P_{H_2O}^{sat})}{RT}\right) \tag{2.2}$$

where
P_i^{sat} is the saturation pressure of component *i*,
ϕ_i is the fugacity coefficient of the gas phase for component *i*,
$\mathcal{H}_i$ is the Herny constant for component *i*, in concentration units,
$\gamma_i{}^{\infty}$ is the infinite dilution activity coefficient for gas species in water,
V_i^l is the molar volume of pure solvent at saturation pressure,
V_i^{∞} is Brelvi-O'Connell partial molar volume for CO_2 at infinite dilution in H_2O,
y_i is the *real* or true mole fraction in the vapour phase of component *i*, and,
x_i is the *real* or true mole fraction in the liquid phase of component *i*.

Since the operating pressures of post-combustion capture do not exceed a few bars, the factor the Poynting (the exponential term in both expressions) can be neglected and the fugacity coefficients are close to unity. The ionic components of the liquid phase are considered as non-volatiles, thus their saturation pressure is set to zero. As discussed in Section 2.1, the activity coefficient for CO_2 is set to unity as the non-idealities are taken into account in the evaluation of equilibrium constants. Since the interaction between nitrogen and both water and amine are weak, the activity coefficient of N_2 is also set to unity.

The influence of water activity was found to be significant in the modelling of gas-liquid transfer phenomena, specifically for the desorption step for CO_2 post-combustion capture with chemical liquid absorbents [79]. Therefore, in this work, activity coefficients for water and MEA were established as only composition dependent. The expressions are provided below with values fitted from [75].

For water:

$$\gamma_{H_2O} = 0.85 + 0.15 {x_{H_2O}}^2 \tag{2.3}$$

For MEA:

$$\gamma_{MEA} = 0.7 + 0.3 {x_{MEA}}^2 \tag{2.4}$$

The equality of liquid and vapour chemical potential can now be formulated as a function of the phase equilibrium constant $\mathcal{K}_i^{VLE}$.

$$y_i = \mathcal{K}_i^{VLE} x_i \tag{2.5}$$

For the vapour species:

$$\mathcal{K}_i^{VLE} = \frac{\gamma_i P_i^{sat}}{P} \tag{2.6}$$

and for the gas species:

$$\mathcal{K}_i^{VLE} = \frac{\mathcal{H}_i C_l^{tot}}{P} \tag{2.7}$$

The partial pressure of each compound is calculated using the Equation 2.5, for the respective true mole fraction in the liquid phase, which is at chemical equilibrium. The Henry constant has been taken from [80] and the saturation pressures from [75].

2.2. Chemical Equilibrium

The chemical equilibrium describing species distribution, or speciation, of the liquid phase is based on the formulation provided by Astarita et al. [81]. For the purpose of this work, the equations are expressed for the Monoethanolamine (MEA), but it can be easily adapted to other aqueous amine liquid absorbents.

2.2.1. Chemical Reactions Involved

The involved set of independent chemical reactions is as follows:
Water ionization:

$$H_2O \overset{K_1}{\Leftrightarrow} H^+ + OH^- \tag{2.8}$$

Dissolved CO_2 dissociation:

$$CO_2 + H_2O \overset{K_2}{\Leftrightarrow} H^+ + HCO_3^- \tag{2.9}$$

Bicarbonate dissociation:

$$HCO_3^- \overset{K_3}{\Leftrightarrow} H^+ + \ CO_3^{-2} \tag{2.10}$$

Dissociation of protonated amine:

$$MEAH^+ \overset{K_4}{\Leftrightarrow} MEA + H^+ \tag{2.11}$$

Carbamate formation:

$$MEA + HCO_3^- \overset{K_5}{\Leftrightarrow} MEACOO^- + \ H_2O \tag{2.12}$$

This set of chemical reactions is commonly expressed in terms of the following reactions:

Free CO_2 absorption, combination of Equations 2.9, 2.11 and 2.12:

$$CO_2 + 2MEA \overset{K_6}{\Leftrightarrow} MEACOO^- + H_2O \tag{2.13}$$

Carbonate formation, combination of Equations 2.10 and 2.11:

$$HCO_3^- + MEA \overset{K_7}{\Leftrightarrow} MEAH^+ + CO_3^{-2} \tag{2.14}$$

Bicarbonate formation, combination of Equations 2.12 and 2.13:

$$CO_2 + MEA + H_2O \overset{K_8}{\Leftrightarrow} HCO_3^- + MEAH^+ \tag{2.15}$$

The equilibrium of a chemical reaction occurs when the Gibbs free energy of the system reaches its minimum value. At this point, the relation between the activities of each compound is only temperature dependent and corresponds to the equilibrium constant. For a reaction *j*, the equilibrium is formulated as a function of the activity of compound *i*, as follows:

$$K_j = \prod_i {a_i}^{\nu_{i,j}} \qquad \text{where } a_i = \gamma_i C_i \tag{2.16}$$

where $\nu_{i,j}$ stands for the stoichiometric coefficient of the compound *i* in the reaction *j*. As discussed in Section 2.1, since the equilibrium constants account for the nonidealities of the system, Equation 2.16 can be directly formulated as a function of the molar concentration C of the species *i*:

$$K_j = \prod_i {C_i}^{\nu_{i,j}} \tag{2.17}$$

2.2.2. Mathematical Formulation based on the Extent of Reaction

In order to calculate the concentration of the species at chemical equilibrium for a given initial concentration, the concept of *extent of reaction* is introduced. For a reaction *j*, the extent of reaction ξ, describes the variation of the molar concentration from an initial value C_i^0, to a final value C_i. Such value satisfies the molar balance for each species:

$$C_i = {C_i}^0 + \sum_j \nu_{i,j}\xi_j \tag{2.18}$$

The value of the extent of reaction at chemical equilibrium must satisfy Equation 2.17:

$$K_j = \prod_i \left(C_i^{\,0} + \sum_j \nu_{i,j} \xi_j \right)^{\nu_{i,j}} \tag{2.19}$$

The overall molar balances for the molecular species, or *apparent*[8] species, may be written as follows:

For MEA:

$$C_{MEA}^{tot} = C_{MEA} + C_{MEACOO} + C_{MEAH} \tag{2.20}$$

For CO_2:

$$C_{CO_2}^{tot} = \alpha C_{MEA}^{tot} = C_{CO_2} + C_{MEACOO} + C_{HCO_3} + C_{CO_3} \tag{2.21}$$

For water:

$$C_{H_2O}^{tot} = C_{H_2O} + C_{HCO_3} + C_H + C_{OH} + C_{CO_3} \tag{2.22}$$

where α stands for the total moles of CO_2 per mole of MEA. This ratio is also known as the CO_2 loading. It is convenient for the speciation computing, to express the loading of chemically-bound CO_2:

$$\dot{\alpha} C_{MEA}^{tot} = \alpha C_{MEA}^{tot} - C_{CO_2} \tag{2.23}$$

The principle of the Astarita formulation is that the speciation may be calculated independent of the concentration of the absorbing and volatile species. Accordingly, the chemical equilibrium is split into two separated steps:

1) The CO_2 and the MEA react to form only bicarbonate and the protonated amine, which corresponds to Equation 2.15. At this stage, the molar balances provide the initial concentration for the chemical reactions between the amine and CO_2.
   For MEA:

$$C_{MEA}^{0} = C_{MEA}^{tot}(1 - \dot{\alpha}) \tag{2.24}$$

   For $MEAH^+$:

[8] The term "apparent" was used in the publications related to the adiabatic modelling of membrane contactors.

$$C^0_{MEAH^+} = C^{tot}_{MEA}\dot{\alpha} \tag{2.25}$$

For $MEACOO^-$:

$$C^0_{MEACOO^-} = 0 \tag{2.26}$$

For HCO_3^-:

$$C^0_{HCO_3^-} = C^{tot}_{MEA}\dot{\alpha} \tag{2.27}$$

For CO_3^{-2}:

$$C^0_{CO_3^{-2}} = 0 \tag{2.28}$$

For water:

$$C^0_{H_2O} = C^{tot}_{H_2O} - C^0_{HCO_3^-} \tag{2.29}$$

2) The reactions between the bicarbonate and the amine, which correspond to Equations 2.12 and 2.14, now take place. The molar balance equations may be expressed as functions of the respective extents of reaction.

For MEA:

$$C_{MEA} = C^0_{MEA} - \xi_5 - \xi_7 \tag{2.30}$$

For $MEAH^+$:

$$C_{MEAH^+} = C^0_{MEAH^+} + \xi_7 \tag{2.31}$$

For $MEACOO^-$:

$$C_{MEACOO^-} = C^0_{MEACOO^-} + \xi_5 \tag{2.32}$$

For HCO_3^-:

$$C_{HCO_3^-} = C^0_{HCO_3^-} - \xi_5 - \xi_7 \tag{2.33}$$

For CO_3^{-2}:

$$C_{CO_3^{-2}} = C^0_{CO_3^{-2}} + \xi_7 \tag{2.34}$$

For water:

$$C_{H_2O} = C^0_{H_2O} + \xi_5 \tag{2.35}$$

Substituting the set of Equation 2.30 to Equation 2.35 into Equation 2.19, for the chemical reaction corresponding to Equation 2.12 and Equation 2.14, a system is obtained comprised of two equations and two variables. The solution of this system results in the value of the extent of reactions at chemical equilibrium, which are substituted in Equation 2.30 with Equation 2.35, and leads to the speciation of the liquid phase at chemical equilibrium.

$$K_5 = \frac{C_{MEACOO^-}}{C_{HCO_3^-} C_{MEA}} = \frac{\xi_5}{(C^{tot}_{MEA}\dot{\alpha} - \xi_5 - \xi_7)(C^{tot}_{MEA}(1-\dot{\alpha}) - \xi_5 - \xi_7)} \tag{2.36}$$

$$K_7 = \frac{C_{MEAH^+} C_{CO_3^{-2}}}{C_{HCO_3^-} C_{MEA}} = \frac{(C^{tot}_{MEA}\dot{\alpha} + \xi_7)\ \xi_7}{(C^{tot}_{MEA}\dot{\alpha} - \xi_5 - \xi_7)(C^{tot}_{MEA}(1-\dot{\alpha}) - \xi_5 - \xi_7)} \tag{2.37}$$

A good approximation consists in neglecting the carbonate formation, Equation 2.14. Thus, ξ_7 is equal to zero and the solution is reduced to a second-order polynomial. The root satisfying physical meaning (e.g. no negative values) is given as:

$$\xi_5 = \frac{C^{tot}_{MEA} + {}^1\!/_{K_5} - \sqrt{\left(C^{tot}_{MEA} + {}^1\!/_{K_5}\right)^2 - 4{C^{tot}_{MEA}}^2 \dot{\alpha}(1-\dot{\alpha})}}{2} \tag{2.38}$$

Finally, the concentration of molecular CO_2 is calculated using the equilibrium constant of the reaction of the free CO_2 absorption (Equation 2.13):

$$C_{CO_2} = \frac{C_{MEAH} C_{MEACOO}}{C_{MEA} K_6} = \frac{C_{MEAH} C_{MEACOO}}{C_{MEA}} \frac{K_2 K_4}{K_5} \tag{2.39}$$

It is worth mentioning that, since the chemically-bounded CO_2 loading is used, the procedure is straightforward and no iteration procedure is needed. This is valid for loadings lower than 0.1, as the concentration of molecular CO_2 is negligible. A secant method was then added to the procedure in order to pass from chemically-bound to total CO_2 loading. The result can be obtained after only a few iterations.

2.3. Heat of Absorption of CO_2

An important thermodynamic parameter in gas treatment processes is the heat of CO_2 dissolution and the reaction between CO_2 and amine. These are often combined and referred to as the heat of absorption. The magnitude of the heat of absorption is a significant factor in determining the thermal effects observed in both absorption and stripping sections. Since CO_2 solubility, reaction kinetics and diffusion coefficients are strongly temperature dependent, estimating the heat of absorption is essential for predicting the performance of both absorption and desorption processes.

Several model complexities of heat of absorption are proposed in literature, varying from constant values [82], empirical correlations [68] and more elaborated excess enthalpy models [74], [75], [83]. The constant values and empirical correlations are not adequate for modelling the process in conditions outside the range of validity, especially for high temperatures. Models with physical meaning, such as those for excess enthalpy, are preferred when extrapolations are required.

The approach used in this work to estimate the heat of the absorption of carbon dioxide in aqueous amine solutions is based on the formulation proposed by Kim et al. [84]. Indeed, while it is not an excess enthalpy model, its thermodynamic formulation is sufficiently solid to allow for extrapolations and was appropriate for implementation into the present work, given that the solubility model approach was used. The concept of the approach is that each chemical reaction involved in the speciation contributes to the overall enthalpy of the CO_2 absorption.

$$\Delta H^{o}_{abs} = \sum_{j} \frac{\Delta \mathrm{n}_j}{\Delta \mathrm{n}_{CO_2}} \Delta H^{o}_{j} \tag{2.40}$$

The enthalpy of a reaction can be determined using the Van't Hoff's equation, which relies the variation of the equilibrium constant with respect to the temperature and the standard enthalpy of reaction. In fact, this relation does not take into account the excess enthalpy.

$$\frac{d}{dT}(\ln K_j) = \frac{\Delta H^{o}_{j}}{RT^2} \tag{2.41}$$

In order to estimate the individual heat contribution of each chemical reaction described in Section 2.1, the variation of moles from an initial state to the chemical equilibrium is required ($\Delta \mathrm{n}_j$). The values of $\Delta \mathrm{n}_j$ for each of the chemical reactions in the MEA-H_2O-CO_2 system may be calculated with the following equations:

Water ionization:

$$\Delta \mathrm{n}_1 = {n_{OH^-}}^{eq} - {n_{OH^-}}^{0} \tag{2.42}$$

Dissolved CO_2 dissociation:

$$\Delta n_2 = \left[n_{HCO_3^-}{}^{eq} - n_{HCO_3^-}{}^0\right] + \left[n_{CO_3^{-2}}{}^{eq} - n_{CO_3^{-2}}{}^0\right] + \left[n_{MEACOO^-}{}^{eq} - n_{MEACOO^-}{}^0\right] \tag{2.43}$$

Bicarbonate dissociation:

$$\Delta n_3 = \left[n_{CO_3^{-2}}{}^{eq} - n_{CO_3^{-2}}{}^0\right] \tag{2.44}$$

Dissociation of protonated amine:

$$\Delta n_4 = \left[n_{MEAH^+}{}^{eq} - n_{MEAH^+}{}^0\right] \tag{2.45}$$

Carbamate formation:

$$\Delta n_5 = \left[n_{MEACOO^-}{}^{eq} - n_{MEACOO^-}{}^0\right] \tag{2.46}$$

Finally, the total amount of CO_2 absorbed is given by:

$$\Delta n_{CO_2} = \Delta n_2 + \left[n_{CO_2}{}^{eq} - n_{CO_2}{}^0\right] \tag{2.47}$$

where n_{CO_2} stands for the moles of molecular CO_2 dissolved in the liquid phase, its heat contribution is estimated applying Equation 2.41 while using Henry's law as the corresponding equilibrium constant. The initial state ${n_i}^0$may represent concentrations of the unloaded liquid absorbent.

2.4. Parameter Estimation of Equilibrium Constants

The speciation of CO_2 in amine aqueous solutions is controlled essentially by the chemical reactions involving both components. In fact, whether they are for the local interaction contributions in the elec-NRTL model, or for the residual contribution in the e-UNIQUAC model, the parameters concerning the carbamate and the protonated amine are the most significant [72], [74], [75], [83]. Therefore, the parameters of the equilibrium constants of the dissociation of protonated amine, Equation 2.11, and of the carbamate formation, Equation 2.12, are subject to fitting with the experimental data of CO_2 solubility.

The temperature dependence of the equilibrium constants, which are in molar basis, is given as

$$\ln(K_j) = \frac{c_1}{T} + c_2 \ln(T) + c_3 T + c_4 \tag{2.48}$$

The parameter adjustment is performed to minimize the objective function, defined as the sum of the squares of the relative deviation between the calculated and experimental CO_2 partial pressure. The minimization problem is therefore formulated as $\min_{C_k} f_{obj}(C_k)$.

$$f_{obj} = \sum \left(\frac{P_{CO_2}^{exp} - P_{CO_2}^{calc}(C_k)}{P_{CO_2}^{exp}} \right)^2 \tag{2.49}$$

The minimization is conducted using a quasi-Newton algorithm from the *fminunc* routine of Matlab ®. Literature values of equilibrium constants for diluted solutions are used for the initial guess, as the result is highly dependent on the initial value. The quality of the minimization is evaluated by the averaged absolute relative deviation:

$$AARD = \frac{1}{n}\sum_{i=1}^{n}\frac{|Y_i^{exp} - Y_i^{calc}|}{Y_i^{exp}} \tag{2.50}$$

2.4.1. Equilibrium Constants for CO_2 Solubility

The parameter values of the equilibrium constants obtained by the parameter adjustment are highlighted in bold in Table 2-1[9]. The parameters corresponding to K_1, K_2 and K_3 are taken from [71], since they are not adjusted. Regression analysis results are considerably different from those for equilibrium constants of diluted solutions published in others studies [71], [73]. The difference may be attributed to two factors: first, the nonidealities of the system were lumped into the expressions of K_4 and K_5 and second, the minimization is strongly dependent on the initial guess. Fluctuations in the results due to the second factor were smoothed by setting the literature values, those of the diluted solution, as for the initial estimation.

Table 2-1 Temperature dependence of the equilibrium constants for CO_2 solubility

	c_1	c_2	c_3	c_4
K_1	-13445.9	-22.4773	0	140.932
K_2	-12092.1	-36.7816	0	235.482
K_3	-12431.7	35.4819	0	220.067
K_4	99.9966	-2.5951	0.0665	0.457
K_5	100.0027	2.0748	-0.0333	1.4337

The model predictions are illustrated in Figure 2.2. The evaluation of the parameter adjustments is shown in **Erreur ! Source du renvoi introuvable.**. The AARD obtained for the entire interval of MEA mass fractions was satisfactory, despite the fact that the regression was performed using numerous sources of experimental data [68], [74], [83], [86], [87], which increased the overall experimental uncertainty. Furthermore, by regressing only 8 parameters, the approach developed in this chapter predicts CO_2 solubility and total vapour pressures with deviations of the same order of magnitude as those obtained using more complex models, such as elec-NRTL (Hilliard et al., 30% AARD and Aronou

[9] The regressed values presented here are different to those published in [85], due to the use of different expressions of the chemical speciation.

et al., 24% AARD [75], [83]) or e-UNIQUAC (Neveux et al., 20.6% [72]). Wagner et al. [74] obtained excellent agreements between the model results and the experimental data (AARD<10%). However, by using the elec-NRTL approach, they adjusted more than 30 parameters, including equilibrium constants of both the amine protonation and the carbamate formation reactions. Puxty et al. [73] obtained AARD values lower than 20% using the SIT approach. However, their regression analysis used only experimental data from [83]. Moreover, for MEA concentrations of 30% wt., considered as a reference solution for PCC processes, the deviation of the model results is lower than 20%.

The true composition obtained with this model is compared against experimental data used in [74]. There is good agreement between both observed results. Therefore, this approach provides a chemical speciation of the liquid phase with real physical meaning, crucial for reaction rate calculations.

The largest deviations between experimental data and model predictions were obtained from bubble and dew point pressure estimations (see Figure 2.2b). Normally, an activity model is needed for predicting vapour-liquid equilibria for the binary H_2O-MEA system. However, for the domain of MEA molar fractions in which CO_2 capture is performed, i.e. lower than 0.15, predictions using Equation 2.6 are acceptable.

Table 2-2 Model deviations of the CO_2 solubility and total vapour pressure

System	Variable	wt% MEA	CO_2 loading	n_{points}	AARD (%)
MEA-H_2O-CO_2	P_{CO2}	15-60	0-0.7	337	29.3
		30	0-0.7	53	18.7
	P_{TOT}	30	0.3-0.55	38	14.5

a) Parity plot of CO_2 partial pressure in MEA aqueous solutions. Data from [68], [74], [83], [86], [87]

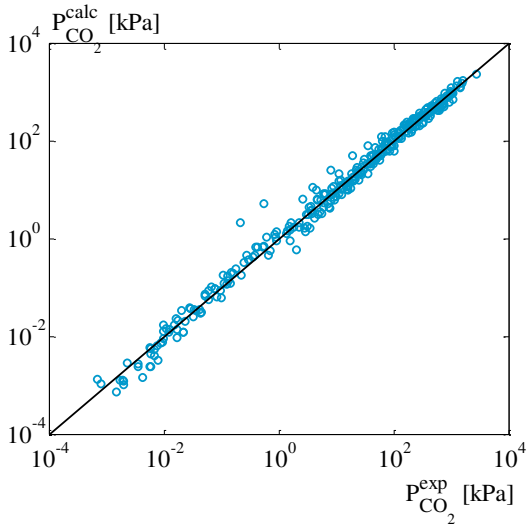

b) Dew and bubble pressure of the binaray system MEA - H_2O. Data taken from [11]

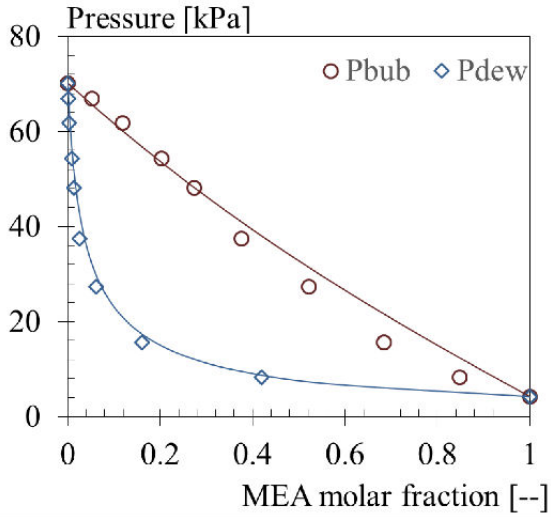

c) CO_2 solubility in 30% wt. MEA. Data from [68], [74], [83], [86], [87]

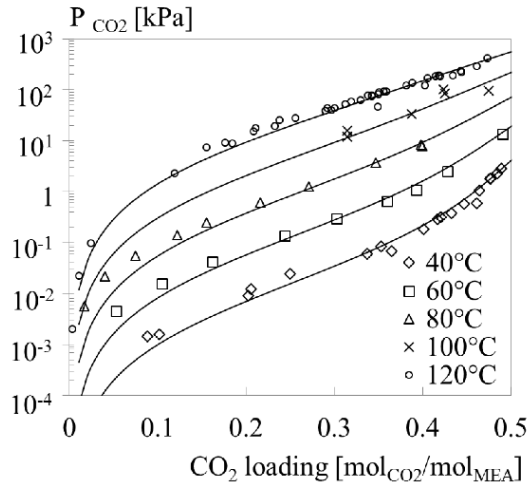

d) Total pressure of 30% wt. MEA. Data from [5], [6]

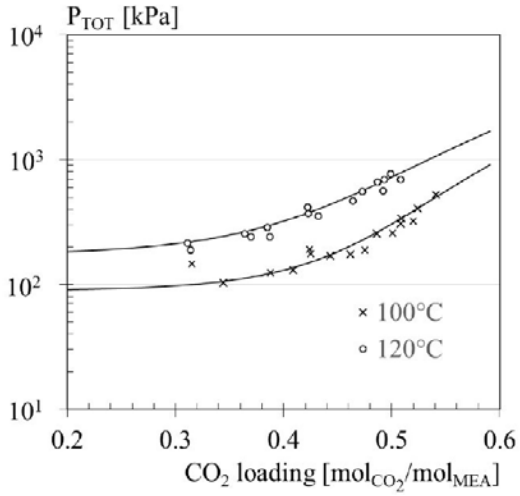

e) Chemical speciation of 30% wt. MEA. T=293K [74]

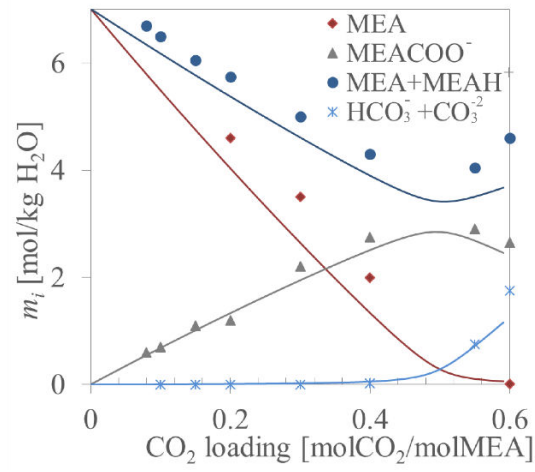

f) Chemical speciation of 30% wt. MEA. T=333K [74]

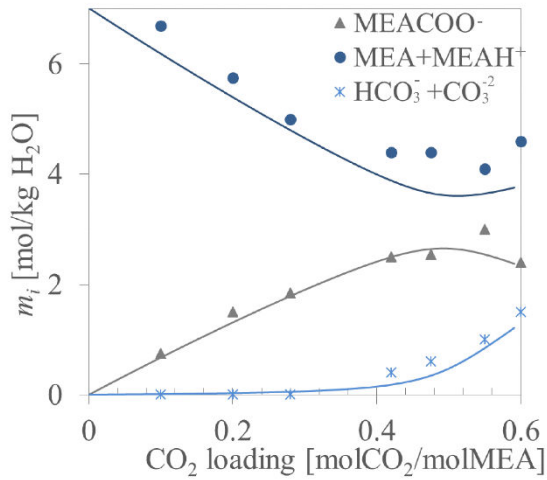

Figure 2.2 Results of the thermodynamic model of the system CO_2-MEA-H_2O. Solid lines: model predictions. Points: experimental data.

2.4.2. Equilibrium Constants for CO_2 Heat of Absorption

The influence of excess enthalpy on the enthalpy of absorption in the MEA-H_2O-CO_2 system is known to be significant [75]. The most reliable method for predicting this parameter is by implementing a Gibbs free energy thermodynamic model. Using the equilibrium model featured in this work which considers apparent equilibrium constants (with no activity coefficient), expressions fitted for CO_2 solubility would not be expected to account for this excess property. Therefore, temperature dependence of the equilibrium constants of the amine protonation and the carbamate formation were fitted to experimental data. A similar procedure was used in [84].

To perform the parameter adjustment, the objective function (Equation 2.49) was modified by replacing the CO_2 partial pressures with the heat of absorptions. The experimental data here were taken from [88]. The results are shown in **Erreur ! Source du renvoi introuvable.**. Figure 2.3 illustrates model predictions for different temperatures. Despite the simplicity of the model, it produced acceptable predictions for the variation of heat of absorption with temperature and CO_2 solvent loading. Extrapolations at this stage are considered suitable due to the thermodynamic fundamentals of this procedure.

Table 2-3 Temperature dependence of the equilibrium constants for CO_2 heat of absorption

	c_1	c_2	c_3	c_4
K_4	99.9966	-1.9526	0.0033	-0.4044
K_5	100.0027	-1.8038	0.1033	-0.3733

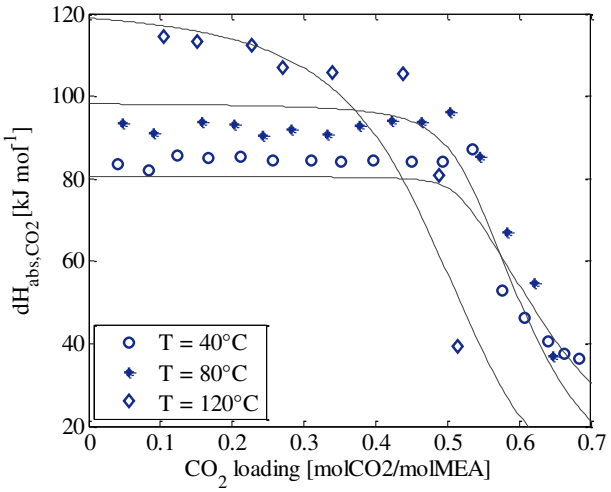

Figure 2.3 CO_2 heat of absorption in 30% MEA aqueous solution. Solid lines: model predictions, dots: experimental data.

2.5. Auxiliary Operations of the CO_2 Capture Process

This section explains the thermodynamic models of reboilers, condensers, flash stripers and mixers required in the process simulation of the absorption-desorption loop. Such unit operation models are based on *flash separation*, in which the gas and liquid phases are separated from a stream at thermodynamic equilibria, while different conditions are set. As the procedures and equations used in this investigation are similar to those proposed in [72], only a brief explanation is provided here.

A flash operation with chemical reactions should take into account both vapour-liquid and chemical equilibria. In a typical flash calculation (without chemical reaction), the true global composition, i.e. the inlet composition, is established and the operation is calculated using the Rachford-Rice equation [70], which relates the liquid-vapour equilibria with vapour fraction and true global molar composition. The solution to this equation is iterative and is numerically solved using, for instance, a Newton algorithm. However, the true global composition is intrinsically unknown when chemical reactions occur, which in this case occur only in the liquid phase. Therefore, this composition is first guessed and the commonly used flash calculation is performed, as described above. The chemical equilibrium is then computed with the novel liquid concentration and the true global composition is again calculated and compared to that of the previous iteration. The iterative process is executed until the deviation between iterations fall below an imposed tolerance. In this work, the number of iterations required was extremely high (around 1500) and it is probably due to the chemical equilibrium formulation.

For the flash operation, two degrees of freedom are required to completely describe the system. **Erreur ! Source du renvoi introuvable.** shows the manner in which the unit operations used in this investigation are calculated by solving the flash separation. T, P and Q represent respectively temperature, pressure and heat duty of the operation.

Table 2-4 Unit operations based on flash calculation by specifying different variables

Type of flash	Specified variables	Unit operation
TP	T fixed and $\Delta P=0$	Simple heat exchanger (condenser)
QP	Q=0 and P fixed	Expansion valve
QP	Q fixed and $\Delta P=0$	Reboiler
QP	Q=0 and $\Delta P=0$	Mixer

2.6. Reaction Kinetics of the CO_2-MEA-H_2O System

Two approaches are frequently used in order to represent the reaction mechanism occurring between CO_2 and primary and secondary amines: the zwitterion formation introduced by [89] and the termolecular reaction mechanism introduced by [90]. The modified termolecular mechanism, depicted on the left as proposed by [69], provides a good representation of the reaction kinetics at high CO_2 loadings and concentrated aqueous MEA solutions. This mechanism considers a single-step reaction between CO_2 and MEA wherein the initial product is a loosely bound encounter complex. 'Base' represents any species that may act as a base (i.e. MEA, H_2O or OH^-), such that it accepts a proton from the zwitterion. The complex breaks up to give reagent molecules again or to react with a second molecule of amine, or a water molecule, to give ionic products. Based on this reaction mechanism, the general reactions are:

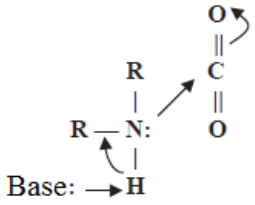

Figure 2.4 Schema of termolecular mechanism

$$2MEA + CO_2 \overset{K_6}{\Leftrightarrow} MEACOO^- + MEAH^+ \tag{2.51}$$

$$MEA + H_2O + CO_2 \overset{K_9}{\Leftrightarrow} MEACOO^- + H_3O^+ \tag{2.52}$$

The kinetics of reaction can be expressed using an apparent reaction kinetics, as given by [69]:

$$r_{CO2} = -(k_{MEA}[MEA] + k_{H2O}[H_2O]) * [MEA][H_2O] \tag{2.53}$$

This formulation is convenient for 1D rate-based models, since no parallel reactions need to be formulated and thus only one enhancement factor is required in order to describe mass-transfer with chemical reaction[10]. However, for rate-based models when the liquid-film (i.e. where chemical reactions and mass-transfer occur) is discretised, Equation 2.53 is no longer suitable, thus the reaction kinetics need to be formulated for every single reaction. Due to the deemed negligible contribution to the general reaction (corroborated a-posteriori), the second reaction represented by Equation 2.52 can be neglected. The reaction kinetics can thus be presented as follows:

$$r_{CO_2} = k_r C_{CO_2} C_{MEA}{}^2 - k_r{}' C_{MEACOO^-} C_{MEAH^+} \quad \text{where } K_6 = {}^{k_{r1}}\!/_{k_{r1}{}'} \tag{2.54}$$

[10] Details of the enhancement factor theory and its application are given in [91], [92]. Its utilisation is explained in Section 3.2

Expressions of kinetic constants were obtained using the experimental data from [69] and applying the thermodynamic model developed in the previous sections. Further detailed work on the calculation and reasoning behind the reaction kinetics employed are provided in [93]. The influence of temperature on the reaction kinetics was taken into account using the Arrhenius model, within the temperature range of the experimental data, i.e. between 290 and 330K. Values of the kinetic constants are provided in Table 2-5.

Table 2-5 ***Reaction kinetics constants of the forward and backward reaction between CO_2 and MEA***

Kinetic constant	Expression
Forward, k_r [$m^6.mol^{-2}.s^{-1}$]	$4.2919 \times 10^3 . exp\left[\frac{-4389.8}{T(K)}\right]$
Backward, k_r' [$m^3.mol^{-1}.s^{-1}$]	$3.1792 \times 10^{10} . exp\left[\frac{-12687}{T(K)}\right]$

2.7. Summary and Conclusions

Modelling for thermodynamics of CO_2 absorption in chemical solvents is complex since it consists of numerous phenomena (dissolution, chemical reaction and component interactions) involving several compounds (molecules and ions). The simplest models, such as correlations of CO_2 solubility or the diluted species, are not appropriate if the aim is to describe a vast domain of operation. Membrane contactors models tend to require high numbers of calculations, which render complex thermodynamic models less advantageous. The approach presented in this chapter has been shown to be able to provide reliable estimations of CO_2 solubility, as well as other thermodynamic properties such as the bubble and dew point pressures or the heat of absorption, in a straightforward manner. Additionally, the model is consistent enough to be applied to modelling of auxiliary unit operations involved in the CO_2 capture process.

Using a simple yet robust formulation of reaction kinetics, the model presented in this chapter represents the first stage of modelling gas-liquid contactors for the absorption and stripping of CO_2.

2.8. Résumé et conclusions

La modélisation de la thermodynamique de l'absorption du CO_2 dans des solvants chimiques est complexe, car elle se compose de différents phénomènes (dissolution, réactions chimiques et interactions entre constituants). Le plus simple des modèles, consistant à corréler la solubilité du CO_2 à sa pression partielle, n'est pas approprié car il ne permet pas de couvrir de grands domaines opératoires. Les modèles de transfert dans les contacteurs membranaires, requièrent quant à eux, un nombre élevé de calculs, ce qui rend les modèles thermodynamiques plus complexes, moins avantageux.

L'approche décrite dans ce chapitre permet donc de fournir d'une manière directe, des estimations fiables de la solubilité du CO_2, ainsi que d'autres propriétés thermodynamiques telles que les pressions de bulle, les points de rosée ou la chaleur d'absorption. En outre, le modèle proposé est suffisamment cohérent pour être appliqué à la modélisation des opérations unitaires auxiliaires intervenant dans le procédé de captage du CO_2.

Ainsi, en utilisant une formulation simple mais robuste de la cinétique de réaction, le modèle présenté dans ce chapitre représente la première étape de la modélisation des contacteurs gaz-liquide pour l'absorption et le stripage du CO_2.

Chapter 3. Isothermal Modelling of Membrane Contactors

Membrane gas separation processes are generally considered to be isothermal. Most of the scientific community devoted to membrane research and the study of membrane contactors assume that their operation shows isothermal behaviour. For the case of CO_2 post-combustion capture by means of membrane contactors, nine out of ten scientific papers follow this pattern. In fact, under commonly applied laboratory scale operating conditions, with high excess of liquid flow and/or unloaded liquid absorbents, this assumption is valid. Furthermore, analysing experimental results is considerably simpler to perform when isothermal behaviour has been established and only CO_2 is transferred. Indeed, the number of equations that require solutions in order to perform the analysis is considerably reduced when isothermal single-component transfer is assumed. Additionally, thermal effects accompanying the transfer process can perturb the measurements and the interpretation of results. Therefore, isothermal modelling represents an important tool for analysing membrane contactor experiments.

The first section of this chapter presents a study of mass-transfer through microporous membranes, through the analysis of convection inside the membrane pores and membrane wetting in a context of post-combustion CO_2 capture. Isothermal modelling of hollow fibre membrane contactors at different levels of complexity is addressed in the second section. Finally, a summary and conclusions are presented.

3.1. Mass-transfer Modelling of Microporous Membranes

The main objective of membrane gas-separation experiments is to quantify the membrane permeability at specific values of temperature, pressure and composition. In gas-liquid membrane contactors, where mass-transfer selectivity is imposed by the liquid rather than the membrane, the concept of membrane permeability is not appropriate. Instead, the membrane mass-transfer coefficient carries more significance.

A typical absorption experiment using membrane contactors to quantify this coefficient, consists in performing several tests at different gas and liquid flow rates. Once the inlet temperature, pressure and compositions of both gas and liquid are set, the measurement of the outlet composition and flow rates allows for the calculation of the total flux per unit of membrane surface of, in this case, CO_2 which has been absorbed by the liquid.

The value of the flux, N_{CO2}, can be related to an overall mass-transfer coefficient, K_{ov}, using Equation 3.1.

$$N_{CO_2} = \frac{(Y_{CO_2}^{in} - Y_{CO_2}^{out})g}{A} = K_{ov,CO_2} C_{LM,CO_2} \tag{3.1}$$

where g represents the inert gas molar flow rate, A is the membrane surface area based on the liquid-membrane interface and Y_{CO2} is the gas mole fraction of CO_2 in dry basis. $C_{LM,CO2}$ represents the log-mean average concentration driving force between the bulk gas and liquid phases. If the liquid absorbent is unloaded and in large excess, the CO_2 concentration in the liquid bulk can be neglected. Therefore, the log-mean average concentration driving force is simply approximated by the log-mean average concentration of the CO_2 concentration in the gas phase, between the inlet and the outlet. It is worth mentioning that this approach is only considered valid for low local variations of the gas flow rate[11], that is, for low CO_2 capture ratios. In the case of a flat membrane, the overall mass-transfer coefficient $K_{ov,CO2}$ takes into account the transfer resistances carried by the gas, the membrane and the liquid, in an in-series approach shown in Equation 3.2.

$$\frac{1}{K_{ovCO_2}} = \frac{1}{k_{G,CO_2}} + \frac{1}{k_{M,CO_2}} + \frac{\mathcal{K}_{CO_2}^{VLE}}{E_{CO_2} k_{L,CO_2}} \tag{3.2}$$

The right side of Equation 3.2 illustrates the mass-transfer resistance corresponding to the gas, the membrane and the liquid, from left to right respectively. Once the gas and liquid mass-transfer resistances are calculated, the membrane mass-transfer coefficient, $k_{M,CO2}$, can be estimated using Equation 3.1 and Equation 3.2. It is also worth noting here that the assumption of constant liquid and gas resistance is only valid when high excess of liquid reactant and low CO_2 capture are applied. It is important here to properly estimate the value of these resistances to arrive at a coherent value of the membrane mass-transfer resistance and thus understand the transfer process through the membrane. Local variations of mass-transfer resistance for both gas and liquid phases are explained in Section 3.2.

The overall goal of modelling consists in calculating process outcomes in a completely predictive manner, i.e. without adjustable parameters, while at the same time developing simple but robust modelling expressions. Developing a model for membrane-mass transfer requires physically meaningful expression which thus calls for an interpretation of the

[11] For absorption operations, the *operating curve* (in a Y vs X plot, being Y and X the mole fraction in gas and liquid, respectively) must be rectilinear in order to derive the log mean average concentration driving force [94].

phenomena. Two phenomena behind membrane mass-transfer are discussed in the following sections; convection inside membrane pores and membrane wetting.

3.1.1. Convection inside Membrane Pores

It is generally assumed that membrane pores are filled with a stagnant phase, which means only mass diffusion and heat conduction occur inside the membrane itself. However, in some modelling investigations addressing solvent evaporation in HFMC, correlations considering natural convection for water mass-transfer inside the porous medium have been implemented without further explication of its application [95], [96]. Additionally, experiments performed by our research team aiming to describe water evaporation through HFMC concluded that, when using microporous membranes, the membrane water mass-transfer resistance decreased with increased gas velocity, which varied from 0.5 to 30 ms^{-1}. The results suggested that at such high gas velocities, the stagnant phase inside the membrane pores may be destabilized, leading to the appearance of velocity gradients inside the porous medium [97].

Convection inside the membrane pores can thus be related to two distinct phenomena. In the case of solvent evaporation, free convection may appear to be caused by temperature gradients inside the membrane. In the case of high gas velocities, forced-convection may appear in the vicinity of gas-membrane interface, due to the gas drag. However, typically, temperature gradients throughout the membrane are small, as shown in Section 4.1. Hence, only forced convection was studied to determine its influence on the mass transfer.

Modelling and simulation for this phenomenon allows for rapid identification of zones where the convection inside the membrane, in the context of membrane contactors for PCC, would be significant. In order to simplify the problem, only one fibre transporting gas stream has been modelled, as illustrated in Figure 3.1. In order to simulate liquid water flow outside the fibres, a constant water concentration, which corresponds to the saturating concentration at 40°C, is set on the outer face of the fibre. Computational Fluid Dynamics (CFD) was used to model momentum- and mass- transfer in the porous medium and in the gas stream,

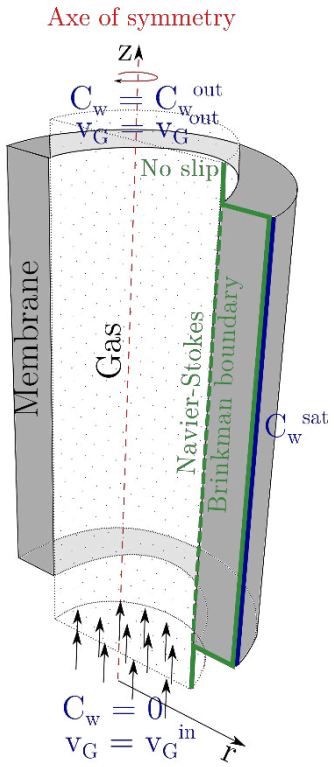

Figure 3.1 Modelled hollow fibre by CFD and boundary notations

for the case in which the convection inside the membrane pores is considered, and for the case in which it is neglected.

The simulation parameters are presented in Table 3-1. The fibre was short enough to avoid gas saturation. The inlet-outlet gas pressure difference was set at boundary conditions to permit flow, i.e. $P^{z=Z}= 0$. The inlet gas corresponded to a dry nitrogen stream. The porous medium is considered to be formed by spheres confined in a given volume. Membrane porosity and tortuosity values are those typically used in literature.

The momentum conservation corresponding to gas flow in the tube was modelled using the Navier-Stokes equations, presented as follows:

$$\begin{gathered} \rho \frac{\partial \boldsymbol{v}}{\partial t} + \nabla \bullet [-\mu(\nabla \boldsymbol{v} + (\nabla \boldsymbol{v})^T) + P\boldsymbol{I}] = -\rho(\boldsymbol{v} \bullet \nabla)\boldsymbol{u} \\ \nabla \bullet \boldsymbol{v} = 0 \end{gathered} \tag{3.3}$$

where μ denotes the dynamic viscosity, $\boldsymbol{v}$ refers to the velocity in the tube, $\boldsymbol{\rho}$ is the fluid's density and P is the pressure. The first term on the left-hand side together with the term on the right correspond to the inertial forces, and the second term on the left-hand side corresponds to viscous and pressure forces. The second equality corresponds to the continuity equation.

The momentum conservation corresponding to gas flow through the porous domain was modelled by applying the Brinkman equations, presented as follows:

$$\begin{gathered} \frac{\rho}{\varepsilon_p}\frac{\partial \boldsymbol{v}}{\partial t} + \nabla \bullet \left[-\frac{\mu}{\varepsilon_p}(\nabla \boldsymbol{v} + (\nabla \boldsymbol{v})^T) + P\boldsymbol{I}\right] = -\frac{\mu}{\kappa}\boldsymbol{v} \\ \nabla \bullet \boldsymbol{v} = 0 \end{gathered} \tag{3.4}$$

where κ denotes the hydrodynamic permeability of the porous medium and ε_p is the membrane porosity. The hydrodynamic permeability is commonly related to the pore size using a Darcy formulation, as:

$$\kappa = f d_p^2 \tag{3.5}$$

where d_p corresponds to the membrane pore diameter and f is a shape factor. In this work, the latter is assumed to be 1, i.e. spheres representing the porous domain. The term on the right-hand side of Equation 3.3, corresponding to the momentum transported by convection, is replaced in Equation 3.4 by a contribution associated with the drag force experienced by the fluid flowing through the membrane pores.

The law of conservation of mass is used to describe the transfer of water through both gas and membrane domains. Since there is not chemical reaction, the equations are written, for the gas and membrane domains are respectively:

$$\nabla \bullet (-D_w \nabla C_{w,G} + \boldsymbol{v} C_{w,G}) = 0 \tag{3.6}$$

And:

$$\nabla \bullet \left(-\frac{D_w \varepsilon_p}{\tau} \nabla C_{w,M} + \boldsymbol{v} C_{w,M} \right) = 0 \tag{3.7}$$

where D_w stands for the diffusion coefficient of water, $C_{w,G}$ and $C_{w,M}$ represent water molar concentration in the gas and membrane domains, respectively. τ represents membrane tortuosity.

Table 3-1 Parameters of CFD simulations of gas humidification using a hollow fibre

Parameter	Value	Units
Gas		
Water molar fraction	$y_w^0 = 0$	--
Temperature	T = 313	K
Density	$\rho = 1$	kgm^{-3}
Water diffusion coefficient	$D_w = 1.6 \times 10^{-5}$	m^2s^{-1}
Water saturating pressure	7376	Pa
Viscosity	$\eta = 1 \times 10^{-5}$	Pa-s
Velocity	$\boldsymbol{v}$ = 1-20	ms^{-1}
Fibre (Microporous membrane)		
External fibre radius	$r_e = 2 \times 10^{-4}$	m
Internal fibre radius	$r_i = 1.5 \times 10^{-4}$	m
Fibre length	$Z = 5 \times 10^{-3}$	m
Membrane porosity	$\varepsilon_p = 0.3$	--
Membrane tortuosity	$\tau = 4$	--
Porous medium permeability	$\kappa = 10^{-14}$-10^{-9}	m^2

The partial differential equation system, which consists of simultaneously applying the momentum- and mass-conservation laws, i.e. from Equation 3.3 to Equation 3.7, was solved using COMSOL Multiphysics. This software provided an effortless interface for combining free flow, porous medium flow and mass-transfer.

The fluid streamlines obtained by simulations are illustrated in Figure 3.2a, for a gas velocity of 10 ms^{-1} and a porous medium permeability of 10^{-12} m^2. The latter corresponded to a membrane pore size of about 1 µm. This made it possible to observe how the fluid passes through the porous medium and develops a flow pattern, in stark contrast to simulations that omit this phenomenon. Corresponding radial velocity profiles are illustrated in Figure 3.2b. Interestingly, the presence of the porous medium actually modified the velocity profile of the gas phase, differing to that obtained when the porous nature of the membrane was neglected. The enlarged section in Figure 3.2b shows an established velocity profile inside the membrane, however the velocity magnitude is about 10 times lower than that for the gas phase.

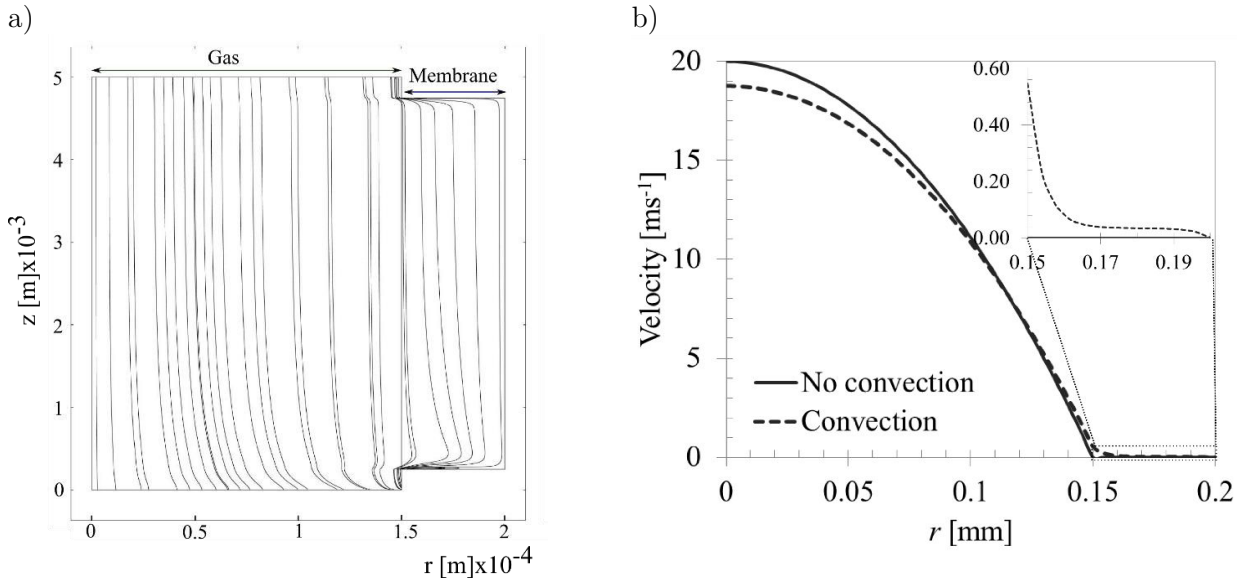

Figure 3.2 CFD simulations results for the case of gas velocity, v_G, of 10 ms^{-1} and porous medium permeability, κ, of 10^{-12} m^2. a) Flow streamlines, b) radial velocity profiles

The value of the velocity inside the membrane will be higher for more permeable membranes, since the gas would require less effort to cross the porous medium, as for high gas velocities. The increase of the velocity inside the membrane leads to improved mass-transfer through the membrane. In order to identify this impact, a parametric study was performed varying the gas velocity at different membrane permeabilities. The results are shown in Figure 3.3, presented as the ratio between the total transmembrane flux with and without the occurrence of velocity profiles inside the membrane pores. As expected, the increase of the gas velocity enhanced the membrane mass-transfer rate rendering this impact more significant than for membranes with high permeability.

In post-combustion CO_2 capture, gas velocity is constrained by gas pressure drop specifications (e.g. 50 mbar), leading to gas velocities below 2 ms^{-1} (see Section 3.2). Moreover, microporous membranes which are interesting for this application have pore sizes of between 0.1 and 10 microns, which corresponds to porous medium permeabilties of between 10^{-14} and 10^{-11} m^2. Therefore, the influence of the convection inside the membrane pores can be clearly neglected. For other applications involving membrane modules, such as gas membrane separation, gas velocity values may be higher and the membrane porous support is more permeable, allowing associated mass-transfer resistance to be neglected.

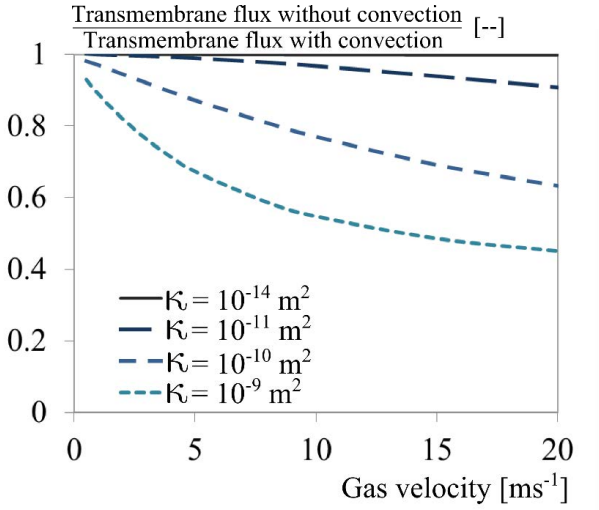

Figure 3.3 Variation of the ratio between the transmembrane flux, neglecting and taking into account convection inside the membrane pores, with the gas velocity for different porous medium permeabilities (κ).

3.1.2. Membrane Mass-transfer in Wetted Membranes

General considerations

Predicting the membrane mass-transfer coefficient is particularly complex as it depends on module geometry, operating conditions, physicochemical properties of absorption, liquid-membrane interaction and membrane geometric characteristics (Equation 3.8). The last two parameter groups are extremely difficult to quantify and introduce important uncertainties. Estimation of these characteristics is, however, necessary.

$$k_M = \mathcal{F}\left(\underbrace{\varphi, \frac{\delta}{r_{ext}}, r_{ext}, Z, z,}_{\text{Geometry}}\ \underbrace{P_L^{in}, P_G^{in}, T_L, u_G, u_L,}_{\text{Operating conditions}}\ \overbrace{\theta, \beta, \gamma_L,}^{\text{Solvent nature \& solvent-membrane interaction}}\ \underbrace{d_{pore}, f_{pore}, \varepsilon, \tau, w_M}_{\text{Membrane characterization Adjustable parameter}}\right) \quad (3.8)$$

For instance, the value of the wetting fraction, w_M, might be predicted by establishing (or measuring) pore size distribution. This method consists in the estimation of a *critical radius*, defined as the radius at which the breakthrough pressure of the membrane (ΔP_{break}) equals transmembrane pressure ($\Delta P_{L\text{-}G}$). Consequently, the related pore is completely wetted. Then, the wetting fraction is given by the ratio of the volume of the liquid filled pores and the volume of all pores [98]. This method is questionable as it depends on numerous unknown parameters in industrial conditions, such as, for example, pore size geometry and distribution and the membrane-liquid contact angle. Moreover, the

wetting fraction may vary significantly over the contactor length, as operating conditions may also vary.

Alternatively, the wetting fraction can be estimated by adjusting it to fit experimental results such as those described in Section 3.1. In this work, orders of magnitude of the membrane mass-transfer coefficient for CO_2 cited in literature for HFMC technologies are given in Table 3-2 as a function of membrane type and wetting state. The variation of the membrane mass-transfer coefficient with the wetting fraction is discussed hereunder.

Table 3-2 Orders of magnitude of membrane mass transfer coefficient for PCC using HFMC. The values are given for reference conditions of 40°C and 1 bar [11], [58].

Membrane type and wetting state	Microporous Gas filled	Microporous Partially wetted	Microporous Totally wetted	Composite Gas filled	Dense self-standing
$k_{M,CO2}^{eq}$	10^{-3} - 10^{-2}	10^{-4} - 10^{-3}	$< 10^{-4}$	10^{-4} – 10^{-3}	$<10^{-5}$

Variation of the membrane mass-transfer coefficient with wetting fraction

As has been shown in Section 3.1.1, the membrane pores are filled by a stagnant phase, thus only mass diffusion and heat conduction occur inside the membrane. The mass-transfer coefficient of a partially wetted membrane ($k_{i,M}$) is computed using a series resistance approach, taking into account the volumetric wetting fraction, w_M, Equation 3.9, defined as the ratio between the liquid volume in the pores and the total pore volume [99], [100]:

$$\frac{1}{k_{i,M}} = \frac{(1-w_M)}{k_{i,M,g}} + \frac{w_M \mathcal{K}_i^{VLE}}{k_{i,M,w} E_{i,M}} + \frac{\mathcal{K}_i^{MS}}{k_{i,M,d}} \tag{3.9}$$

where $k_{i,M,g}$, $k_{i,M,w}$, $k_{i,M,d}$, stand respectively for the mass transfer coefficient in the gas filled pores, the liquid filled pores and the dense-skin. K_i^{VLE} and K_i^{MS}, are the relative volatility of the species i and the sorption coefficient of the species i on the dense-skin, respectively. $E_{i,M}$ is the enhancement factor related to the chemical reaction in the wetted section of the membrane, assuming that the membrane pores are liquid-filled because of liquid breakthrough. For the case of membrane wetting by capillary condensation, the value of the enhancement factor is equal to unity. The transfer resistance corresponding to the dense-film layer, i.e. composite membranes, is presented in Equation 3.9 making the latter a general expression. While it is certain that composite membranes membrane wetting by liquid breakthrough would not occur, wetting by capillary condensation may still be possible (see Section 1.2.4).

The mass transfer coefficients can be computed using a Fick diffusion mechanism:

$$k_{i,M,g} = \frac{\varepsilon D_{i,M}}{\tau\delta} \quad k_{i,M,w} = \frac{\varepsilon D_{i,L}}{\tau\delta} \quad k_{i,M,d} = \frac{\varepsilon D_{i,dense}}{\delta_{dense}} \quad \text{where:} \quad \frac{1}{D_{i,M}} = \frac{1}{D_{i,G}} + \frac{1}{D_{i,k}} \qquad (3.10)$$

Gas filled pores *Liquid filled pores* *Dense skin*

where $D_{i,M}$, $D_{i,L}$ and $D_{i,dense}$, stand for the diffusion coefficients in the three media. The effective diffusion coefficient in the gas-filled pores, $D_{i,M}$, depends on the molecular diffusion in the gas phase ($D_{i,G}$) as well as on the Knudsen diffusion ($D_{i,k}$), as the pore size is typically lower than 1 µm. The influence of the wetting on the membrane transfer is described in Equation 3.10, since diffusion in liquids is about four orders of magnitude lower than that in gases. The diffusion coefficient in the dense skin is roughly 10^{-9} m^2s^{-1}, but its thinness is around only 5 µm, leading to a reasonably high dense skin mass transfer coefficient.

The influence of wetting of microporous membranes in the CO_2 post-combustion context is illustrated in Figure 3.4. This chart was built by solving Equation 3.9 and Equation 3.10 with a pore diameter of 0.5 µm and a membrane porosity and tortuosity of 0.3 and 4, respectively. These values are typical for microporous PP membranes. The membrane thicknesses used for this illustration correspond to those found in commercially available modules. Since Equation 3.9 considers chemical reactions occurring within the liquid filled pores, only membrane wetting by liquid breakthrough is illustrated. The reactants concentrations inside the liquid filled pores depend on their corresponding concentrations in the liquid stream. Therefore, Figure 3.4 was obtained for different CO_2 solvent loading in order to simulate the liquid phase MEA depletion.

The high sensitivity of the membrane mass-transfer coefficient can be observed by considering the value of wetting fraction. For instance, only 10% of membrane wetting may decrease the membrane mass-transfer coefficient in two orders of magnitude. In addition, high reactant concentrations (simulated here by low CO_2 solvent loadings) compensate the negative effect of membrane wetting to a certain extent, i.e. $w_M<0.1$. Given this limit, even with the occurrence of chemical reaction, the mass-transfer coefficient decreases dramatically with the wetting fraction. Similar conclusions have been found when using a 2D approach for the membrane mass-transfer [51], [53], [101]. The literature values of membrane mass-transfer coefficient as functions of wetting state, shown in Table 3-2, are in agreement with the calculated values depicted in Figure 3.4.

Under industrial conditions, high MEA conversions and high CO_2 capture ratio are required which consequently define the liquid-to-gas flow rate ratio, and a local variation of the CO_2 solvent loading can be expected. Therefore, assuming that the fibres are

partially wetted, the membrane mass-transfer coefficient may vary significantly, leading to a local profile of this variable.

Post-combustion CO_2 capture presents conditions in which membrane wetting is likely to occur: flue gases pressure often fluctuates, chemical solvents degrade the membrane properties and capillary condensation due to water transfer may occur. It is therefore appropriate to accept that membrane wetting happens in this context. Moreover, this phenomenon has been observed experimentally in several laboratory and pilot plant scale investigations (see Section 1.2.5 and Section 1.2.6). Therefore, assuming membrane mass-transfer coefficients of about 10^{-2} ms^{-1}, corresponding to dry membranes, would not be appropriate, even if these values have previously been used in some investigations [50], [56].

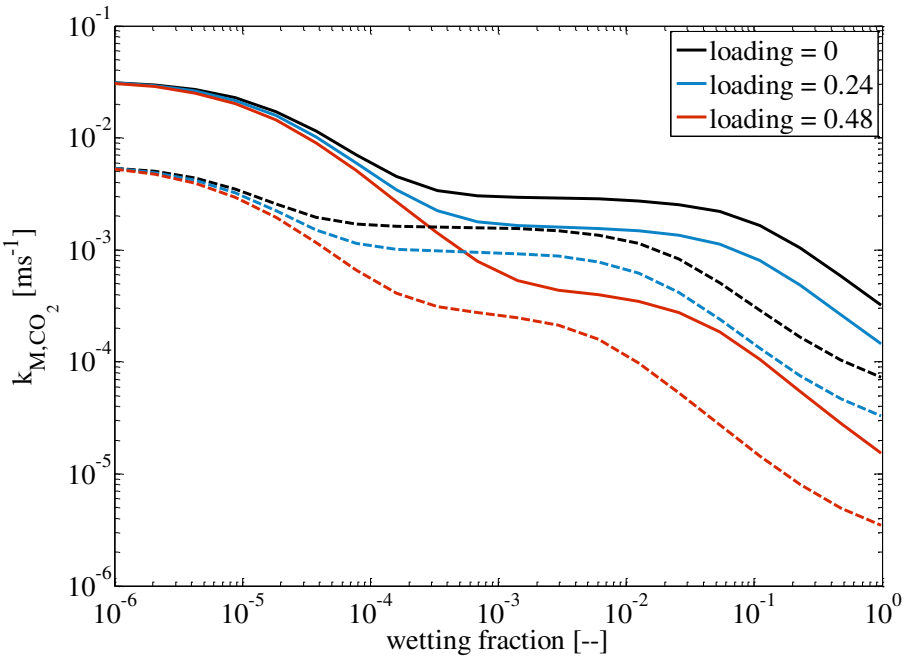

Figure 3.4 Variation of the mass-transfer coefficient of microporous membranes with wetting fraction, for different liquid absorbent CO_2 loading. $\varepsilon = 0.3$, τ=4, T=40°C, MEA 30% wt. y_{CO2} = 0.15. Solid lines: δ=40 µm. Dashed lines: δ=240 µm.

3.2. Isothermal One- and Two-Dimensional Modelling of HFMC

As mentioned in the chapter introduction, under certain conditions, isothermal is valid and highly useful. Section 3.1 discussed the necessity of correct estimation of the local mass-transfer resistances for both gas and liquid phases in order to properly estimate membrane mass-transfer coefficients. This becomes even more relevant when the modelling purpose is aimed at process simulation and/or equipment sizing.

In a previous investigation, Rode et al. 2012 [48], a one-dimensional model of CO_2 chemical absorption by means of hollow fibre membrane contactors was developed, which assumed, among other factors, isothermal behaviour and considered CO_2 as the solely transferred species. They concluded that, under relevant industrial operating conditions, the mass-transfer of both gas and liquid vary locally, principally due to MEA depletion. Moreover, they concluded that the interstitial gas velocity should not be higher than 1.5 ms^{-1} when considering industrial geometric features of HFMC, i.e. fibre radiuses comprised between 0.2 and 1 mm and packing fraction of 0.6, and the process was constrained by a gas pressure drop of 50 mbar. Despite the serious assumptions considered in their investigation, certainly at the time it was published, it was the first publication to address contactor sizing in a process involving such levels of constraints, as is PCC.

The fact that three in five modelling investigations have been conducted by implementing a two-dimensional model approach makes selecting model complexity particularly difficult. To clarify this issue, an investigation comparing the 1D and 2D modelling approaches was performed and published in 2014 in the *Journal of Membrane Science*. This chapter section is thus presented here in its publication form. The corresponding online version can be downloaded from the following URL:

http://www.sciencedirect.com/science/article/pii/S0376738813009654

Detailed literature review addressing modelling of HFMC for PCC was presented and discussed. Accordingly, the model assumptions were in agreement with those involved in several published investigations. Both 1D and 2D modelling strategies were analysed and the simulations results were compared. The simulations were performed under well-defined industrial conditions and by varying the geometrical characteristics of the module. As a result, 1D and 2D models led to almost identical averages of CO_2 absorption fluxes, thus demonstrating the quality of the 1D approach, as it requires less calculation time.

This investigation was performed with the collaboration of the following authors:

Author	Contribution
David Albarracin Zaidiza	2D model development 1D and 2D simulations and result analysis Manuscript writing
Joseph Billaud	Former 2D model development
Bouchra Belaissaoui	Manuscript writing
Sabine Rode	1D model development Manuscript writing
Denis Roizard	Manuscript reviewing
Eric Favre	Manuscript reviewing

Journal of Membrane Science 455 (2014) 64–74

Contents lists available at ScienceDirect

Journal of Membrane Science

journal homepage: www.elsevier.com/locate/memsci

Modeling of CO_2 post-combustion capture using membrane contactors, comparison between one- and two-dimensional approaches

David Albarracin Zaidiza, Joseph Billaud, Bouchra Belaissaoui, Sabine Rode [n], Denis Roizard, Eric Favre

Laboratoire Réactions et Génie des Procédés (LRGP) (UMR 7274), Université de Lorraine, ENSIC, 1, rue Grandville – BP 20451., 54001 Nancy Cedex, France

article info

Article history:
Received 19 August 2013
Received in revised form
4 December 2013
Accepted 7 December 2013
Available online 27 December 2013

Keywords:
Carbon dioxide capture
Modeling
Hollow fiber membrane contactor
Reactive absorption
Intensification

abstract

This work presents a numerical comparison between a one-dimensional and a two-dimensional model for CO_2 capture through solvent absorption with chemical reaction in a hollow fiber membrane contactor. The relevance of the two approaches is discussed. Industrially relevant operational conditions of post-combustion capture using MEA as reactive solvent were applied for both models. Variable gas and liquid mass transfer resistances, depending on the concentrations and the fluids velocity, were employed for the one-dimensional approach, while differential mass-balances considering convection, diffusion and reaction contributions were employed for the two-dimensional approach. The space-averaged specific molar CO_2 absorbed flux estimated by both models was almost identical, with a maximum relative difference of 5.73% for membrane permeabilities (ε/τ) comprised between 0.001 and 0.2 and external fiber radiuses comprised between 0.2 and 0.9 mm. Thus it turns out that the one-dimensional approach provides results similar to a two-dimensional approach in the investigated domain with significant lower calculation times.

& 2014 Elsevier B.V. All rights reserved.

1. Introduction

Post-combustion carbon dioxide capture presents tremendous challenges from a chemical engineering perspective. In the first generation of industrial installations, gas–liquid absorption using chemical solvents in packed columns is classically considered to be the best available technology [1]. However, the following two major challenges must be addressed to achieve the technical and economic targets: first, the decrease of the energy requirement of the process through novel solvents or heat-integration approaches, and second, the decrease of the size of the installation through process intensification. A promising strategy for the intensification of the gas–liquid absorption step is the use of hollow fiber membrane contactors (HFMC) rather than packed columns. The specific interfacial area for mass transfer in HFMC is the membrane surface area per contactor volume. For commercially available hollow fiber membrane modules, this ranges from 1500 to 3000 m^{-1}, depending on the diameter and packing density of the hollow fibers [2]. This area is much higher than the specific contact areas that are available in conventional packed columns used for chemical absorption of CO_2, which are approximately 200–300 m^{-1} in typical situations [3].

1.1. Literature review on two dimensional (2D) process modeling

Two dimensional (2D) process models of CO_2 absorption in HFMC of various complexities have been developed. Table 1 presents a review of modeling strategies and assumptions made in the papers cited hereunder. Table 2 presents the geometrical and operational investigated domain as well as simulation results. Almost all investigations were performed assuming liquid feed with fresh solvent ($\alpha^z = 0$) and almost all papers present experimental investigations for model validation using laboratory-scale absorption modules.

A very rigorous 2D modeling approach was published by Hoff et al. [4]. The chemical equilibrium speciation was calculated using an ionic solution model. By difference with other investigations, the temperature variations were taken into account, leading to varying physicochemical properties. The study revealed that in the applied operation conditions, the main mass transfer resistance was located in the liquid phase. The considered fiber diameter was relatively large, leading to low capture ratios (see Table 2).

Considering a two dimensional approach for the liquid phase and a one-dimensional plug-flow model for the gas phase, Wang et al. [5] showed that, using as solvent the AMP and DEA, the liquid flow velocity, the initial liquid concentration and the fiber length as well as the fiber radius have significant impacts on the CO_2 absorption flux.

Employing an equivalent model and performing experiences in a co-current arrangement, Zhang et al. [6] used a solvent with a

[n] Corresponding author.
E-mail address: sabine.rode@univ-lorraine.fr (S. Rode).

0376-7388/$ - see front matter & 2014 Elsevier B.V. All rights reserved.
http://dx.doi.org/10.1016/j.memsci.2013.12.012

D. Albarracin Zaidiza et al. / Journal of Membrane Science 455 (2014) 64–74

moderate reaction rate (DEA). The authors found that the absorbed CO_2 flux was significantly influenced by the inlet gas velocity, while the liquid velocity had only a modest effect. Keshavarz et al. [7] took into account the influence of partial membrane wetting. They concluded that membrane wetting, even at very low fractions, can decrease the absorption flux significantly. Eslami et al. [8] proposed a 2D approach for the process absorption with an aqueous solution of potassium glycinate, a solvent faster than DEA, and their simulation results showed that CO_2 absorption flux is influenced, among others, by the concentration of potassium glycinate and CO_2 and liquid and gas flow rates. Faiz et al. [9] included in the 2D model the gas velocity variation due to the absorption process. They outlined the significant influence of the initial CO_2 concentration on gas velocity variations and on absorption efficiency.

Another 2D model for both liquid and gas phases was proposed by Boucif et al.[10]; the Navier–Stokes momentum conservation equations were used to model the gas phase and modeling complex reaction kinetics were considered in the liquid phase modeling. Their results indicated that the performance of the HFMC is dependent on the gas velocity as well as on the module's geometry.

The operational conditions of the cited papers are shown in Table 2. In these investigations, atmospheric pressure and isothermal behavior (except for [4]) were considered for the absorption process [5–10,12,13]. Contradictions remain regarding the influence of some parameters (i.e. liquid and gas velocities) on the contactor performance and a current trend of increasing models complexity is observed. Although these models were validated for particular operation conditions (e.g., fresh solvent feed and high excess of liquid-side reactant in the process), they were not applied to industrial operating conditions, where both solvent recycling and high solvent conversion are required. However the investigations of Hoff et al. [4] included initially loaded solutions.

Table 1
Overview of 2D model assumptions and model strategies reported for HFMC in post-combustion CO_2 capture.

General model assumptions and features [4–10], [13]	
1.	2D modeling of the liquid phase
2.	Cylindrical geometry
3.	Steady state
4.	Ideal gas behavior
5.	Convective mass transfer in gas-filled membrane pores neglected
6.	Liquid in the fiber lumen
7.	Laminar liquid flow with fully developed velocity profiles
Model assumptions and features (made in part of the cited papers)	
8.	Constant temperature and liquid viscosity, all except [4]
9.	Constant liquid density, all except [4]
10.	Diffusion coefficients for diluted species, all except [4]
11.	Henry's law describing gas–liquid equilibrium, all except [4]
12.	Laminar flow on gas side, all except [4]
13.	Countercurrent, all except [6] which considers co-current
14.	Non-wetted membrane, all except [7] and [9] which consider partially wetted membranes
15.	Varying gas velocity (due to reagent consumption), all except [5] and [8] which consider constant gas velocities
16.	Fully developed velocity profile in the gas phase, all except [10] which considers Navier–Stokes equation in the gas phase
17.	Axial diffusion neglected in the two phases, all except [8] and [9]
18.	Gas phase plug flow [4–7]
19.	Fully developed concentration profile in gas phase (constant k_G) [5–6]
20.	Constant gas pressure, all except [4], [10] and [13]
21.	2D modeling of the gas phase 2D [8–10], [13]
22.	Kinetics including reaction reversibility, all except [13] which considers irreversible second order reaction kinetics.

1.2. Accuracy of a one-dimensional (1D) modeling approach

Complex 2D approaches model resolution requires important calculation time and high processor performance. Therefore it is tedious to investigate large parameter domains. The identification of the most efficient model strategy, which would ideally combine a rigorous approach without excessive complexity, is obviously a key issue in this area.

Kumar et al. [11] applied approximate solutions to predict the overall enhancement factor for reactive absorption in an HFMC. Comparing 1D and 2D simulations, they showed that for reasonably fast irreversible reactions characterized by thin reaction films, the computed overall enhancement factors of the 1D and the 2D approach were comparable. However, solely situations with only slightly varying reactant concentrations were explored.

Taking into account industrial relevant operating conditions [3], Rode et al. [12] developed a 1D model that allowed one to estimate the required length of the HFMC as well as the required feed velocities as a function of geometric module characteristics and operational constraints (pressure drops, capture ratio, inlet and outlet solvent loading).

Table 2
Overview of operational parameters in HFMC in post-combustion CO_2 capture studies reported in the literature.

Reference	Operational conditions[a]				Membrane characteristics					θ [dimensionless]
	u_L^0/u_G^0 [dimensionless]	x_A^0 [dimensionless]	$[Solvent]^Z$ [mol m^{-3}]	α^Z [$mol_A\ mol_B^{-1}$]	r_e [mm]	δ/r_e [dimensionless]	Φ [dimensionless]	ε/τ [dimensionless]	Z [mm]	
[4]	3×10^{-3} to 4.8×10^{-3}	0.05–0.1	$[MEA]^Z$: \$ 5000 $[MDEA]^Z$: \$ 1200	0–0.4	1.74	0.14	0.43	0.38	430	o 0.12
[5]	NS v_L: 0.1 m s^{-1}	~ 1	$[AMP]^Z$: 1560 $[DEA]^Z$: 1200 $[MDEA]^Z$: 1200	0	0.2	NS	NS	0.03–0.2[b]	200	NS
[6]	0.8–2.3	0.2	$[DEA]^Z$: 2000	0	0.15	0.26	NS	NS	113	θ> 0.9
[7]	1.3–4	0.2	$[DEA]^Z$: 2000	0 not clear	0.15	0.26	NS	NS	113	0.85–0.95
[9]	0.93	0.08–0.2	[PG]: 500–3000	0	0.22	0.22	0.213	0.225	150	0.75–0.95
[10]	2	0.05–0.5	$[MEA]^Z$: 5	0	0.15	0.26	0.08	0.2	228	0.85–0.99
[11]	1.6×10^{-2}–1.04	0.12	$[MEA]^Z$: 1200	0	0.19	0.26	0.046	0.0625	240 to 10^3	0.3–0.95
[12]	4.79×10^{-3}	0.15	$[MEA]^Z$: 1200	0.242	0.2–1	0.2–0.6	0.2–0.6	0.001–0.2	Varying	0.9
[13]	5×10^{-3}–10^{-2}	0.05–0.15	$[MEA]^Z$: ~ 3200–~ 5000	0–0.242	0.435	0.505	0.13–0.59	0.0012–0.014	300	0.1–0.99

NS: Not specified.

[a] Near atmospheric pressure and isothermal condition (generally 313 K) are considered in all papers.

[b] Estimated. The value of δ/r_e was supposed to 0.2, allowing one to calculate ε/τ using Eq. (6).

Recently, Chabanon et al. [13] presented a comparison between several modeling strategies (varying from a constant overall mass resistance to a 2D complex model) of the CO_2 capture utilizing MEA as the solvent in HFMCs. Using the model and operational constraints of Rode et al.[12], they concluded that a 1D model approach considering a variable global mass transfer coefficient led to results which were comparable to 2D models. However the simulation conditions were not presented in detail. Besides, the authors claimed that the 1D approach with a constant global mass transfer coefficient was only suitable for unvarying liquid-side reactant concentrations throughout the fiber.

In order to go further into the choice of the most relevant modeling approach, this paper presents a detailed comparison between a 1D and a 2D approach in an industrial relevant operational domain. It focuses on CO_2 absorption in monoethanolamine (MEA), but it is easily extended to other solvents. The paper is structured as follows. The considered geometrical characteristics, model assumptions and parametric and operational domain are exposed in Section 2. The hydrodynamics of the gas and the liquid flows, the mass transfer and the mathematical formulation for the one-dimensional as well as for the two-dimensional approaches are detailed in Sections 3 and 4, respectively. Finally, in Section 5, the simulation results are discussed and compared.

2. Overall system characteristic

For a membrane module with a hydrophobic microporous membrane, the absorption accompanied by a chemical reaction is a three step process, as illustrated in Fig. 1b. The solute species is transferred from the gas phase to the internal pore mouth of the membrane, then through the membrane pores, and finally absorbed by the liquid solution where it reacts. The geometrical characteristics and the operational domain were similar to those chosen in Rode et al. [12].

2.1. System geometry and flow configuration

The membrane contactor consists of a bundle of hydrophobic cylindrical hollow fibers. A single fiber is considered in the modeling as shown in Fig. 1. The fiber has an overall length Z, an external radius (r_e, varied from 0.2 to 0.9 mm), a shell radius r_s (estimated by Happel's free surface consideration [14]), varied from 0.26 to 1.16 mm corresponding to a fiber volume fraction φ of 0.6. The fiber has a relative thickness (δ/r_e, set to 0.2 and 0.6) permitting one to estimate an internal radius r_i and a membrane thickness δ. The most relevant geometrical characteristics of the porous medium that is created by the fiber bundle are presented in Table 3. The solvent (an aqueous solution of monoethanolamine, MEA) flows with a fully developed laminar parabolic velocity profile in the lumen side, whereas the gas mixture (saturated air and carbon dioxide) flows in the shell side surrounding the hollow fiber with a laminar velocity profile in a counter-current flow arrangement (Fig. 1a).

2.2. Operational domain and constraints

The operational parameters and constraints that were applied to all simulations are reported in Table 4. They were chosen to represent industrially relevant operating conditions for carbon dioxide capture. A mixture of 15% volumetric CO_2 and oxygen-depleted air, which is typical of a model coal power plant post-combustion flue gas, was considered. The inlet pressure of the gas-phase was 50 mbar above atmospheric pressure.

The liquid phase was a 30%(w/w) aqueous MEA solution that was circulated at 313 K. As recommended in the literature [3] to minimize the overall energy requirement of the capture process, the inlet solvent loading (α^Z, lean amine) was set to 0.242, whereas the outlet solvent loading was set to a value of 0.484. This was possible, for a given CO_2 capture ratio, by setting the inlet superficial gas to liquid velocity ratio to the appropriate value, as reported in Table 4. It is noteworthy mentioning that the almost

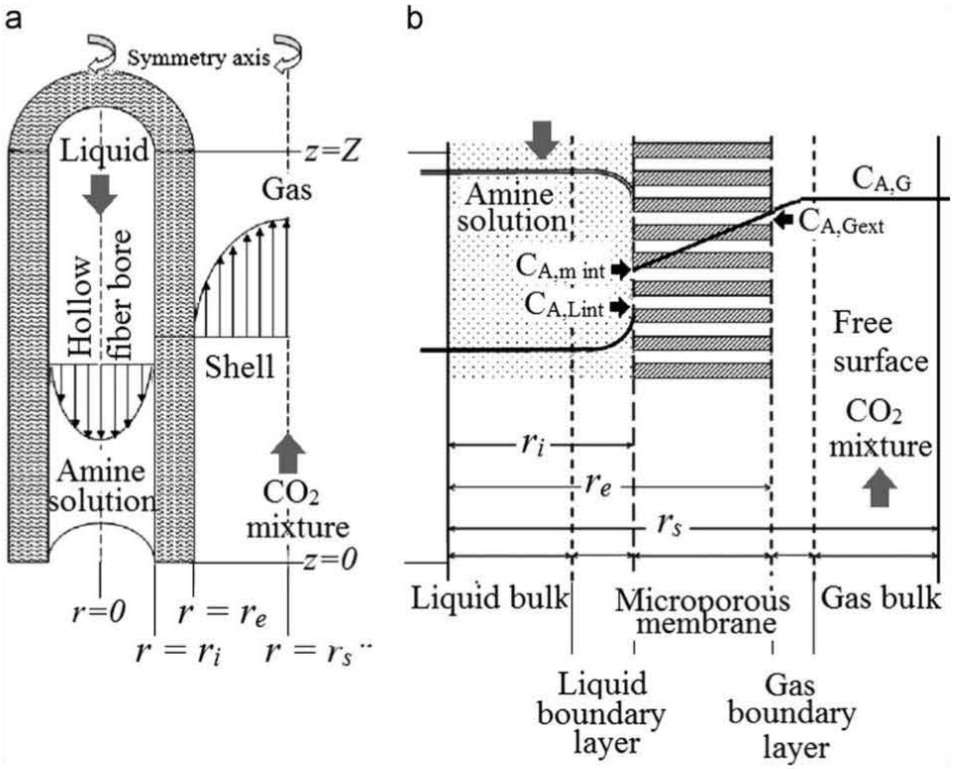

Fig. 1. Schematic representation of the hollow fiber membrane contactor; (a) velocity profiles of gas and liquid phases; (b) local concentration gradients.

Table 3
Definition and expression of geometrical characteristics of the hollow fiber bundle.

Parameter	Definition	Mathematical expression		Units
		External volume	Internal volume	
Fiber volume fraction	$\frac{\text{Volume occupied by the fibers}}{\text{Overall reactor volume}}$	$\varphi = \frac{N\pi r_e^2}{\Omega}$		dimensionless
Specific flow section	$\frac{\text{Flow section}}{\text{Overall reactor section}}$	$\varepsilon_{ext} = 1 - \varphi$	$\varepsilon_{int} = \varphi\,(1 - \delta/r_e)^2$	dimensionless
Hydraulic diameter	$\frac{4\text{Flow section}}{\text{Fluid/membrane interfacial area}}$	$d_{h,ext} = 2r_e\frac{1-\varphi}{\varphi}$	$d_{h,int} = 2r_e\,(1 - \delta/r_e)$	m
Relative membrane thickness	$\frac{\text{Membrane thickness}}{\text{external fiber radius}}$	δ/r_e		dimensionless
Specific interfacial area	$\frac{\text{Fluid/membrane interfacial area}}{\text{contactor volume}}$	$a_{ext} = 2\varphi/r_e$	$a_{int} = 2\varphi\,(1/\delta/r_e)\,r_e$	m

Table 4
Geometrical and operational parameters and physicochemical and reaction characteristics used in the simulations.

Type	Parameter description	Value or range	Units
Geometrical parameter range	External fiber radius	$2 \times 10^{-4} < r_e < 0.9 \times 10^{-3}$	m
	Relative membrane thickness	$0.2 < \delta/r_e < 0.6$	dimensionless
	Membrane permeability	$0.001 < \varepsilon/\tau < 0.2$	dimensionless
	Fiber volume fraction	$\varphi = 0.6$	dimensionless
Operational parameters and constraints[3]	Molar inlet fraction of CO_2	$x_A^0 = 0.15$	dimensionless
	Molar inlet concentration of CO_2	$C_{A-G}^0 = 6.052$	$mol_A\,m^{-3}$
	Capture ratio[a]	$\theta = 0.905$	dimensionless
	Total mass fraction of MEA	$y_{B-tot-mass} = 0.3$	$kg_B\,kg_L^{-1}$
	Inlet solvent loading of CO_2	$\alpha^Z = 0.242$	$mol_A\,mol_B^{-1}$
	Inlet solvent concentration of free MEA	$C_{B-L}^Z = 2544$	$mol_B\,m^{-3}$
	Outlet solvent loading of CO_2[a]	$\alpha^Z = 0.484$	$mol_A\,mol_B^{-1}$
	Inlet superficial velocity ratio	$u_L/u_G^0 = 4.79 \times 10^{-3}$	dimensionless
	Inlet pressure of the gas-phase	$P_G^0 = 1.05 \times 10^5$	Pa
	Overall gas-phase pressure drop	$\Delta P_G = 5 \times 10^3$	Pa
	Operating temperature	$T = 313$	K
Gas–liquid equilibrium	Definition of the equilibrium constant	$C_{A-L-i} = mC_{A-G-i}$	
	Equilibrium constant [22]	$m = 0.610$	$m_G^3\,m_L^{-3}$
Physicochemical and mass-transfer characteristics [15], [23], [24]	Liquid phase		
	Density	$\rho_L = 1004$	$kg\,m^{-3}$
	Viscosity	$\mu_L = 1.67 \times 10^{-3}$	Pa s
	Diffusion coefficient of CO_2	$D_{A-L} = 1.29 \times 10^{-9}$	$m^2\,s^{-1}$
	Diffusion coefficient of MEA	$D_{B-L} = 1.04 \times 10^{-9}$	$m^2\,s^{-1}$
	Gas phase		
	Viscosity	$\mu_G = 1.67 \times 10^{-3}$	Pa s
	Diffusion coefficient of CO_2	$D_{A-G} = 1.65 \times 10^{-5}$	$m^2\,s^{-1}$
Reaction characteristics [16]	Stoichiometry	$2B(L) + A(L) = B_2A(L)$	
	Kinetic expression	$R = k_r C_{A-L} C_{B-L}$	$mol_A\,m_L^{-3}\,s^{-1}$
	Kinetic constant	$K_r = 4.4 \times 10^8 \exp(-54{,}000/T)$	$m_L^3\,mol_B^{-1}\,s^{-1}$

[a] Only for the 1D approach. In the 2D approach these values are calculated.

complete conversion of not only the gas-side, but also the liquid-side reactant, i.e. MEA, is an important feature of industrial relevant operating conditions, although it is regrettably seldom applied in laboratory-scale investigations, as can be seen in Table 3.

The physicochemical characteristics, the diffusion coefficients and the reaction kinetics were estimated, using correlations that are available in the literature [15,16]. The values considered are given in Table 4.

In the 1D approach, the CO_2 capture ratio θ was set to 0.9 to reflect the classic guidelines of carbon dioxide capture [17]; the outlet solvent loading (α^0, rich amine) was fixed at 0.484. In the 2D approach, both θ and α^0 were calculated because the fiber length Z and the initial velocity of gas u_G^0 were imposed (see Section 5).

2.3. Model assumptions

Model assumptions made in this work for the 1D as well as for the 2D approach were those typically encountered in the literature, respectively, assumptions 2–18 of Table 1 for the 1D model and assumptions 1–17 and 21 of Table 1 for the 2D model.

The system was considered to be isothermal and the effect of CO_2 loading on viscosity and transport properties was not taken into account. These assumptions are important and may lead to miscalculations. However they are often reported in the literature (see Table 1).

The kinetics of the chemical reaction was considered to be non-reversible and second order (see Table 4). Furthermore, for the 2D model, the shell-side velocity distribution in the radial coordinate was computed using Happel's free surface consideration [14].

3. One-dimensional modeling approach

3.1. Hydrodynamics, mass transfer and chemical reaction

Liquid and gas flow were considered to be laminar with developed velocity profiles. In the operational conditions considered in this work, these assumptions were shown to be valid

in [12]. The superficial velocity ratio between the liquid and gas phases (u_L/u_G) was fixed considering a macro-balance. The interstitial fluid velocities (v_L and v_G) were calculated as follows (see Table 3 for the definitions).

$$v_L = \frac{u_L}{\varepsilon_{int}} \tag{1}$$

$$v_G = \frac{u_G}{\varepsilon_{ext}} \tag{2}$$

The mass transfer phenomenon was modeled, in the 1D approach, through the estimation of a local overall mass transfer coefficient K_{ov}, defined with respect to the internal fiber area. The latter was obtained by the summation of the mass transfer resistances of the three considered domains. The corresponding expression is given by

$$\frac{1}{K_{ov}} = \frac{1}{mEk_L} + \frac{1-\delta/r_e}{\delta/r_e}\ln\left(\frac{1}{1-\delta/r_e}\right)\frac{1}{k_M} + \frac{1-\delta/r_e}{k_G} \tag{3}$$

where k_L, k_M and k_G are the mass transfer coefficients in the liquid, membrane and gas domains, respectively. m is the CO_2 volumetric gas–liquid partition coefficient and E stands for the enhancement factor. The latter is related to the chemical reaction in the diffusion boundary layer and its calculation is performed based on classical relationships as detailed in Appendix A.

In laminar flow and for dilute species systems and low mass transfer rates, the mass and the heat transfer processes are commonly treated by transfer analogies [18,19]. In laminar flow through a cylindrical pipe, the convective heat and mass-transfer coefficients can thus be estimated by integrating the Graetz equation for suitable boundary conditions [20]. The two dimensionless numbers characterizing the resulting mass-transfer relation are the Sherwood and the Graetz number, denoted by Sh_F and Gz_F, respectively. It is noteworthy that the computed Sherwood values and mass transfer coefficients are related to the mixing cup concentration at the axial coordinate z. For low Graetz numbers, at the pipe entrance, the convective-diffusion boundary layer is under development, and the local Sherwood number decreases with increasing distance from the pipe entrance. For sufficiently high Graetz numbers (i.e., Gz_F4 0.03), the radial concentration profile is fully developed, and the local Sherwood number attains a limiting value. For the gas and liquid phases, non-fully developed concentration profiles are assumed at gas and liquid inlets. Taking this into account, the Sherwood number is estimated by [20]

$$Gz_F < 0.03 \quad Sh_F = 1.3Gz_F^{-1/3} \tag{4}$$

$$Gz_F > 0.03 \quad Sh_F = 4.36 \tag{5}$$

where Gz_F and Sh_F are the Graetz number and the Sherwood number, respectively. They are defined as

$$Gz_F = \frac{D_{j,F}\, z}{v_F d_h^2} \tag{6}$$

$$Sh_F = \frac{k_F\, d_h}{D_{j,F}} \tag{7}$$

The value of the limiting Sherwood number (i.e. 4.36) corresponds to uniform mass flux as boundary condition.

The membrane mass transfer coefficient is computed using a Fick diffusion mechanism

$$k_M = \frac{\varepsilon D_{A,G}}{\tau\ \delta} \tag{8}$$

3.2. Differential equations

The balance equations that characterize the system are presented in this section. According to the correlations chosen for the Sherwood number, the considered axial concentrations and velocities are the space-averaged values of the section. The differential equation system is as follows:

CO_2 differential molar balance

$$\frac{dC^*_{A,G}}{dz^*} = \frac{C^*_{A,G}}{P^*_G}\left(\frac{dP^*_G}{dz^*} - \frac{K^*_{ov}}{1-x^0_A}\left(P^*_G - C^*_{A;G}x^0_A\right)^2\right) \tag{9}$$

MEA differential molar balance

$$\frac{dC^*_{B,L}}{dz^*} = 2\frac{u^0_G}{u_L}K^*_{ov}C^*_{A;G} \tag{10}$$

Gas momentum balance

$$\frac{dP^*_G}{dz^*} = -A\frac{(1-x^0_A)u^{0^2}_G}{(P^*_G - C^*_{A,G}x^0_A)} \tag{11}$$

With

$$A = \frac{2\kappa\mu_G}{r_e}\frac{\varphi}{(1-\varphi)^3}\frac{1}{(1-(\delta/r_e))k_{max}P^0_G} \tag{12}$$

$$\kappa = 5{,}50\varphi^2 - 7{,}87\varphi + 7{:}43\ ;0{,}3 < \varphi < 0{,}6 \tag{13}$$

The 1D equation system has been expressed in the dimensionless form: the spatial coordinate was divided by the minimum height of transfer units, HTU_G, which was estimated using the greatest possible mass-transfer coefficient, k_{max} (as defined in Appendix A), and gas–liquid interfacial area, a_{int}.The reactant concentrations were divided by the inlet concentration of the gaseous reactant, and the local gas-phase pressure was divided by the inlet gas-phase pressure. The local overall mass transfer coefficient was divided by k_{max}.

$$z^* = \frac{z}{HTU_G};\quad HTU_G = \frac{u^0_G}{k_{max}a_{int}};\quad NTU_G = \frac{Zk_{max}a_{int}}{u^0_G} \tag{14}$$

$$C^*_{A;G} = \frac{C_{A,G}}{C^0_{A,G}};\quad C^*_{B,L} = \frac{C_{B,L}}{C^0_{A,L}};\quad P^*_G = \frac{P_G}{P^0_G} \tag{15}$$

With the following conditions at the fiber boundaries, forced using flow inlet conditions, defining an appropriate value for the gas to liquid flow ratio and finally adjusting the inlet gas velocity ($u_G{}^0$) and fiber length, in order to obtain the desired overall gas-phase pressure drop (i.e. 50 mbar) [12].

$$\text{Conditions at } z^* = 0: \quad C^{*,0}_{A;G} = 1 \quad C^{*;0}_{B;L} = 26.07 \quad P^{*;0}_G = 1 \tag{16}$$

$$\text{Conditions at } z^* = 1: \quad C^{*,Z}_{A,G} = 0.1047 \quad C^{*;Z}_{B;L} = 420.3 \quad P^{*;Z}_G = 0.952 \tag{17}$$

The integration of the differential system results in the determination of the gas and liquid velocities and the overall fiber length. The mass-transfer characteristics (i.e., reactant concentration and local flux) are computed all over the fiber length.

The space-averaged specific molar absorbed flux ($\phi_{A;mean}$), (designed henceforth by average absorbed flux) denotes the CO_2 absorbed flux per unit of volume of the contactor. This parameter, which provides a process intensification factor, was used in order to compare the 1D and 2D simulations. It was calculated with the

following equation obtained from macro-balances for the gas phase:

$$\phi_{A;mean;1D} = \frac{u_G^0 C_{A;G}^0 \theta}{Z} \quad (18)$$

By definition of the local overall mass transfer coefficient, the local specific molar absorbed flux (namely local absorbed flux) is

$$\phi_{A;1D} = K_{ov} a_{int} C_{A;G} \quad (19)$$

4. Two-dimensional modeling approach

4.1. Hydrodynamics, mass transfer and chemical reaction

In the 2D approach, the mass transfer is modeled taking into account the convection and diffusion contributions in the gas and liquid phases as well as the reaction contribution in the liquid phase. Inside the membrane, only the mass diffusion phenomenon is considered and the diffusion coefficient of CO_2 is estimated using a permeability approach.

4.1.1. Gas velocity

In a 2D approach, the gas pressure drop and gas velocity variations over the contactor length are often neglected in the HFMC models ([6–21]). However, the variations of local gas velocity, gas pressure and CO_2 absorbed flux are interconnected. On the one hand, as the CO_2 absorbed flux increases, the interstitial gas velocity decreases. On the other hand, as the pressure drop increases, the interstitial gas velocity increases. In practice, the first phenomenon is frequently dominant, leading to an increase of the gas residence time in the contactor, even at low concentrations of CO_2 [9].

To consider the two effects, the following approach was used for the estimation of the local gas phase velocity. The mean interstitial velocity in the axial coordinate was obtained by macro-balance over the shell compartment (Eq. (20)).

$$\overline{v_G} = \frac{u_G^0}{\varepsilon_{ext}} \frac{(1 - x_A^0)}{(\bar{P}_G - C_{A;G}^* x_A^0)} \quad (20)$$

This equation is also valid for the 1D approach. The local pressure has to be known and can be estimated using the Navier–Stokes equations. However, this approach requires important calculation time and the resulting radial velocity profile is very close to Happel's free surface model with a similar geometry and operational conditions [10]. Hence, for sake of simplicity, the Happel approach was used, leading to the following radial velocity profile [14]:

$$v_{G;Z} = 2\overline{v_G}(r_s^2 - r_e^2)\left[\frac{r^2 - 2r_s^2 \ln\left(\frac{r}{r_e}\right) - r_e^2}{3r_s^4 - 4r_s^2 r_e^2 + r_e^4 - 4r_s^4 \ln\left(\frac{r_s}{r_e}\right)}\right] \quad (21)$$

In addition, a linearly decreasing pressure profile was implemented:

$$\bar{P}_G = 1 - \left[\frac{\Delta P_G}{P_G^0}\right] z \quad (22)$$

The pressure variations of the 1D approach (Kozeny equation – Eq. (11)) and the linear pressure decay used in the 2D approach are shown in Fig. 2. The two curves are almost superimposed, leading to comparable gas velocity profiles in the two approaches. This equivalent treatment of the gas phase in the two approaches was necessary to allow their comparison in terms of reaction and mass transfer.

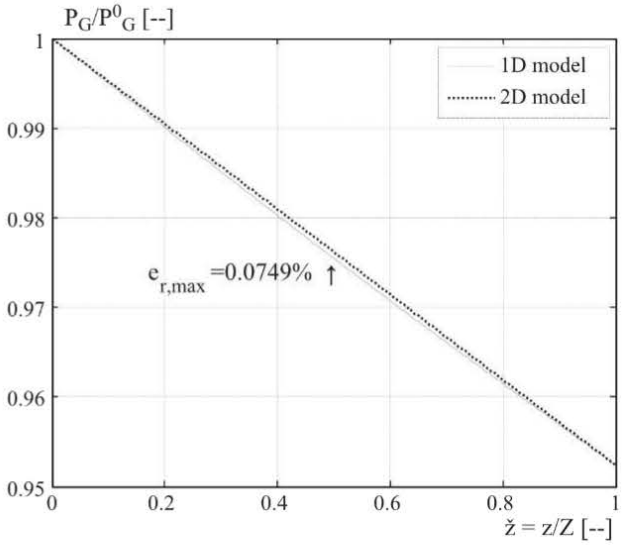

Fig. 2. Dimensionless pressure profile in the fiber length in the 1D and 2D approaches.

4.1.2. Liquid velocity

The fluid velocity distribution over the radial coordinate in the hollow fiber bore was calculated by integrating the momentum balance in a cylindrical shell in laminar flow, with no slip condition at the inner fiber wall:

$$v_{L;z} = 2\overline{v_L}\left[1 - \left(\frac{r}{r_i}\right)^2\right] \quad (23)$$

The average velocity L was determined to respect the following process constraint $u_L/u_G^0 = 4.79 \times 10^{-3}$ (see also Table 4).

4.2. Differential equations

The scaled 2D differential equation system is shown as follows:

– Liquid phase:

$$v_L \frac{\partial C_{A;L}}{\partial z} = \frac{1}{r}\frac{\partial}{\partial r}\left(r D_{A;L} \frac{\partial C_{A;L}}{\partial r}\right) + \frac{\partial}{\partial z}\left(D_{A;L} \frac{\partial C_{A;L}}{\partial z}\right) - R_A \quad (24)$$

$$v_L \frac{\partial C_{B;L}}{\partial z} = \frac{1}{r}\frac{\partial}{\partial r}\left(r D_{B;L} \frac{\partial C_{B;L}}{\partial r}\right) + \frac{\partial}{\partial z}\left(D_{B;L} \frac{\partial C_{B;L}}{\partial z}\right) - 2R_A \quad (25)$$

– Membrane:

$$0 = \frac{1}{r}\frac{\partial}{\partial r}\left(r D_{A;M} \frac{\partial C_{A;M}}{\partial r}\right) + \frac{\partial}{\partial z}\left(D_{A;M} \frac{\partial C_{A;M}}{\partial z}\right) \quad (26)$$

– Gas phase:

$$v_G \frac{\partial C_{A;G}}{\partial z} = \frac{1}{r}\frac{\partial}{\partial r}\left(r D_{A;G} \frac{\partial C_{A;G}}{\partial r}\right) + \frac{\partial}{\partial z}\left(D_{A;G} \frac{\partial C_{A;G}}{\partial z}\right) \quad (27)$$

The 2D equation system was expressed in a scaled form: the spatial coordinate was divided by the shell radius (r_s) and the axial coordinate was divided by the length of the fiber (Z). Considering that the system was scaled, the interstitial velocity and diffusion

coefficients were divided by the corresponding scale factor:

- Radial coordinate ($\check{r}$) = r/r_s
- Axial coordinate ($\check{z}$) = z/Z
- Interstitial velocity $\check{v}_{Fluid} = v_F/Z$
- Diffusion coefficient in radial coordinate $\check{D}_{j\,\text{À domain}} = D_{j\,\text{À domain}}/r_s^2$
- Diffusion coefficient in axial coordinate $\check{D}_{j\,\text{À domain}} = D_{j\,\text{À domain}}/Z^2$

Fig. 3 indicates the boundaries of the system modeled in the 2D approach. Table 5 presents the considered boundary conditions. The 2D simulations require the parameters and operational conditions from Table 4 as well as an initial gas velocity u_G^0 and a fiber length Z. The integration of the differential system leads to the determination of concentration profiles and velocity profiles in the three compartments.

Neglecting the mass transport by diffusion in the axial coordinate, the average absorbed flux (mol m^{-3} s^{-1}) was estimated as follows:

$$\phi_{A;mean;2D} = 2\int_{r_e}^{\check{r}_s} \check{r}\left(\left[\check{v}_G C_{A;G}\right]^{\check{z}=0} - \left[\check{v}_G C_{A;G}\right]^{\check{z}=1}\right) d\check{r} \quad (28)$$

Whereas the local absorbed flux (at a given coordinate z) was given by

$$\phi_{A;2D} = 2\frac{d}{d\check{z}}\int_{r_e}^{\check{r}_s} \check{r}\left[\check{v}_G C_{A;G}\right] d\check{r} \quad (29)$$

4.3. Mesh sizing

The model equations were solved using COMSOL Multiphysics Modeling version 4.1. This software uses the finite element method.

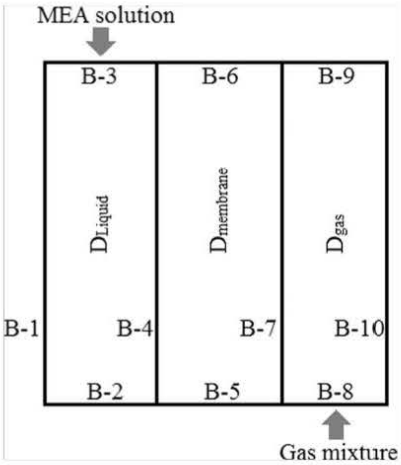

Fig. 3. Schematic representation of the contactor boundaries.

Table 5
2D Boundary conditions considered.

Boundary	Type	Equation assuming
B-1	Axial-symmetry	$\partial C_A/\partial\check{r} = \partial C_B/\partial\check{r} = 0$
B-2	Convective flux	$-D_{j;L}\nabla C_j = 0$
B-3	Concentration	$C_{A\text{-}B3} = 0$; $C_{B\text{-}B3} = C_{B;L}^{Z}$;
B-4	Concentration	$C_{A;L\text{-}B4} = mC_{A;M\text{-}B4}$
	No-Flux	$-N_B = 0$
B-5 and B-6	No-Flux	$-N_A = 0$
B-7	Flux	$C_{A;G\text{-}B7} = C_{A;M\text{-}B7}$
B-8	Concentration	$C_{A\text{-}B8} = C_{A;G}^{0}$
B-9	Concentration	$C_{A\text{-}B8} = C_{A;G}^{Z}$
B-10	Axial-symmetry	$\partial C_A/\partial\check{r} = \partial C_B/\partial\check{r} = 0$

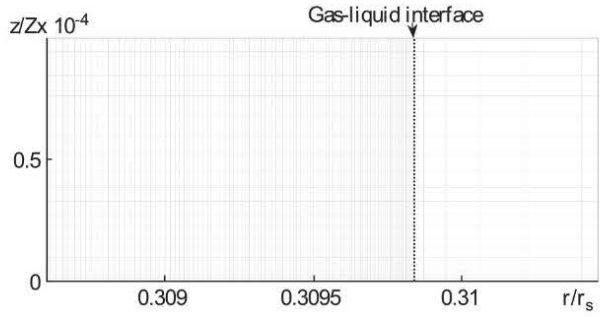

Fig. 4. Mesh zoomed representation for the lower right corner of the fiber bore.

Modeling was tricky because the reaction occurs very close to the gas–liquid interface. A careful meshing was essential to obtain correct results. Consequently, the space-scale of the mesh was selected of the same order of magnitude as the space-scale of the mass-transfer and reaction phenomena, leading to 2.5 million elements approximately for the overall system, including the three compartments. The shape of the elements was rectangular in accordance with the two main directions of transport phenomena (r, z). Fig. 4 shows a zoomed representation of the mesh distribution at the lower right corner of the fiber bore. Around boundaries, where the mass transfer layers were extremely thin, the meshes were refined using arithmetic progressions. However for the radial meshing of the liquid phase, a geometric progression was used as it proved to be most suitable. As can be seen in Fig. 4, elements size in the fiber bore in the vicinity of the gas–liquid interface was particularly small, as it is where the reaction takes place.

5. Simulations and discussion

To compare 1D and 2D approaches, the operating parameters had to be fixed to identical values. Respecting operational constraints, geometrical parameters and physicochemical and reaction characteristics (shown in Table 4), the length of fiber (Z) and the inlet gas velocity (u_G^0) were calculated from the integration of the 1D model with a capture ratio and a gas pressure drop imposed, as discussed in Rode et al. [12]. Later, these two operating parameters calculated with the 1D model, Z and u_G^0, were used as input data of the 2D model. Obviously, the outlet characteristics calculated using the 2D model may vary from those specified in the related 1D simulation. Results of both simulations were compared.

5.1. Simulations for an infinitely high gas and membrane mass transfer coefficient

To determine the difference between the models with respect to the mass transfer and reaction in the liquid phase, simulations were performed, neglecting the mass transfer limitation in the gas and membrane compartments. This was done imposing extremely high values for both, the gas diffusion coefficient (i.e. 100 times the real value) and the membrane permeability (i.e. ε/τ¼1), leading to flat concentration profiles in the gas-filled compartments. The influence of the external fiber radius (r_e) was studied.

5.1.1. Reactant radial profiles in the liquid phase

Results in the 2D simulations were analyzed to understand the influence of liquid species mass transfer limitations. Liquid phase concentration profiles for the highest investigated value of the external fiber radius (i.e. r_e¼0.9 mm) are shown in Fig. 5. Indeed, for this radius, the mass transfer limitations were the most important.

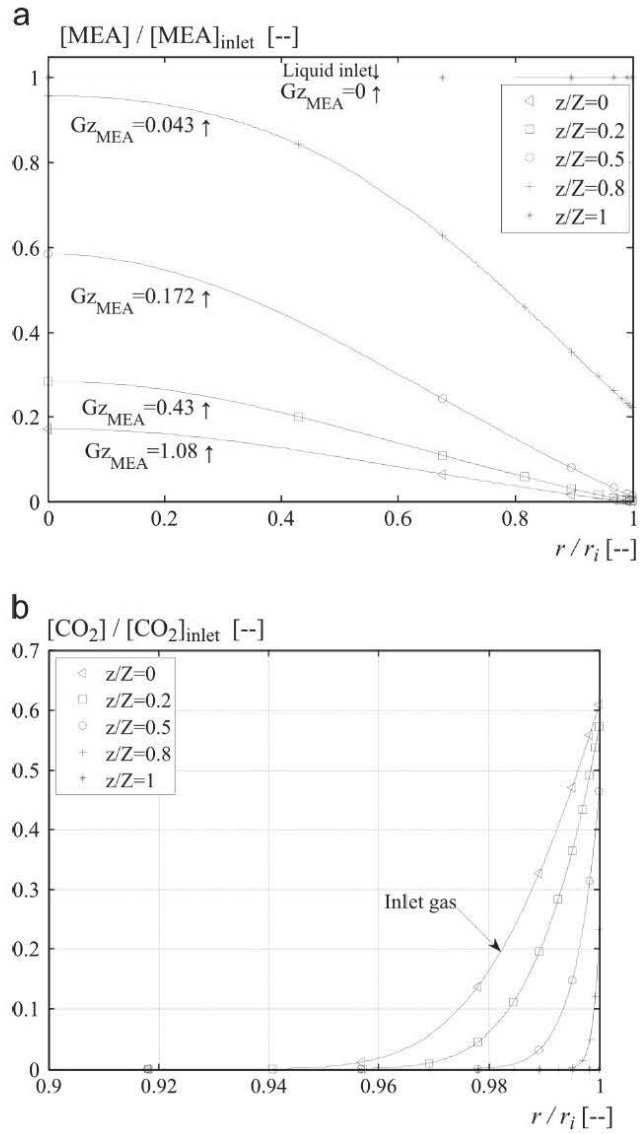

Fig. 5. Dimensionless liquid phase reactant concentrations as a function of the relative internal radius(r/r_i); different axial positions are shown; simulations performed for r_e= 0.9 mm, δ/r_e= 0.6, u_G^0= 0.74 m s^{-1}, Z= 3.03 m and no gas-membrane mass-transfer limitations; (a) MEA; (b) CO_2.

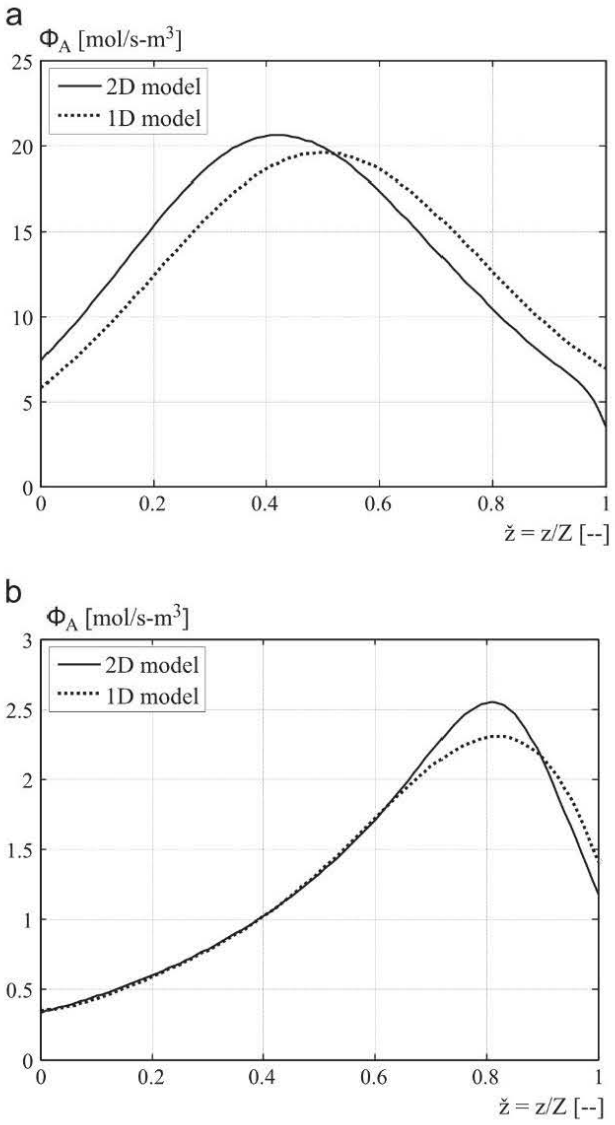

Fig. 6. Variation of the local absorbed flux with the dimensionless axial coordinate; no gas-membrane mass transfer limitations for δ/r_e= 0.6; (a) r_e= 0.2 mm, u_G^0¼0.53 m $s^{Á1}$, Z= 0.21 m; (b) r_e= 0.9 mm, u_G^0= 0.74 m s^{-1}, Z= 3.03 m.

The radial MEA concentration profiles in the liquid phase for different positions in axial coordinate are presented in Fig. 5a. A complete concentration profile development is observed in more than 80% of the fiber length. Under these conditions, the mass-transfer coefficient is solely a function of the diffusion coefficient and the hydraulic flow diameter and is independent of the flow velocity. These results validate the approach of the liquid-side mass transfer calculations made in the 1D approach. Moreover, the important concentration drop close to the liquid–gas interface indicates a limitation in the mass transfer of MEA.

Fig. 5b illustrates the CO_2 concentration in the liquid phase at several positions of the axial coordinate. Close to the liquid inlet section, at z/Z= 0.8, the CO_2 profile extends about a fraction of 0.005 into the fiber, whereas close to the gas inlet section, at z/Z, the CO_2 profile extends about a fraction of 0.03 of the tube. As r_e was 0.9 mm and δ/r_e was 0.6 in the illustrated simulation, r_i was 0.36 mm. This leads to film thicknesses of respectively 2 μm close to the gas outlet and 10 μm close to the gas inlet, values which are very small, indicating that the reaction occurs in the vicinity of the gas–liquid interface, thus validating the flat modeling approach of the gas–liquid reactive mass-transfer in the 1D model.

5.1.2. Spatial variation of the local absorbed flux

Fig. 6 shows the variation of the local absorbed flux in the membrane contactor with the non-dimensional coordinate z/Z, for both 1D and 2D simulations. Two external radiuses are illustrated (i.e., r_e= 0.2 mm and r_e= 0.9 mm). For both radiuses and both simulations, the local absorbed flux passes through a maximum value. For a small fiber radius (Fig. 6a) and for low values of the axial coordinate, the local absorbed flux of CO_2 is underestimated by the 1D model, with respect to the 2D model. However, for high values of the axial coordinate, it is overestimated, resulting in a kind of compensation. For a high fiber radius (Fig. 6b), the "compensation" is observed for high values of the axial coordinate, close to the gas outlet.

5.1.3. Variation of the average absorbed flux with the fiber radius

The average absorbed flux is the most relevant parameter for the industry, because it is related to the absorbed quantity of CO_2 per unit of volume of the contactor. It might be also taken as an intensification index knowing that the mean industrial value is around 1 mol m^{-3} s^{-1} for conventional technologies using packed

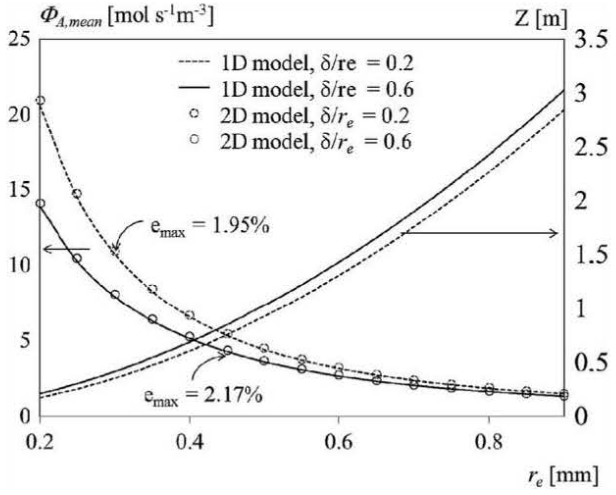

Fig. 7. Variation of the average absorbed fluxes (left axis) and of the contactor length (Z, right axis) with the external fiber radius; no gas-membrane mass-transfer limitations; u_G^0 varied between 0.53 m s^{-1} and 0.78 m s^{-1}.

columns [3]. Fig. 7 illustrates the variation of the average absorbed flux (left axis) and of the fiber length (right axis) with the fiber external radius for both 1D and 2D simulations and two extreme fiber thicknesses, i.e. δ/r_e set to 0.2 and 0.6. The maximal relative error between 1D and 2D approaches is indicated. Clearly, the "compensation" observed in the local absorbed flux leads for all simulations to only slight differences (< 2.17%) in the average absorbed flux estimated by the two approaches.

5.2. Simulations including the influence of the gas-and-membrane mass transfer resistances

In order to model the entire mass-transfer process and to identify an eventual difference between the simulations with regard to the gas-and-membrane mass transfer, simulations were performed using the real CO_2 diffusion coefficient in the gas phase and varying the relative permeability ($\varepsilon r_e/\delta\tau$) in a realistic domain, according to the values given in Table 4. As proposed in Rode et al. [12], the relative membrane conductance was defined as the ratio between the membrane mass-transfer coefficient, k_M, and a liquid mass transfer velocity, $D_{B,L}/r_e$.

5.2.1. Spatial variation of the local absorbed flux

Fig. 8 illustrates the variation of the local absorbed flux in the membrane contactor with the non-dimensional coordinate z/Z, for the two approaches and for high and low membrane permeabilities (respectively Fig. 8a and b). In order to maximize the effect of membrane resistance, thick membranes, i.e. δ/r_e= 0.6, were considered. Results are shown for a single external fiber radius, i.e. r_e= 0.2 mm. As in Section 5.1.2, the local absorbed flux went through a maximum value and "compensation" between the two approaches was observed. For high values of membrane permeability (Fig. 8a), the curves were very similar to those observed without gas-phase resistance (Fig. 6a). For low values of membrane permeability (Fig. 8b), the local absorbed fluxes were less important and the "compensation" was observed close to the gas inlet.

5.2.2. Influence of gas and membrane conductance on contactor performance

1D and 2D simulations were performed taking into account the gas-and-membrane conductance for a membrane permeability, ε/τ varied from 0.001 to 0.2, leading to a variation of the relative membrane conductance, $\varepsilon\delta/\tau r_e$, between 0.0083 and 0.34. Fig. 9 illustrates the variation of the ratio between the average absorbed

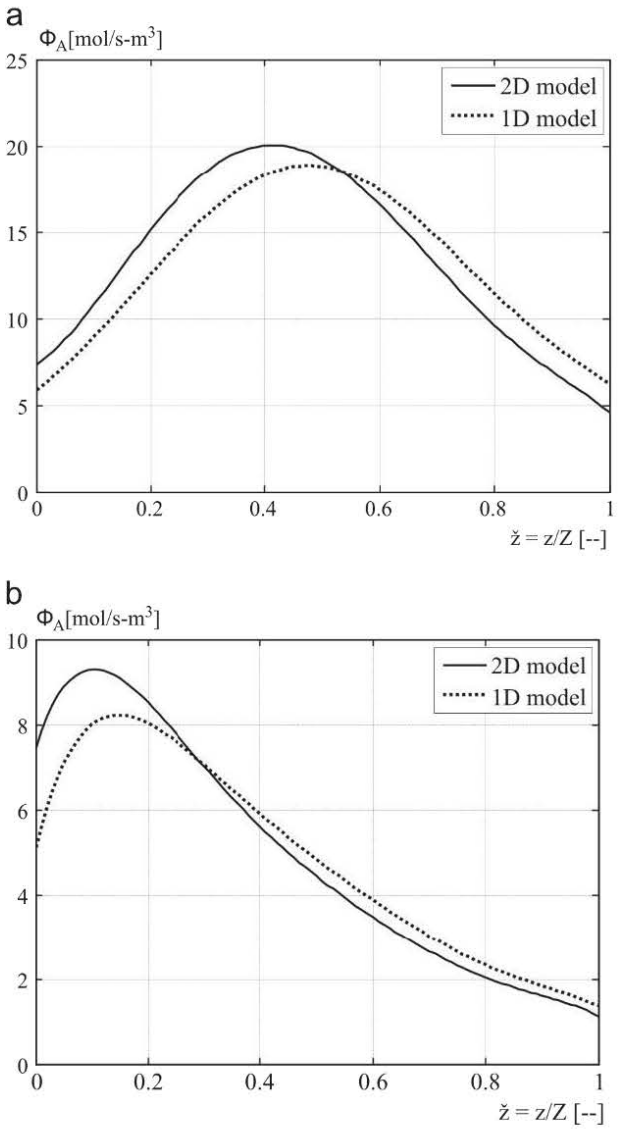

Fig. 8. Variation of the local absorbed flux with the dimensionless axial coordinate; simulations performed for r_e= 0.2 mm and δ/r_e= 0.6; (a) ε/τ= 0.2, u_G^0= 0.53 m s^{-1}, Z= 0.21 m; (b) ε/τ= 5 x 10^{-3}, u_G^0= 0.32 m s^{-1}, Z= 0.36 m.

fluxes (left axis) as well as of the ratio between the fiber lengths (right axis) calculated respectively with and without gas-and-membrane mass transfer limitations, as a function of the relative membrane conductance. Again, the 1D and the 2D simulations led to very similar predictions. However, for high membrane permeabilities, and for high external fiber radiuses, the estimated ratio of the average absorbed fluxes was higher in the 1D model, with a maximum difference between the two approaches of 3.56% The difference is due to the fact that the 1D and the 2D models lead to different gas-side conductances.

The estimation of the maximal difference of the average absorbed fluxes between the two approaches is explained in Appendix B. For all simulations performed, the maximal difference was of 5.73% thus clearly validating the quality of the 1D approach in the parametric domain considered.

6. Conclusions

The aim of the present work was to compare 1D and 2D modeling approaches for reactive absorption in hollow fiber membrane contactors. The comparison was performed considering the reactive

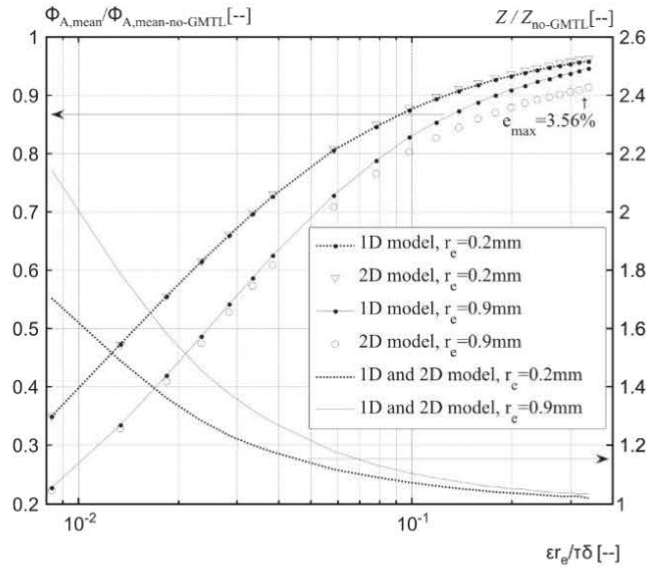

Fig. 9. Variation of (left axis) the ratio between the average absorbed fluxes calculated respectively with and without gas-and-membrane mass transfer limitations and (right axis) the ratio between the fiber lengths calculated respectively with and without gas-and-membrane mass transfer limitations, with the relative membrane conductance for $\delta/r_e = 0.6$; u_G^0 varied between 0.32 m s^{-1} and 0.72 m s^{-1}.

absorption of CO_2 in MEA under industrial relevant operation conditions. The developed methodology may be applied to other reactive systems. It turned out that in the investigated parametric domain the two approaches predicted an almost identical specific average molar CO_2 absorbed flux (mol m^{-3}_{HFMC} s^{-1}), which led to a maximal difference of 5.73%for membrane permeabilities (ε/τ) comprised between 0.001 and 0.2 and external fiber radiuses comprised between 0.2 and 0.9 mm. It is thus shown, that in some situations, with rapid reactions resulting in thin reaction films and soluble reaction products, it is not necessary to use a 2D approach to estimate the overall absorption flux, considering that the 1D approach provides almost the same results with significant lower calculation times. It turns out that industrial relevant operation conditions for CO_2 capture with MEA seem to respond to these conditions. This result is essential, as the consistent choice of the model complexity is an important issue in research and development of the HFMC technology. Even though the simulations presented here were not validated using experiments, the assumptions of the 2D model which are similar to literature assumptions were previously validated by several research groups [5–8,10,11,13]. However, the integrations of temperature variations in both 1D and 2D approaches, as well as an experimental validation of the approaches applying industrial relevant operation conditions are complying outlooks.

Appendix A

In the 1D approach, the mass transfer with chemical reaction is conventionally modeled using the enhancement factor (E) which depends on the reaction regime. The three regimes are as follows:

The diffusion of MEA is not limiting (the reaction located in the vicinity of the gas–liquid interface)

$$\frac{E_{iim}}{Ha} > 50 \text{ then } E = \sqrt{1 + Ha^2} \qquad (A1)$$

The diffusion of MEA is limiting (a sharp reaction front is formed in the vicinity of the gas–liquid interface)

$$\frac{E_{iim}}{Ha} < 0{:}02 \text{ then } E = E_{iim} \qquad (A2)$$

The diffusion of MEA is partially limiting (intermediate situation)

$$0.02 < \frac{E_{iim}}{Ha} < 50 \text{ then } E = \frac{Ha\sqrt{(E_{iim} - E)/(E_{iim} - 1)}}{\tanh\left(Ha\sqrt{\frac{E_{iim} - E}{E_{iim} - 1}}\right)} \qquad (A3)$$

where Ha (Hatta number) represents the ratio between the reaction kinetics and the maximal local material flux when the MEA diffusion is not limiting. Its expression is

$$Ha = \frac{\sqrt{D_{A;L} k_r C_{B;L}}}{k_{L;A}} \qquad (A4)$$

And E_{iim} (limiting enhancement factor) represents the ratio between the diffusion distance without reaction and the diffusion distance with reaction when the MEA is limiting. Its expression is

$$E_{iim} = 1 + \frac{C_{B;L} D_{B;L}}{2 m C_{A;G} D_{A;L}} \qquad (A5)$$

The maximum mass transfer coefficient, assuming no diffusion limitation, is calculated in the 1D approach as follows:

$$k_{max} = m\sqrt{C^Z_{B;L} k_r D_{A;L}} \qquad (A6)$$

Appendix B

From the industrial viewpoint, it is interesting to determine the maximal deviation of the 1D model with respect of the 2D model with regard to the average molar absorbed flux of CO_2. This value can be determined, for the two models, as

$$\bar{\phi}_A = \phi^{No\,GMTL}_{A;mean} * \frac{\phi_{A;mean}}{\phi^{No\,GMTL}_{A;mean}} \qquad (B1)$$

where $\phi^{No\,GMTL}_{A;mean}$ is the average molar absorbed flux of CO_2 without gas and membrane mass transfer limitations, which corresponds to the calculations in Section 5.1.3, and $\phi_{A;mean} = \phi^{No\,GMTL}_{A;mean}$ is the ratio of the average molar absorbed flux of CO_2 with and without gas and membrane mass transfer limitations corresponding to Section 5.2.2. The maximal deviation between the approaches can thus be estimated as follows:

$$\frac{\partial\bar{\phi}_A}{\bar{\phi}_A}_{max} = \frac{\partial(\phi^{No\text{-}GMTL}_{A;mean})}{\phi^{No\text{-}GMTL}_{A;mean}} + \frac{\partial(\phi_{A;mean}/\phi^{No\text{-}GMTL}_{A;mean})}{\phi_{A;mean}/\phi^{No\text{-}GMTL}_{A;mean}} = e^{No\text{-}GMTL}_{max} + e^{with/without\ GMTL}_{max} \qquad (B2)$$

Nomenclature

Latin symbols

a	specific interfacial area (m^2 $m^{-3}_{Reactor}$)
C	molar concentration (mol m^{-3})
D	diffusion coefficient (m^2 s^{-1})
d_h	hydraulic diameter (m)
E	enhancement factor (dimensionless)
Gz	material Graetz number (dimensionless)
Ha	Hatta number (dimensionless)
HTU_G	height of a gas-side transfer unit (m)
k	local mass transfer coefficient (m s^{-1})
k_r	kinetic constant (m_L^3 mol_B^{-1} s^{-1})
K	overall mass transfer coefficient (m s^{-1})
m	CO_2 gas–solvent volumetric partition coefficient (m^3_G m^{-3}_L)
M_B	molecular weight of MEA (kg mol^{-1})

N	number of fibers in the module (dimensionless)
NTU_G	number of gas-side transfer units (dimensionless)
P	pressure (Pa)
r_e	external fiber radius (m)
r_i	internal fiber radius (m)
r_s	shell radius (m)
R	reaction rate ($mol_A\ m_L^{-3}\ s^{-1}$)
Sh	Sherwood number (dimensionless)
T	temperature (K)
u	superficial flow velocity ($m\ s^{-1}$)
v	interstitial flow velocity ($m\ s^{-1}$)
x	mole fraction in the gas feed mixture (dimensionless)
$y_{B\text{-tot-mass}}$	MEA mass fraction in the liquid phase ($kg_B\ kg_L^{-1}$)
z	axial coordinate in the reactor (m)
Z	fiber length (m)

Greek symbols

α	solvent loading of CO_2 ($mol_A\ mol_B^{-1}$)
δ	membrane thickness (m)
ΔP	overall pressure drop (Pa)
ε	membrane porosity or flow section (dimensionless)
Φ_A	specific molar flux of the gaseous reactant ($mol_A\ m_{reactor}^{-3}\ s^{-1}$)
φ	fiber or cylinder volume fraction or packing factor
μ	dynamic viscosity (Pa s)
θ	capture ratio (dimensionless)
ρ	density ($kg\ m^{-3}$)
τ	membrane pore tortuosity (dimensionless)

Subscripts

A	gas-phase reactant (CO_2)
B	liquid-phase reactant (MEA)
ext	relative to the external hollow fiber bundle volume (shell)
F	relative to the fluid
G	relative to the gas phase
j	relative to component j
int	relative to internal hollow fiber bundle volume
L	relative to the liquid phase
lim	limiting value
m	relative to the membrane
max	maximal
mean	averaged
ov	overall

Superscripts

GMTL	gas and mass transfer limitations
Z	liquid-inlet and gas-outlet section of the HFMC
0	gas-inlet and liquid-outlet section of the HFMC
n	dimensionless variable or number
˜	reduced variable (2D approach)

References

[1] R. Steeneveldt, B. Berger, T.A. Torp, CO_2 capture and storage: closing the knowing–doing gap, Chem. Eng. Res. Des. 84 (9) (2006) 739–763.
[2] P.S. Kumar, J.A. Hogendoorn, P.H.M. Feron, G.F. Versteeg, New absorption liquids for the removal of CO_2 from dilute gas streams using membrane contactors, Chem. Eng. Sci. 57 (9) (2002) 1639–1651.
[3] F.A. Tobiesen, H.F. Svendsen, O. Juliussen, Experimental validation of a rigorous absorber model for CO_2 postcombustion capture, AIChE J. 53 (4) (2007) 846–865.
[4] K.A. Hoff, O. Juliussen, O. Falk-Pedersen, H.F. Svendsen, Modeling and experimental study of carbon dioxide absorption in aqueous alkanolamine solutions using a membrane contactor, Ind. Eng. Chem. Res. 43 (16) (2004) 4908–4921.
[5] R. Wang, D.F. Li, D.T. Liang, Modeling of CO_2 capture by three typical amine solutions in hollow fiber membrane contactors, Chem. Eng. Process.: Process Intensif. 43 (7) (2004) 849–856.
[6] H.-Y. Zhang, R. Wang, D.T. Liang, J.H. Tay, Modeling and experimental study of CO_2 absorption in a hollow fiber membrane contactor, J. Membr. Sci. 279 (1–2) (2006) 301–310.
[7] P. Keshavarz, J. Fathikalajahi, S. Ayatollahi, Analysis of CO_2 separation and simulation of a partially wetted hollow fiber membrane contactor, J. Hazard. Mater. 152 (3) (2008) 1237–1247.
[8] S. Eslami, S.M. Mousavi, S. Danesh, H. Banazadeh, Modeling and simulation of CO_2 removal from power plant flue gas by PG solution in a hollow fiber membrane contactor, Adv. Eng. Softw. 42 (8) (2011) 612–620.
[9] R. Faiz, M.H. El-Naas, M. Al-Marzouqi, Significance of gas velocity change during the transport of CO_2 through hollow fiber membrane contactors, Chem. Eng. J. 168 (2) (2011) 593–603.
[10] N. Boucif, J.P. Corriou, D. Roizard, E. Favre, Carbon dioxide absorption by monoethanolamine in hollow fiber membrane contactors: a parametric investigation, AIChE J. 58 (9) (2012) 2843–2855.
[11] P. Kumar, J. Hogendoorn, P.H. Feron, G. Versteeg, Approximate solution to predict the enhancement factor for the reactive absorption of a gas in a liquid flowing through a microporous membrane hollow fiber, J. Membr. Sci. 213 (1–2) (2003) 231–245.
[12] S. Rode, P.T. Nguyen, D. Roizard, R. Bounaceur, C. Castel, E. Favre, Evaluating the intensification potential of membrane contactors for gas absorption in a chemical solvent: a generic one-dimensional methodology and its application to CO_2 absorption in monoethanolamine, J. Membr. Sci. 389 (2012) 1–16.
[13] E. Chabanon, D. Roizard, E. Favre, Modeling strategies of membrane contactors for post-combustion carbon capture: a critical comparative study, Chem. Eng. Sci. 87 (2013) 393–407.
[14] J. Happel, Viscous flow relative to arrays of cylinders, AIChE J. 5 (2) (1959) 174–177.
[15] S. Cheng, A. Meisen, A. Chakma, Predict amine solution properties accurately, Hydrocarbon Process. 75 (2) (1996).
[16] G.F. Versteeg, L.A.J. Van Dijck, W.P.M. Van Swaaij, On the kinetics between CO_2 and alkanolamines both in aqueous and non-aqueous solutions. An overview, Chem. Eng. Commun. 144 (1) (1996) 113–158.
[17] B. Metz, O. Davidson, H. de Coninck, M. Loos, L. Meyer, IPCC Special Report on Carbon Dioxide Capture and Storage, Cambridge University Press, New York, NY (United States), 2005.
[18] W.J. Beek, K.M.K. Muttzall, J.W. Heuven, Transport Phenomena, Wiley, 1999.
[19] A.H. P. Skelland, Diffusional Mass Transfer, R.E. Krieger Pub. Co., 1985.
[20] A. Lévêque, Les Lois de la transmission de chaleur par convection, Dunod, Paris, France, 1928.
[21] S. Boributh, S. Assabumrungrat, N. Laosiripojana, R. Jiraratananon, A modeling study on the effects of membrane characteristics and operating parameters on physical absorption of CO_2 by hollow fiber membrane contactor, J. Membr. Sci. 380 (2011) 21–33.
[22] S. Ma'mun, R. Nilsen, H.F. Svendsen, O. Juliussen, Solubility of carbon dioxide in 30 mass % monoethanolamine and 50 mass % methyldiethanolamine solutions, J. Chem. Eng. Data 50 (2) (2005) 630–634.
[23] G.F. Versteeg, W. Van Swaalj, Solubility and diffusivity of acid gases (carbon dioxide, nitrous oxide) in aqueous alkanolamine solutions, J. Chem. Eng. Data 33 (1) (1988) 29–34.
[24] E.D. Snijder, M.J.M. te Riele, G.F. Versteeg, W.P.M. van Swaaij, Diffusion coefficients of several aqueous alkanolamine solutions, J. Chem. Eng. Data 38 (3) (1993) 475–480.

3.3. Summary and Conclusions

This chapter presented isothermal modelling of HFMC. A detailed analysis was presented for the mass-transfer mechanism through the membrane, i.e. convection inside the membrane pores and membrane wetting. Even if convection through the porous medium occurs, it can be neglected in the context of CO_2 absorption. Conversely, membrane wetting dramatically increases the membrane mass-transfer resistance. Chemical reactions occurring inside the liquid filled pores may compensate for this increase but not for values exceeding 10% of wetting fraction. Membrane wetting renders the prediction of the membrane mass-transfer coefficients complex. However, since in PCC membrane wetting is likely to occur, it was possible to identify an interval of membrane mass-transfer coefficients. The one- and two-dimensional modelling approaches were compared assuming isothermal behaviour and considering CO_2 to be the solely transferred species. Both models led to almost identical average CO_2 absorption fluxes, thus demonstrating the quality of the 1D approach, as it requires less calculation time.

3.4. Résumé et conclusions

Ce chapitre décrit l'approche isotherme de l'absorption du CO_2 en utilisant des contacteurs membranaires à fibres creuses. Les mécanismes de transfert de matière à travers de la membrane, i.e. la convection dans les pores de la membrane et le mouillage de la membrane, ont été analysés en détail. Les résultats de la simulation montrent que même si la convection à travers les pores de la membrane se produit, elle peut être négligée dans le cadre de l'absorption du CO_2. A l'inverse, le mouillage des membranes augmente significativement la résistance au transfert de matière de la membrane. L'accélération du transfert de matière due à la réaction chimique se produisant à l'intérieur des pores remplis de liquide, peut compenser l'effet négatif du mouillage quand la fraction de mouillage ne dépasse pas 10%.

La prédiction des coefficients de transfert de matière dans la membrane est complexe en raison du phénomène de mouillage. Néanmoins, étant donné que dans les conditions industrielles de captage du CO_2 en postcombustion, le mouillage est très probable, il a été possible d'identifier un intervalle de validité des coefficients de transfert de matière de la membrane.

Les approches monodimensionnelle (1D) et bidimensionnelle (2D) ont été comparées en considérant l'opération d'absorption comme étant isotherme et mono-constituant (i.e. CO_2). Les deux modèles ont conduit à des flux moyens d'absorption de CO_2 quasiment identiques, prouvant ainsi l'intérêt d'une modélisation 1D, puisque nécessitant moins de temps de calcul.

Chapter 4. Adiabatic Modelling of Membrane Contactors

The large majority of industrial unit operations can be considered to be adiabatic, since the equipment used to perform these operations are typically large in size and are characterised by low external surface-to-volume ratios. As such, heat transference toward the environment can be neglected. The absorption of CO_2 in aqueous amine solutions is known for its exothermic nature. For instance, in relatively concentrated MEA solutions, the heat of the absorption is about 80 kJ per mole of CO_2, which is almost two times higher than the latent heat of water. In steady state, the energy of dissolution-reaction is thus released to the gas and the liquid, leading to an increase of temperature or to the evaporation of the volatile species within the system. Given that almost all physicochemical and thermodynamic properties are temperature dependent, the thermal effects are expected to influence the performance of the operation.

In the context of membrane science, temperature variations affect the membrane-liquid interactions, such as the contact angle or the pore shape, as well as the membrane structural stability. Furthermore, as volatile components, such as water vapour, are transferred through the membrane, they might interfere with the CO_2 transport, or they might condensate in the membrane pores due to local over-saturations and the confined space.

From a modelling perspective, this type of approach is challenging as it becomes considerably more complex than that for isothermal modelling. However, it is more rigorous and allows for a more complete description of the operation in a large domain, covering both laboratory and industrial conditions. This is of particular interest for optimization, process flow-sheeting and flow configuration analysis purposes.

In this chapter, the adiabatic 1D and 2D modelling approaches of HFMC are presented and evaluated under both mild and severe conditions. The approaches have been verified through modelling of well-documented CO_2 chemical absorption by means of packed columns. Membrane mass-transfer aspects are discussed, such as the multicomponent transfer and the distribution of the membrane mass-transfer coefficient. A study of different flow configurations related to the membrane technology is presented, followed by a summary and conclusions.

4.1. Adiabatic One-Dimensional Modelling of HFMC

This section is presented in its publication form, which was published in the *Journal of Membrane Science* in June, 2015. This paper aims to investigate the thermal effects of the absorption operation in membrane contactors, including water evaporation and condensation, as this aspect has been neglected by most investigations and yet can influence the membrane transfer. To do this, an adiabatic one-dimensional multicomponent model of HFMC was developed. Moreover, for the first time, CO_2 chemical absorption using HFMC was simulated in both laboratory and industrial conditions which allowed for improved quantification of the intensification potential of this technology with respect to packed columns. The simulation results were compared to those obtained by an isothermal model. The implications of the thermal effects on the membrane contactor performance were discussed.

A copy of the paper is presented hereunder. The corresponding online version can be downloaded from the following URL:

http://www.sciencedirect.com/science/article/pii/S0376738815005396

This investigation was performed with the collaboration of the following authors:

Author	Contribution
David Albarracin Zaidiza	1D adiabatic model development Simulations and result analysis Manuscript writing
Bouchra Belaissaoui	Manuscript writing
Sabine Rode	Manuscript writing
Thibaut Neveux	Advice on modelling Manuscript reviewing
Camel Makhloufi	Manuscript reviewing
Christophe Castel	Experimental data Manuscript reviewing
Denis Roizard	Manuscript reviewing
Eric Favre	Manuscript reviewing

Journal of Membrane Science 493 (2015) 106–119

Contents lists available at ScienceDirect

Journal of Membrane Science

journal homepage: www.elsevier.com/locate/memsci

Adiabatic modelling of CO_2 capture by amine solvents using membrane contactors

David Albarracin Zaidiza, Bouchra Belaissaoui, Sabine Rode[n], Thibaut Neveux, Camel Makhloufi, Christophe Castel, Denis Roizard, Eric Favre

Laboratoire Réactions et Génie des Procédés (LRGP) (UMR 7274), Université de Lorraine, ENSIC, 1, rue Grandville, BP 20451, 54001 Nancy Cedex, France

article info

Article history:
Received 3 February 2015
Received in revised form
3 June 2015
Accepted 4 June 2015
Available online 25 June 2015

Keywords:
CO_2 capture
Chemical absorption
Membrane contactor
Adiabatic modeling
Capillary condensation

abstract

The modelling of CO_2 chemical absorption using hollow fiber membrane contactors is addressed. A one-dimensional, multicomponent adiabatic model for the CO_2 absorption using an aqueous solution of monoethanolamine is established. The model is validated using both, laboratory and pilot-scale experiments. The simulation results are compared to those from an isothermal model in order to investigate the influence of heat release on contactor performance. When industrial relevant operating conditions are applied, the adiabatic simulations show significant axial temperatures peaks, up to 30 °C. Correspondingly, local gas-phase vapor molar fractions values of up to 0.4 are attained. If compared to simulations from an isothermal model, deviations of about 60% were obtained, thus clearly demonstrating the necessity of adiabatic modelling under industrial conditions. Intensification factors comprised of between 2 and 10, for external fiber radiuses in the range of 300–100 μm are attained. The mass transfer coefficient is varied from 10^{-4} to 10^{-3} m s^{-1} which corresponds to experimentally observed values of microporous membranes that are presumably resistant to liquid breakthrough. However, wetting remains a major problem in microporous as well as composite membranes, as capillary condensation is likely to occur.

2015 Elsevier B.V. All rights reserved.

1. Introduction

Post-combustion carbon dioxide capture is a key issue for achieving greenhouse gas emission reductions. Gas–liquid absorption using aqueous monoethanolamine (MEA) solutions in packed columns is currently considered as the most adequate technology for post-combustion applications. Two major challenging targets are aimed in order to meet both, technical and economic constraints: the decrease of process energy requirement through novel solvent or heat integration approaches, and the decrease of equipment size through process intensification. An alternative technology, the hollow fiber membrane contactor (HFMC), shows promising intensification potential, because its specific contact area of 1500–3000 m^{-1}, values far above those encountered in conventional packed columns (about 200 m^{-1} [1]).

Experimental and theoretical researches have been published on HFMC for CO_2 capture using amine solutions, addressing material, mass transfer and process design issues. However, in these studies the performance of the process has been essentially evaluated considering fresh amine solvent (non-loaded), and low amine conversion leading to isothermal behavior. Moreover water transfer has been neglected. These conditions are convenient in laboratory research but are not relevant in an industrial context. The present work is intended to fill the gap: a multicomponent adiabatic model for CO_2 capture in a membrane contactor under industrial relevant conditions is developed.

The paper is structured as follows: published isothermal and adiabatic studies are discussed in Section 1. In Section 2, the overall system characteristics are presented in detail. Section 3 exposes the modelling approach which comprises of physico-chemical, thermodynamic, kinetic and mass- and heat transfer aspects. Simulation results are presented and discussed in Section 4. Finally, the model results are compared to available, non-isothermal experimental data.

1.1. Literature overview

General literature reviews concerning the use of HFMC in CO_2 reactive absorption are presented in [2,3]. An increase of the specific CO_2 flux, when using HFMC has been obtained by numerous authors. For microporous membranes, wetting was considered to be the main problem of this technology.

A literature review focusing on modelling issues is given in [3] and [4]. Process models of various complexities have been

[n] Corresponding author.
E-mail address: sabine.rode@univ-lorraine.fr (S. Rode).

http://dx.doi.org/10.1016/j.memsci.2015.06.015
0376-7388/& 2015 Elsevier B.V. All rights reserved.

developed considering isothermal conditions and neglecting water transfer. Simple models based on an average overall mass transfer coefficient have been suggested [5]. The principal assumption of these models is the invariance in conductance for each of the gas-side, membrane- and liquid-side, over the entire fiber length. They cannot be applied to operating conditions in which the liquid-side conductance varies widely over the reactor length [6]. For this case, one dimensional models based on series resistance approaches were proposed, considering varying gas- and liquid-side conductances [6]. Simultaneously, supported by the rapid development of CFD facilities, two dimensional models were published [4,7,8]. These models are based on the resolution of the convective diffusion equations coupled with the equations of the chemical reactions, using cylindrical geometry coordinates, and applied to a binary feed gas mixture of CO_2 and N_2.

In a previous paper [4], a comparison of one and two dimensional approaches assuming isothermal behavior and neglecting water transfer was performed for CO_2 capture with amine solution using membrane contactors. The aim was to identify the most efficient model strategy. The results showed comparable simulation results, with a maximum relative deviation of 2.2% thus indicating the quality of the 1D approach.

To our knowledge, few research papers tackle the adiabatic multi-component modelling of HFMC for chemical absorption of CO_2 [9–13]. Hoff et al. [9,10] developed and validated a two-dimensional diffusion-reaction model in a relatively large range of operation conditions. It is however not clear whether industrially relevant conditions were attained. Moreover, no temperature profiles were shown. The authors considered that in HFMC with reversible chemical reactions, the liquid-phase product diffusion is the limiting factor. For scaling purposes, they pointed out that 2D models are too complicated and that 1D models are preferable, provided that they have been validated with more rigorous approaches.

A similar 2D model, but including the membrane wetting, has been proposed by Iliuta et al. [12]. They concluded that non-isothermal simulations reveal that the hollow-fiber membrane module operation can be considered as quasi-isothermal. However, the operating and simulation conditions were far from industrial concern (i.e. very high liquid-to-gas flow ratio and MEA conversions lower than 0.2.).

The solvent evaporation in CO_2 absorption using HFMC has been addressed by Ghasem et al. [13]. In their model, free convection of water inside the membrane pores was considered to evaluate the mass flux across the membrane. Since they used aqueous NaOH solution as solvent, the solvent evaporation is mainly due to the use of dry inlet gas. This situation does not correspond to that in CO_2 postcombustion capture by amine solvents.

Finally, Rongwong et al. [11] developed a one-dimensional model including membrane wetting. The model was validated using experimental data from literature. Again, the operating and simulation conditions were far from industrial concern, the corresponding temperature variations were almost linear and lower than 2 K.

In summary, the influence of water transfer and of CO_2 reactive absorption heat, on temperature has been scarcely studied in HFMC. The intensification potential of the technology needs to be estimated within industrial relevant operating conditions. The aim of the present paper is to fill this knowledge gap. A one-dimensional, adiabatic, multi-component model for reactive CO_2 absorption using HFMC is developed. The simulation results are compared with available pilote-scale experimental data as well as with isothermal modelling.

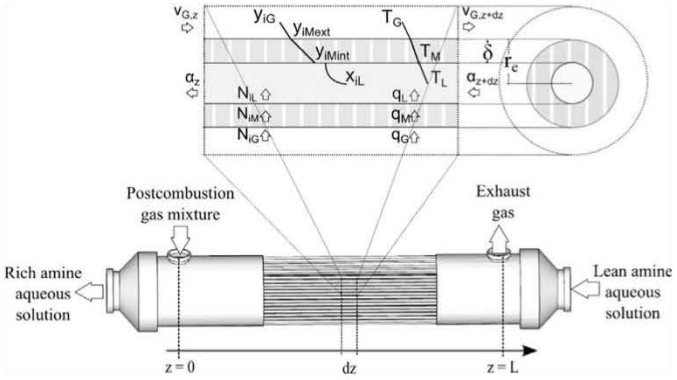

Fig. 1. Schematic representation of the hollow membrane contactor for CO_2 capture in MEA 30 wt aqueous solution.

2. Overall system characteristic

The mass and heat transfer in a membrane module with a hydrophobic microporous membrane is described as a three step process, as illustrated in Fig. 1. Mass transfer is considered for four species (i = CO_2, H_2O, N_2 or MEA). The illustrated reactive species (i = CO_2) is transferred from the gas phase to the external face of the membrane, it then diffuses through the membrane pores, and is finally absorbed by the liquid solution where it reacts.

The membrane contactor consists of a bundle of hydrophobic cylindrical hollow fibers. The contactor has an effective length L, an external radius r_e, varied from 100–500 mm, a fiber volume fraction φ of 0.6 and a relative thickness δ/r_e, set to 0.2. Since content of particles (e.g. ashes) in the postcombustion gases is significant, the amine solvent flows in the lumen to prevent fiber closure. The gas mixture (saturated air and carbon dioxide) flows in the shell surrounding the hollow fibers in a counter-current flow arrangement.

2.1. Operational domain and constraints

The operational parameters and constraints that were applied to all simulations are reported in Table 1. They were chosen in order to represent industrially relevant operating conditions for carbon dioxide capture. A mixture of 0.15 volumetric CO_2, on a dry

Table 1
Operating conditions and geometrical characteristics of the HFMC used in the simulations.

Parameter	Value	Units
Gas		
CO_2 molar fraction	$y_{CO_2}^{in} = 0.14$	–
H_2O molar fraction	$y_{H_2O}^{in} = 0.07$	–
Inlet temperature	$T_G^{in} = 313$	K
Inlet pressure	$P_G^{in} = 1.05 - 105$	Pa
Pressure drop	$\Delta P_G = 5 - 103$	Pa
CO_2 capture ratio	$\Theta = 0.9$	–
Liquid		
MEA total mass fraction	$w = 0.3$	$kg_{MEA}\,kg_L^{-1}$
CO_2 loading of lean solvent	$\alpha^{in} = 0.242$	$mol_{CO_2}\,mol_{MEA}^{-1}$
CO_2 loading of rich solvent	$\alpha^{out} = 0.484$	$mol_{CO_2}\,mol_{MEA}^{-1}$
Resulting MEA conversion	$\xi = 0.932$	–
Outlet pressure	$P_L^{out} = 1.05 - 105$	Pa
Inlet temperature	$T_L^{in} = 313$	K
Contactor		
External fiber radius	$r_e = 1 - 5 \times 10^{-4}$	m
Relative fiber thickness	$\delta/r_e = 0.2$	–
Packing fraction	$\varphi = 0.6$	–
CO_2 mass transfer coefficient in membrane	$k_{M,CO_2}^{ref} = 10^{-4} - 10^{-2}$	$m\,s^{-1}$

basis, and oxygen-depleted saturated air was considered, which is typical of a model coal power plant post-combustion flue gas. The inlet pressure of the gas-phase was set to 50 mbar above atmospheric pressure.

The liquid phase was a 30%(w/w) aqueous MEA solution that was fed at 313K. The CO_2 capture ratio was set to 0.9 to reflect the classic guidelines of carbon dioxide capture [14]. As recommended in literature [1], in order to minimize the overall energy requirement of the capture process, the inlet solvent loading (α^{in}, lean amine) was set to 0.242, whereas the outlet solvent loading was set to a value of 0.484. The inlet and outlet solvent loadings are related to the MEA conversion, ξ, as follows:

$$\xi = \frac{\left(1 - 2\alpha^{in}\right) - \left(1 - 2\alpha^{out}\right)}{\left(1 - 2\alpha^{in}\right)} \quad (1)$$

It is noteworthy mentioning that the almost complete conversion of not only the gas-side, but also the liquid-side reactant, i.e. MEA, is an important feature of industrial relevant operating conditions. Even though, it is rarely applied in laboratory-scale investigations [4]. The liquid pressure is always higher than the gas pressure in order to prevent bubbling. Then, the value of the liquid pressure is set to that of the inlet gas pressure.

Three commercially available microporous membranes are commonly used for CO_2 capture in HFMC: polypropylene (PP), polyvinylidene fluoride (PVDF) and polytetrafluoroethylene (PTFE). The membrane performance is characterized by the CO_2 mass-transfer coefficient of the membrane (k_M), which is within 10^{-4} and 10^{-2} m s^{-1} for microporous membranes [2]. The PP and PVDF membranes are promising for the CO_2 absorption, due to their high mass transfer coefficients (between 10^{-3} and 10^{-2} m s^{-1}). However, these membranes become easily wetted after short time of operation [15–18]. By difference, the PTFE membranes show good resistance to wetting with acceptable k_M values (between 10^{-4} and 10^{-3} m s^{-1} [17–19]). One of the aims of this work is to study the effect of the membrane resistance on the performance of the HFMC. Thus the mass transfer coefficient of the membrane is varied in the range of the previously mentioned values, representing industrial conditions.

3. Modelling approach

Rate-based models explicitly consider heat and mass transfer rates. The driving force for the mass-transfer is the gradient of chemical potential, whereas for heat-transfer it is the temperature gradient. As the liquid flows in the lumen, the gas–liquid interface is formed at the inner surface of the fiber [20], where thermodynamic equilibrium occurs. The boundary-layer theory was used to describe the gas and liquid-side mass and heat-transfer. Accordingly, mixing-cup concentrations and mixing-cup temperatures were considered (see also Section 3.6). The mixing-cup concentrations in the liquid phase were at chemical equilibrium whereas in the boundary-layer, the reactions were kinetically controlled. In order to describe the diffusion in the boundary-layers, the effective diffusivity method for all compounds (molecules and ions) was used [21–23].

The model assumptions made in this work are summarized in Table 2. The assumptions are discussed in the following sections.

3.1. Physicochemical properties

The physicochemical properties were estimated using available literature correlations. The considered value ranges are given in Table 3. The following points should be emphasized:

Table 2
Model assumptions.

Model assumptions and features
Flow
1. Steady state in gas and liquid phase
2. 1D modeling (CO_2 does not reach the center of the liquid flow [4])
3. Laminar flow
4. Plug flow, no axial dispersion [8]
5. Constant liquid velocity
Transfer phenomena
6. Effective membrane mass transfer coefficient values reported in literature.
7. Condensation or evaporation of water occurs only at the liquid–membrane interface.
8. Chilton–Colburn analogy for mass and heat-transfer
9. Adiabatic (no heat losses)
Thermodynamics
10. Ideal gas
11. Semi-empirical liquid speciation
Reaction
12. Kinetically controlled reversible reaction in the liquid boundary
13. Liquid mixing-cup concentrations at chemical equilibrium

i. All properties, except the latent heat of water, are temperature, pressure and concentration-dependent.
ii. The correlations take into account the excess specific heat of the liquid as well as the excess heat of absorption of CO_2.
iii. The diffusion coefficients of the molecular species in the liquid phase are corrected by the modified Stokes–Einstein relation.
iv. Concerning the diffusion of ionic species, a detailed discussion can be found in Hoff et al. [9]. In order to satisfy electroneutrality of the solution, the ionic products were considered as complexes MEA^+ $MEACOO^-$ characterized by a single apparent diffusion coefficient. The authors provided a correlation in order to estimate this diffusion coefficient, however not covering the temperature-range explored in the present paper. In any case, the introduction of the correlation in the present model did not lead to significant changes in simulation results. Thus, the diffusion coefficients of the products were estimated using classical formulations [21–23].

3.2. Chemical speciation

The chemical speciation of the aqueous MEA-CO_2 solution is characterized by the following reactions:

Water ionization:

$$2H_2O \underset{K_1}{\Leftrightarrow} HO^- + H_3O^+ \quad (2)$$

Dissolved CO_2 dissociation:

$$CO_2 + 2H_2O \underset{K_2}{\Leftrightarrow} HCO_3^- + H_3O^+ \quad (3)$$

Bicarbonate dissociation:

$$HCO_3^- + H_2O \underset{K_3}{\Leftrightarrow} CO_3^{-2} + H_3O^+ \quad (4)$$

Carbamate reversion to bicarbonate:

$$RNHCOO^- + H_2O \underset{K_4}{\Leftrightarrow} RNH_2 + HCO_3^- \quad (5)$$

Dissociation of protonated MEA:

$$RNH_3^+ + H_2O \underset{K_5}{\Leftrightarrow} RNH_2 + H_3O^+ \quad (6)$$

The correlations of the equilibrium constants used in this work are given in Appendix A.1. It is worth mentioning that the non-

Table 3
Physicochemical properties of both, the gas and liquid phases.

Property	Symbol [units]	Gas		Liquid	
		Value ranges	Reference	Value ranges	Reference
Specific heat	C_p [J mol^{-1} K^{-1}]	(29–33)	[22]	(3.2–3.8) x 10^3	[23]
Density	ρ [kg m^{-3}]	(0.8–1.2)	Ideal gas	(1.0–1.1) x 10^3	[24]
Viscosity	m[Pa s^{-1}]	(1.6–1.9) x 10^{-5}	[22]	(1.0–2.6) x 10^{-3}	[24]
Diffusion coefficients	D_i [m^2 s^{-1}]	(1.8–3.5) x 10^{-5}	[22]	CO_2: (0.9–4) x 10^{-9}	[25]
				MEA: (0.8–3) x 10^{-9}	[26]
Thermal conductivity	λ [W m^{-1} K^{-1}]	(2.4–2.8) x 10^{-2}	[22]	(0.39–0.41)	[27]
Heat of absorption of CO_2	ΔH_{abs} [J mol^{-1}]	(8–10) x 10^4			[28]
Water latent heat	ΔH_{vap} [J mol^{-1}]	(4.1–4.3) x 10^4			[23]
Surface tension	γ [N m^{-1}]			(5–7) x 10^{-2}	[29]

ideality of the system was lumped into the expressions of K_4 and K_5. Furthermore, as usually suggested in literature, the OH^-, H_3O^+ and CO_3^{-2} concentrations were neglected, since the solvent loading (α) was always lower than 0.5.

The chemical speciation of the system was estimated using the equilibrium model of Astarita et al. [24]. Model equations are given in Appendix A.2. The total concentrations of the components mentioned below, labeled as pseudo-species, were estimated as follows:

$$[MEA]_{ps} = [RNH_2] + [RNHCOO^-] + RNH_3^+ \quad (7)$$

$$[CO_2]_{ps} = [RNHCOO^-] + [CO_2] + [HCO_3^-] \quad (8)$$

$$[N_2]_{ps} = x_{N2,ps} C_{tot} \quad (9)$$

$$[H_2O]_{ps} = x_{H2O,ps} C_{tot} \quad (10)$$

where C_{tot} and $x_{i,ps}$ are respectively the total molar concentration of the liquid phase and the molar fraction of pseudo-species i. These variables are defined by the following equations:

$$C_{tot} = \frac{\rho_L}{M_L} \quad (11)$$

$$x_{i,ps} = \frac{w_{i,ps}/M_i}{\sum_{i=1}^{Nc} w_{i,ps}/M_i} \quad (12)$$

where M_L is the molar mass of the liquid phase calculated as the sum of the products of the molar fraction of pseudo-components and their molecular mass M_i. w_i is the mass fraction of pseudo-component i. Finally the real water concentration is defined as

$$[H_2O] = C_{tot} - [MEA]_{ps} - [CO_2]_{ps} + [RNHCOO^-] \quad (13)$$

3.3. Vapor–liquid and gas–liquid equilibria (VLE and GLE)

In this section, nitrogen and carbon dioxide are referred to as gaseous compounds in the gas phase and as solutes in the liquid phase, whereas water and MEA are referred to as vapor compounds in the gas phase, and solvent and solute in the liquid phase respectively. The phase equilibria are described through equality of liquid and vapor chemical potentials for each compound, which can be expressed as follows:

$$y_i = {}_i^{GLE}x_i \quad (14)$$

and

$$y_i = {}_i^{VLE}x_i \quad (15)$$

where ${}_i^{GLE}$ is the gas–liquid equilibrium constant and ${}_i^{VLE}$ is the vapor–liquid equilibrium constant for the species i. The ideal gas model was suitable for representing the gas phase as the temperature and pressure were moderate.

In order to represent the gas–liquid equilibrium (GLE), Henry's law was applied. Concerning the CO_2, Herny's law of CO_2 in water was used [25] as the non-idealities were taken into account for the chemical speciation. Concerning the N_2, Henry's law was suitable as the interactions between the N_2 and the amine are week and the solubility of N_2 in water is relatively low. In order to represent the vapor–liquid equilibrium (VLE), Raoult's law was considered, since the activity coefficients (within the range of operating conditions) of these compounds are very close to unity [26]. Following these considerations, the GLE constant was expressed as

$${}_i^{GLE} = \frac{{}_iC_i^{tot}}{P_g} \quad (16)$$

whereas the VLE constant was estimated using:

$${}_i^{VLE} = \frac{P_i^{sat}}{P_g} \quad (17)$$

Finally the ionic components were considered as non-volatile. The accuracy of this approach is demonstrated in Fig. 2. Both, the experimentally determined and the calculated partial CO_2 pressure are plotted over the CO_2 loading for different temperatures. Experimental data and model estimations are in good agreement over the considered temperature range.

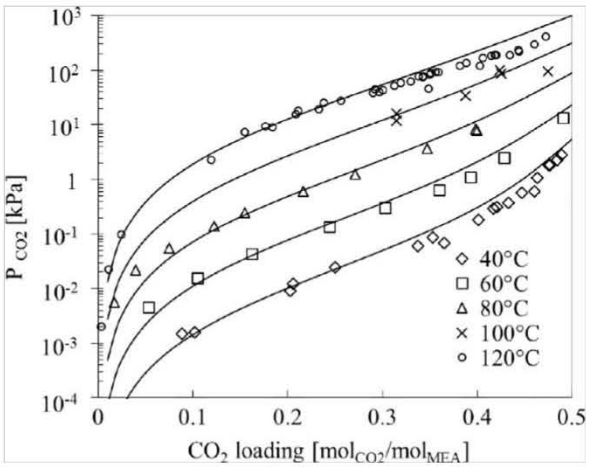

Fig.2. CO_2 partial pressure for an aqueous MEA 30 wt% solution at different temperatures; solid lines: model predictions. Points are experimental values taken from [32,33].

3.4. Reaction kinetics

Two approaches are frequently used in order to represent the reaction mechanism between CO_2 and primary and secondary amines: the zwitterion formation introduced by [27] and the termolecular reaction mechanism introduced by [28]. The modified termolecular mechanism as suggested by [29] leads to a good representation of the reaction kinetics at high CO_2 loadings and concentrated aqueous MEA solutions. This mechanism considers a single-step reaction between CO_2 and MEA where the initial product is a loosely bound encounter complex. The complex breaks up to give reagent molecules again or to react with a second molecule of amine, or a water molecule, to give ionic products. Based on this reaction mechanism, the general reactions are the following:

$$2RNH_2 + CO_2 \overset{K_6}{\Leftrightarrow} RNHCOO^- + RNH_3^+ \tag{18}$$

$$RNH_2 + H_2O + CO_2 \overset{K_7}{\Leftrightarrow} RNHCOO^- + H_3O^+ \tag{19}$$

These reactions are the results of combination of Eqs. (3), (5) and (6) and Eqs. (3) and (5) respectively. The apparent reaction kinetics is presented as follows [29]:

$$r_{CO_2} = -\left(k_{RNH_2}[RNH_2] + k_{H_2O}[H_2O]\right)[RNH_2][CO_2] + \frac{1}{K_{RNH_2}}[RNHCOO^-]\,H_3O^+ \tag{20}$$

Since the H_3O^+ concentration was neglected, the second term of the right-hand side of Equation 20 vanished, leading to non-reversibility of the overall absorption reaction.

3.5. Mass and heat transfer and balance equations

3.5.1. Mass and heat transfer

The mass-conservation law establishes the continuity of molar fluxes between the three considered domains (see Fig. 1). It was formulated as follows:

$$N_{i,G}r_e = N_{i,M}r_M = N_{i,L}r_i \tag{21}$$

where N_i is the molar flux (mol m^{-2} s^{-1}) of compound i (i.e. CO_2, MEA, H_2O and N_2), which was defined for each phase as follows:

$$N_{i,G} = k_{i,G}\frac{P_G}{RT_G}\left(y_{i,G} - y_{i,Mext}\right) + N_{tot,G}y_{i,G} \tag{22}$$

$$N_{i,M} = k_{i,M}\frac{P_G}{RT_G}\left(y_{i,Mext} - y_{i,Mint}\right) + N_{tot,M}y_{i,M} \tag{23}$$

$$N_{i,L} = E_i k_{i,L}C_{tot,L}\left(x_{i,Mint} - x_{i,L}\right) + N_{tot,L}x_{i,L} \tag{24}$$

where $k_{i,G}$, $k_{i,M}$ and $k_{i,L}$ are the mass-transfer coefficients respectively in the gas, membrane and liquid domain. E_i denotes for the enhancement factor of the species i. The latter is related to the chemical reaction in the diffusion boundary layer and its calculation was performed using classical relationships as detailed in Appendix A.3. $N_{tot,j}$ denotes for the total molar flux transferred from phase j (j = G,M or L).

Eqs. (14)–(17) together with Eqs. (21)–(24) form a non-linear equation system (NLES) whose dependent variables are the molar fractions of the different species at the external and internal membrane-surface. The independent variables are the mixing-cup molar fractions of both, the gas and the liquid phase. Due to the fact that the values of the dependent variables are necessary for the calculation of the limiting enhancement factor, the procedure to solve the non-linear equations system is iterative.

The interface heat flux was computed as follows:

$$q = U\left(T_G - T_L\right) \tag{25}$$

where U is an overall heat-transfer coefficient obtained combining the heat-transfer coefficients of the three phases and defined with respect to the external fiber area. The corresponding expression is

$$\frac{1}{U} = \frac{1}{h_G} + \frac{r_e}{\delta}\frac{\ln\frac{1}{1-\frac{\delta}{r_e}}}{h_M} + \frac{1}{1-\frac{\delta}{r_e}}\frac{1}{h_L} \tag{26}$$

where h_G, h_M and h_L are the local heat transfer coefficients in the gas, the membrane and the liquid respectively.

3.5.2. Balance equations

The balance equations were formulated assuming adiabatic behavior, steady state, and plug flow for both, the gas and the liquid phase. These assumptions are currently made in literature for 1D modelling [4]. Since the ionic compounds were considered as non-volatile, the balance equations were formulated only for the pseudo-species. Moreover counter-current flow was considered.

The gas-phase balance equations, describing the variation of the molar fraction of the species, the velocity, the pressure and the temperature are as follows:

$$\frac{dy_{i,G}}{dz} = -\frac{4}{d_{h-ext}}\frac{k_{i,G}}{v_G}\left(y_{i,G} - y_{i,Mext}\right) \tag{27}$$

$$\frac{dv_G}{dz} = -\frac{RT_G}{P_G}v_G\frac{T_G\frac{dP_G}{dz} - P_G\frac{dT_G}{dz}}{RT_G^2} + \frac{4}{d_{h-ext}}N_{tot,G} \tag{28}$$

$$\frac{dP_G}{dz} = -\mu_G v_G K_{koz} \tag{29}$$

$$\frac{dT_G}{dz} = -\frac{4}{d_{h-ext}}\frac{RT_G}{P_G}\frac{U}{v_G Cp_G}\left(T_G - T_L\right) \tag{30}$$

where K_{koz} is the Kozeny constant for the phase flowing in the shell side, discussed in more detail in Section 3.6.1. $d_{h\text{-}ext}$ and v_G stand for the external hydraulic diameter and the interstitial gas velocity, respectively.

In the considered geometrical and operating parameter range (Table 1), the total axial liquid flux is much higher than the total flux transferred between phases. In addition, the total molar liquid-concentration increases as the solvent loading increases. Considering both, it can be assumed that the liquid velocity and the molar fractions of water and total MEA are invariable over the contactor length. Moreover, for a given section, the mixing-cup concentrations in the liquid phase correspond to chemical equilibrium [30]. Therefore, the compositions in the liquid phase can be described using solely the CO_2 solvent-loading. The liquid-phase balance equations describing respectively the variation of the CO_2 solvent-loading, the temperature and the pressure are as follows:

$$\frac{d\alpha}{dz} = -\frac{4}{d_{h-int}}\frac{E_{CO_2}k_{CO_2,L}}{C_{MEA,L}{}^0 v_L}\left(x_{CO_2,Mint} - x_{CO_2,L}\right) \tag{31}$$

$$\frac{dT_L}{dz} = -\frac{4}{d_{h-int}\left(1-\frac{\delta}{r_e}\right)}\frac{U\left(T_G - T_L\right) + \sum_{i=1}^{Np}N_{i,L}\Delta H_{i,abs/vap}}{v_L Cp_L C_{tot,L}} \tag{32}$$

$$\frac{dP_L}{dz} = -\frac{8}{r_e^2\left(1-\frac{\delta}{r_e}\right)^2}v_L \quad (33)$$

The balance equations (Eqs. (27)–(33)) form a system of ordinary differential equations subject to boundary conditions (boundary value problem or BVP).

3.5.3. Differential enthalpy balance

In order to analyze temperature variations of both, the gas and the liquid phase over the fiber length, a differential enthalpy balance was written:

$$\left(H_G^z - H_G^{z+dz}\right) - \left(H_L^{z+dz} - H_L^z\right) = 0 \quad (34)$$

where H_j is the local enthalpy flux (Js^{-1}) of the considered phase (j ¼ L or G) . The differential enthalpy balance can be formulated, in order to express explicitly the local variation of the sensible heat of the phases ($Q_{sens,j}$) and the sum of the variation of the absorption heat and the latent heat ($Q_{abs/vap}$):

$$Q_{sens,G} + Q_{sens,L} + Q_{abs/vap} = 0 \quad (35)$$

where

$$Q_{sens,G} = v_G \varepsilon_{ext} \frac{P_G}{RT_G} \int_{T_G^z}^{T_G^{z+dz}} Cp_G^z dTG \quad (36)$$

$$Q_{sens,L} = v_L \varepsilon_{int} C_{tot} \int_{T_L^{z+dz}}^{T_L^z} Cp_L^z dT_L \quad (37)$$

$$Q_{abs/vap} = -dz \sum_{i=1}^{Np} a_{ext} N_{i,G} \Delta H_{abs/vap} \quad (38)$$

where ε_{ext} and ε_{int} are the external (shell) and internal (lumen) specific flow section, respectively. The specific external fiber area is denoted by a_{ext}.

3.6. Hydrodynamics and mass-and-heat transfer coefficients

3.6.1. Hydrodynamics

Liquid and gas flow were considered to be laminar with fully developed velocity profiles. In the operating domain considered in this work, these assumptions were shown to be valid in [6] and confirmed with Reynolds number lower than 100 for both phases. Due to the fact that the CO_2 capture ratio, the MEA conversion as well as the contactor geometry were fixed (see Table 1), the ratio between the interstitial liquid and gas velocities (v_L/v_G) was constrained.

In laminar flow, the pressure drop of the fluid passing through the shell can be described by Darcy's law with a Kozeny constant as given hereunder for packing fractions lower than 0.6 [31].

$$K_{koz} = \frac{8\varphi}{2\ln\left(\frac{1}{\varphi}\right) - 3 + 4\varphi - \varphi^2 r_e^2} \quad (39)$$

For the fluid passing through the lumen, the Hagen–Poiseuille equation for pipe flow is used.

3.6.2. Mass transfer coefficients

In laminar channel flow through HFMC, the concentration polarization is predominant [20]. Two mass transfer zones are observed when the residence time is sufficiently high: the entry zone, characterized by a developing concentration boundary layer and high mass transfer coefficients, and the developed boundary layer zone, characterized by low mass transfer coefficients. The boundary layer on both, the liquid and the gas side, were computed by integrating the Graetz equation for the suitable hydraulic diameter [32]. For given ranges of the Graetz number, the Sherwood number is estimated by

$$Gz_F < 0.03; \quad Sh_F = 1.3Gz_F^{-1/3} \quad (40)$$

$$Gz_F > 0.03; \quad Sh_F = 4.36 \quad (41)$$

where Gz_F and Sh_F are the Graetz number and is the Sherwood number respectively. They are defined as

$$Gz_F = \frac{D_{j,F} z}{v_F d_h^2} \quad (42)$$

$$Sh_F = \frac{k_F d_h}{D_{j,F}} \quad (43)$$

It is worth noting that the computed Sherwood values and mass transfer coefficients are related to the mixing cup concentration at the axial coordinate z. The value of the limiting Sherwood number (i.e. 4.36), corresponds to a boundary condition of uniform mass flux.

Several investigations have been made in order to describe the mass transfer in the shell as a function of the packing fraction. The values of the Sherwood numbers have been estimated to be of about 10–60 in the entry zone and 3–5 in the developed boundary layer zone, for random packing fractions varying from 0.2 to 0.7 [33–35]. Given that the gas flows in the shell and that the contribution to the global mass transfer resistance of the gas phase is not preponderant, the effects of poor flow distribution as a result of random packing are neglected in this work.

The random packed fiber bundles as well as the non-uniform distribution of the external fiber radii lead to non-uniform velocity distribution in the shell, whereas the non-uniform distribution of fiber thickness leads to non-uniform velocity distribution in the lumen [36]. The influence of the flow maldistribution on the mass transfer coefficient in the lumen has been studied by Wickramasinghe et al. [36]. However, in practice when the liquid flows in the lumen, the impact can be expected to be insignificant [37].

The mass transfer coefficient for a microporous membrane, k_M, depends on the fiber thickness and on the membrane porosity, ε, and tortuosity, τ, as well as on the pore-size distribution. The wide range of both, pore-sizes and pore-shapes, leads to a hardly-reliable measurement of the tortuosity and of the pore sizes. Therefore different mass transfer coefficients have been reported for the same material, not to mention wetting issues [17].

When membrane wetting occurs, the evaluation of this mass transfer coefficient becomes more complex. Membrane wetting due to liquid breakthrough has been widely studied [18]. In general, the calculation of the wetted k_M resides in the estimation of a corresponding wetted portion of the membrane [38,39]. This supposes that wetting occurs in a specific location of the membrane and requires a well-defined characterization of the membrane, which itself is complicated, as discussed before. Nevertheless, an estimation of the membrane susceptibility toward liquid breakthrough can be easily provided using the well-known Laplace (Cantor) equation [40]:

$$\Delta P_{break} = -\frac{4\beta\gamma\cos(\theta)}{d_p^{max}} \quad (44)$$

where γ stands for the solvent surface tension, θ is the solvent–membrane contact angle, d_p^{max} is the largest pore size, as that is the most vulnerable to wetting. The coefficient β is the geometric factor for non-cylindrical pores. Based on the results obtained using PTFE membranes, the dependence of the geometric factor on temperature has been described by the following equation [40]:

$$\beta = 0.97 - 7 \times 10^{-3} T\ (°C) \quad \text{for} \quad 25\ °C < T < 70\ °C$$
$$\beta = 0.5 \quad \text{for} \quad T > 70\ °C \quad \text{and} \quad \beta = 0.8 \quad \text{for} \quad T < 50\ °C \qquad (45)$$

Another, albeit less studied, cause for membrane wetting is capillary condensation. As condensable vapors pass through the membrane pores, it is likely for these vapors to condense within the membrane structure. For the CO_2 reactive absorption, the vapor is essentially composed of water. For the typical range of pore size in microporous membranes (0.1–0.8 mm), the Kelvin equation gives a good approximation for the oversaturation at which capillary condensation occurs in hydrophobic materials, S_{cond} [41]:

$$S_{cond} = \exp\left(-\frac{4\gamma_w \cos(\theta) V_w}{d_p R T_M}\right) \qquad (46)$$

where γ_w stands for the water surface tension, d_p is the average pore size and V_w is the water molar volume.

More generally, the saturation of the gas phase in water within the membrane, designed in the following by S_M, is defined as the molar fraction of water in the membrane divided by the dew point water molar fraction calculated at the membrane temperature (T_M).

From a chemical engineering point of view, it is common to have a lumped variable in the modelling of unit operations. For example, in packed columns, the influence of all the hydrodynamic and interfacial aspects (e.g. flow regime and gas–liquid-packing contact, respectively) on the mass transfer are lumped into the expressions of the interfacial area [42]. In this work, the wetting phenomena caused by liquid breakthrough and/or capillary condensation are lumped in the value of the k_M^{ref}. The value of the latest was fixed to typical values (see Table 1), and is not related to the fiber thickness and the material. In addition, it is considered that these phenomena affect all the components in the same way. For this reason, the mass transfer coefficient of the specie i was determined by Eq. (47).

$$k_{M,i} = \frac{k_{M,CO_2}^{ref}}{D_{CO_2,G}^{ref}} D_{i,G} \qquad (47)$$

where the reference conditions were set to 40 °C and 100 kPa.

3.6.3. Heat transfer coefficients

In cross-flow HFMC with laminar flow (Happel's hydrodynamics), the estimated and measured values of the Nusselt number were very similar to those of the Sherwood number [43,44]. Such results indicate that the application of the Chilton–Colburn analogy is appropriate [45]. This analogy was successfully used in similar transfer systems (e.g. air humidification) [46]. For these reasons, it was applied here to estimate the heat transfer coefficients of both, the liquid and the gas phases. The heat transfer coefficient of the membrane was computed using the isostress or series model, as recommended by [47]

$$h_M = \left(\frac{1}{\delta}\left(\frac{(1-\varepsilon)}{\lambda_M} + \frac{\varepsilon}{\lambda_G}\right)\right)^{-1} \qquad (48)$$

For heat transfer calculations, the membrane porosity was set to 0.5 and the membrane thermal conductivity to 0.15 $W\ m^{-1}\ K^{-1}$.

4. Simulations and discussion

The heat and mass transfer equations system (or NLE) exposed in Section 3.5.1 was solved at each point of integration of the differential equation system (or BVP) consisting of the balance equations exposed in Section 3.5.2. The NLE were solved using the trust-region-dogleg algorithm from the routine fsolve of Matlab. Because the relatively high heat of absorption, the BVP was likely to be stiff and in order to solve this problem, the Lobatto IIIA, a collocation method from the routine bvp4c of Matlab, was used [48]. The isothermal model was identical to the adiabatic model except that the energy balances were neglected.

In order to compare isothermal and adiabatic approaches, the operating parameters had to be fixed to identical values. Respecting operational constraints and geometrical parameters (shown in Table 1), the length of fiber (L) and the inlet gas velocity (v_G^0) were calculated from the integration of each model with a capture ratio and a gas pressure drop imposed, as discussed in [6]. The simulation results are compared in the following sections.

4.1. Temperature and gas-phase composition profiles

Fig. 3 illustrates the variation of the liquid and gas temperatures with the dimensionless contactor length. With the exception of the fiber section of the inlet gas, the gas and liquid temperatures are very close in value. This is related to the rapid heat transfer in the gas, the liquid and the membrane. The peak of temperature obtained shows that isothermal behavior may not be what would be expected under industrial operating conditions. It is worth mentioning that such temperature peaks have been observed and modeled in the Esbjerg pilot plant, during the both CASTOR and CESAR campaigns ([49,1])

In order to understand these temperature profiles, the local heat contributions of the differential enthalpy balance (Eq. (35)) are plotted in Fig. 4. As the terms of the sensible heat were related to the flow-direction, the negative or positive values indicate that the phases are cooled or warmed up, respectively, relative to their inlets. The terms of latent and absorption heats can be understood as heat sinks. Therefore, the negative and positive values indicate respectively release and absorption of energy by the fluids.

In Fig. 4, the heat contributions were divided by the contactor volume. The figure allows the lector to know where the energy is transferred to. In the vicinity of the gas inlet (z= 0), the sensible heat of the liquid and the heat of absorption of the CO_2 are principally converted to latent heat of evaporation and to sensible heat of the gas. In other words, the gas phase is warmed up, the liquid is cooled and the CO_2 releases its heat of absorption, leading to water evaporation. This behavior is observed in the contactor from the gas inlet until the point where the temperatures reach their maximal values. At this location, the heat of absorption of CO_2 is converted in latent heat of water evaporation. In the remaining

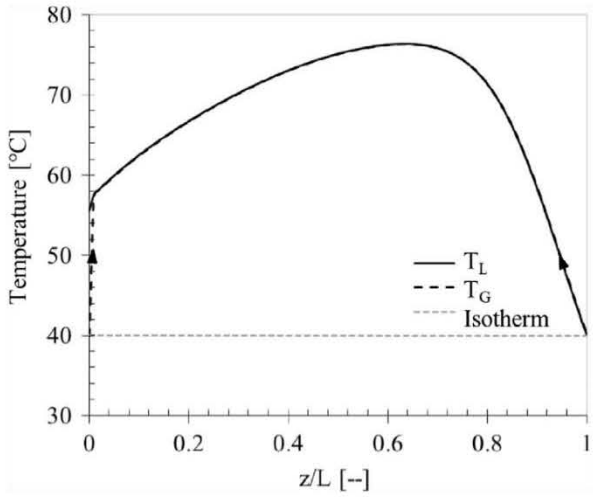

Fig. 3. Gas and liquid local temperatures as functions of the dimensionless contactor length. The gas temperature is superimposed by the liquid temperature. $k_{M,CO_2}^{ref} = 10^{-3}$ m s^{-1}, r_e= 200 mm.

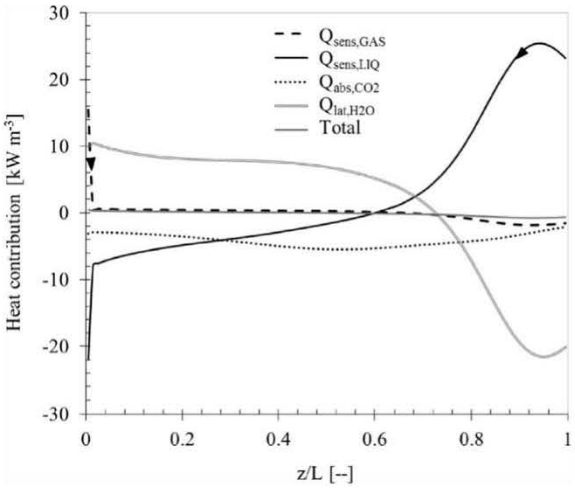

Fig. 4. Local heat contributions in the energy balance as a function of the dimensionless contactor length. k_{M,CO_2}^{ref} = 10^{-3} m s^{-1}, r_e= 200 mm.

part of the fiber, the liquid is quickly warmed up firstly by vapor condensation, and secondly by the sensible heat of the gas phase (the gas is cooled) and by the heat of absorption of CO_2.

Fig. 5 illustrates the local molar fractions of water vapor and CO_2 in the gas phase. According to the temperature profiles, water vapor fractions in the gas phase are locally high. In the model, water vapor condensation was considered to occur solely at the liquid–membrane interface. However, as heat is conducted by the solid material and matter not, heat has an advantage over mass to be transferred through the membrane; in other words, in the membrane the mass transfer is slower than the heat transfer. Given this, it is likely that condensation occurs elsewhere: in the gas bulk (aerosol formation), at the external fiber-surface (gas side) and in the pores of the membranes (capillary condensation).

The aerosol formation, observed in packed columns for the CO_2 absorption in amine solvents [50,51], may lead to solvent losses. The condensation on the external fiber-surface may lead to a formation of a liquid film, increasing the overall mass transfer resistance. The capillary condensation may wet the membrane, thus decreasing dramatically the contactor performance [38]. However, as far as is known, no experiments under relevant conditions in HFMC have been performed to corroborate the occurrence of these phenomena.

The rigorous modelling of this phase formation at any place of the membrane or of the gas phase is arduous and requires additional information such as surface characterization inside the membrane, which is itself very difficult—if not impossible—to determine. Therefore, being able to take into account such phenomena in a simpler way becomes interesting in order to improve the confidence of the model in scale up and/or optimization purposes.

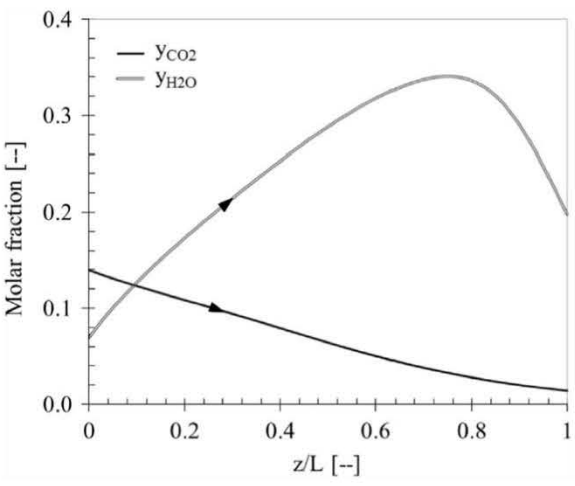

Fig. 5. Water vapor and CO_2 molar fraction in the gas phase as a function of the dimensionless contactor length. k_{M,CO_2}^{ref} = 10^{-3} m s^{-1}, r_e= 200 mm.

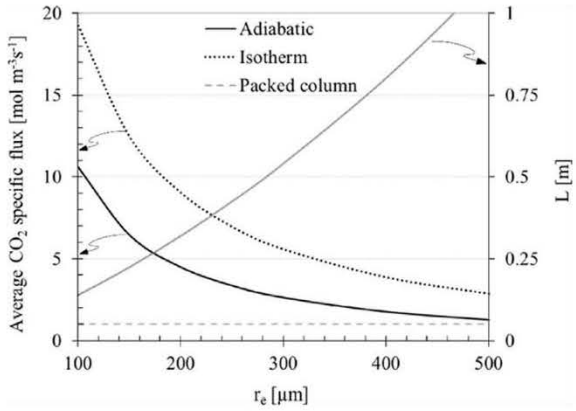

Fig. 6. Variation of the average CO_2 specific absorbed flux with the external fiber radius. k_{M,CO_2}^{ref} = 10^{-3} m s^{-1}.

4.2. Influence of the fiber characteristics on the contactor performance

The average CO_2 specific absorbed flux, defined as the absorbed quantity of CO_2 per unit-volume of contactor, is one of the most relevant parameters for industry. It might be taken as an intensification index, the mean value being around 1 mol m^{-3} s^{-1} for conventional commercial technologies using packed columns [1].

Fig. 6 illustrates the variation of the average CO_2 specific absorbed flux (left axis) with the fiber external radius for both isothermal and adiabatic simulations together with the mean value in packed columns. Moreover, the effective contactor length (L, right axis) obtained by the adiabatic simulations is shown. Again, the difference between the prediction of both, the adiabatic and the isothermal model, is significant, indicating that the variation of the local temperatures has an important (and negative) impact on the contactor performance.

With regard to the results of adiabatic simulations, in order to have a significant intensification factor, fibers should have an external radius less than 200 mm and should be no longer than 0.3 m. With such short contactors and a large flux of flue gas to treat, the number of modules set in parallel will be important; hence, distribution and collection issues, typical of parallel circuits, should be studied rigorously.

Fig. 7 illustrates the variation of the average CO_2 specific absorbed flux as a function of the CO_2 mass transfer coefficient of the membrane (k_{M,CO_2}^{ref}) for three external fiber radiuses. Only adiabatic simulations are shown and k_{M,CO_2}^{ref} was varied in a large range, from 10^{-5} to 10^{-2} m s^{-1}, in order to illustrate trends. In addition, the published range of k_{M,CO_2}^{ref} values is indicated. The simulations indicate that a variation of one order of magnitude in the value of k_{M,CO_2}^{ref}, i.e. from 10^{-3} to 10^{-4} m s^{-1}, removes the intensification potential of the HFMC. In this sense, it must be pointed out that membrane wetting decreases dramatically the membrane mass transfer coefficient [17,19,38].

Membranes which are composed of a microporous support and a dense film, known as composite membranes, might prevent membrane wetting, due to the dense thin film on the liquid-side of the membrane which avoids the liquid breakthrough. However capillary and film condensation may still occur. Long-term experiments on composite membranes were previously performed

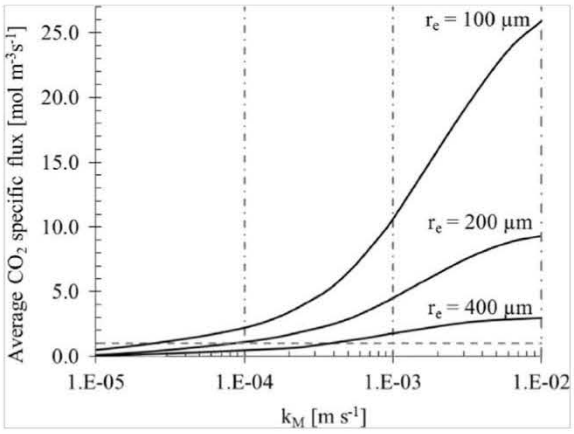

Fig. 7. Influence of the mass transfer coefficient of the membrane, k_{M,CO_2}^{ref}, on the average CO_2 specific absorbed flux for three external fiber radiuses; dash-dotted lines: lower and upper published values of k_{M,CO_2}^{ref}; dashed line: packed columns.

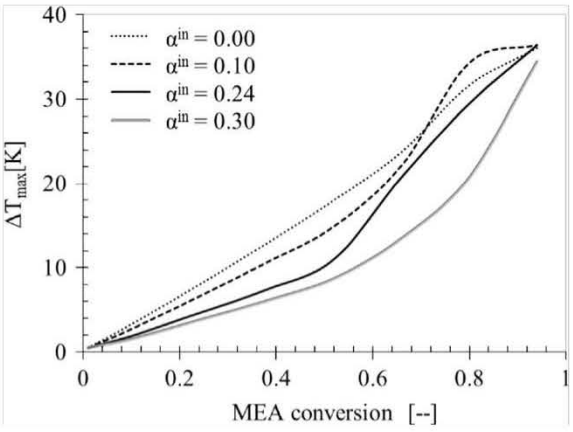

Fig. 9. Maximal temperature difference with respect to the liquid inlet as a function of the amine conversion at different inlet CO_2 solvent loadings. ΔP_G= 50 mbar, k_{M,CO_2}^{ref} = 10^{-3} m s^{-1}, r_e= 200 mm.

[17] and, interestingly, no condensation was observed. Nevertheless, high solvent-excess was applied, leading probably to almost isothermal behavior, thus limiting water transfer. Consequently, experiences in non-isothermal conditions, focusing on water transfer through hollow fibers membrane contactors need to be performed, in order to determine the influence of the phenomena mentioned here-over.

4.3. Influence of the amine conversion and the lean solvent loading

4.3.1. Isothermal versus adiabatic modelling

In literature, even simple, isothermal models lead to good agreement in laboratory conditions, characterized by low amine conversions and low CO_2 solvent loadings [4]. On the other hand, an important difference between the isothermal and the adiabatic approach was found in the present work. In order to understand this discrepancy, simulations varying both, the amine conversion and the lean solvent loading were performed, while maintaining the other operating parameters exposed in Table 1.

Fig. 8 illustrates the ratio between the average CO_2 specific absorbed flux estimated using the adiabatic and the isothermal model, as a function of the MEA conversion (ξ). Different lean solvent loadings (α^{in}) are illustrated. For MEA conversions of less than 0.6, it is shown that both models lead to comparable results, regardless the lean solvent loading. For higher MEA conversions, simulation results depend on the lean solvent loading. The trends can be explained as follows.

The contactor performance is a trade-off between reaction kinetics, liquid-phase diffusion coefficients and CO_2 solubility,

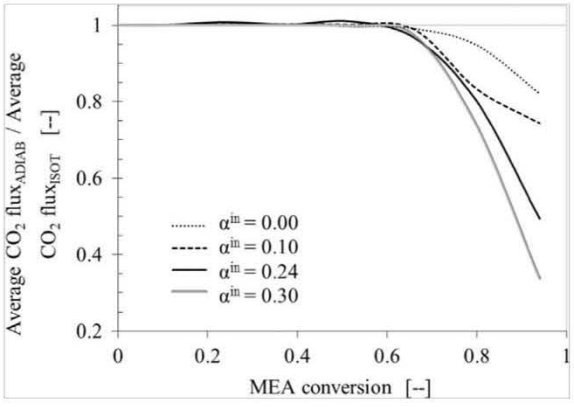

Fig. 8. Ratio between the averaged CO_2 specific absorbed flux using isothermal and adiabatic models over the amine conversion for different inlet CO_2 solvent loadings. ΔP_G= 50 mbar, k_{M,CO_2}^{ref} = 10^{-3} m s^{-1}, r_e= 200 mm.

considering that the major mass transfer resistance is located in the liquid phase. On one hand, reaction kinetics and diffusion coefficients increase with temperature and a CO_2 loading decrease, leading to better contactor performance. On the other hand, the CO_2 solubility decreases when both, the temperature and the CO_2 loading increase, diminishing contactor performance. The overall results depend on the relative importance of the different phenomena.

Fig 9 shows the value of the liquid-phase temperature peak, defined as the maximum temperature difference with respect to liquid inlet. The temperature peak value increases with the MEA conversion, as high conversions impose low liquid flow-rates and thus for a given energy flux more heating. The temperature peak value is slightly smaller for high lean-solvent loadings, because of the higher liquid flow-rates involved.

It turns out that for low amine conversions and low lean solvent loadings, typical for laboratory experiences, the negative impact of the CO_2 solubility is compensated by the positive impact of the reaction kinetics and diffusion coefficients, thus leading to comparable results obtained from both, the isothermal and adiabatic approaches (see Fig. 8). However, under industrial relevant operating conditions (i.e. high MEA conversion and relatively high CO_2 solvent loading) the compensation mentioned previously does not take place, leading to differences higher than 60%between the two approaches.

4.3.2. Membrane wetting

It is interesting to know the operating conditions at which membrane wetting occurs. Fig. 10 shows the maximal ratio between the liquid–gas pressure difference and the membrane breakthrough pressure. Therefore, if this value is higher than 1, membrane wetting due to liquid breakthrough occurs. It is noticed that membrane wetting occurs for amine conversions lower than 0.3 because of the high liquid flow, which increases the liquid pressure drop. On the other hand, for conversions higher than 0.7, this phenomenon occurs due to the temperature peak, which decreases the membrane breakthrough pressure. Nevertheless, if the HFMC is made of composite membranes, there is no risk of the occurrence of this phenomenon.

Fig. 11 illustrates the maximal ratio between the vapor saturation within the membrane, S_M, and the vapor oversaturation at which capillary condensation occurs, S_{cond} as defined by Eq. (46). Therefore, if this value is higher than 1, membrane wetting due to capillary condensation occurs. It is observed that membrane wetting due to capillary condensation occurs for amine conversions higher than 0.6. This is due to the high values of the temperature peak. This phenomenon does not occur for low amine

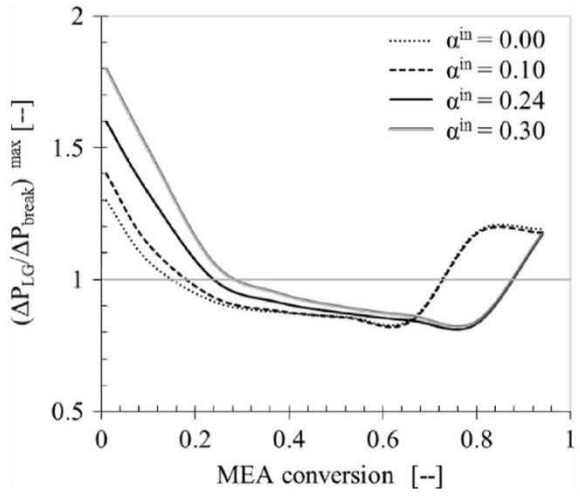

Fig. 10. Maximal ratio between the liquid–gas pressure difference (ΔP_{LG}) and the membrane breakthrough pressure (ΔP_{break}) over the amine conversion for different inlet CO_2 solvent loadings. ΔP_G= 50 mbar, $k_{M,CO2}^{ref} = 10^{-3}$ m s^{-1}, r_e= 200 mm.

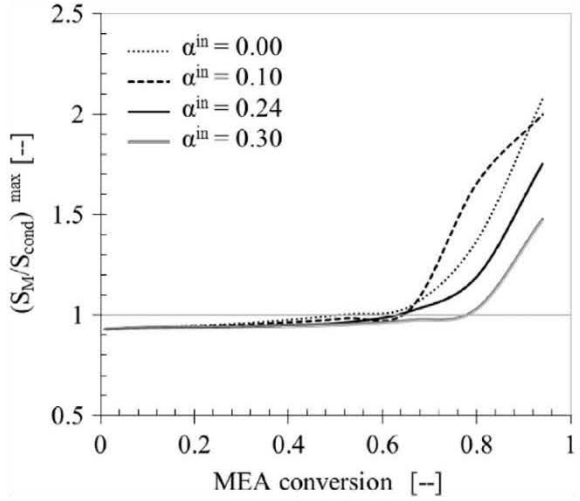

Fig. 11. Maximal ratio between the water vapor saturation at the membrane core (S_M) and the water vapor oversaturation at which capillary condensation occurs (S_{cond}), over the amine conversion for different inlet CO_2 solvent loadings. ΔP_G = 50 mbar, $k_{M,CO2}^{ref} = 10^{-3}$ m s^{-1}, r_e= 200 mm.

conversions as the temperature peak is less important, which means low water transfer. Unlike the membrane wetting due to liquid breakthrough, capillary condensation may occur in composite membranes because of its porous support.

4.4. Comparison between experimental and simulation results

Simulation results were compared to laboratory and pilot-scale experiments in order to validate the developed models. Based on the literature review, regardless of model type, achievement of well-fitted model predictions without the need for parameter adjustment is unrealistic. Accordingly, the k_M value was taken as the single adjustable parameter.

Currently, the mass transfer coefficient of a partially wetted membrane is calculated by taking into account a fraction of the wetting w_M. The value of this wetting fraction can be estimated by establishing (or measuring) a pore size distribution, or by adjusting it in order to fit experimental results such as those presented here. All of this having a sufficient knowledge of the solvent–membrane interaction, operating conditions and module geometry. Therefore, the local estimation of the k_M is tricky, and its accuracy will depend, mainly, on the incertitude of the membrane characterization as well as the solvent–membrane interaction. Nevertheless, from literature, one can identify the range in which the k_M values have been observed. Therefore, the model presented here sets a k_M value, namely $k_{M,CO2}^{ref}$, which itself takes into account the wetting, in between the range of gas filled membrane pores (10^{-2} m s^{-1}) and of wetted membrane (10^{-4} m s^{-1}).

The considered experimental result was the CO_2 capture ratio and the MEA conversion was calculated accordingly. The average deviation between simulations and experiments was quantified using the average absolute relative deviation (AARD).

4.4.1. Laboratory scale investigations

Laboratory-scale experiments previously performed are detailed in [5] and only a brief outline detailed here. A HFMC of about 5 x 10^{-2} m^2 of exchange-surface was used, the liquid flowing through the fibers and the gas flowing in counter-current through the shell. The gas phase was a mixture of 15% of CO_2 and the balance N_2; the liquid-phase, a fresh aqueous solution of MEA 30 wt% The experiments were performed with large excess of liquid reactant and at ambient temperature and atmospheric pressure. In total, 14 experiments with varying gas and liquid flowrates were considered; the k_M value was fitted to $10^{Å3}$ m s^{Å1}.

Fig. 12 shows parity plots of the CO_2 capture ratio and the MEA conversion, including adiabatic and isothermal simulations. The deviation bars in Fig. 12A correspond to a 20% variation of the fitted $k_{M,ref}$ value. It can be seen that there is not just a single value of $k_{M,ref}$ which fits perfectly to all data; however, the simple approach of fitting a single value leads to model agreement within 10%for most of the experiments, which is reasonable, considering that the experimental relative deviation is about 6% Similar values of the AARD for both models were obtained. Indeed, most of the experiments were performed at low MEA conversions and relatively low CO_2 capture ratios, conditions where the isothermal and adiabatic provide comparable results.

4.4.2. Pilot plant scale investigations

In order to test the suitability of the model of a larger scale, 11 experiments from the EnergiCapt project, funded by the Agence Nationale de la Recherche (ANR) grant Energicapt, were simulated. The small pilot plant[n1] consists of a 10 m^2 exchange-surface HFMC in which the aqueous solution of about 30 wt%of MEA is fed in the lumen, whereas the flue gas from a natural gas power plant (mixture of 10%of CO_2 and saturated air) flows through the shell in counter-current. Overall contactor features are presented in Table 4.

The membrane contactor had previously been used intermittently for several months. The k_M value was fitted to 5 x 10^{-4} m s^{-1}, this value is lower than the value fitted for the same membrane type in the laboratory-scale experiments, the difference being most probably to membrane aging.

Membrane aging refers to a structural change of the membrane due to its exposition to temperature and pressure gradients, and chemical attack. This change may induce an increase in the average pore size and shape, and a decrease in the contact-angle. Hence, pore wetting is more likely to occur in an aged membrane contactor leading to lower lumped k_M values.

Fig. 13 shows parity plots of the CO_2 capture ratio and the MEA conversion, including adiabatic and isothermal simulations. The deviation bars in Fig. 13A correspond to a 20 % variation of the fitted $k_{M,ref}$ value. As for the laboratory-scale experiments, there is not just a single value of $k_{M,ref}$ which fits perfectly to all data; however, the simple approach of fitting a single value leads to

[1] HFMC elaborated by Polymem. http://www.polymem.fr.

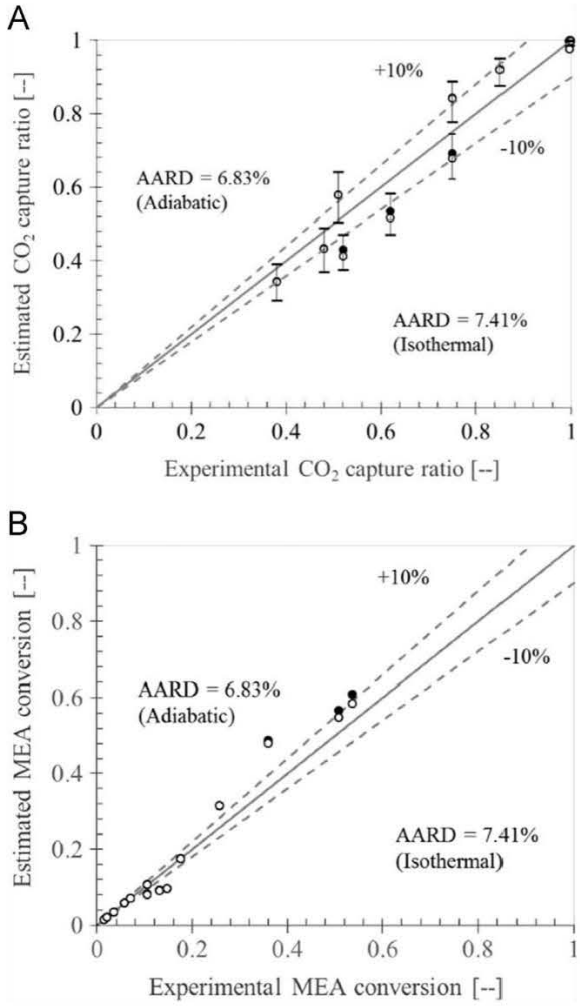

Fig. 12. Comparison of simulation results and experimental data taken from [5]. The filled and open symbols represent simulations using respectively the adiabatic and the isothermal model. (A) CO_2 capture ratio. (B) MEA conversion. $k_{M,CO2}^{ref} = 10^{-3}$ m s^{-1}. Deviation bars correspond to a variation of +/-20% of $k_{M,CO2}^{ref}$ and are included only for adiabatic simulations.

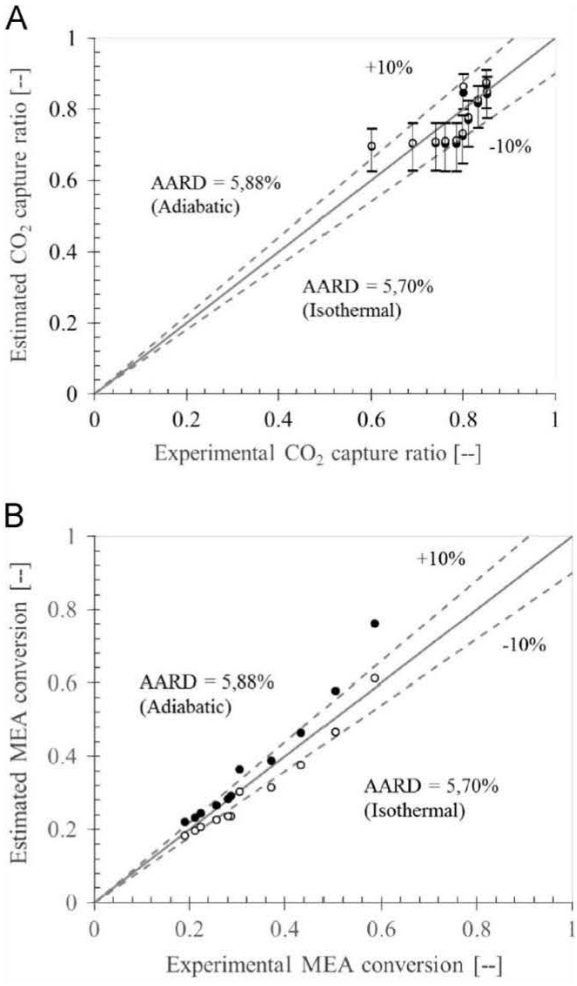

Fig. 13. Comparison of simulation results and experimental data from EnergieCapt project. The filled and open symbols represent simulations using respectively the adiabatic and the isothermal model. (A) CO_2 capture ratio. (B) MEA conversion. $k_{M,CO2}^{ref} = 5 \times 10^{-4}$. m s^{-1}. Deviation bars correspond to a variation of +/- 20% of $k_{M,CO2}^{ref}$ and are included only for adiabatic simulations.

Table 4
Operating conditions and geometrical characteristics of the HFMC used in EnergieCapt project.

Parameter	Value	Units
Gas		
CO_2 molar fraction	0.10	–
H_2O molar fraction	0.10	–
Inlet temperature	323–326	K
Inlet pressure	1×10^5	Pa
Gas flow rate	11–18	N m^3 h^{-1}
Liquid		
MEA total mass fraction	0.3	kg_{MEA} kg_L^{-1}
CO_2 loading of lean solvent	0–0.16	mol_{CO_2} mol_{MEA}^{-1}
Inlet temperature	~ 289	K
Inlet pressure	1.05×10^5	Pa
Liquid flow rate	30-80	[L h^{-1}]
Contactor		
External fiber radius	4.35×10^{-4}	m
Relative fiber thickness	0.5	–
Packing fraction	0.58	–
Effective contactor length	0.88	m
Contactor diameter	0.105	m

model agreement within 10% for most of the pilot-scale experiments, which again seems to be reasonable, considering experimental uncertainties. Similar values of the AARD for both models were obtained for the same reason that in the laboratory-scale experiments.

5. Concluding remarks and outlook

The aim of the present work was to investigate the influence of heat release on the functioning of HFMC as a means of chemical absorption of CO_2 using aqueous MEA solutions. When common laboratory conditions (amine conversion values less than 0.2 and fresh solvent) are applied, isothermal and adiabatic simulations lead to comparable results in terms of contactor performance. However, it turns out that in industrial relevant operating conditions, significant temperature peaks occur in the contactor. This is, after all, not astonishing, as the same phenomena were often reported in packed columns under comparable operating conditions [1]. Moreover, when compared to isothermal modelling, the intensification factor computed in adiabatic modelling can be significantly lower, resulting in deviations of about 60%

The use of fibers with an external radius of less than 400 mm is necessary in order to obtain a significant intensification. In addition, membrane mass-transfer coefficients must not be less than 5×10^{-4} m s^{-1}. It is worth mentioning that, because of the significant temperature peaks and rapid heat transfer in microporous as well as in composite membranes, capillary condensation and thus membrane wetting may occur. These phenomena will,

Table 5
Temperature dependence of the equilibrium constants for reactions (1)–(5).

	C_1	C_2	C_3	C_4
K_1	- 13,445.9	- 22.4773	0	140.932
K_2	- 12,092.1	- 36.7816	0	235.482
K_3	- 12,431.7	35.4819	0	220.067
K_4	- 3084.32	- 39.254	0.1311	189.56
K_5	- 5844.22	- 40.358	0.125	191.51

accordingly, deteriorate the membrane performance. This represents a challenge to this type of contactors and its impact should be taken into account in scale-up process.

Finally, with the membrane mass transfer coefficient as the only one adjustable parameter, model simulations are in general agreement (within 10%) of the results from experiments performed in both, laboratory and pilot plant scales. The comparison of Adiabatic 1D and 2D approaches are out of the scope of this paper, but will be addressed in the future.

Acknowledgments

The authors acknowledge the ANR Energicapt Grant ANR-10-EESI-0003 for the provided experimental data.

Appendix A

A.1. Equilibrium constants

The equilibrium constants K_i are expressed in molar concentration units.

$$\ln K_i = \frac{C_1}{T} + C_2 \ln(T) + C_3 T + C_4 \tag{49}$$

The values of the correlation parameters C_1–C_4 regressed in this work are reported in Table 5.

A.2. Speciation equations

The chemical equilibrium for a chemical reaction is given by Eq. (50):

$$K_m(T) = \Pi_m [A]^{v_{i,m}} \tag{50}$$

where A denotes a real species i in a reaction m, and v its stoichiometric factor. In the formulation of the speciation given by Astarita et al. [24], it is assumed that all chemically combined CO_2 is captured in form of bicarbonate. Thus, the solution of the chemical equilibrium of the CO_2 absorption is straightforward. Writing the mass balance for the pseudo-components, as seen in Section 3.2, in terms of the total MEA mass fraction (w) and the CO_2 loading (α) and combining it with the chemical equilibrium (Eq. (50)), the speciation can be calculated as follows:

$$[RNHCOO^-] = \frac{\left(K_4 + C_{MEA,tot}\right) - \sqrt{\left(K_4 + C_{MEA,tot}\right)^2 - 4\alpha(1-\alpha)C_{MEA,tot}^2}}{2} \tag{51}$$

$$RNH_3^+ = \alpha C_{MEA,tot} \tag{52}$$

$$[HCO_3^-] = \alpha C_{MEA,tot} - [RNHCOO^-] \tag{53}$$

$$[CO_2] = \frac{K_5 K_4}{K_2} \frac{[RNHCOO^-]\ RNH_3^+}{[RNH_2]^2} \tag{54}$$

A.3. Enhancement factor

The mass transfer with chemical reaction is conventionally modeled using the enhancement factor (E). For a second-order reversible reaction, the formulation from [52] can be used for hollow fibers membrane contactors with high loaded chemical solvents, as shown by [53,30].

$$E_i = \frac{-Ha_i^2}{2(E_{im}-1)} + \sqrt{\frac{Ha_i^4}{4(E_{im}-1)^2} + \frac{E_{im}\,Ha_i^2}{(E_{im}-1)} + 1} \tag{55}$$

where Ha (Hatta number) represents the ratio between the reaction kinetics and the maximal local mass flux when the MEA diffusion is not limiting. Its expression is

$$Ha_i = \frac{\sqrt{v_i k_r C_{MEA,L} D_{i,L}}}{k_{i,L}} \tag{56}$$

The limiting enhancement factor, E_{iim}, represents the ratio between the diffusion distance without reaction and the diffusion distance with reaction when the MEA diffusion is limiting. The reversibility of the reaction is taken into account by the introduction of a E_{iim} for reversible reactions [30]. In this work, the formulation given by [54] is used, which considers Eq. (18) as the kinetically controlled reversible reaction. The corresponding expression is

$$E_{iim,CO_2} = 1 + \frac{D_{P,L}}{D_{CO_2,L}} \frac{\sqrt{K_6}\, C_{MEA,L}}{\left(1 + 2\frac{D_{P,L}}{D_{MEA,L}}\sqrt{K_6 C_{CO_2,L-Mint}}\right)\left(\sqrt{C_{CO_2,L-Mint}} + \sqrt{C_{CO_2,L}}\right)} \tag{57}$$

Nomenclature

AARD	average absolute relative deviation $AARD = \frac{1}{n}\sum_{i=1}^{n} \frac{\left\lvert f_i^{exp} - f_i^{est}\right\rvert}{f_i^{exp}}$
Cp	specific heat ($J mol^{-1} K^{-1}$)
d_h	hydraulic diameter = 4 x flow volume/fluid–membrane interfacial area
D_i	diffusion coefficient ($m^{-2} s^{-1}$)
E	enhancement factor (dimensionless)
Gz	Graetz number = $\frac{D_{j,F} Z}{v_F d_h^2}$ (dimensionless)
h	heat transfer coefficient ($W m^{-2} K^{-1}$)
H	enthalpy (J)
ΔH	enthalpy difference ($J mol^{-1}$)
K	chemical equilibrium constant (molar scale) or Kozeny constant (m^{-2})
k	mass transfer coefficient ($m s^{-1}$) or kinetic constant (molar scale)
L	effective contactor length (m)
M	molar mass ($kg mol^{-1}$)
N_i	molar flux ($mol m^{-2} s^{-1}$)
P	pressure (Pa)
q	heat flux ($W m^{-2}$)

r_e	external fiber radius (m)
r_{CO_2}	reaction rate relative to CO_2 (mol $m^{-3} s^{-1}$)
R	gas constant (J $mol^{-1} K^{-1}$)
S	gas-phase saturation
Sh	Sherwood number = $\frac{k_F d_h}{D_{j,f}}$ (dimensionless)
T	temperature (K)
U	overall heat transfer coefficient (W $m^{-2} K^{-1}$)
V	contactor volume
xi	molar fraction in liquid (dimensionless)
yi	molar fraction in gas (dimensionless)
v	interstitial fluid velocity (m s^{-1})
w	mass fraction of pseudo-compounds (dimensionless)

Greek symbols

α	CO_2 solvent loading ($mol_{CO_2} mol_{MEA}^{-1}$)
δ	fiber thickness (m)
φ	fiber volume fraction (dimensionless)
λ	thermal conductivity (W $m^{-1} K^{-1}$)
m	viscosity (Pa s^{-1})
ρ	density (kg m^{-3})
Θ	CO_2 capture ratio (dimensionless)
ξ	MEA conversion (dimensionless)
H	Henry constant (Pa m^3 mol^{-1})
K	GLE or VLE constant

Subscripts

i	compound
r_e	external fiber radius (m)
G	relative to gas
F	relative to fluid
L	relative to liquid
M	relative to the membrane
abs	absorption
cond	relative to condensation
int	internal surface of the fibers
ext	external surface of the fibers
sens	relative to sensible heat
tot	addition of all compounds
vap	vaporization
ps	pseudo-specie

Superscripts

ref	relative to reference
in	at liquid or gas inlet
out	at liquid or gas outlet

References

[1] F.A. Tobiesen, H.F. Svendsen, O. Juliussen, Experimental validation of a rigorous absorber model for CO_2 postcombustion capture, AIChE J. 53 (4) (2007) 846–865.

[2] P. Luis, T. Van Gerven, B. Van der Bruggen, Recent developments in membrane-based technologies for CO_2 capture, Prog. Energy Combust. Sci. 38 (3) (2012) 419–448.

[3] Z. Cui, D. deMontigny, Part 7: a review of CO_2 capture using hollow fiber membrane contactors, Carbon Manag. 4 (1) (2013) 69–89.

[4] D. Albarracin Zaidiza, J. Billaud, B. Belaissaoui, S. Rode, D. Roizard, E. Favre, Modeling of CO_2 post-combustion capture using membrane contactors, comparison between one- and two-dimensional approaches, J. Membr. Sci. 455 (2014) 64–74.

[5] E. Chabanon, D. Roizard, E. Favre, Modelling strategies of membrane contactors for post-combustion carbon capture: a critical comparative study, Chem. Eng. Sci. 87 (2013) 393–407.

[6] S. Rode, P.T. Nguyen, D. Roizard, R. Bounaceur, C. Castel, E. Favre, Evaluating the intensification potential of membrane contactors for gas absorption in a chemical solvent: a generic one-dimensional methodology and its application to CO_2 absorption in monoethanolamine, J. Membr. Sci. 389 (2012) 1–16.

[7] N. Boucif, E. Favre, D. Roizard, Capture in HFMM contactor with typical amine solutions: a numerical analysis, Chem. Eng. Sci. 63 (22) (2008) 5375–5385.

[8] R. Faiz, M.H. El-Naas, M. Al-Marzouqi, Significance of gas velocity change during the transport of CO_2 through hollow fiber membrane contactors, Chem. Eng. J. 168 (2) (2011) 593–603.

[9] K.A. Hoff, O. Juliussen, O. Falk-Pedersen, H.F. Svendsen, Modeling and experimental study of carbon dioxide absorption in aqueous alkanolamine solutions using a membrane contactor, Ind. Eng. Chem. Res. 43 (16) (2004) 4908–4921.

[10] K.A. Hoff, H.F. Svendsen, Membrane contactors for CO_2 absorption – application, modeling and mass transfer effects, Chem. Eng. Sci. 116 (2014) 331–341.

[11] W. Rongwong, S. Assabumrungrat, R. Jiraratananon, Rate based modeling for CO2 absorption using monoethanolamine solution in a hollow fiber membrane contactor, J. Membr. Sci. 429 (2013) 396–408.

[12] I. Iliuta, F. Bougie, M.C. Iliuta, CO_2 removal by single and mixed amines in a hollow-fiber membrane module—investigation of contactor performance, AIChE J 61 (2014) 955–971.

[13] N. Ghasem, M. Al-Marzouqi, N. Abdul Rahim, Modeling of CO_2 absorption in a membrane contactor considering solvent evaporation, Sep. Purif. Technol. 110 (2013) 1–10.

[14] B. Metz, O. Davidson, H. de Coninck, M. Loos, L. Meyer, IPCC Special Report on Carbon Dioxide Capture and Storage, Cambridge University Press, New York, NY, United States, 2005.

[15] D. deMontigny, P. Tontiwachwuthikul, A. Chakma, Using polypropylene and polytetrafluoroethylene membranes in a membrane contactor for CO_2 absorption, J. Membr. Sci. 277 (2006) 99–107.

[16] H.-Y. Zhang, R. Wang, D.T. Liang, J.H. Tay, Theoretical and experimental studies of membrane wetting in the membrane gas–liquid contacting process for CO_2 absorption, J. Membr. Sci. 308 (2008) 162–170.

[17] E. Chabanon, D. Roizard, E. Favre, Membrane contactors for postcombustion carbon dioxide capture: a comparative study of wetting resistance on long time scales, Ind. Eng. Chem. Res. 50 (13) (2011) 8237–8244.

[18] S. Mosadegh-Sedghi, D. Rodrigue, J. Brisson, M.C. Iliuta, Wetting phenomenon in membrane contactors – causes and prevention, J. Membr. Sci. 452 (2014) 332–353.

[19] S. Khaisri, D. deMontigny, P. Tontiwachwuthikul, R. Jiraratananon, Comparing membrane resistance and absorption performance of three different membranes in a gas absorption membrane contactor, Sep. Purif. Technol. 65 (3) (2009) 290–297.

[20] J.-L. Li, B.-H. Chen, Review of CO_2 absorption using chemical solvents in hollow fiber membrane contactors, Sep. Purif. Technol. 41 (2) (2005) 109–122.

[21] E.N. Fuller, P.D. Schettler, J.C. Giddings, New method for prediction of binary gas-phase diffusion coefficients, Ind. Eng. Chem. 58 (5) (1966) 18–27.

[22] C.R. Wilke, P. Chang, Correlation of diffusion coefficients in dilute solutions, AIChE J. 1 (2) (1955) 264–270.

[23] J.B. Talbot, Handbook of Aqueous Electrolyte Solutions: Physical Properties, Estimation and Correlation Methods, A.L. Horvath (Ed.), Ellis Horwood Limited, 1985, 631 p., $154.95, AIChE J. 33 (1) (1987) 169–170.

[24] G. Astarita, D.W. Savage, A. Bisio, Gas Treating with Chemical Solvents, John Wiley, 1983.

[25] R. Crovetto, Evaluation of solubility data of the system CO_2–H_2O from 273 K to the critical point of water, J. Phys. Chem. Ref. Data 20 (3) (1991) 575–589.

[26] M.D. Hilliard, A predictive thermodynamic model for an aqueous blend of potassium carbonate, piperazine, and monoethanolamine for carbon dioxide capture from flue gas, Aug. 2008.

[27] P.V. Danckwerts, The reaction of CO_2 with ethanolamines, Chem. Eng. Sci. 34 (4) (1979) 443–446.

[28] J.E. Crooks, J.P. Donnellan, Kinetics and mechanism of the reaction between carbon dioxide and amines in aqueous solution, J. Chem. Soc. Perkin Trans. 2 (4) (1989) 331–333.

[29] A. Aboudheir, P. Tontiwachwuthikul, A. Chakma, R. Idem, Kinetics of the reactive absorption of carbon dioxide in high CO_2-loaded, concentrated aqueous monoethanolamine solutions, Chem. Eng. Sci. 58 (2003) 5195–5210.

[30] J.A. Hogendoorn, R.D. Vas Bhat, J.A.M. Kuipers, W.P.M. van Swaaij, G. F. Versteeg, Approximation for the enhancement factor applicable to reversible reactions of finite rate in chemically loaded solutions, Chem. Eng. Sci. 52 (24) (1997) 4547–4559.

[31] J. Happel, Viscous flow relative to arrays of cylinders, AIChE J. 5 (2) (1959) 174–177.

[32] A. Lévêque, Les Lois de la transmission de chaleur par convection, Dunod, 1928.

[33] L. Bao, B. Liu, G.G. Lipscomb, Entry mass transfer in axial flows through randomly packed fiber bundles, AIChE J. 45 (11) (1999) 2346–2356.

[34] L. Bao, G.G. Lipscomb, Well-developed mass transfer in axial flows through randomly packed fiber bundles with constant wall flux, Chem. Eng. Sci. 57 (1) (2002) 125–132.

[35] L. Bao, G. Glenn Lipscomb, Mass transfer in axial flows through randomly packed fiber bundles with constant wall concentration, J. Membr. Sci. 204 (1–2) (2002) 207–220.

[36] S. Wickramasinghe, M. Semmens, E. Cussler, Mass-transfer in various hollow fiber geometries, J. Membr. Sci. 69 (3) (1992) 235–250.
[37] H. Kreulen, C.A. Smolders, G.F. Versteeg, W.P.M. van Swaaij, Microporous hollow fibre membrane modules as gas–liquid contactors. Part 1. Physical mass transfer processes: a specific application: mass transfer in highly viscous liquids, J. Membr. Sci. 78 (3) (1993) 197–216.
[38] E. Favre, H.F. Svendsen, Membrane contactors for intensified post-combustion carbon dioxide capture by gas–liquid absorption processes, J. Membr. Sci. 407–408 (2012) 1–7.
[39] S. Boributh, R. Jraratananon, K. Li, Analytical solutions for membrane wetting calculations based on log-normal and normal distribution functions for CO_2 absorption by a hollow fiber membrane contactor, J. Membr. Sci. 429 (2013) 459–472.
[40] R.B. Saffarini, B. Mansoor, R. Thomas, H.A. Arafat, Effect of temperature-dependent microstructure evolution on pore wetting in PTFE membranes under membrane distillation conditions, J. Membr. Sci. 429 (2013) 282–294.
[41] I. Brovchenko, A. Oleinikova, 4 – Phase diagram of confined water, in: I. Brovchenko, A. Oleinikova (Eds.), Interfacial and Confined Water, Elsevier, Amsterdam, 2008, pp. 91–119.
[42] B. Hanley, C.-C. Chen, New mass-transfer correlations for packed towers, AIChE J. 58 (1) (2012) 132–152.
[43] R. Jang, M. Yang, S. Chen, S.-M. Huang, X. Yang, Fluid flow and heat transfer across an elliptical hollow fiber membrane tube bank with randomly distributed features, Int. J. Heat Mass Transf. 76 (2014) 559–567.
[44] S.-M. Huang, M. Yang, Heat and mass transfer enhancement in a cross-flow elliptical hollow fiber membrane contactor used for liquid desiccant air dehumidification, J. Membr. Sci. 449 (2014) 184–192.
[45] T.H. Chilton, A.P. Colburn, Mass transfer (absorption) coefficients prediction from data on heat transfer and fluid friction, Ind. Eng. Chem. 26 (11) (1934) 1183–1187.
[46] L.-Z. Zhang, S.-M. Huang, Coupled heat and mass transfer in a counter flow hollow fiber membrane module for air humidification, Int. J. Heat Mass Transf. 54 (2011) 1055–1063.
[47] J. Phattaranawik, R. Jraratananon, A.G. Fane, Heat transport and membrane distillation coefficients in direct contact membrane distillation, J. Membr. Sci. 212 (2003) 177–193.
[48] S. González Pinto, S. Pérez Rodríguez, JI. Montijano Torcal, On the numerical solution of stiff IVPs by Lobatto IIIA Runge–Kutta methods, J. Comput. Appl. Math. 82 (1997) 129–148.
[49] R. Dugas, P. Alix, E. Lemaire, P. Broutin, G. Rochelle, Absorber model for CO_2 capture by monoethanolamine — application to CASTOR pilot results, Energy Procedia 1 (1) (2009) 103–107.
[50] P. Moser, S. Schmidt, S. Wallus, T. Ginsberg, G. Sieder, I. Clausen, J.G. Palacios, T. Stoffregen, D. Mihailowitsch, Enhancement and long-term testing of optimised post-combustion capture technology – results of the second phase of the testing programme at the Niederaussem pilot plant, Energy Procedia 37 (2013) 2377–2388.
[51] P. Khakharia, L. Brachert, J. Mertens, A. Huizinga, B. Schallert, K. Schaber, T.J.H. Vlugt, E. Goetheer, Investigation of aerosol based emission of MEA due to sulphuric acid aerosol and soot in a post combustion CO_2 capture process, Int. J. Greenh. Gas Control 19 (2013) 138–144.
[52] W.J. DeCoursey, Enhancement factors for gas absorption with reversible reaction, Chem. Eng. Sci. 37 (10) (1982) 1483–1489.
[53] P. Kumar, J. Hogendoorn, P.H. Feron, G. Versteeg, Approximate solution to predict the enhancement factor for the reactive absorption of a gas in a liquid flowing through a microporous membrane hollow fiber, J. Membr. Sci. 213 (1–2) (2003) 231–245.
[54] R.H. Weiland, M. Rawal, R.G. Rice, Stripping of carbon dioxide from monoethanolamine solutions in a packed column, AIChE J. 28 (6) (1982) 963–973.

4.2. Verification of the Rate-Based Model of the Contactor

Due to the lack of available experimental data, the membrane contactor model could not be validated in applicable industrial operating conditions. To compensate for this gap, use of the thermodynamic approach, physicochemical properties and reaction kinetics, was tested by modelling CO_2 chemical absorption using packed columns. Indeed, by setting the adequate mass-transfer correlations [102] and removing the terms related to the membrane, the 1D approach proved to be adaptable to model packed columns. The model approach of packed columns is described and simulation results are compared against experimental results in the following sections.

4.2.1. Packed Column Model Equations

Details of packed columns modelling are found in [64], [76], [77]. The differential balance as well as the transfer correlations are shown in Table 4-1. In addition, the Sherwood number and the interfacial specific area correlations are included for the IMPT-50 packing used in the Esbjerg pilot plant. The model assumptions of this model are similar to those of HFMC modelling, except for those relative to the membrane and the gas-phase flow regime, i.e. turbulent flow.

Table 4-1 Model equations of CO_2 absorption using packed columns. Transfer coefficients for packing IMPT-50, taken from [102]

	Mass	Energy
Transfer equations	Gas and liquid: $\frac{d}{dz}G_i = \frac{d}{dz}L_i = -N_i$ With: $G_i = \overline{u_G}\overline{C_{i,G}}$ $\quad L_i = \overline{u_L}\overline{C_{i,L}}$ $N_i = a_I k_{i,ov}\left(\overline{C_{i,G}} - \overline{C_{i,L}^*}\right)$ $\frac{1}{k_{i,ov}} = \frac{1}{k_{i,G}} + \frac{K_i^{VLE}}{E_i k_{i,L}}$	Gas: $\frac{d\,\overline{T_G}}{dz} = -\frac{a_I U(\overline{T_G}-\overline{T_L})}{C_{pG}\sum_i \overline{u_G}\overline{C_{i,G}}}$ Liquid: $\frac{d\,\overline{T_L}}{dz} = -\frac{a_I U(\overline{T_G}-\overline{T_L}) \;+\sum_i N_i \Delta H_{abs/vap}}{C_{pL}\sum_i \overline{u_L}\overline{C_{i,L}}}$ With: $\frac{1}{U} = \frac{1}{h_G} + + \frac{1}{h_{i,L}}$
Transfer coefficients	Dimensionless numbers: $Re_f = \frac{\rho_f u_f d_h}{\mu_f}$; $Sc_{i,f} = \frac{\mu_f}{\rho_f D_{i,f}}$ $Sh_{i,f} = \frac{k_{i,f}\, d_h}{D_{i,f}}$; $We_f = \frac{d_h \rho_f u_f^2}{\sigma_f}$ $Fr_f = \frac{u_f^2}{g d_h}$ Gas: $Sh_{i,G} = 0.00473\ Re_G Sc_{i,G}^{1/3}$ Liquid: $Sh_{i,L} = Re_f Sc_{i,G}^{1/3}$	Dimensionless numbers: $Pr_f = \frac{\mu_f Cp_f}{\lambda_f}$ $Nu_f = \frac{h_f\, d_h}{\lambda_f}$ Chilton-Colburn analogy $Sh_{i,f} {Sc_{i,f}}^{-1/3} = Nu_f {Pr_f}^{-1/3}$

With:

$$d_h = \frac{4\epsilon}{a_d}$$

$$\frac{a_I}{a_d} = 0.332 Re_G^{0.132} Re_L^{-0.102} We_L^{0.194} Fr_L^{-0.2} \left(\frac{\rho_G}{\rho_L}\right)^{-0.154} \left(\frac{\mu_G}{\mu_L}\right)^{0.195}$$

4.2.2. Simulation Results and Model Validation

Simulations were conducted for tests performed during the CASTOR campaign at the Esbjerg pilot plant [103]. Operating conditions for these simulations are shown in Table 4-2. Partially loaded lean solvent, high CO_2 capture ratio as well as high MEA conversions characterize these experimental tests. The absorber column of 17 m height with a diameter of 1.1 m, was filled with IMPT-50 packing. While operating at its energetic optimum at 2 bars of reboiler pressure, the pilot plant was able to absorb 0.46 mole of CO_2 per cubic meter of absorber volume, with a corresponding reboiler heat duty of 3.74 GJ per ton of absorbed CO_2.

The comparison between simulations and experiments are illustrated in Figure 4.1. The model correctly predicted temperature profiles, as shown in Figure 4.1a, which is evidence of non-isothermal behaviour of the absorption unit. Moreover, as shown in Figure 4.1b, the packed column performances are predicted within an uncertainty lower than 5%, thus demonstrating the quality of the CO_2 solubility approach used in this work.

Table 4-2 Operating conditions of the CASTOR campaign from the Esbjerg pilot plant [103]

RUN	Q_G [Nm3/h]	Y_{CO2} [%]	Q_L [m3/h]	w_{MEA} [wt.]	α^{in} $[\frac{mol_{CO_2}}{mol_{MEA}}]$	α^{out} $[\frac{mol_{CO_2}}{mol_{MEA}}]$	θ [--]	ΔP_G [kPa]	P_G [kPa]	T_G [°C]	T_L (°C)
1A	4920	13.2	22.9	0.323	0.275	0.45	90	5.3	98	40	47.8
1B	5010	13.4	18.9	0.33	0.249	0.46	90	4.9	98	40	49.1
1C	4940	13.1	16.6	0.324	0.224	0.47	90	4.5	97	40	48.6
1D	4930	13.5	14.7	0.328	0.193	0.47	91	4.3	97	40	48.8
1E	4990	13.1	12.4	0.323	0.166	0.47	90	4.2	96	40	49.2
2A	4880	13.3	15.4	0.322	0.192	0.46	94	4.4	97	40	49.8
2B	4934	13.3	15.4	0.322	0.223	0.46	84	4.3	97	40	49.8
2C	5019	13.2	15.4	0.315	0.27	0.47	66	4.3	96	40	46.9
3A	4917	12.3	15.4	0.317	0.209	0.46	90	4.5	97	40	48
3B	4771	12.5	14.9	0.311	0.207	0.47	88	4.5	97	40	49
3C	4935	11.3	16.9	0.31	0.224	0.46	93	4.5	97	40	47.8
3D	4874	11.4	18.9	0.302	0.241	0.45	92	4.5	97	40	47

It is worth mentioning that the temperature peak measured in packed beds when using a high MEA conversion and a high CO_2 capture ratio was significant, reaching 75 °C. Similar high peaks can be expected to occur in membrane contactors with similar boundary conditions. This is in accordance with simulation results obtained in Section 4.1.

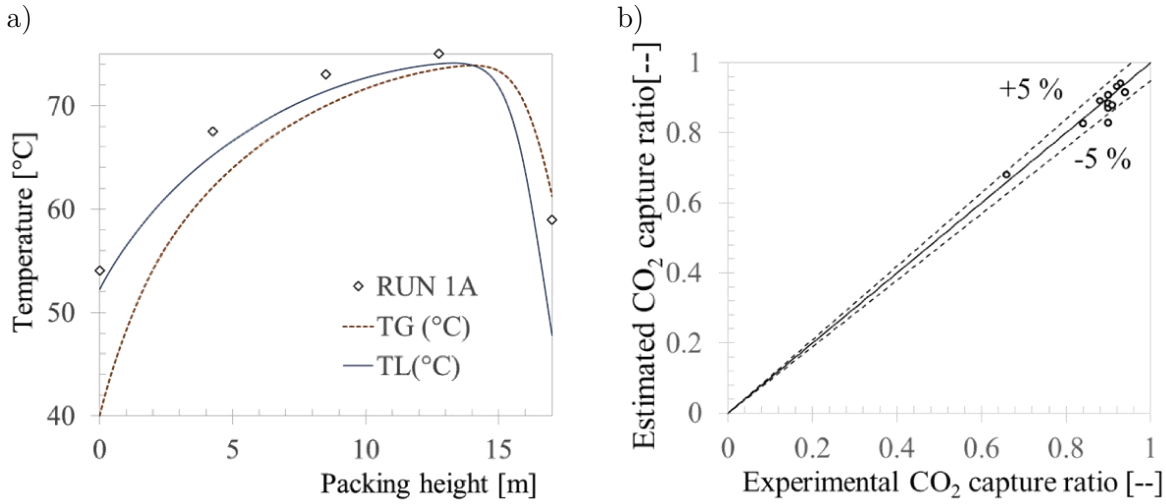

Figure 4.1 Simulation results of the packed column model. Solid and dotted lines: model predictions. Dots: experimental data. a) Temperature profile of the absorber for the Run 1A, b) parity plot of CO_2 capture ratio

4.3. Influence of Total Trans-membrane Flux on the Model Predictions

One important aspect of multicomponent transmembrane mass-transfer is the counter-diffusion of the species. Depending on the affinity of the compounds towards each phase, this phenomenon may either improve or deteriorate the rates of mass transfer. The counter-diffusion can be illustrated by applying the law of conservation of mass to a surface separating two hypothetical points, A and B. The resulting expression of the specific molar flux is as follows:

$$N_i = k_{i,f} C_{tot,f} (y_i^A - y_i^B) + y_i^A \sum_i N_i \tag{4.1}$$

where $k_{i,f}$ stands for the mass-transfer coefficient of species i in the phase f. $C_{tot,f}$ is the total molar concentration of the phase and y_i represents the molar fraction of component i. In order to perform an accurate calculation, the diffusion coefficients involved in the calculation of $k_{i,f}$ need to be dependent on the composition. As detailed in Section 4.1, the solution of this equation is as iterative as the expression is implicit. A common simplification consists in neglecting the last term, which is equivalent to assuming equimolar flux or diluted species, thus rendering a straightforward calculation.

The influence of this assumption on the model predictions is briefly investigated in this section through performed simulations, both accounting for and discounting this influence. The operating conditions correspond to those set in Section 4.1, for an external fibre radius of 200 microns and a CO_2 membrane mass-transfer coefficient of 10^{-3} ms^{-1}.

The axial profiles of the transmembrane flux of CO_2 and water are illustrated in Figure 4.2.a and Figure 4.2.b, respectively. Both flux formulations lead to different profiles indicative of non-equimolar behaviour. The profiles are different but display the same trends. For instance, the value of the CO_2 transmembrane flux passes through a maximum but is slightly displaced and higher for the total-flux formulation. Similarly, this was observed for the water transfer. Nonetheless, the values of the average transmembrane fluxes for all species (i.e. CO_2, MEA and water) are almost identical, with a difference of less than 0.8%. Of course, this is only one particular case with defined operating conditions and no general conclusions can be drawn. However, in terms of performance prediction of hollow fibre membrane contactors under industrial conditions, the influence of the total flux may be neglected.

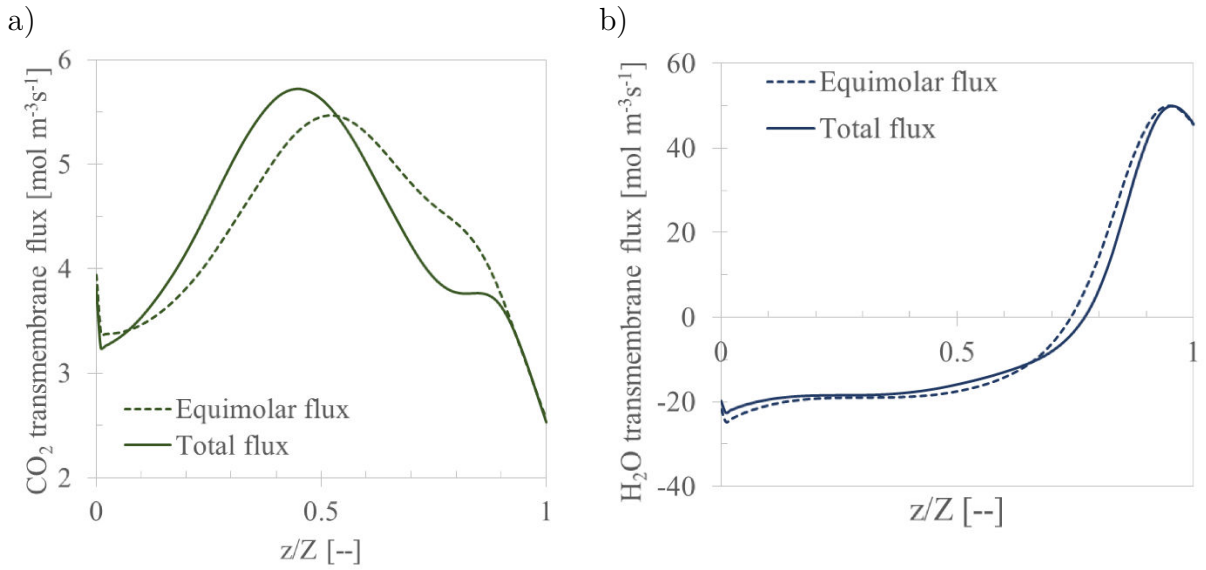

Figure 4.2 Axial profiles of transmembrane flux per unit volume of contactor obtained by using the equimolar flux and the total flux formulations. Simulation conditions are identical to those presented in Section 4.1. r_e = 200 m, $k_{M,CO2}^{eq}$ = 10^{-3} ms^{-1} a) CO_2 b) H_2O.

As a result of variation in the local profiles of transmembrane fluxes between both mass-transfer formulations, the temperature profiles, illustrated in Figure 4.3, are quite different. Indeed, they follow similar trends but the temperature peak predicted using the equimolar flux assumption is about 5 °C higher than that obtained taking into account the total flux. Moreover, the outlet liquid temperature predicted from both approaches is very close. Therefore, in terms of temperature profiles, the influence of the total flux may be neglected.

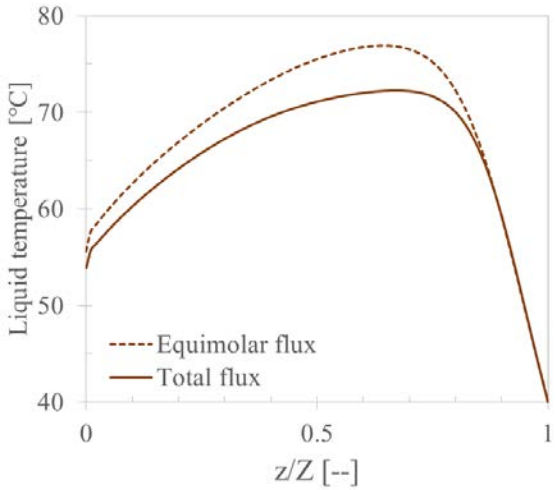

Figure 4.3 Axial liquid temperature profile obtained by using the equimolar flux and the total flux formulations. Simulation conditions are similar to those presented in Section 4.1

4.4. Adiabatic Two-Dimensional Modelling of HFMC

The main advantage of the 2D approach over the 1D approach is that more rigorous computations of transfer fluxes and reaction rates are possible. The main drawback is that model resolution requires significant calculation time and a high processor performance. It is therefore tedious and not appropriate for investigating large parameter domains. Identification of an efficient model strategy, ideally both rigorous yet robust while not overly complex, is key. In Section 3.2, a comparison of 1D and 2D approaches assuming isothermal behaviour, irreversible reactions and neglecting water transfer was performed for CO_2 capture with amine solution using membrane contactors. The aim was to identify the most efficient model strategy. The results showed comparable simulation results, with a maximum relative deviation of 2.2%, indicating the quality of the 1D approach. In this section, 1D and 2D approaches are compared applying more realistic assumptions, i.e. adiabatic behaviour, multi-component transfer and reversible reactions. Both mild and severe operating conditions are considered. Indeed, unloaded solvent and relatively low amine conversion are representative of most of the available experimental data; whereas preloaded solvent and high amine conversion illustrate an industrial context.

4.4.1. Model Assumptions

The assumptions made in this work are mostly based on the general consensus found in other published work. The two models consider the non-isothermal nature of the overall absorption process, including the solvent transfer across the membrane. Wetting of the membrane was considered by adjusting an equivalent mass-transfer coefficient to that obtained for partially wetted membranes, as described in Section 3.1.2 [58], [104].

The model assumptions made for both 1D and 2D approaches are summarised in Table 4-3. The main differences between the models reside in the assumptions made in the mass- and heat-transfer and reaction. The 1D model simplifies the partial differential balance equations used in the 2D modelling approach by employing an enhancement factor, a local overall mass-transfer coefficient and transfer analogies. The enhancement factor describes the chemical reaction in the liquid-side diffusion boundary layer, and its definition and implementation involve numerous assumptions. Only CO_2 is considered capable of diffusing through the gas-liquid phase boundary, and hence the membrane. Furthermore, the liquid-side diffusion coefficient of each species is considered to be constant [105]. Finally, liquid mixing-cup concentrations, which are assumed to be at chemical equilibrium, are considered. In contrast, the 2D model considers local concentrations.

Table 4-3 1D and 2D modelling assumptions

Hydrodynamics	
1. Steady state [24], [50], [52], [55], [57], [58], [78], [95], [106], [107]	
2. Laminar liquid and gas flow with fully developed velocity profiles, i.e. no radial velocity components [24], [50], [52], [55], [58], [78], [95], [106], [107]	
3. Plug flow, i.e. non-uniform flow distribution due to random packing neglected [24], [50], [52], [55], [57], [58], [78], [95], [106], [107]	
Thermodynamics	
4. Henry's law used to represent the gas-liquid equilibrium [24], [52], [55], [57], [58], [95], [106], [107]	
5. Solubility of N_2 neglected	
6. Semi-empirical liquid speciation [78]	
7. Ideal gas behaviour [24], [50], [52], [55], [57], [58], [78], [95], [106], [107]	
Reaction and Mass- and Heat-Transfer	
8. Kinetics including reaction reversibility [28], [67], [78]	
9. Ionic products considered as one complex-product with a single apparent diffusion coefficient [67], [78]	
10. Membrane mass transfer modelled using Fick diffusion through porous media, thus neglecting convective contributions. Effective membrane mass-transfer coefficient value as reported in literature. For heat transfer, solid conduction is added. [24], [50], [52], [55], [57], [58], [78], [106], [107]	
11. Condensation or evaporation of water occurs only at the liquid-membrane interface [67], [78]	
12. Adiabatic behaviour thus neglecting heat- losses	
<u>One dimensional:</u>	<u>Two dimensional:</u>
13. Axial diffusion neglected in all phases	13. Axial diffusion considered for gas, liquid and membrane.
14. Sherwood and Nusselt numbers calculated using the Graetz equation for the gas and the liquid phase. Mixing-cup-concentrations and temperatures are considered. Uniform wall flux is taken as boundary condition [108]. Reaction taken into account by an enhancement factor using liquid mixing-cup concentrations at chemical equilibrium. Kinetically controlled reversible reaction restricted to a reaction boundary-layer.	14. Contributions of advection, diffusion and reaction to mass balances solved using local concentrations. Analogously, contributions of convection, conduction and heat of reaction to energy balances solved using local temperatures.

4.4.2. Model Equations and Boundary Conditions

A comparison of the principal model equations for both one-dimensional (1D) and two-dimensional (2D) modelling approaches are shown in Table 4-4. Mass- energy- and momentum differential balances are established in steady state. Further details on 1D and 2D modelling can be found in [16], [50], [85], [109].

Generally, an increase in CO_2 loading is accompanied by an increase in liquid density and thus the variation of the axial velocity of the liquid can be neglected. Conversely, the variation of the axial gas velocity may be important due to the high CO_2 capture ratios and should be taken into account.

The liquid viscosity varies with both CO_2 loading and temperature. It turns out that, in industrial operating conditions, the outlet value of the liquid viscosity may be up to three times higher than its inlet value which strongly influences the mass transfer and the hydrodynamics.

The 1D model is a boundary value problem of an ordinary differential equation system. Depending on the boundary conditions, the solution can be stiff and hence, finite-difference methods (e.g. collocation) are recommended. In this work, a collocation method from the routine *bvp5c* of Matlab® was used.

The 2D model is a boundary value problem of a partial differential equation system which is generally solved using finite elements technics. Commercial software (e.g. COMSOL multiphysics, Fluent) including meshing facilities can handle the resolution of these systems with relative ease. Determining system resolution is, however, more problematic due to the fact that the reaction occurs very close to the gas-liquid interface. At the same time, the space-scale of the mesh should be of the same order of magnitude than that for the space-scale of the mass-transfer and reaction phenomena, leading typically to over a million of elements for the whole system [44], [95], [109].

As concluded in Section 4.1, when low absorbent conversion (e.g. lower than 0.2 for the MEA system), are imposed, simulations indicate that the contactor can be considered to be isothermal. If, in addition, the inlet liquid absorbent is unloaded, the reaction can be considered to be pseudo-first order and irreversible. In this case, the mass balance equations can be solved for only one species (i.e. CO_2). However, for high absorbent conversion and partially loaded inlet liquid absorbent, temperature gradients and liquid evaporation and condensation are significant. Hence, the multicomponent mass transfer as well as the heat balance equations should be considered.

Table 4-4 Principal model equations of HFMC

	One-dimensional modelling approach	Two-dimensional modelling approach
Mass balance	Gas and liquid: $\frac{d}{dz}G_i = \frac{d}{dz}L_i = -N_i$ With: $G_i = \overline{u_G}\overline{C_{i,G}} \qquad L_i = \overline{u_L}\overline{C_{i,L}}$ $N_i = a_M k_{i,ov}\left(\overline{C_{i,G}} - \overline{C_{i,L}^*}\right)$ $\frac{1}{a_M k_{i,ov}} = \frac{1}{a_{ext}k_{i,G}} + \frac{1}{a_M k_{i,M}} + \frac{K_i^{VLE}}{a_{int}E_i k_{i,L}}$ $k_{M,i} = \frac{k_{M,CO_2}^{\ eq}}{D_{CO_2,G}^{\ ref}}\ D_{i,G}$	Gas: $\frac{\partial}{\partial z}(v_G C_{i,G}) - \left[\frac{1}{r}\frac{\partial}{\partial r}\left(rD_{i,G}\frac{\partial C_{i,G}}{\partial r}\right) + \frac{\partial}{\partial z}\left(D_{i,G}\frac{\partial C_{i,G}}{\partial z}\right)\right] = 0$ Membrane: $\left[\frac{1}{r}\frac{\partial}{\partial r}\left(rD_{i,M}\frac{\partial C_{i,M}}{\partial r}\right) + \frac{\partial}{\partial z}\left(D_{i,M}\frac{\partial C_{i,M}}{\partial z}\right)\right] = 0$ Liquid: $\frac{\partial}{\partial z}(v_L C_{i,L}) - \left[\frac{1}{r}\frac{\partial}{\partial r}\left(rD_{i,L}\frac{\partial C_{i,L}}{\partial r}\right) + \frac{\partial}{\partial z}\left(D_{i,L}\frac{\partial C_{i,L}}{\partial z}\right)\right] = R_{i,L}$ With: $D_{i,M} = D_{i,G}\frac{k_{M,CO_2}^{\ eq}}{D_{CO_2,G}^{\ ref}}\delta$
Energy balance	Gas: $\frac{d\,\overline{T_G}}{dz} = -\frac{a_M U(\overline{T_G}-\overline{T_L})}{C_{pG}\sum_i \overline{u_G}\overline{C_{i,G}}}$ Liquid: $\frac{d\,\overline{T_L}}{dz} = -\frac{a_M U(\overline{T_G}-\overline{T_L}) \ + \sum_i N_i \Delta H_{abs/vap}}{C_{pL}\sum_i \overline{u_L}\overline{C_{i,L}}}$ With: $\frac{1}{a_M U} = \frac{1}{a_{ext}h_G} + \frac{1}{a_M h_M} + \frac{1}{a_{int}h_{i,L}}$	Gas: $\rho_G Cp_G v_G \frac{\partial T_G}{\partial z} - \left[\frac{1}{r}\frac{\partial}{\partial r}\left(r\lambda_G\frac{\partial T_G}{\partial r}\right) + \frac{\partial^2 T_G}{\partial z^2}\right] = 0$ Membrane: $\left[\frac{1}{r}\frac{\partial}{\partial r}\left(r\lambda_M\frac{\partial T_M}{\partial r}\right) + \frac{\partial^2 T_M}{\partial z^2}\right] = 0$ Liquid: $\rho_L Cp_L v_L \frac{\partial T_L}{\partial z} = \left[\frac{1}{r}\frac{\partial}{\partial r}\left(r\lambda_L\frac{\partial T_L}{\partial r}\right) + \frac{\partial^2 T_L}{\partial z^2}\right] + R_{CO_2}\Delta H_{rxn}$
Momentum balance	Fluid in lumen: $\frac{d\,P_{int}}{dz} = -\frac{8\mu_{int}\overline{v_{f,int}}}{r_i^2}$ Fluid in shell: $\frac{d\,P_{ext}}{dz} = -\mu_{ext}\overline{v_{f,ext}}\boldsymbol{K}_{koz}$ With: $\boldsymbol{K}_{koz} = \frac{8\varphi}{[2ln(1/\varphi)-3+4\varphi-\varphi^2]r_e^2}$	Idem 1D
Radial velocity profiles	Does not apply	Fluid in lumen: Hagen-Poiseuille equation $v_{f,int} = 2\overline{v_{f,int}}\left[1-\left(\frac{r}{r_{int}}\right)^2\right]$ Fluid in shell: Happel free surface approach [63] $v_{f,ext} = 2\overline{v_{f,ext}}(r_s^2 - r_{ext}^2)\left[\frac{r^2 - 2r_s^2\ln\left(\frac{r}{r_{ext}}\right) - r_{ext}^2}{3r_s^4 - 4r_s^2 r_{ext}^2 + r_{ext}^4 - 4r_s^4\ln\left(\frac{r_s}{r_{ext}}\right)}\right]$ With: $r_s = r_e\sqrt{1/\varphi}$ N.B: Fully developed velocity profiles.

Remarks	$\bar{T}$ and $\bar{C}$ denote the mixing-cup temperature and concentration respectively at a given axial position, z. $\overline{u_f}$ stands for the mean superficial velocity at a given axial position z. The mass transfer coefficients, $k_{i,G}$, $k_{i,M}$ and $k_{i,L}$ are computed as described in Appendix A. * Denotes equilibrium conditions	In order to take into account membrane wetting, a fourth domain corresponding to the wetted section is added. The equations are similar to those for the membrane domain.

An appropriate mesh is necessary for conducting the finite element analysis. It is sufficiently understood that the absorption process is controlled by liquid-side resistance to mass-transfer and that accurate modelling requires a rigorous absorption model and ensured sufficient discretisation of the liquid phase in the radial direction. One must also take into account the fact that the chemical absorption reaction occurs very close to the liquid-membrane interface. Consequently, the space-scale of the mesh was selected as being of the same order of magnitude as that for the coupled mass-transfer and reaction phenomena [78], [109].

The elements are rectangular in shape in accordance with the two main directions of transport, as schematised in Figure 4.4. Around boundaries, where the mass-transfer layers are extremely thin, the meshes are refined using arithmetic progressions, except for the liquid-membrane boundary where a geometric progression proved to be more efficient. Finally, a vast number of elements, i.e. about 3 millions, require solutions.

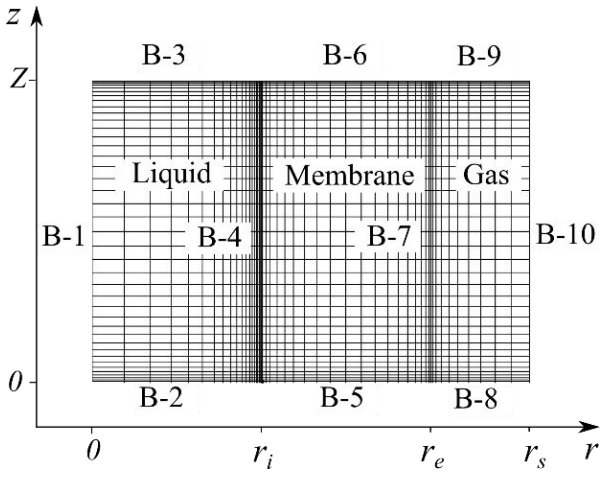

Figure 4.4. Schematic representation of the meshing, domains and boundaries in the 2D model.

The boundary conditions and corresponding expressions for the mass and energy balance equations across the domains are summarised in Table 4-5. With reference to Figure 4.4, the positive direction is taken from left to right, e.g. from the liquid to membrane to gas phase. The inlet liquid phase at boundary B-3, an aqueous solution of MEA, is assumed to be pre-loaded with carbon dioxide and at chemical equilibrium.

Table 4-5 Boundary conditions for 2D mass- and energy-transport equations.

Boundary	Condition	Mass-Transfer	Heat-Transfer
B-1	Axial-symmetry	$-\frac{dC_{i,L}}{dr}=0$	$-\frac{dT_L}{dr}=0$
B-2	Convective flux at liquid outlet	$-D_{i,L}\frac{dC_{i,L}}{dz}=0$	$-k_L\frac{dT_L}{dz}=0$
B-3	Initial liquid conditions	$C_{i,L}=C_{i,L}{}^{z=Z}$	$T_L=T_L{}^{z=Z}$
B-4	Continuity at interface & evaporation of liquid	$C_{i,L}=m_iC_{i,M}$	$T_L=T_M$ $-k_L\frac{dT_L}{dr}=-k_M\frac{dT_M}{dr}-\sum D_{i,M}\frac{dC_{i,M}}{dr}\Delta H_{vap,i}$
B-5	No-flux	$-D_{i,M}\frac{dC_{i,M}}{dz}=0$	$\frac{-dT_M}{dz}=0$
B-6	No-flux	$-D_{i,M}\frac{dC_{i,M}}{dz}=0$	$\frac{-dT_M}{dz}=0$
B-7	Continuity at interface	$C_{i,M}=C_{i,G}$	$T_M=T_G$
B-8	Initial gas conditions	$C_{i,G}=C_{i,G}{}^{z=0}$	$T_G=T_G{}^{z=0}$
B-9	Convective flux at gas outlet	$-D_{i,G}\frac{dC_{i,G}}{dz}=0$	$-k_G\frac{dT_G}{dz}=0$
B-10	Axial-Symmetry	$-\frac{dC_{i,G}}{dr}=0$	$-\frac{dT_G}{dr}=0$

4.4.3. Simulation Results in an Industrial Context

Operating conditions

Operating conditions that would be present in an industrial MEA absorption plant are characterized by a nearly complete solvent conversion as well as a partially loaded lean solvent. These conditions, reported in Table 4-6 together with geometrical parameters, are recommended by literature to minimise overall energy requirements [64]. In addition, the liquid pressure should always be higher than that of the gas phase in order to prevent

bubbling; hence, the liquid-side pressure is fixed to that of the inlet gas pressure. Simulations were performed using a microporous membrane with an equivalent membrane mass-transfer coefficient between that of a dry and a partially wetted membrane [58].

Table 4-6 Operating conditions and geometrical characteristics of the HFMC used in the simulation with typical industrial operating conditions

Parameter	Value	Units
Gas (shell side)		
CO_2 molar fraction	0.14	--
H_2O molar fraction (saturated flue gas)	0.07	--
Inlet temperature	313	K
Inlet pressure	1.05×10^5	Pa
Pressure drop	5×10^3	Pa
Superficial inlet gas velocity	0.19	ms^{-1}
Liquid (lumen side)		
MEA total mass fraction	0.3	$kg_{MEA}kg_L^{-1}$
CO_2 loading of lean solvent	0.242	$mol_{CO2}mol_{MEA}^{-1}$
Outlet pressure	1.05×10^5	Pa
Inlet temperature	313	K
Superficial inlet liquid velocity	8.6×10^{-4}	ms^{-1}
Contactor (Counter-current parallel flow)		
External fibre radius	2×10^{-4}	m
Relative fibre thickness	0.2	--
Packing fraction	0.6	--
Fibre length	0.32	m
CO_2 mass-transfer coefficient in membrane	$k_{M,CO2}{}^{eq} = 10^{-3}$	$m\ s^{-1}$

In order to meet both gas-phase pressure drop requirements, i.e. 50 mbar, and CO_2 capture ratio, i.e. 89.5%, the contactor length was only 0.32 m for a superficial inlet gas velocity of 0.19 m s^{-1} when simulated using the 2D model. This fibre length and superficial inlet gas velocity were then input into the 1D model.

Radial concentration profiles

Radial profiles can only be computed using the 2D approach as the 1D approach utilizes average radial values. In the following figures, only radial profiles of the liquid phase are plotted as this is where the main transfer resistance of the system is located.

Radial concentration profiles of CO_2, MEA and reaction product ($MEAH^+MEACOO^-$) in the liquid phase are shown in Figure 4.5a, 6b, 6c respectively for different axial positions.

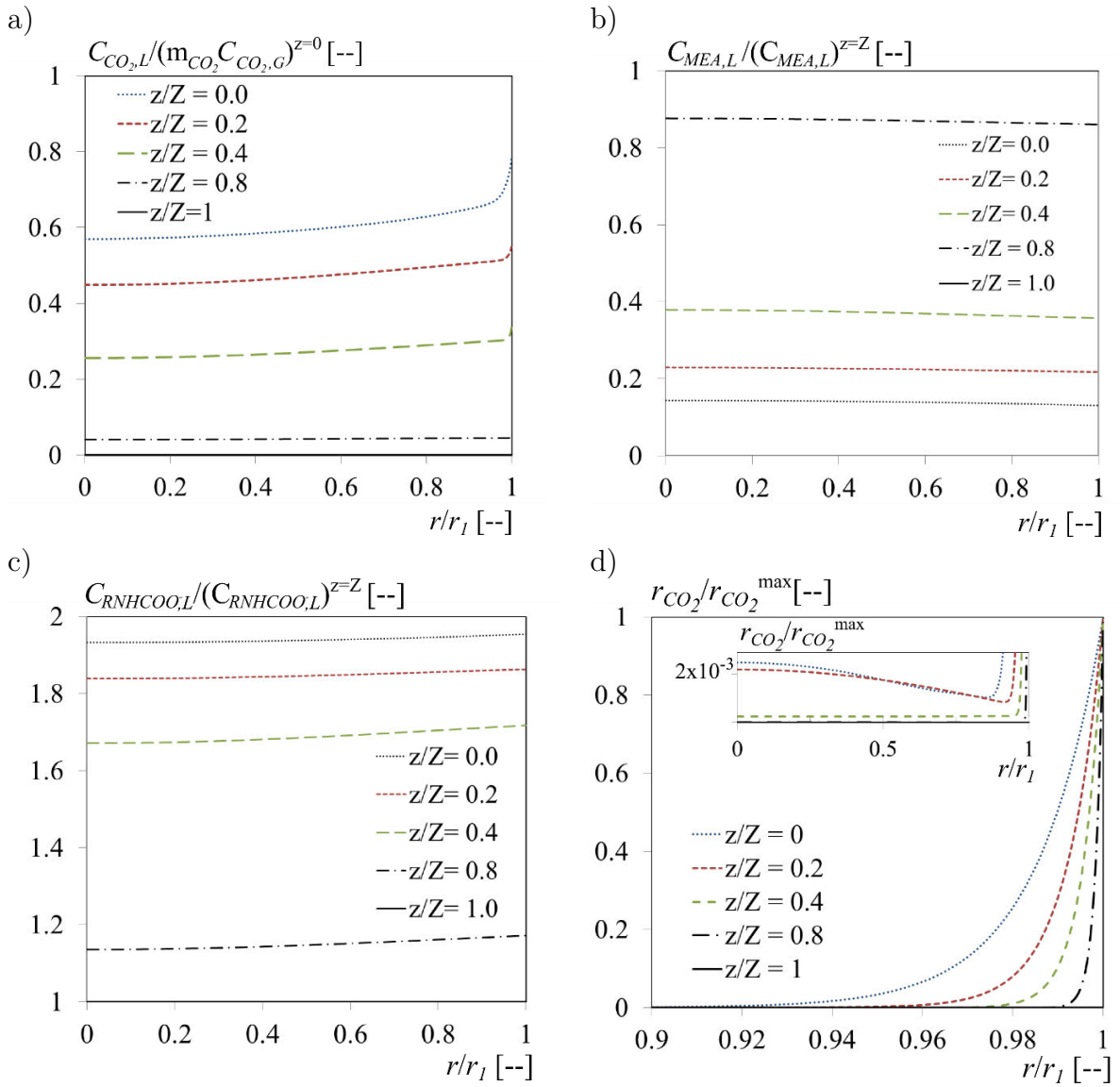

Figure 4.5 Dimensionless liquid phase species concentration and reaction kinetics as functions of the relative internal radius, 2D approach a) CO_2, b) MEA and c) $RNH_3^+RNHCOO^-$ complex d) Overall reaction rate

At the contactor inlet section, the liquid phase was assumed to be at chemical equilibrium and concentrations were homogeneous. The radial concentration profiles for all components and for all positions were relatively flat, except those close to the liquid-membrane interface for CO_2. The almost homogenous radial concentration distributions indicate that diffusion of the different species was not a limiting factor. Figure 4.5a shows the gradual enrichment of the solvent by CO_2 along the fibre length. This demonstrates

that the reversibility of the reaction must be taken into account when high solvent conversions are required. Figure 4.5b and 6c illustrate the depletion of MEA and the enrichment of reaction products respectively along the fibre length.

Figure 4.5d illustrates radial profiles of the overall reaction rate of CO_2, r_{CO2}, for different axial positions. In order to observe trends, the reaction rate was normalised by its maximal value at the corresponding axial position. The maximal penetration depth of CO_2 into the liquid phase was observed at the liquid inlet and corresponded to about 20 microns. This value is almost two times higher than that estimated when an irreversible reaction was assumed [109]. Since the reaction rate rapidly reached values close to zero, for nearly the entire liquid domain, the mixed-cup concentrations could be considered to be at chemical equilibrium. The influence of reaction-products diffusion on the local reaction rate can be observed in the additional char shown in Figure 4.5d. The curvature of the reaction rate profiles is typical for a diffusion-reaction system where concentration profiles are observed. However, the reaction rate far from the liquid-membrane interface is very small and its influence on the overall absorption rate can thus be neglected. The published work of Hoff et al. [50], [78] suggest that the diffusivity of complex-products should have a significant impact on the overall CO_2 absorption. However the operating conditions in that study were very different to those used in this work where a much faster liquid velocity is present (between 1 to 5 $cm.s^{-1}$), allowing for the build-up of radial concentration gradients.

Axial profiles of temperature and trans-membrane flux

Figure 4.6a, 7b and 7c show axial profiles of the specific trans-membrane fluxes of CO_2, water and MEA, respectively. Positive values indicate the absorption or condensation of the component at the membrane-liquid interface; conversely, negative values indicate desorption or evaporation. Illustrations depict simulation results of the 1D and the 2D models. While similar trends were observed, the profiles do not completely correspond to each other.

For CO_2, (Figure 4.6a), both models render profiles that pass through a maximum value of the absorbed specific flux close to half-way along the length of the fibre. For low axial coordinate values, near the liquid outlet, the 1D model overestimated relative to the 2D model; particularly at the liquid outlet, $z/Z = 0$, where the local absorbed flux for the 1D and 2D models were approximately 3 and 1.5 $mol.m^{-3}.s^{-1}$, respectively. Whereas the 2D model itself passed through a greater maximum of 5 $mol.m^{-3}.s^{-1}$.

For both water and MEA vapours (Figure 4.6a and 4.7c), flux reversal occurred, i.e. vapour condensation, at the vicinity of the liquid inlet. Since the local specific trans-membrane molar flux of water is more than 10 and 100 times higher than that of CO_2

and of MEA, respectively, the condensate is mainly composed of water. The transfer of water across the membrane is crucial because the more water that passes through the membrane, the more likely it is for the membrane to become wet as a result of the condensation of water vapour [67].

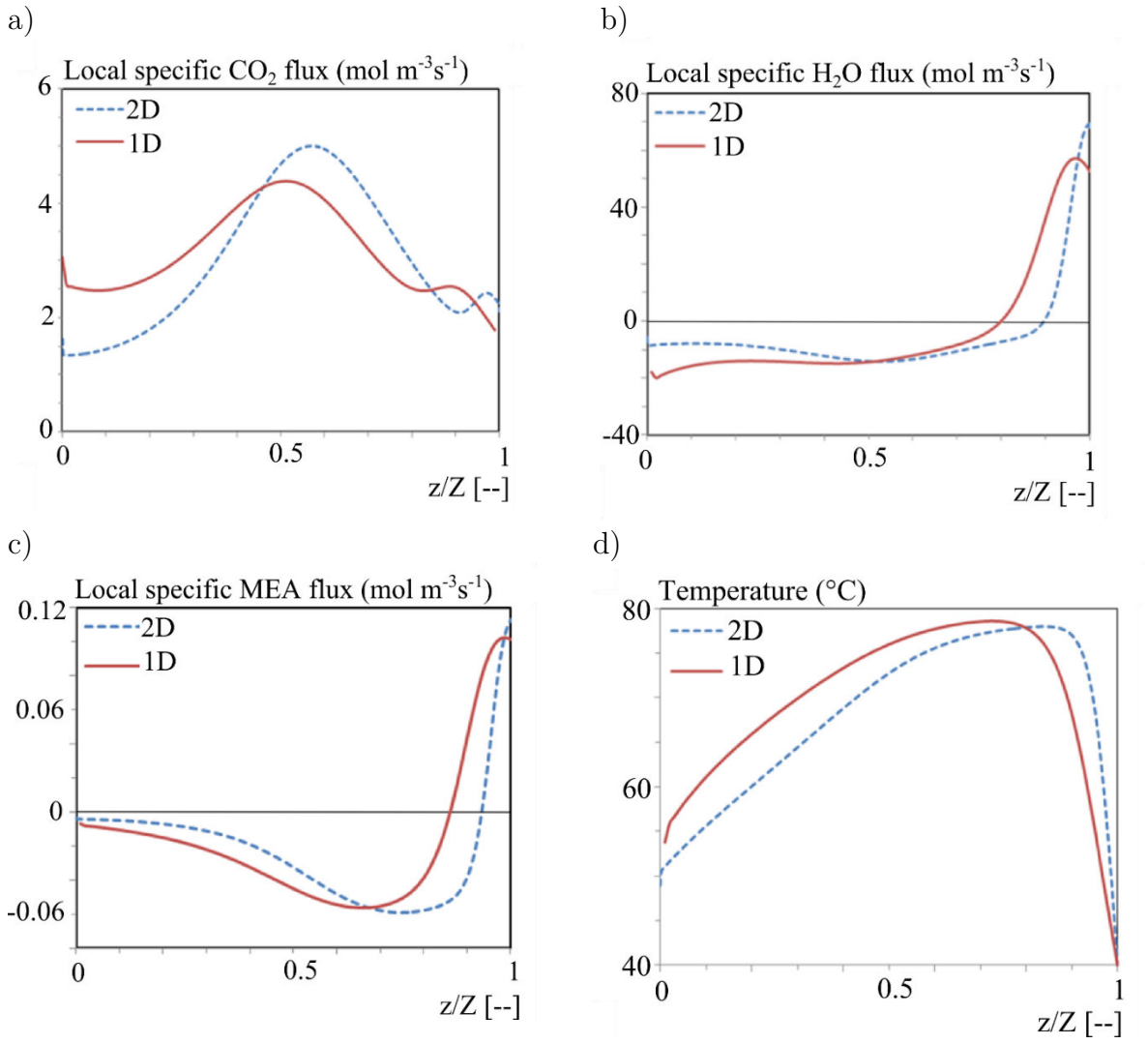

Figure 4.6 Axial profiles of trans-membrane specific flux of transferred species and temperature estimated from both 1D and 2D modelling approaches. a) CO_2, b) H_2O, c) MEA and c) Liquid temperature.

Figure 4.6d compares the liquid phase axial temperature profiles predicted by the 1D and 2D adiabatic models. The temperature shown is that of the fibre centre. As a result of the excellent radial heat transfer between the phases, virtually no radial temperature gradient exists. Both models predict that along the length of the hollow fibre, the temperature profile passes through a maximum temperature of approximately 80°C near the

liquid inlet. In fact, the liquid is warmed up near the liquid inlet by the water condensation and is then cooled by the water evaporation [67]. Compared to the 2D model, the 1D temperature profile passes through its maximum further away from the liquid inlet. Furthermore, the outlet temperature of the liquid phase predicted by the 2D model shows a cooler temperature than that of the 1D model, approximately 50 ^{o}C and 55 ^{o}C, respectively.

It should be noted that, as illustrated in Section 4.2, the temperature peak value is comparable to that measured in packed beds when using similar boundary conditions and CO_2 capture ratios. This is related to the fact that the systems, developing counter-current plug flow, are very similar in nature.

Average specific trans-membrane fluxes

Erreur ! Source du renvoi introuvable. shows the averaged trans-membrane molar fluxes per unit contactor volume for CO_2, water and MEA. Even if the profiles for the specific flux of CO_2 and water do not exactly correspond, they lead to comparable values for the average specific flux with relative differences lower than 3%. No further information was obtained using the 2D approach in terms of CO_2 capture ratio. Moreover, estimations of the amount of transferred water from the solvent to the gas were similar for both models. However, MEA fluxes across the membrane differed. The 1D model under predicted MEA losses in the absorption unit with a relative difference of 20%. Given that the MEA is a relatively non-volatile solvent, this difference must be considered when using more volatile solvents, e.g. NH_3.

Table 4-7 Averaged specific fluxes estimated from both 1D and 2D approaches

	1D Specific flux ($molm^{-3}s^{-1}$)	2D Specific flux ($molm^{-3}s^{-1}$)	Relative difference (%)
CO_2	3.13	3.04	2.96
H_2O	- 3.50	- 3.60	-2.78
MEA	$-1.76x10^{-2}$	$-2.20x10^{-2}$	-20.0

Solvent loss is important to consider in terms of running costs and contactor performance, especially for long periods of continuous operation. The predicted MEA concentrations in the outlet gas were 1.4 and 2.1 g/Nm^3, from the 1D and 2D models respectively. Both values far exceeded the maximum limit for the design of post-combustion CO_2 capture plants (i.e. 12 mg/Nm^3 for MEA) [110]. In addition, water losses were significant. For illustration purposes, considering solely the absorption operation unit, the total solvent losses would be of about 0.5 ton H_2O and 4.6 kg of MEA per ton of CO_2 captured. For a model coal power plant of 500 MW including carbon capture, these

outputs would correspond to losses of around 5000 tons of water and 50 tons of MEA per day. Therefore, in practical terms, a scrubbing section following the HFMC would be required for solvent recovery. This issue represents an opportunity for possible advances in membrane contactor technology. Indeed, a dense-film composite membrane, being selective to the MEA, would reduce the amine vapour outflow. Just such a study is however beyond the scope of this present work.

4.4.4. Comparison of Experimental and Simulation Results

Both models were compared against experimental data to identify the most appropriate model. The compared variables of simulation results are the CO_2 capture ratio and the liquid outlet temperature. These variables are of particular interest because they provide important information, such as process intensification factors and increasing solvent temperatures, which are essential to performing process energy consumption calculations.

The experimental data were taken from the EnergiCapt project, funded by the ANR (Agence Nationale de la Recherche) grant Energicapt. The small pilot plant consists of a 10 m^2 exchange-surface HFMC in which the aqueous solution, approximately 30% wt. of MEA, was fed in the lumen, whereas the flue gas from a natural gas power plant, a mixture of 10% of CO_2 and water saturated air, flowed through the shell in a counter-current arrangement. As a result of the liquid-to-gas ratio fixed during the experiments, relatively low MEA conversions were obtained, i.e. lower than 0.6. In addition, it should be noted that for a total of 11 experiments, 10 were performed using fresh solvent. Despite the use of real flue gases and an important exchange area, these conditions are still far from actual industrial conditions.

The membrane contactor had been previously used intermittently over several months. The $k_{M,CO2}^{eq}$ value was set to $5 \cdot 10^{-4}$ m s^{-1}, as found in Section 4.1. The contactor features and operating conditions are presented in the same section.

Figure 4.7a and 4-7b depict parity plots between experiments and simulations of the CO_2 capture ratio and the liquid outlet temperature respectively. Simulation results of both the 1D and 2D models are also shown. From Figure 4.7a, it can be seen that both models predicted the CO_2 capture ratio within an agreement of 10% for respective experiments. Moreover, simulation results for the 1D and the 2D approaches can almost be superimposed.

Figure 4.7b demonstrates the non-isothermal nature of the process, as the solvent is shown to be heated to at least 18 K. The 2D model estimates a solvent warming of at least 30 K, whereas the warming estimated in the 1D model is significantly lower. Even though, the predicted capture ratios of the 1D and the 2D models are close. It seems, as

though the average volumetric absorption flux was not very sensitive to the liquid outlet temperature, as multiple compensations are likely to occur over the contactor length. The experimental temperature increase is in-between. The temperature variation is closely related to the trans-membrane water transfer. The important temperature increase shows that the understanding of the latter is crucial and needs to be improved

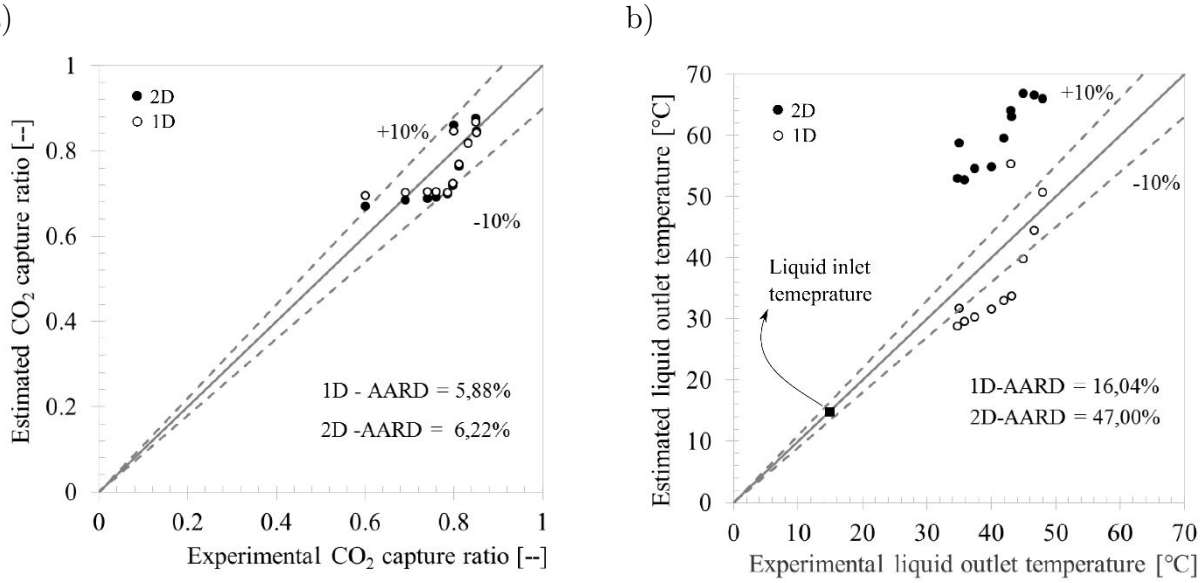

Figure 4.7 Comparison of simulation results and experimental data taken from EnergiCapt project. a) CO_2 capture ratio b) Liquid outlet temperature. $k_{M,CO2}^{eq} = 5x10^{-4}$ ms^{-1}.

4.5. Influence of Axial Distribution of the Membrane Mass-transfer Coefficient

The previous simulations were performed assuming an equivalent membrane mass-transfer coefficient, $k_{M,CO2}^{eq}$, which is constant over the contactor length. However, membrane wetting may occur, leading to an axial distribution. Indeed, liquid breakthrough and capillary condensation are likely to occur in the vicinity of the liquid inlet due to, respectively, the increase of transmembrane pressure (P_L - P_G), and water condensation. This section aims to investigate the influence of the distribution of the membrane mass-transfer coefficient on simulation results. The estimation of membrane wetting due to liquid breakthrough and capillary condensation is extremely complex, as it depends on many parameters unknown in industrial conditions, such as, for example, the pore size geometry and distribution and the membrane-liquid contact angle.

Nevertheless, in order to make a first guess about the influence of an axial distribution of the membrane mass-transfer coefficient on the overall process performance, a simple distribution was set, as shown in Equation 4.2:

$$k_{M,i} = k_{M,CO_2}^{eq}[1 + \beta(1 - 2 * z/Z)]\frac{D_{i,G}}{D_{CO_2,G}{}^{ref}} \quad (4.2)$$

where β stands for the deviation from the equivalent membrane mass-transfer coefficient. Simulations were performed with the 1D model using conditions shown in Table 4-6, however by setting a gas pressure drop of 50 mbar and a CO_2 capture ratio of 0.9, obtained by the 1D approach.

Figure 4.8a and 4.8b illustrate respectively the variation of the membrane mass-transfer coefficient (estimation using Equation 4.2) and the liquid temperature with the contactor length. Two scenarios are presented. The base case with nearly uniform distribution, β =0, and the case in which membrane wetting leads to a deviation of 90% from the average value, β =0.9. In the latter, as shown in Figure 4.8a, one part of the module exhibits high mass-transfer coefficients ($k_{M,CO2} > 10^{-3}$ ms^{-1} for z/Z < 0,5) standing for almost totally dry membranes, whereas the other part exhibits much lower mass-transfer coefficients ($k_{M,CO2} = 10^{-4}$ ms^{-1} for z/Z=1) standing for partially wetted membranes.

Figure 4.8b shows that the values of the liquid temperature peaks obtained for both, almost uniform and non-uniform distribution of $k_{M,CO2}$, are shown to be very close. However, in the non-uniform distribution, the peak is shifted to the module zone with higher membrane mass-transfer coefficients. Indeed, since the transfer through the membrane has been deteriorated in the zone near the liquid inlet, the condensation zone is extended.

a) b)

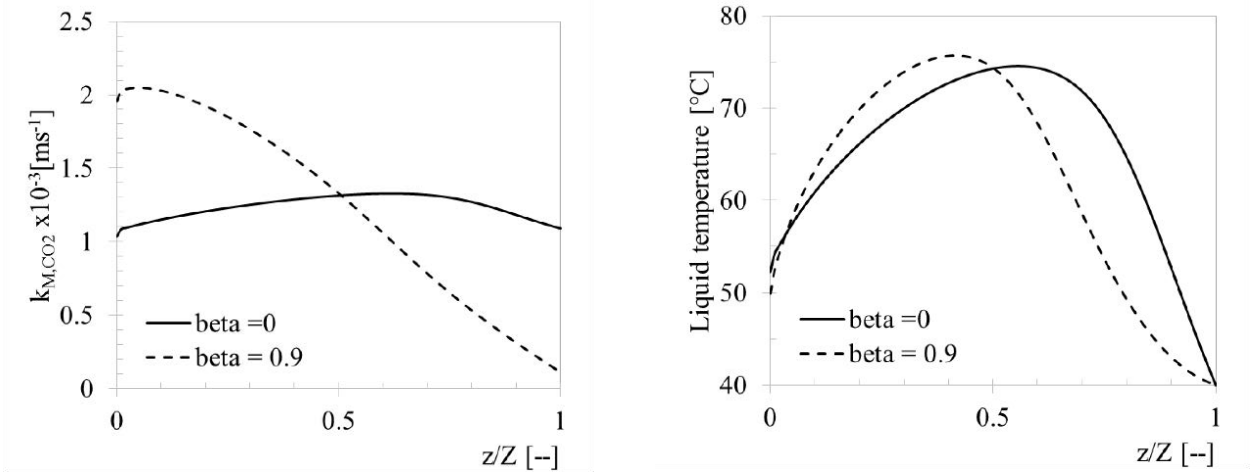

Figure 4.8 Axial profiles obtained using the 1D model; CO_2 capture ratio of 0.9; gas pressure drop of 50 mbar; $k_{M,CO2}^{eq} = 10^{-3}$ ms^{-1} with a distribution given by Equation 4.2 ; a) membrane mass-transfer coefficient ; b) liquid temperature

Figure 4.9 illustrates the variation of the average CO_2 specific absorbed flux with the equivalent membrane mass-transfer coefficient for the two scenarios β =0 and β =0.9.

The reduction of the equivalent membrane mass-transfer coefficient by one order of magnitude significantly impacts the contactor performance. Moreover, the non-uniform distribution of $k_{M,CO2}$ decreases the average performance of the module. However, the deviation from the base case is less than 15% which is of the same order of experimental uncertainty (i.e. about 10 %). Hence, the use of an average equivalent membrane mass-transfer coefficient appears to be adequate for modelling of the membrane contactor.

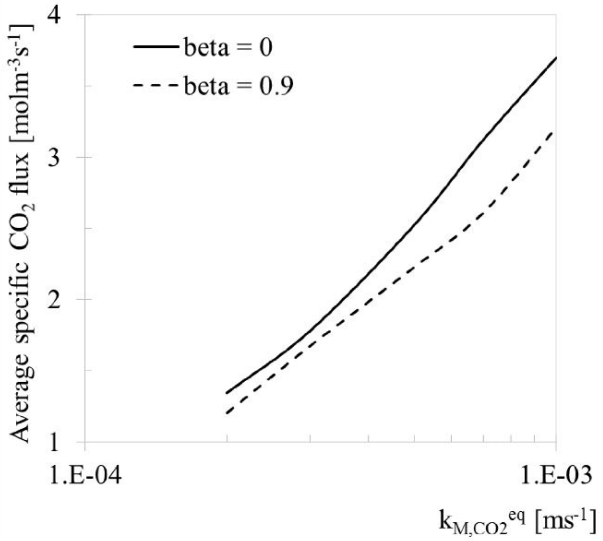

Figure 4.9 Influence of the mass-transfer coefficient of the membrane on the average CO_2 specific absorbed flux, applying a local distribution of $k_{M,CO2}^{eq}$. CO_2 capture ratio of 0.9 and gas pressure drop of 50 mbar.

4.6. Flow Configuration Analysis

One of the advantages of hollow fibre membrane contactors is their ability to handle different flow configurations due to the physical separation, represented by the membrane, between the gas and the liquid phases. Counter-current as well as co-current flow arrangements are easily obtainable. In addition, the gases may flow through the outside of the fibres (or *in-shell*) or through the inside of the fibres (or *in-lumen*). Indeed, depending on the geometric characteristics of the module, the difference between the inner and outer membrane specific areas can be significant. Since the intensification potential of HFMC is mainly related to the specific interfacial area, the contactor performances estimated for both, *in-shell* and *in-lumen* configurations, are expected to be different.

Both flow-configurations, i.e. co-current and gas in-lumen, are investigated and the pertinence of their application for PCC is discussed in the following subsections.

4.6.1. Co-current Flow Arrangement

The treatment of post-combustion flue gases imposes low gas pressure drops, in order to prevent a potential energy penalty in compression, but not so low as to jeopardize the gas distribution in the module. Therefore, a gas pressure drop is unavoidable and, since liquid breakthrough may occur at a given transmembrane pressure (i.e. $\Delta P_{L\text{-}G} > \Delta P_{break}$), the way in which this pressure drop is distributed along the contactor could ideally help to prevent membrane wetting.

Moreover, due to the exothermic nature of the absorption, the temperature peak obtained for the co-current arrangement is expected to be lower than that calculated for the counter-current arrangement. In order to illustrate this situation, simulations under operating conditions similar to those shown in Table 4-6 were performed for both configurations and the results are presented in Figure 4.10. The liquid temperature profile illustrated in Figure 4.10a shows that the temperature peak corresponding to the co-current arrangement is of 20 °C less than that obtained using counter-current flow. Indeed, as illustrated in Figure 4.10b, there is no water reversal flux, or water condensation, in co-current flow and thus, all the released energy of the CO_2 absorption is employed for water evaporation and to warm up the liquid. This is actually advantageous as there is no risk of capillary condensation, thus reducing the possibility of membrane wetting. In terms of intensification potential, both configurations have shown average CO_2 transmembrane flux values of about 4 $molm^{-3}s^{-1}$.

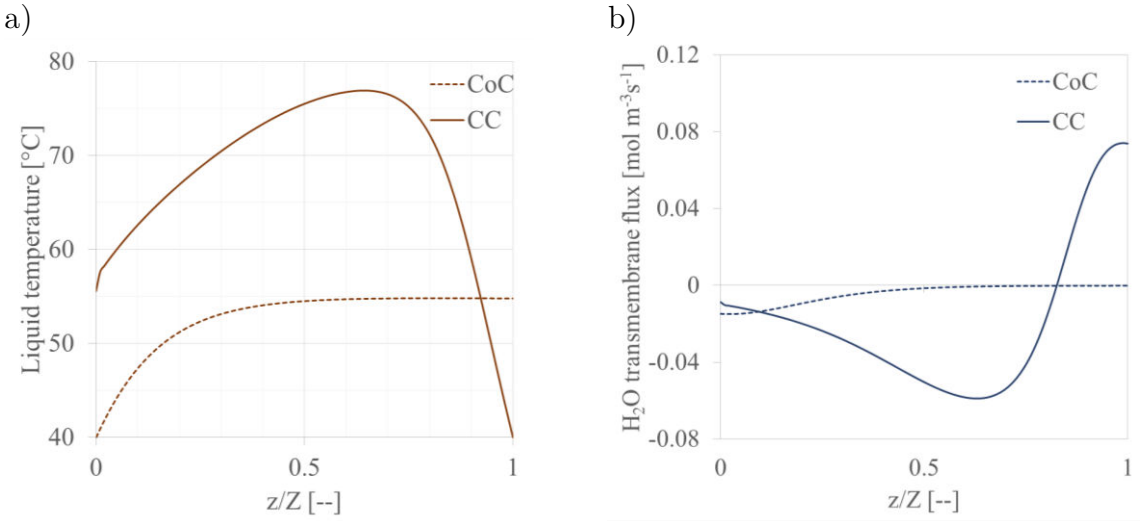

Figure 4.10 Axial profiles for both counter-current and co-current flow arrangement setting MEA conversion of 0.95 and 0.67, respectively. CO_2 capture ratio of 0.9. $\alpha^{lean} = 0.242$ $mol_{CO2}mol_{MEA}^{-1}$. $w_{MEA} = 30\%$ wt. $T_L^{in} = T_G^{in} = 40°C$. $y_{CO2}^{in} = 0.15$. $P_G^{in} = 1.05$ bar. $r_e = 200$ µm. $\delta/r_e = 0.2$. $\varphi = 0.6$. $k_{M,CO2}^{eq} = 10^{-3}$ ms^{-1}. a) Liquid temperature, b) Water transmembrane flux

The co-current flow arrangement, however, is limited by the thermodynamics. Therefore, in order to achieve the desired CO_2 capture ratio, a MEA conversion of 0.7 needed to be set. This implies the use of higher liquid flow rates. In order to identify the maximal CO_2 capture ratio that could be obtained by setting a co-current flow, simulations were performed for gas inlet conditions identical to those presented in Table 4-6 and for different lean liquid loadings. In Figure 4.11 the results of these simulations are plotted over the MEA conversion, and in Figure 4.12 over the liquid inlet temperature. It can be seen that in order to achieve a CO_2 capture ratio specification of 0.9, the MEA conversion must be set to values between 0.67 and 0.74. The influence of the lean liquid loading is not significant. This specification cannot be achieved by cooling the lean liquid absorbent before the absorption step.

The modification of the operating conditions in the absorption step will change the heat duty of the liquid absorbent regeneration step. Indeed, for the system MEA-H_2O-CO_2, low MEA conversion as well as low lean solvent loadings require high heat duties due to, respectively, the increase of liquid absorbent which needs to be warmed up, and the increase of the amount of sweep gas (i.e. water vapour which does not condense within the stripper) in order to increase the driving force in the desorption step. Therefore, even if the co-current would allow for improved functioning of the membrane contactor, for the desired CO_2 capture ratio, it would require a higher energy consumption than setting the module in a counter-current flow arrangement.

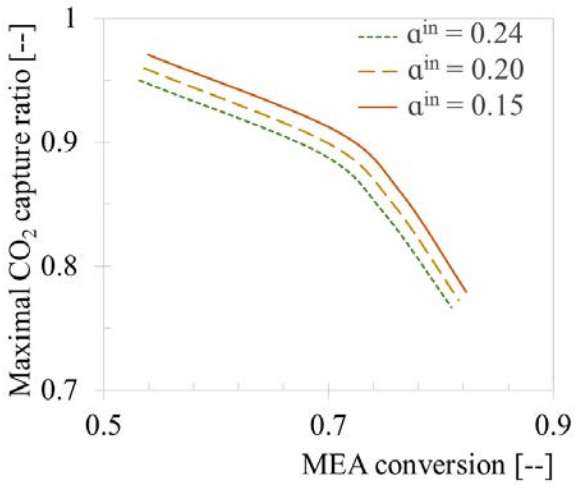

Figure 4.11 Maximal CO_2 capture ratio as a function of MEA conversion for different CO_2 lean solvent loadings. w_{MEA} = 30% wt. $T_L^{in} = T_G^{in}$ = 40°C. y_{CO2}^{in} = 0.15. P_G^{in} = 1.05 bar. r_e = 200 µm. δ/r_e = 0.2. φ=0.6. $k_{M,CO2}^{eq} = 10^{-3}$ ms^{-1}

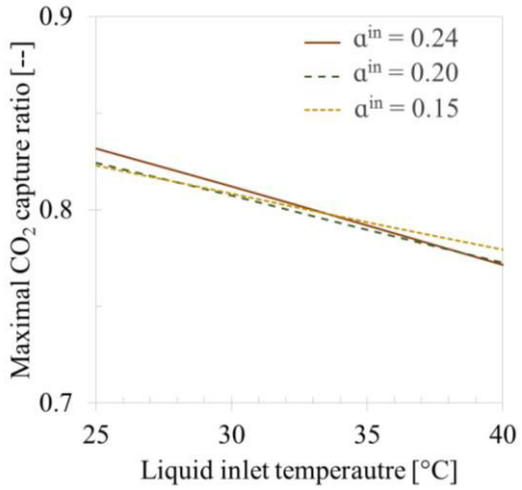

Figure 4.12 Maximal CO_2 capture ratio as a function of liquid inlet temperature for different CO_2 lean solvent loadings. MEA conversion between 0.81 and 0.84. w_{MEA} = 30% wt. y_{CO2}^{in} = 0.15. P_G^{in} = 1.05 bar. r_e = 200 µm. δ/r_e = 0.2. φ=0.6. $k_{M,CO2}^{eq} = 10^{-3}$ ms^{-1}

4.6.2. Liquid *in-shell* Flow Configuration

In order to choose the adequate flow configuration for PCC process by means of HFMC, the process design engineer must consider the following aspects:

- The pressure drop per unit of contactor length is higher in the shell, for fibre packing fractions of industrial interest, i.e. around 0.6, as illustrated in Figure 4.13.
- The content and size of ashes in the flue gases may lead to fibre plugging.
- If the membrane is asymmetric, the face having the smaller pore size must be in contact with liquid to prevent liquid breakthrough.
- The interfacial area per unit of contactor volume of the outer face of the fibres is higher than that of the inner face, as illustrated in Figure 4.14.
- The flow *in-shell* is subject to canalization issues, which increases the mass-transfer resistance (See Appendix A).

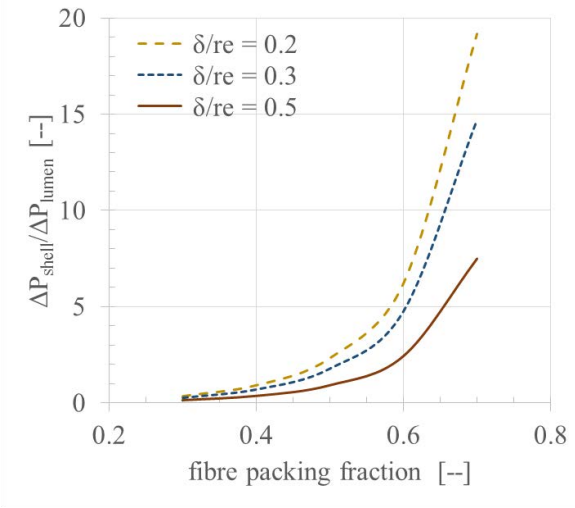

Figure 4.13 Shell and lumen pressure drop ratio as function of the fibre packing fraction

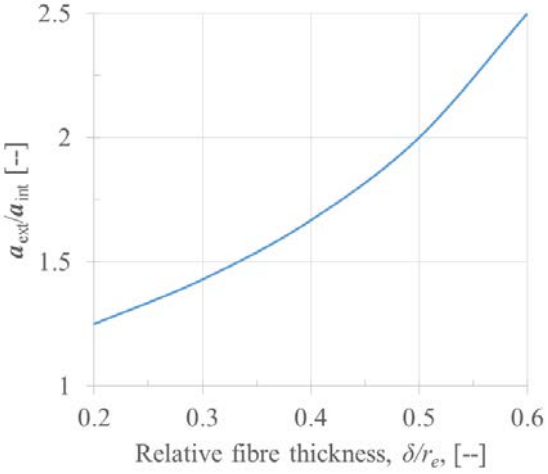

Figure 4.14 Ratio between the external and the internal specific interfacial area as function of the relative fibre thickness

The first three items are specific to the process conditions/requirements/constraints and are not discussed in this section. The last two items specifically concern the liquid phase, as it represents the principal mass-transfer resistance of the system. Large membrane surfaces in contact with the liquid would increase the contactor performance, whereas a poor mass-transfer would decrease it. However, the possibility of adding baffles in the shell side in order to create mixing points, would improve the mass-transfer and therefore, it could be advantageous to pass the liquid through the shell.

The influence of passing the liquid through the shell with and without mixing points has been investigated by Hoff and Svendsen [78]. They concluded that a significant absorption rate enhancement can be achieved by using this mode flow and mixing points, as this results in a significantly improved transfer of the reaction products. However, this study was performed under very different conditions than those in an industrial context.

In this section, the influence of the liquid *in-shell* mode flow, with and without mixing points, on the contactor performance is studied under industrial operating conditions, shown in Section 4.1. This is performed by simulating the process using the 1D modelling approach detailed in Section 4.1.

The liquid *in-shell* and *in-lumen* flow modes are illustrated in Figure 4.15. In order to simulate the baffles in terms of mass-transfer, the liquid Graetz numbers are reset to their inlet value at every baffle location. By doing this, a perfect mixing in the shell at the corresponding baffle location is assumed. In this theoretical investigation, the baffles are located every 1 cm. It is worth mentioning that for the operating conditions imposed in Section 4.1, the liquid Graetz numbers were sufficiently low to attain the limiting Sherwood values, i.e. $Sh_{i,L} = 4.3$. By contrast, for the case where mixing points were introduced, the Sherwood values of liquid phase were comprised between 9 and 4.3, every 1 cm. The hydrodynamic consequences of the presence of baffles were not taken into account.

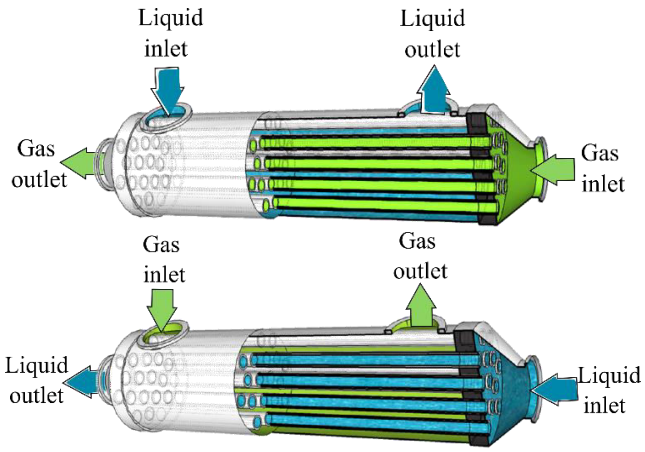

Figure 4.15 Liquid in-lumen (top) and liquid in-shell (bottom) flow configurations of HFMC

The average CO_2 absorbed flux per unit of contactor volume as a function of the external fibre radius is illustrated in Figure 4.16, for the two flow modes, i.e. liquid in-lumen and liquid in-shell with and without mixing points. The increase of the contactor performance by switching the operating mode from liquid in-lumen to in-shell can be appreciated. This improvement is due to the increase of the membrane area in contact with the liquid, as shown in Figure 4.14, which for the simulated cases was of 25% with respect to the inner surface. The increase of the contactor performance obtained by the introduction of mixing points is of about 20%. This improvement is attributed to the enhancement of the reactant diffusion, i.e. CO_2 and MEA. Indeed, due to the MEA depletion imposed by the low liquid-to-gas flow rate ratio, there is a zone of the module in which the reaction between CO_2 and MEA is limited by the supply of reactant [48].

It should be mentioned that the liquid pressure drop changes from 15 to 90 mbar as a consequence of the flow mode. This is expected to be more significant when introducing the baffles. In addition to increasing the energy penalty by liquid pumping, the increase of the liquid pressure drop increases the probability of membrane wetting caused by liquid breakthrough (see Section 1.2.4).

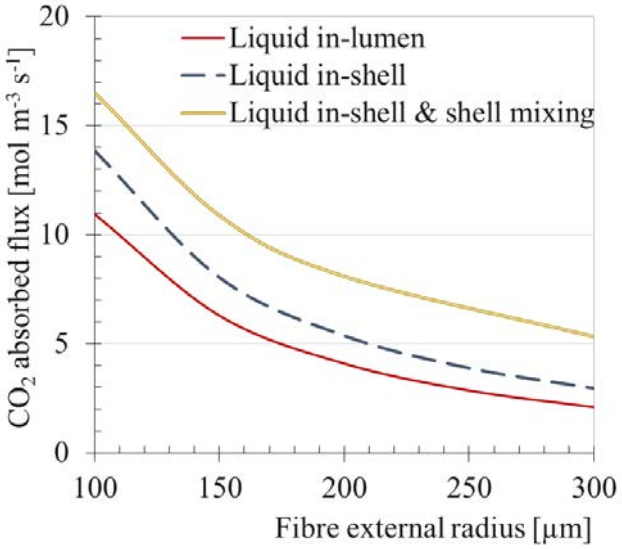

Figure 4.16 Variation of the average CO_2 absorbed flux per unit volume of contactor with the external fibre radius, for different flow configurations. δ/r_e=0.2, φ = 0.6 $k_{M,CO2}^{eq} = 10^3 ms^{-1}$.

4.8. Summary and Conclusions

The adiabatic multicomponent modelling of HFMC for PCC was detailed in this chapter. This approach was verified by means of the modelling and simulation of the CO_2 chemical absorption using packed columns. The corresponding simulations were in excellent agreement with experimental data from a pilot plant under industrial operating conditions. The 1D and 2D approaches were compared under mild and severe operating conditions in which the two models led to comparable transmembrane specific fluxes. Under severe conditions, the intensification factor computed in adiabatic modelling is significantly lower than that computed in isothermal modelling. The adiabatic multicomponent approach allowed to highlight that solvent transmembrane flux reversal occurs inside the module (i.e. evaporation and condensation), leading to significant temperature peaks. In addition, the operating conditions in which membrane wetting may occur by liquid breakthrough and by condensation in membrane's microporous support, were identified. Based on 1D simulations, the diluted species (or its equivalent equimolar flow) mass-transfer formulation is sufficient to predict contactor performances. Simulations indicate that membrane wetting can be simulated conveniently, using an average equivalent membrane mass-transfer coefficient rather than local values.

The co-current flow arrangement lead to several advantages in terms of the functioning of HFMC, however, in order to achieve a CO_2 capture ratio of 0.9, the entire CO_2 capture process would consume more energy. Passing the liquid through the shell could enhance the performance of the module in terms of mass-transfer, however this could potentially jeopardize the functioning of the device.

4.9. Résumé et conclusions

La modélisation adiabatique et multi-constituante des CMFC pour le PCC a été décrite La modélisation adiabatique et multi-constituante des CMFC pour le captage du CO2 en postcombustion est décrite dans ce chapitre. Dans un premier temps, la modélisation et la simulation de l'absorption chimique du CO_2 dans des colonnes à garnissage a permis une vérification de cette approche. En effet, les résultats des simulations de l'opération d'absorption dans les colonnes à garnissage sont en excellent accord avec les données expérimentales obtenues dans des conditions d'intérêt industriel. Les approches monodimensionnelles et bidimensionnelles pour la modélisation des CMFC ont été comparées pour des conditions opératoires modérées et sévères. Dans les deux types de conditions, les deux approches ont montré des flux transmembranaires très proches. Dans les conditions opératoires sévères, la modélisation en isotherme surestime la performance du procédé. L'approche adiabatique et multi-constituante a mis en évidence l'apparition de deux zones d'évaporation et de condensation du solvant, conduisant à d'importants pics

de température au sein du contacteur. De plus, grâce à ce type d'approche, il a été possible d'identifier les conditions opératoires dans lesquelles le mouillage des membranes, lié à une percée du liquide ou à une condensation capillaire, est susceptible de se produire. Les résultats de simulation en monodimensionnel ont permis de montré que le modèle d'espèces diluées, servant à estimer le transfert de matière à travers la membrane, est satisfaisant pour prédire les performances des contacteurs membranaires. De plus, le mouillage des membranes peut être simulé d'une façon satisfaisante par l'utilisation d'un coefficient moyen équivalent de transfert de matière de la membrane, plutôt que par l'utilisation de valeurs locales.

Le mode d'écoulement en co-courant rapporte plusieurs avantages en termes de fonctionnement des contacteurs membranaires, cependant, le captage du CO_2 serait plus énergivore pour le même taux de capture, i.e. 90%. L'écoulement de la phase liquide à travers la calandre (i.e. à l'extérieur des fibres) pourrait améliorer le transfert de matière des espèces en revanche, ce mode pourrait compromettre le fonctionnement du contacteur.

Chapter 5. Interest of Membrane Contactors for CO_2 Stripping

The stripping phase, or liquid absorbent regeneration, is the step in the process where the CO_2 captured in the absorption step is then stripped from the liquid absorbent. The driving force behind this operation is, as it is for absorption, the chemical potential difference between the gas and the liquid. This can be generated through decreasing CO_2 solubility by increasing liquid temperature, or/and through reducing the gas CO_2 partial pressure by vacuum or by using a sweep gas with low CO_2 content. Since the regeneration process is highly endothermic, in adiabatic steady state a system temperature drop may occur, thus affecting the driving force. Therefore, energy as well as counter-current plug flow during the stripping step are essential to obtain good process performances.

Contrary to one- or two-stages flash separators, counter-current gas-liquid contactors, such as packed columns, are the conventional technology to perform the stripping since they can offer driving force distributions. Moreover, when employing water vapour as sweep gas, good energy distributions can be reached, as the latent heat of its condensation provides the energy for desorption. Additionally, after stripping, CO_2 can be easily separated from water vapour in a condenser at mild conditions. Therefore, the regeneration process is industrially performed using packed columns with a sweep gas generated by a partial evaporation of the liquid absorbent at high temperature (e.g. 120°C), as described in Section 1.1.3.

Due to the ease of flow mode handling, i.e. co-current, counter-current or cross-flow, and to the huge interfacial area offered, the HFMC technology can deliver driving force distributions as good as in packed columns, with the advantage of process intensification.

The number of studies dedicated to the stripping of CO_2 using hollow fibre membrane contactors has increased over the last five years. Using modelling techniques and/or experimental setups, solely the low temperature liquid absorbent regeneration boosted by vacuum or by the use of non-condensable sweep gases, such as nitrogen, has been investigated. Indeed, HFMC technology is difficult to implement as choices for suitable membrane materials that can withstand high temperatures are limited. On the other hand, to our knowledge, the stripping section using HFMC under industrial operating conditions has not been addressed in the literature (see Section 1.2.5).

In this chapter, both low- and high-temperature stripping techniques by means of membrane contactors are studied by modelling and simulation, applying industrial conditions. These techniques are compared to the conventional process performed using packed columns. The latter is also modelled and simulated in order to obtain an accurate comparison between the three stripping processes.

5.1. Stripping using Packed Columns

The stripping process using packed columns corresponds to a high temperature stripping technique. Contrary to the absorption step, where the section is solely constituted by the gas-liquid contactor, the stripping step is constituted by a whole set of unit operations, as illustrated in Figure 5.1. The mixers, the heat exchanger, the condenser and the reboiler are calculated as described in Section 2.5. The packed column was modelled using the equations shown in Table 4-1. Nevertheless, since the operation is performed at high temperature, the chemical reactions are assumed to be at chemical equilibrium. The pre-condenser consists in an extra packed bed placed at the top of the column and it should be modelled as such. However, in order to reduce calculation time, it was simulated as a one-stage unit-operation at thermodynamic equilibrium by using a mixer followed by a flash separator. The results of modelling this operation using a packed bed indicated that this assumption was adequate.

The numerical scheme used to solve the process flowsheet is based on a successive substitution method and is presented in Table 5-1. Global mass and energy balances were calculated in order to verify the simulation results.

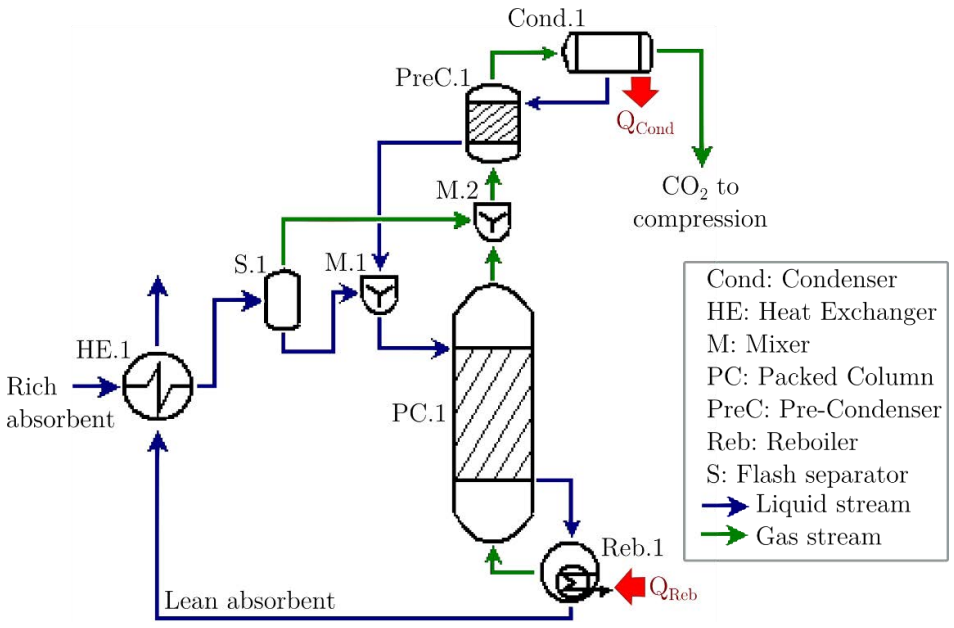

Figure 5.1 Simulation flowsheet of the stripping section for high temperature stripping

Table 5-1 Algorithm of resolution of stripping section (shown in Figure 5.1)

Select: Q_{Reb}
! Initialise $l_i^{in}{}_{Reb.1}{}^{(0)}$ & $T^{in}{}_{Reb.1}{}^{(0)}$ | k=0
External loop: Packed column - Reboiler
k= k+1
Solve Reb.1, print: *lean solvent loading*
Solve HE.1
Solve S.1
Solve PC.1, print: $l_i^{in}{}_{Reb.1}{}^{(k)}$ & $T^{in}{}_{Reb.1}{}^{(k)}$
Solve M.2
! Initialise $g_i^{in}{}_{Cond.1}{}^{(0)}$ & $T^{in}{}_{Cond.1}{}^{(0)}$ | kk=0
    Internal loop: Condenser - Pre-condenser
    kk=kk+1
    Solve Cond.1, print: $g_i^{in}{}_{Cond.1}{}^{(kk)}$ & $T^{in}{}_{Cond.1}{}^{(kk)}$
    Solve PreC.1
    If $||g_i^{in}{}_{Cond.1}{}^{(kk+1)} - g_i^{in}{}_{Cond.1}{}^{(kk)}||<10^{-6}$ **then** exit internal loop
    End internal loop
Solve M.1
If $|| \ l_i^{in}{}_{Reb.1}{}^{(k+1)} - l_i^{in}{}_{Reb.1}{}^{(k)}||<10^{-6}$ **then** exit external loop
End external loop
Save results

5.1.1. Model Validation

The tests performed in the CASTOR campaign at the Esbjerg pilot plant were simulated [103]. The operating conditions are shown in

Table 5-2. In this campaign, the liquid absorbent was partially regenerated, which corresponded to regeneration factors of about 0.5 as calculated using Equation 5.1. Moreover, the influence of the absolute pressure of the reboiler on the process energy consumption, i.e. reboiler heat duty per ton of CO_2 captured, was investigated. Indeed, for the MEA-CO_2-H_2O system, the increase of this pressure decreases the amount of the energy requirements [76]. It should be noted that reducing the stripping pressure involves a reduction of the operating temperature. The absorber column of 10 m height and a diameter of 1.1 m, is filled with IMPT-50 packing.

$$RF = 1 - \frac{lean\ liquid\ loading}{rich\ liquid\ loading} \tag{5.1}$$

Table 5-2 Operating conditions of the CASTOR campaign from the Esbjerg pilot plant [103]

RUN	Q_L [m3/h]	w_{MEA} [wt.]	α^{in} $[\frac{mol_{CO_2}}{mol_{MEA}}]$	α^{out} $[\frac{mol_{CO_2}}{mol_{MEA}}]$	RF [--]	P_{strip} [bara]	Q_{reb} [GJ/ton$_{CO2}$]
1A	22.9	0.323	0.275	0.45	0.40	1.85	3.9
1B	18.9	0.33	0.249	0.46	0.45	1.85	3.75
1C	16.6	0.324	0.224	0.47	0.53	1.85	3.73
2A	15.4	0.322	0.192	0.46	0.58	1.85	4
2B	15.4	0.322	0.223	0.46	0.52	1.85	3.9
3A	15.4	0.317	0.209	0.46	0.54	2.19	3.74
3B	14.9	0.311	0.207	0.47	0.55	1.86	3.8
3C	16.9	0.31	0.224	0.46	0.52	1.5	4
Optimal	18	0.3	0.225	0.48	0.54	2	3.75

Comparison between experimental data and simulation results:

The comparison between simulations and experiments are illustrated in Figure 5.2. The model correctly predicts the temperature profiles, as shown in Figure 5.2a. The temperature variation in the stripper is not as high as in the absorber, therefore one could assume that the operation is isothermal. Nevertheless, thermal balances and heat transfer calculations are necessary to estimate the water condensation, which is essential for the functioning of the stripper. Furthermore, as shown in Figure 5.2b, the stripper step performances are predicted within an uncertainty of about 15% which is higher than that of the absorber step. This fact has been similarly obtained in several modelling studies for the stripping section [76], [77], [79]. Indeed, the regeneration step carries many sources of uncertainties associated with experimental uncertainties, unknown reaction kinetics and few experimental data of liquid-vapour equilibria at high temperatures.

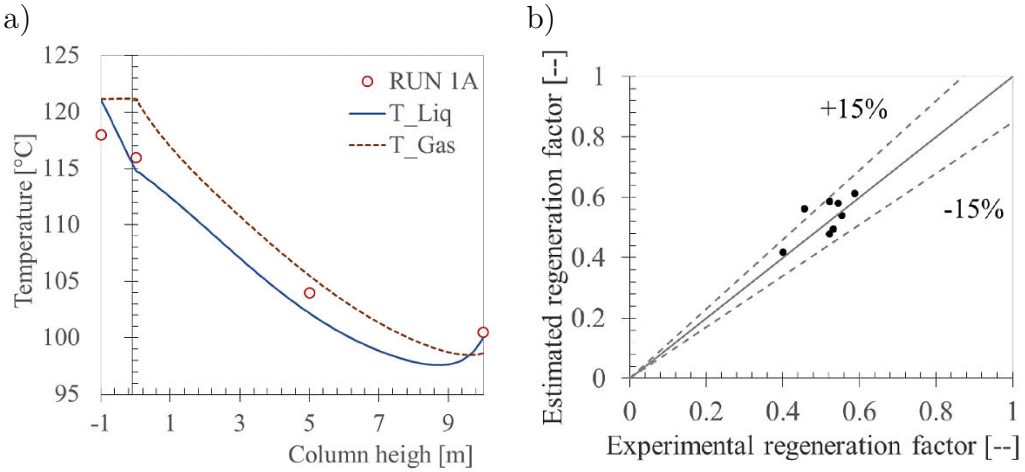

Figure 5.2 Validation of the stripping section simulation of the Esbjerg pilot plant. Solid and dotted lines: model predictions. Dots: experimental data. a) Temperature profile of the stripper for the Run 1A, b) parity plot of regeneration factor for the CASTOR campaign

5.1.2. Simulation Results of the Energetic Optimum

Depending on the absolute pressure exerted in the reboiler, an energetic minimum can be obtained for a given CO_2 capture ratio, resulting in a lean solvent loading and a regeneration factor to be set. The corresponding operating conditions of the Esbjerg pilot plant functioning at its energetic minimum are shown in

Table 5-2. The resulting temperature and interfacial flux axial profiles of the stripper are illustrated in Figure 5.3. Contrary to the absorption column, the temperature variation of the stripper is monotone, as shown in Figure 5.3a, the reboiler temperature being 122.5°C. In Figure 5.3b, the positive values in the vertical axis indicate the mass-transfer from the gas to the liquid. It is observed that no water evaporation takes place inside the column and, consequently, the latent heat of water condensation is converted to CO_2 heat of desorption and to liquid sensible heat. The energy supplied to the reboiler leading to a partial evaporation of the liquid, is released over the column by the water condensation.

The stripping section was able to desorb 0.418 mole of CO_2 per unit volume of bed. The solvent losses and solvent recovery for the different equipment (i.e. column, pre-condenser, and condenser) are shown in Table 5-3. The solvent losses correspond to the water and MEA vapours which do not condense in the column. The principal MEA recovery occurs in the pre-condenser while the main water recovery happens in the condenser. The net losses correspond to the required amount of solvent to supply to the process in steady state. For illustration purposes, considering a model coal power plant of 600 MWe including carbon capture, these outputs would correspond to supplies of around 230 tons of water and 3 tons of MEA per day.

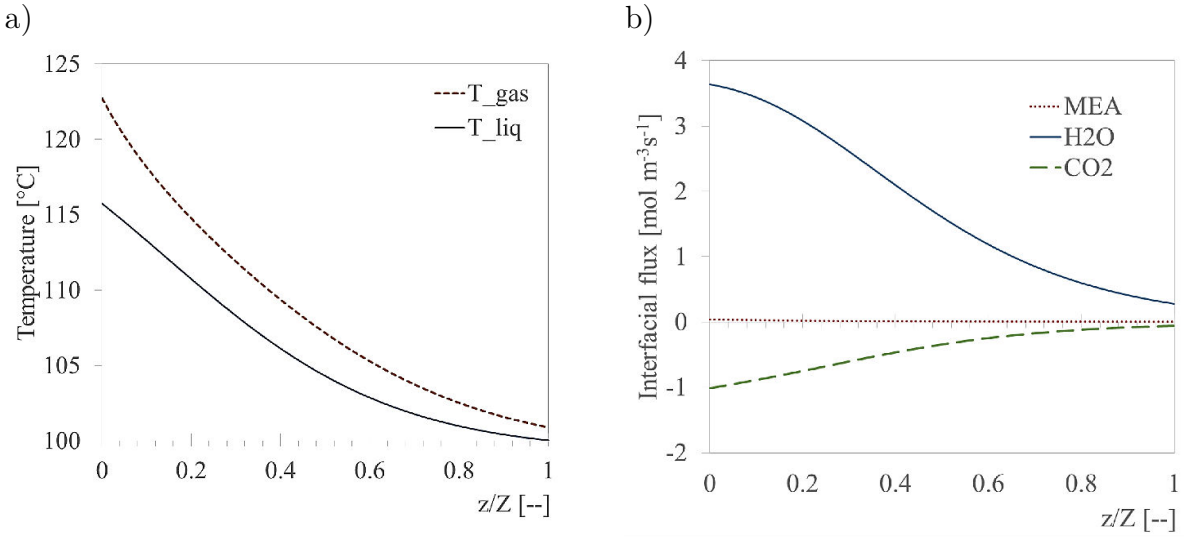

Figure 5.3 Axial profiles of the Esbjerg stripper unit at its energetic optimum, setting 2 bar of pressure. Column bottom at z/Z =0 a) Temperature, b) interfacial specific fluxes.

Table 5-3 Solvent losses and solvent recovery per operation unit using packed columns

	Solvent losses	Solvent recovery		Net loss
	Packed column	Pre-condenser	Condenser	
H_2O (ton ton_{CO2}^{-1})	0.656	0.075	0.556	0.024
MEA (kg ton_{CO2}^{-1})	1.548	1.185	0.058	0.305

5.2. High Temperature Stripping using Membrane Contactors

From a material point of view, high temperature stripping (HTS) by means of membrane contactors presents major challenges because the membranes must be temperature resistant (e.g. chemical of physical change which lead to membrane wetting). Ceramic materials have been proposed in order to implement HFMC for CO_2 stripping at high temperatures where most polymeric membranes would fail to operate [15]. New high-temperature-resistant composite-membranes, composed of poly[1-(trimethylsilyl)-1-propyne] (PTMSP), have also been suggested [111]. These membranes are, however, more expensive than the already expensive PTFE membranes, which are currently the best candidates for HFMC implementation in PCC. In addition, there is no study addressing the intensification potential of HFMC for this stripping technique.

Even if significant challenges exist, is this technology capable of reducing the size of the stripping unit using packed columns? This subsection aims to answer this question by modelling and simulating high temperature stripping using HFMC. The operating conditions in which the two technologies are compared correspond to those of the energetic optimum of the Esbjerg pilot plant, described in Section 5.1.2. The intensification factor, Equation 5.2, is used as comparator.

$$IF = \frac{Packed\ column\ volume}{HFMC\ volume} \tag{5.2}$$

5.2.1. Simulation Results of HTS

The numerical procedure to model the process using HFMC is identical to that described in Section 5.1, replacing the packed column by a membrane module. Accordingly, the liquid flow rate as well as the reboiler heat duty are both defined. Similar to that for the absorption step, the gas was fed through the shell and the liquid through the lumen in a counter-current flow arrangement. Fibres with external radiuses equal to 200 µm and with relative membrane thickness of 0.2 were simulated. The fibre packing fraction was set to 0.6, corresponding to industrial modules. The membrane mass-transfer coefficient was varied from 10^{-4} to 10^{-3} ms^{-1} to simulate dry and partially wetted membranes, respectively. The module diameter was set to 1 m to ensure gas pressure drops of less

than 300 mbar. The contactor length was therefore varied to achieve the same regeneration factor of the energetic optimum of the Esbjerg pilot plant.

Figure 5.4 illustrates the temperature and interfacial flux axial profiles of the HFMC allowing for a regeneration faction of 0.54 to be attained. The temperature profiles of the gas and liquid, shown in Figure 5.4a, are very close due to the excellent heat transfer. The specific transmembrane flux axial profiles illustrated in Figure 5.4b reveal that an important amount of water condenses at the vapour inlet section (z/Z = 0). As discussed in Section 4.1 for the absorption process, this increases the possibility of membrane wetting caused by capillary condensation.

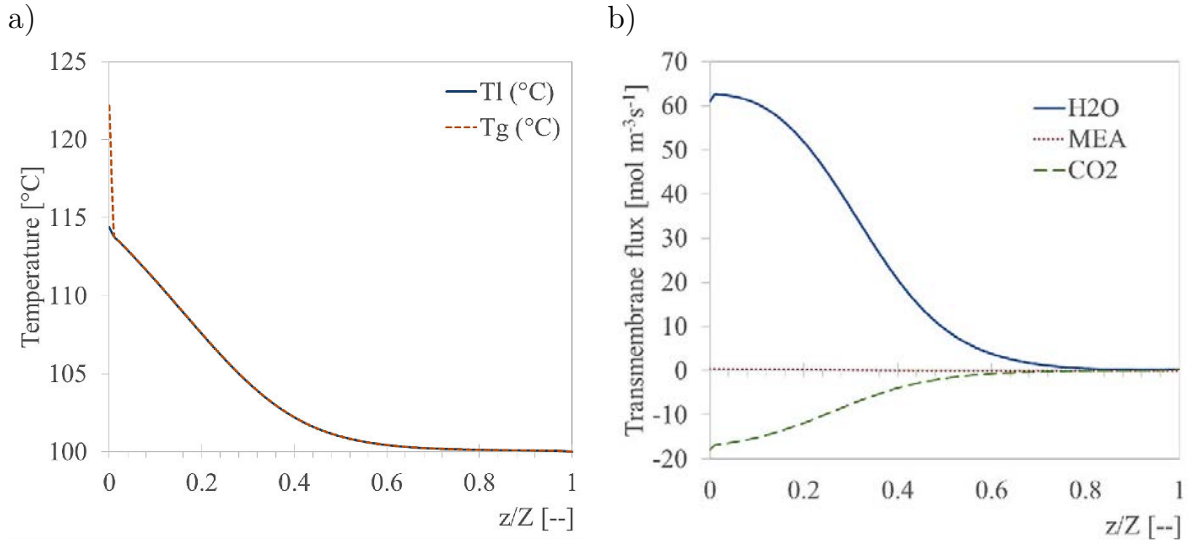

Figure 5.4 Axial profiles of Esbjerg stripper unit at its energetic optimum, setting 2 bar of pressure, using HFMC. $k_{M,CO2}^{eq} = 10^{-3}$ ms^{-1}, Z = 0.5 m. a) Temperature, b) interfacial fluxes.

The local profiles illustrated in Figure 5.4 are very similar to those obtained by employing packed columns, but do not exactly correspond. As a result, different average results were obtained. This is demonstrated by the estimation of solvent losses, shown in Table 5-4. The net losses are smaller than those calculated for packed columns. Although there is still an important amount of water loss, there is almost no MEA loss due to liquid evaporation using HFMC.

Table 5-4 Solvent losses and solvent recovery per operation unit using HFMC

	Solvent losses	Solvent recovery		Net loss
	HFMC	Pre-condenser	Condenser	
H_2O (ton ton_{CO2}^{-1})	0.698	0.081	0.604	0.014
MEA (kg ton_{CO2}^{-1})	1.347	1.285	0.063	~ 0

The axial profile of the CO_2 transmembrane specific flux for each contactor length simulated setting a membrane mass-transfer coefficient of 10^{-3} ms^{-1} are illustrated in Figure 5.5. It can be observed that for contactor lengths higher than 0.5 m, there is almost no CO_2 transmembrane flux in a significant part of the module. This means that the stripper reaches the thermodynamic equilibrium and the increase in the membrane length does not improve the separation performance.

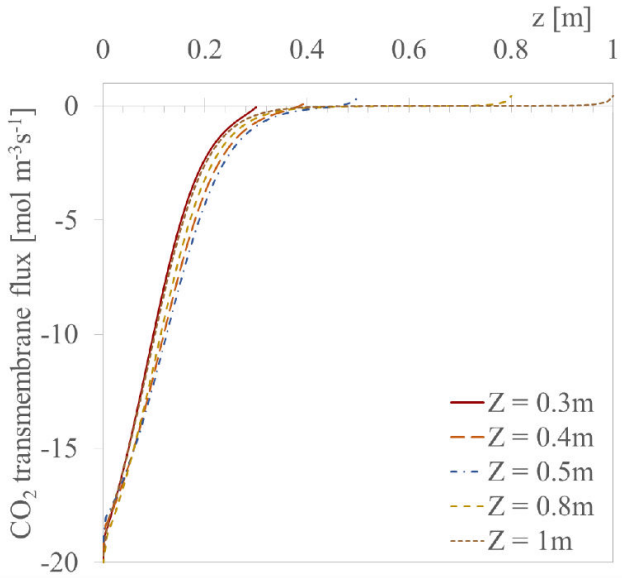

Figure 5.5 Axial profile of the CO_2 transmembrane flux for different membrane contactor lengths. $k_{M,CO2}^{eq} = 10^{-3}$ ms^{-1}

The corresponding regeneration factors as functions of intensification are plotted in Figure 5.6. The oscillatory appearance of the curves are due to the instability of the numerical method used to solve the process flowsheet (see Table 5-1). A similar numerical method has been suggested in literature, pointing out numerical stability as an issue [79]. Broyden's method, a quasi-Newton method, or an equation oriented resolution might solve this problem. However, as they demand further programming efforts, they were not implemented in this present work. Despite the oscillations, it can be observed that when the goal regeneration factor is reached, an intensification factor of about 10 can be achieved using dry membranes. But as seen in the absorption step, membrane wetting, simulated here by the decreasing of the membrane mass-transfer coefficient, appears to significantly affect HFMC intensification potential.

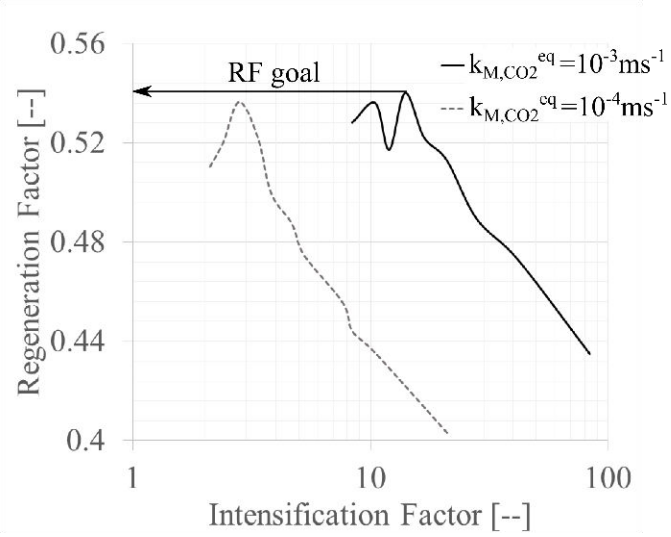

Figure 5.6 Regeneration factor as function of intensification factor for different membrane mass-transfer coefficients.

5.3. Low Temperature Stripping using Membrane Contactors

By applying vacuum on the gas-side, the driving force can be increased and therefore the operation can be performed at low temperatures. However, the amount of vapour to generate would be different than that required in the HTS. This process has been investigated in literature, but by assuming isothermal behaviour, neglecting the water transmembrane transfer and, in some cases, without any detail about the performance predictions of the membrane module [18]–[20]. This subsection intends to determine if it is worth modifying the stripping process to promote HFMC implementation.

In order to study the low temperature stripping (LTS), the stripping section of HTS has been slightly modified, as illustrated in Figure 5.7. The liquid absorbent is not partially evaporated, but instead an external water vapour stream is generated by an evaporator in vacuum conditions. In this way, the driving force is enhanced since the steam is CO_2 free. This also leads to an important reduction in the complexity of the process simulation.

The process energy consumption comprises thermal energy, i.e. heating and production of steam, and electric energy, i.e. vacuum pumping and compression to bring the CO_2 stream from vacuum to compression pressure. Hence, the two stripping techniques are compared with respect to the *equivalent work*. The latter corresponds to the electric work that would be obtained by the steam that is used to supply the thermal energy, plus the electric work of compressor and pumping.

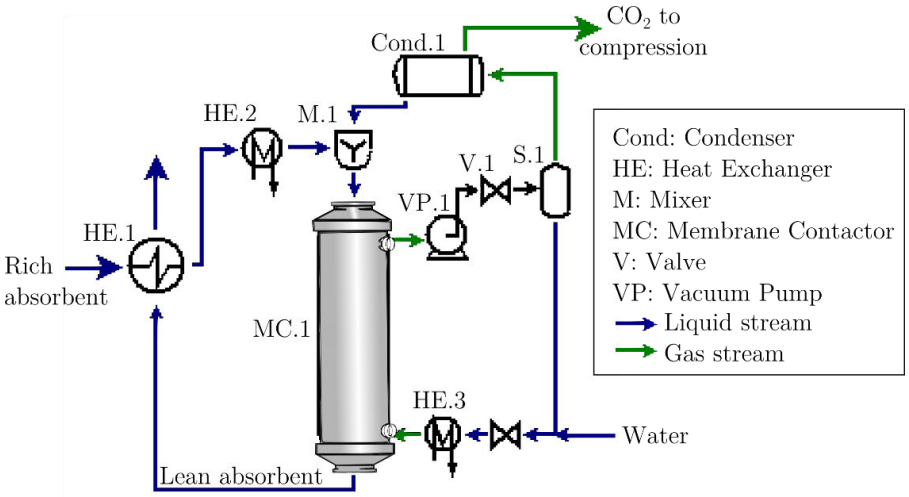

Figure 5.7 Simulation flowsheet of the stripping section for low temperature stripping

The equivalent work for the high temperature stripping is calculated using Equation 5.3:

$$W_{eq}^{HTS} = Q_{reb}\eta_{Carnot} \qquad \text{With } \eta_{Carnot} = \frac{(T_{hot}-T_{cold})}{T_{hot}} \qquad \begin{matrix} T_{hot} = T_{reb} + 10°C \\ T_{cold} = 40°C \end{matrix} \tag{5.3}$$

where η_{Carnot} stands for the Carnot thermal cycle efficiency. T_{hot} and T_{cold} correspond respectively to the temperatures of the hot and cold reservoirs.

The equivalent work of the low temperature stripping corresponds to Equation 5.4:

$$W_{eq}^{LTS} = (Q_{HE.2} + Q_{HE.3})\eta_{Carnot} + W_{vacuum} + W_{comp} \tag{5.4}$$

W_{vacuum} and W_{comp} are the electric work of the vacuum pump and the compressor, respectively. They are computed assuming the compression (or vacuum) process to be isentropic and the gases to be ideal:

$$W = \frac{GRTN\kappa}{(\kappa-1)\eta}\left[\left(\frac{P_{in}}{P_{out}}\right)^{\frac{\kappa-1}{N\kappa}} - 1\right] \tag{5.5}$$

where G stands for the gas molar flow rate, N is the number of stages of compression, κ is the heat capacity ratio and η the compression or vacuum process efficiency, set here to 0.75. P_{in} and P_{out} correspond to the pressures in the suction and exhaust port, respectively.

5.3.1. Simulation Results of LTS

The modelling approach of the stripper at low temperature is described by the equations presented in Section 4.1. Similar to the HTS, the gas was fed through the shell and the liquid through the lumen in a counter- current flow arrangement. In addition, the

same module geometric characteristics has been simulated, except for the contactor diameter which in this case is set to 2 m to ensure gas pressure drops of less than 300 mbar. The membrane mass-transfer coefficient was set to $10^{-3}ms^{-1}$. The operating conditions corresponded to those of the energetic optimum of the Esbjerg plant, shown in Table 5-2, except for the reboiler pressure, which in this case was varied from 30 to 45 kPa. The vacuum is applied only on the shell side, hence, composite membranes would be recommended due to the differences between the gas and liquid pressures. In order to limit the solvent losses during the stripping, the gas pressure was equal to the water vapour pressure at the inlet temperature.

The simulation procedure consisted then in varying the contactor length when setting an inlet gas velocity, in order to achieve the objective regeneration factor. For illustration purposes, the axial profiles of the temperature, transmembrane fluxes and liquid CO_2 loading are plotted in Figure 5.8. As observed in Figure 5.8a, the temperature variation under the operating conditions of LTS is less than 5°C. However, there is an important amount of water condensation, as shown in Figure 5.8b, therefore, the operation cannot be considered as isothermal, since both water transfer and heat transfer are strongly related. It can be seen that the CO_2 transmembrane flux is almost constant for a z/Z<0.7 (mainly linear reduction of the liquid CO_2 loading, Figure 5.8c), at which point the flux increases exponentially.

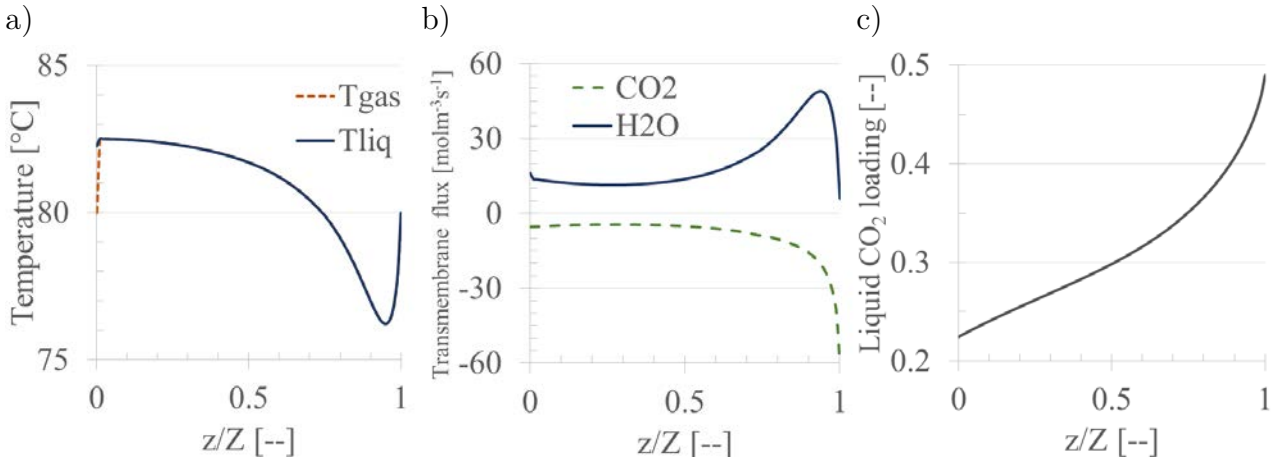

Figure 5.8 Simulation results of LTS. u_G^{in} = 2.8ms^{-1}, $k_{M,CO2}^{eq}$=10^{-3}ms^{-1}. Axial profiles of a) temperature, b) transmembrane flux and c) liquid CO_2 loading

The estimated equivalent work using HFMC as function of the intensification factor, for different vacuum pressures is presented in Figure 5.9. LTS allows for intensification factors up to 10 to be attained, but it requires more energy than the HTS. Furthermore, HTS using membrane contactors may achieve the same intensification factors at lower

energy consumption. A different conclusion was obtained by Wang et al. 2014 [20]. They pointed out that LTS is less energy consuming than HTS with regeneration pressures less than 50 kPa. However, the conditions and the modelling approach used to obtain their estimations were not detailed. Hence, no analysis of this difference could be given.

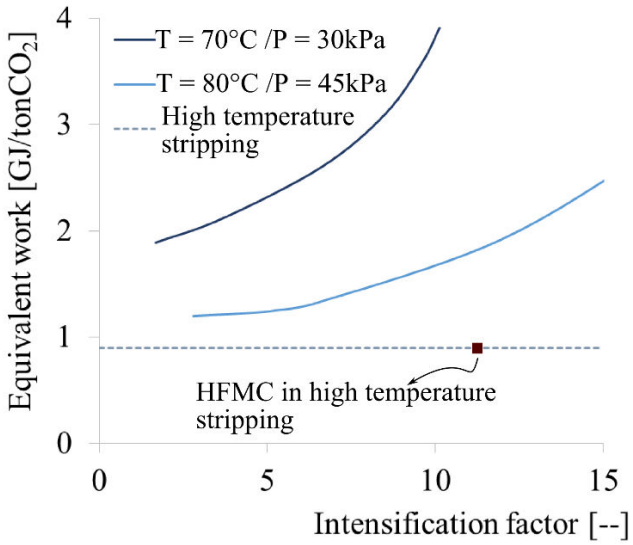

Figure 5.9 Equivalent work of low temperature stripping as function of intensification factor for different vacuum pressures. $k_{M,CO2}^{eq} = 10^{-3}\ ms^{-1}$

5.4. Summary and Conclusions

The implementation of the HFMC in the stripping of CO_2 within the PCC context was addressed in this chapter. Two stripping techniques were studied by modelling and simulation: high and low temperature stripping. These processes where compared against the conventional CO_2 stripping process using packed columns. The latter was also modelled and simulated and good agreement between experimental data and model predictions was obtained. The stripping step is constituted by a whole set of unit operations thus making the modelling more difficult than that used for absorption. HFMC implementation for high temperature stripping is a promising technology, provided that membranes can resist high temperatures and are equally resistant to wetting. Composite membranes currently represent the best candidates. Low temperature stripping requires more energy if similar volumetric contactor reduction factors to those of high temperature stripping using HFMC are desired. It is worth noting that these results are based on the performance of a given packed column, i.e. IMPT-50 packing. Advancements in packed bed technology are also expected, thus the intensification potentials identified here may be affected.

5.5. Résumé et conclusions

L'utilisation de contacteurs membranaires pour le stripage du CO_2 en postcombustion a été étudiée dans ce chapitre. Deux techniques différentes de régénération du solvant ont été évaluées par modélisation et simulation : le stripage à haute et basse température. Ces deux techniques ont été comparées avec le procédé conventionnel du stripage de CO_2 en utilisant des colonnes à garnissage. Ce dernier a été modélisé et simulé d'une manière satisfaisante, avec un excellent accord entre les données expérimentales et les résultats de simulation. L'étape de stripage est constituée d'un ensemble d'opérations unitaires, ce qui rend la modélisation plus complexe que celle utilisée pour l'étape d'absorption. L'implémentation des contacteurs membranaires dans le procédé de stripage est une technique prometteuse, à condition que les membranes soient résistantes à de hautes températures et également au mouillage. Les membranes composites sont à ce jour les meilleures candidates pour cette implémentation.

Le stripage à basse température a besoin de plus d'énergie, (notamment lié à la production de la vapeur d'eau), pour atteindre des facteurs d'intensification équivalent à ceux obtenus par le stripage à haute température.

Il est important de remarquer que ces résultats sont basés sur la performance des colonnes à garnissage connues, i.e. garnissage IMPT-50. Par conséquent, des améliorations de cette dernière technologie pourraient réduire les valeurs des potentiels d'intensification calculées dans ce chapitre.

General Conclusions and Outlook

General Conclusions

This thesis investigates the feasibility of utilising hollow fibre membrane contactors for CO_2 capture by modelling and simulating the process. Both the chemical absorption and desorption of CO_2 with MEA aqueous solutions were studied. Promising results have been reported in literature in terms of intensification potential at the laboratory scale and in pilot plant investigations (i.e. showing intensification factors ranging from 2 to 8). The main concern of this present work was estimating the performance of this technology within the context of relevant industrial conditions, which called for rigorous process models that could be applicable over a wide domain, covering both laboratory and industrial conditions.

The physicochemical properties were calculated using literature correlations showing excellent agreement with experimental data. The thermodynamic model proved to be physically consistent and relatively simple to implement and led to good predictions of thermodynamic properties. The reaction kinetics formulation taken from literature was adapted to be consistent with the thermodynamic model used in this work. The transfer phenomena inside HFMC could therefore be properly analysed.

The preponderant phenomenon in mass-transfer through microporous membranes is wetting in that it dramatically increases the membrane mass-transfer resistance. Chemical reaction occurring inside the liquid filled pores may compensate for this increase, but not for values exceeding 10% of wetting fraction. Membrane wetting is the main problem involved in HFMC, since it is likely to occur under PCC operating conditions. Predicting membrane wetting, however, is excessively complex as it depends on a large number of generally unreliable parameters in given conditions, such as the liquid-membrane contact angle or the pore shape and size. Additionally, the possibility of capillary condensation makes prediction even more complex. To respond to this situation, a domain of experimentally measured membrane mass-transfer coefficients was identified and the corresponding values were used for process simulation.

Transfer models of different complexities were studied, i.e. 1D and 2D isothermal single-component, 1D and 2D adiabatic multi-component, including and excluding variations of the local membrane mass-transfer coefficient. While it is relatively easy to implement, the isothermal single-component is not adequate for modelling the CO_2 capture process when high reactant conversions and high CO_2 capture ratios are required. Over-

estimations of contactor performance at above 50% are possible to obtain, therefore, this approach must be restricted to conditions with high excesses of liquid reactant. Adiabatic simulations revealed the occurrence of temperature peaks of up to 30°C, which were accompanied by the evaporation and condensation of large amounts of water over the length of the contactor. The excellent heat transfer through the membrane together with the high water condensation in a small part of the contactor increases the likeliness of membrane wetting through capillary condensation.

The 1D and 2D modelling approaches led to comparable results in terms of CO_2 capture, in both isothermal and adiabatic modelling, as well as for the water net flux in the adiabatic approach. The good performance of the 1D approach can be explained by the fact that, as the reaction film is very thin, the radial concentrations profiles of the reactants and products in the liquid phase are almost flat. In addition, the influence of the diffusion of the reaction products on the reaction rate was found to be almost negligible. With rapid radial heat transfer, the radial temperature profiles are also flat. Hence, the 1D approach, using mixing-cup concentrations and temperatures, while neglecting diffusion of reaction products proved to be correct in the investigated domain. Consequently, the 1D model might preferably be applied for scaling purposes as the simulation time is significantly reduced compared to that for the 2D approach. That said, slower reaction systems could also potentially lead to significant radial gradients and to situations that necessitate the 2D approach. It is our opinion that if the consistency of the 1D approach is systematically checked against 2D calculations, both 1D and 2D approaches are valuable.

Simulations indicate that membrane wetting can be simulated conveniently, using an average equivalent membrane mass-transfer coefficient rather than local values. Nonetheless, furthering fundamental understanding of wetting mechanisms in relevant industrial conditions would be helpful to further develop reliable and straightforward wetting models that could be implemented in the contactor model.

Under industrial conditions, simulations of the absorption step showed that fibres with an external radius of less than 400 µm are necessary to obtain significant intensification. In addition, membrane mass-transfer coefficients must not be less than $5 \cdot 10^{-4}$ m·s^{-1}. Commercially available PTFE membrane contactors are currently the best candidates since they have shown good resistance to wetting, at least in laboratory conditions. For an external fibre radius of 200 µm and a membrane mass-transfer coefficient of 10^{-3} ms^{-1}, a specific CO_2 absorbed flux of about 4 molm^{-3}s^{-1} can be achieved. The co-current flow arrangement might improve the functioning of HFMC, i.e. no temperature peaks, no solvent condensation and better transmembrane pressure handling. However, in order to achieve a CO_2 capture ratio of 0.9, the overall CO_2 capture process will be more energy

consuming than the counter-current flow arrangement. The liquid in-shell configuration can enhance the performance of the module in terms of mass-transfer, however this could possibly jeopardize the functioning of the device due to the increase of liquid pressure drop.

Due to the current lack of experimental data, the membrane contactor model could not be validated in industrial operating conditions. The transfer model was therefore verified by the modelling, simulation and validation of the CO_2 capture process using packed columns. Indeed, by setting the adequate mass-transfer correlations and by removing the terms related to the membrane, the 1D approach described in this work has been adapted to model packed columns. Good agreements between experimental data and model prediction were obtained for the two process steps, i.e. absorption and stripping.

Finally, the interest of HFMC in the stripping step was investigated. The stripping step constitutes a full set of auxiliary operations which makes modelling more difficult than for absorption. HFMC implementation for high temperature stripping is a promising alternative provided that membranes can resist high temperatures and effectively, wetting. Intensification factors around 10 might be obtained. Composite membranes are considered to be the best candidates. Low temperature stripping requires more energy if similar intensification factors to those of high temperature stripping using HFMC are desired.

It should be noted that these results are based on the performance of a given packed column. Future advancements in packed bed technology are also expected, which could potentially reduce intensification potentials identified in this work. All things considered, application of HFMC technology in PCC may be a promising strategy but is currently still in development. Further research is needed in order to make it competitive with packed columns both in terms of robustness and economic viability.

Outlook

While our understanding of HFMC technology in PCC is progressing rapidly, the following key aspects, among others, should be addressed prior to industrial development: proven feasibility in industrial conditions, reliable prediction of membrane wetting, integration in process flowsheeting and analysis of economic viability.

The model validation with experimental data obtained from HFMC pilot plant experiments characterized by high reactant conversions and high CO_2 capture ratios is mandatory. Experimentation not only allows for model validation but also proves the process feasibility. However, it implies challenging tasks, such as measuring the liquid loading and the temperature profile over the contactor length. In addition, the establishment of

water balances would make it possible to determine whether water condensation occurs on the liquid and/or the gas side. Moreover, module robustness, especially for membrane wetting resistance, can only be demonstrated through long term operation.

The predictive capacity of the model is directly related to the accurate estimation of the membrane mass-transfer resistance, which depends on numerous parameters that need to be identified in a large domain of operating conditions. The latter can be calculated if the wetting fraction is known. Therefore, fundamental understanding of the wetting mechanisms, together with experimentation, are essential to establish robust correlations for wetting fraction estimation.

The 1D model developed in this work can be applied to different solvent formulations. To date, it has been developed in a standalone version. Use of other reaction systems is more complicated as both the thermodynamic data and the physicochemical properties need to be provided. In addition, in order to perform parametric studies, process optimisation and operating cost analysis, the absorption-desorption loop needs to be programmed. This requires modelling of the whole set of auxiliary operations and improvement of the numerical algorithm of process flowsheet simulation to ensure numerical convergence. Commercial process simulation software, such as Aspen plus ® or Pro/II ®, currently already provide robust numerical schemes and thermodynamic data bases to overcome these issues. Implementation of the HFMC model using such software would prove valuable.

Economic considerations of HFMC technology were not included in this work. As soon as reliable cost functions of this technology are available, the economics must be addressed within a process optimisation framework. This can be conveniently performed using process simulators.

Conclusions générales et perspectives

Conclusion générale

Ce travail de thèse porte sur l'étude de faisabilité de l'implémentation des contacteurs membranaires à fibres creuses (CMFC) pour le captage du CO_2 en postcombustion, par une approche de modélisation et simulation. Les procédés successifs d'absorption et de stripage du CO_2 dans des solutions aqueuses de MEA ont été étudiés. La littérature reporte des résultats très prometteurs de l'utilisation des CMFC en termes de potentiel d'intensification à l'échelle laboratoire et l'échelle pilote, se traduisant par des facteurs d'intensification compris entre 2 et 8.

L'intérêt principal de cette recherche a donc consisté à estimer la performance des CMFC dans un contexte industriel. Pour ce faire, des modèles robustes ont été développés dans le but de pouvoir les appliquer à un large domaine opératoire, allant de conditions de laboratoire jusqu'à celles de l'industrie.

Les propriétés physico-chimiques des phases gazeuses et liquides ont été calculées en utilisant des corrélations issues de la littérature, validées par des données expérimentales.

Le modèle thermodynamique développé dans cette thèse a montré qu'il avait un sens physique et qu'il était relativement simple à implémenter, tout en rendant d'excellentes prédictions des propriétés thermodynamiques. La cinétique de réaction, disponible dans la littérature, a été adaptée afin d'être cohérente avec le modèle thermodynamique. A partir de ces modèles, les phénomènes de transfert au sein des CMFC ont pu être analysés correctement.

Le phénomène prépondérant dans le transfert de matière à travers les membranes microporeuses est le mouillage, car il augmente considérablement la résistance au transfert dans la membrane. Les réactions chimiques ayant lieu au sein des pores remplis de liquide peut compenser cette augmentation pour des fractions de mouillage inférieures à 10%. Le mouillage des membranes est alors le principal problème des CMFC car son apparition est très probable dans les conditions opératoires du captage du CO_2 en postcombustion. Prédire le mouillage est par contre un processus très complexe car il dépend de nombreux paramètres tels que l'angle de contact, la forme et la taille des pores, dont les valeurs sont souvent peu fiables et/ou peu connues dans les conditions désirées. La complexité augmente encore quand le phénomène de condensation capillaire se produit. Pour pallier à cette situation, le coefficient de transfert de matière de la membrane a été encadré en

se basant sur des valeurs expérimentales. Ces valeurs ont ensuite été utilisées comme données d'entrée pour la simulation du procédé.

Différentes approches de modèles de transfert ont été développées, i.e. mono-constituant et isotherme et multi-constituant et adiabatique, en variant localement ou pas le coefficient de transfert de matière de la membrane, toutes en monodimensionnel (1D) et bidimensionnel (2D). Malgré sa simplicité d'implémentation, une approche isotherme et mono-constituante n'est pas adéquate pour modéliser le procédé de captage du CO_2, pour de fortes conversions des réactants et taux de capture du CO_2. Des surestimations de la performance des CMFC au-delà de 50% peuvent être obtenues avec cette approche. Par conséquent, une modélisation en isotherme ne doit être implémentée que dans des conditions avec un grand excès du réactif liquide. Des simulations réalisées à partir de l'approche en adiabatique ont mis en évidence l'apparition de pics de température allant jusqu'à 30°C, qui sont liés à l'évaporation et condensation de quantités importantes d'eau le long du contacteur. De ce même fait et dû à l'excellent transfert de chaleur à travers la membrane, il est fortement probable que les membranes soient mouillées à cause d'une condensation capillaire. Les approches 1D et 2D ont rendu des résultats similaires en termes de capture du CO_2, dans les deux modèles en isotherme et en adiabatique, et en termes de flux net d'eau dans le modèle en adiabatique. La bonne performance du modèle 1D est lié au fait que les profils radiaux de concentration des réactifs et produits sont quasiment plats, car le film de réaction est très mince. En outre, il a été constaté que l'influence de la diffusion des produits de la réaction sur la vitesse de réaction peut être négligée. Les profils radiaux de température sont aussi plats car le transfert de chaleur radial est très rapide. Par conséquent, l'approche 1D, utilisant des concentrations et températures du type *mixing-cup* et négligeant la diffusion des produits de la réaction, s'est avéré correcte dans le domaine étudié. Il est donc conseillé d'utiliser cette approche pour des simulations à des échelles plus importantes, étant donné que le temps de calcul est réduit considérablement par rapport à une approche 2D. Cela dit, des systèmes de réaction plus lents pourraient potentiellement conduire à des gradients radiaux importants et à des situations qui nécessitent l'approche 2D. A notre avis, si l'approche 1D est systématiquement vérifiée par des simulations en 2D, les approches 1D et 2D sont utiles.

Les simulations indiquent que le mouillage des membranes peut être simulé d'une façon satisfaisante par l'utilisation d'un coefficient moyen équivalent de transfert de matière de la membrane, au lieu de l'utilisation de valeurs locales. Néanmoins, des études approfondies des mécanismes du mouillage de membranes dans des conditions industrielles seront nécessaires afin de développer des modèles simples et fiables, qui pourront être intégrés dans le modèle du contacteur membranaire.

Dans des conditions d'intérêt industriel, les résultats de simulation de l'étape d'absorption ont montré que, afin d'avoir une intensification significative, le rayon externe des fibres ne doit pas dépasser les 400 µm. En plus, le coefficient de transfert de matière de la membrane doit être supérieur à $5 \cdot 10^{-4}$ $m \cdot s^{-1}$. Des CMFC à fibres en PTFE sont actuellement les meilleurs candidats, grâce à leur résistance au mouillage, au moins dans des conditions modérées. Pour des fibres ayant un rayon externe de 200 µm et un coefficient de transfert de matière de 10^{-3} ms^{-1}, un flux spécifique de CO_2 absorbé équivalent à $4molm^{-3}s^{-1}$ peut être obtenu. Un mode d'écoulement en co-courant pourrait améliorer le fonctionnement du CMFC, i.e. pas de pics de température, pas de condensation du solvant et une meilleure distribution de la pression transmembranaire. Par contre, pour ce mode d'écoulement l'énergie requis pour atteindre un taux de capture de 90% serait plus importante que celle de l'écoulement à contre-courant. L'envoie du liquide à l'extérieur des fibres peut améliorer la performance de captage du module, en revanche, cela peut compromettre le bon fonctionnement du dispositif à cause de l'augmentation de la perte de charge du liquide.

En raison du manque actuel de données expérimentales, le modèle du contacteur membranaire n'a pas pu être validé dans des conditions industrielles. Le modèle de transfert a donc été vérifié par la modélisation, la simulation et la validation du procédé de capture du CO_2 en utilisant des colonnes à garnissage. En effet, en introduisant des corrélations de transfert de masse adéquates et en supprimant les termes liés à la membrane, l'approche 1D décrit dans ce travail a été adaptée pour modéliser des colonnes à garnissage. Comme résultat, un très bon accord entre les données expérimentales et les prédictions du modèle a été obtenu pour les étapes d'absorption et de stripage.

Dans une dernière partie, l'intérêt des CMFC dans l'étape de stripage a été étudié. Cette étape est constituée d'un ensemble d'opérations unitaires, ce qui rend sa modélisation plus difficile que pour l'étape d'absorption. L'implémentation de CMFC dans un stripage à haute température est une alternative prometteuse, à condition que les membranes puissent résister à des hautes températures et, bien entendu, au mouillage. Des facteurs d'intensification autour de 10 peuvent être ainsi obtenus. Les membranes composites sont considérées comme les meilleurs candidats pour cette opération. Le stripage à basse température a besoin de plus d'énergie, (notamment lié à la production de la vapeur d'eau), pour atteindre des facteurs d'intensification équivalent à ceux obtenus par le stripage à haute température.

Il est important de remarquer que ces résultats sont basés sur la performance des colonnes à garnissage connues, i.e. garnissage IMPT-50. Des améliorations de cette dernière technologie sont aussi attendues et donc les valeurs des potentiels d'intensification calculées dans ce chapitre pourraient se voir affectés. Finalement, tout bien considéré,

l'application de la technologie des CMFC en PCC peut être une stratégie prometteuse, mais est actuellement encore en développement. Des recherches complémentaires sont nécessaires pour la rendre compétitive avec les colonnes à garnissage en termes de robustesse mais aussi de viabilité économique.

Perspectives

Bien que notre compréhension de la technologie des CMFC dans le PCC progresse rapidement, les aspects clés suivants, doivent, à notre avis, être adressés avant tout développement industriel : la démonstration de la faisabilité dans des conditions industrielles, la prédiction du mouillage des membranes, l'intégration du modèle dans des simulations des procédés et l'analyse économique.

La validation du modèle avec des données expérimentales obtenues à partir d'expériences à l'échèle pilote, caractérisé par des conversions de réactifs élevés et des taux de capture élevés de CO_2 est absolument nécessaire. L'expérimentation permet non seulement la validation du modèle mais aussi prouve la faisabilité du procédé. Toutefois, ceci implique des tâches difficiles, telles que la mesure du taux de charge du solvant et le profil de température tout au long du contacteur. En plus, la mise en place des calculs de bilans d'eau permettrait de déterminer si la condensation de l'eau se produit du côté du liquide et/ou du côté du gaz. Par ailleurs, une robustesse des modules membranaires, en particulier par rapport au mouillage des membranes, peut être mise en évidence seulement à partir d'expériences à long terme.

Le pouvoir prédictive du modèle est directement lié à l'estimation précise de la résistance de transfert de matière de la membrane, qui dépend de nombreux paramètres qui doivent être identifiés dans un vaste domaine de conditions de fonctionnement. Cette résistance peut être calculée si la fraction de mouillage est connue. Par conséquent, la compréhension fondamentale des mécanismes de mouillage, accompagné par l'expérimentation, sont essentielles pour établir des corrélations solides et estimer cette fraction de mouillage.

Le modèle 1D développé dans ce travail peut être appliqué à différentes formulations de solvants. À ce jour, il a été développé dans une version autonome. L'utilisation d'autres systèmes de réaction est tout aussi complexe étant donné que les données thermodynamiques et les propriétés physico-chimiques doivent être fournis. Par ailleurs, afin d'effectuer des études paramétriques, des optimisations des procédés et d'analyse économiques, la boucle absorption-stripage doit être programmée. Cela nécessite la modélisation de l'ensemble des opérations auxiliaires et l'amélioration de l'algorithme de résolution pour assurer la convergence numérique. Des logiciels commerciaux de simulation de procédés, comme Aspen plus ® ou Pro / II ®, contient déjà des schémas numériques

robustes et bases de données thermodynamiques pour surmonter ces problèmes. La mise en œuvre du modèle des CMFC utilisant un tel logiciel se révélerait utile.

L'analyse économique de l'implémentation des CMFC dans le PCC n'a pas été effectuée dans ce travail. Un tel aspect doit être abordé dans un cadre d'optimisation de procédés, tout en disposant de fonctions de coût fiables de cette technologie. Ceci peut être réalisé d'une façon avantageuse dans des simulateurs de procédés.

Bibliography

[1] J. Cook, D. Nuccitelli, S. A. Green, M. Richardson, B. Winkler, R. Painting, R. Way, P. Jacobs, and A. Skuce, "Quantifying the consensus on anthropogenic global warming in the scientific literature," *Environ. Res. Lett.*, vol. 8, no. 2, p. 024024, Jun. 2013.

[2] GIEC, "Changements climatiques 2007-rapport de synthèse," 2007.

[3] OECD/IEA, *World Energy Outlook Special Report 2015: Energy and Climate Change*. France, 2015.

[4] OECD/IEA, *World Energy Outlook 2012*. 2012.

[5] B. Metz, O. Davidson, H. de Coninck, M. Loos, and L. Meyer, *IPCC special report on carbon dioxide capture and storage*. Cambridge University Press, New York, NY (United States), 2005.

[6] INERIS, "Etat des connaissances sur les risques liés au stockage géologique du CO2 - rapport n°1 : les risques en phase d'injection. Rapport technique, Direction des Risques du Sol et du Sous-sol." 2010.

[7] A. L. Kohl and R. Nielsen, *Gas Purification*. Gulf Professional Publishing, 1997.

[8] Z. (Henry) Liang, W. Rongwong, H. Liu, K. Fu, H. Gao, F. Cao, R. Zhang, T. Sema, A. Henni, K. Sumon, D. Nath, D. Gelowitz, W. Srisang, C. Saiwan, A. Benamor, M. Al-Marri, H. Shi, T. Supap, C. Chan, Q. Zhou, M. Abu-Zahra, M. Wilson, W. Olson, R. Idem, and P. (PT) Tontiwachwuthikul, "Recent progress and new developments in post-combustion carbon-capture technology with amine based solvents," *Int. J. Greenh. Gas Control*.

[9] R. Klaassen, P. Feron, and A. Jansen, "Membrane contactor applications," *Desalination*, vol. 224, no. 1–3, pp. 81–87, Apr. 2008.

[10] S. R. Wickramasinghe, M. J. Semmens, and E. L. Cussler, "Better hollow fiber contactors," *J. Membr. Sci.*, vol. 62, no. 3, pp. 371–388, Oct. 1991.

[11] P. Luis, T. Van Gerven, and B. Van der Bruggen, "Recent developments in membrane-based technologies for CO2 capture," *Prog. Energy Combust. Sci.*, vol. 38, no. 3, pp. 419–448, Jun. 2012.

[12] N. Hilal, A. F. Ismail, and C. Wright, *Membrane Fabrication*. CRC Press, 2015.

[13] E. Favre and H. F. Svendsen, "Membrane contactors for intensified post-combustion carbon dioxide capture by gas–liquid absorption processes," *J. Membr. Sci.*, vol. 407–408, pp. 1–7, 2012.

[14] Z. Cui and D. deMontigny, "Part 7: A review of CO2 capture using hollow fiber membrane contactors," *Carbon Manag.*, vol. 4, no. 1, pp. 69–89, Feb. 2013.

[15] S. Koonaphapdeelert, Z. Wu, and K. Li, "Carbon dioxide stripping in ceramic hollow fibre membrane contactors," *Chem. Eng. Sci.*, vol. 64, no. 1, pp. 1–8, Jan. 2009.

[16] S. Khaisri, D. deMontigny, P. Tontiwachwuthikul, and R. Jiraratananon, "CO2 stripping from monoethanolamine using a membrane contactor," *J. Membr. Sci.*, vol. 376, no. 1–2, pp. 110–118, Jul. 2011.

[17] R. Naim, A. F. Ismail, N. B. Cheer, and M. S. Abdullah, "Polyvinylidene fluoride and polyetherimide hollow fiber membranes for CO2 stripping in membrane contactor," *Chem. Eng. Res. Des.*, vol. 92, no. 7, pp. 1391–1398, Jul. 2014.

[18] S. Yan, M. Fang, Z. Luo, and K. Cen, "Regeneration of CO2 from CO2-rich alkanolamines solution by using reduced thickness and vacuum technology: Regeneration feasibility and characteristic of thin-layer solvent," *Chem. Eng. Process. Process Intensif.*, vol. 48, no. 1, pp. 515–523, Jan. 2009.

[19] M. Fang, Z. Wang, S. Yan, Q. Cen, and Z. Luo, "CO2 desorption from rich alkanolamine solution by using membrane vacuum regeneration technology," *Int. J. Greenh. Gas Control*, vol. 9, pp. 507–521, Jul. 2012.

[20] Z. Wang, M. Fang, Q. Ma, Z. Zhao, T. Wang, and Z. Luo, "Membrane Stripping Technology for CO2 Desorption from CO2-rich Absorbents with Low Energy Consumption," *Energy Procedia*, vol. 63, pp. 765–772, 2014.

[21] S. Yan, S. Zhao, L. Wardhaugh, and P. H. M. Feron, "Innovative Use of Membrane Contactor as Condenser for Heat Recovery in Carbon Capture," *Environ. Sci. Technol.*, vol. 49, no. 4, pp. 2532–2540, Feb. 2015.

[22] S. Zhao, P. H. M. Feron, C. Cao, L. Wardhaugh, S. Yan, and S. Gray, "Membrane evaporation of amine solution for energy saving in post-combustion carbon capture: Wetting and condensation," *Sep. Purif. Technol.*, vol. 146, pp. 60–67, May 2015.

[23] P. H. M. Feron and A. E. Jansen, "CO2 separation with polyolefin membrane contactors and dedicated absorption liquids: performances and prospects," *Sep. Purif. Technol.*, vol. 27, no. 3, pp. 231–242, Jun. 2002.

[24] R. Wang, D. F. Li, and D. T. Liang, "Modeling of CO2 capture by three typical amine solutions in hollow fiber membrane contactors," *Chem. Eng. Process. Process Intensif.*, vol. 43, no. 7, pp. 849–856, juillet 2004.

[25] D. deMontigny, P. Tontiwachwuthikul, and A. Chakma, "Using polypropylene and polytetrafluoroethylene membranes in a membrane contactor for CO2 absorption," *J. Membr. Sci.*, vol. 277, no. 1–2, pp. 99–107, Jun. 2006.

[26] S.-H. Lin, C.-F. Hsieh, M.-H. Li, and K.-L. Tung, "Determination of mass transfer resistance during absorption of carbon dioxide by mixed absorbents in PVDF and PP membrane contactor," *Desalination*, vol. 249, no. 2, pp. 647–653, Dec. 2009.

[27] M. Vogt, R. Goldschmidt, D. Bathen, B. Epp, and H. Fahlenkamp, "Comparison of membrane contactor and structured packings for CO2 absorption," *Energy Procedia*, vol. 4, pp. 1471–1477, 2011.

[28] E. Chabanon, R. Bounaceur, C. Castel, S. Rode, D. Roizard, and E. Favre, "Pushing the limits of intensified CO2 post-combustion capture by gas–liquid absorption through a membrane contactor," *Chem. Eng. Process. Process Intensif.*, vol. 91, pp. 7–22, May 2015.

[29] F. Porcheron, D. Ferré, E. Favre, P. T. Nguyen, O. Lorain, R. Mercier, and L. Rougeau, "Hollow fiber membrane contactors for CO2 capture: From lab-scale screening to pilot-plant module conception," *Energy Procedia*, vol. 4, pp. 763–770, 2011.

[30] F. Korminouri, M. Rahbari-Sisakht, D. Rana, T. Matsuura, and A. F. Ismail, "Study on the effect of air–gap length on properties and performance of surface modified PVDF hollow fiber membrane contactor for carbon dioxide absorption," *Sep. Purif. Technol.*, vol. 132, pp. 601–609, Aug. 2014.

[31] M. Rahbari-Sisakht, D. Rana, T. Matsuura, D. Emadzadeh, M. Padaki, and A. F. Ismail, "Study on CO2 stripping from water through novel surface modified PVDF hollow fiber membrane contactor," *Chem. Eng. J.*, vol. 246, pp. 306–310, Jun. 2014.

[32] P. Kosaraju, A. S. Kovvali, A. Korikov, and K. K. Sirkar, "Hollow Fiber Membrane Contactor Based CO2 Absorption−Stripping Using Novel Solvents and Membranes," *Ind. Eng. Chem. Res.*, vol. 44, no. 5, pp. 1250–1258, Mar. 2005.

[33] C. A. Scholes, A. Qader, G. W. Stevens, and S. E. Kentish, *Sep. Sci. Technol.*, vol. 49, no. 16, pp. 2449–2458, Nov. 2014.

[34] P. T. Nguyen, E. Lasseuguette, Y. Medina-Gonzalez, J. C. Remigy, D. Roizard, and E. Favre, "A dense membrane contactor for intensified CO2 gas/liquid absorption in post-combustion capture," *J. Membr. Sci.*, vol. 377, no. 1–2, pp. 261–272, juillet 2011.

[35] N. Ghasem, M. Al-Marzouqi, and A. Duidar, "Effect of PVDF concentration on the morphology and performance of hollow fiber membrane employed as gas–liquid membrane contactor for CO2 absorption," *Sep. Purif. Technol.*, vol. 98, pp. 174–185, Sep. 2012.

[36] R. Naim, A. F. Ismail, and A. Mansourizadeh, "Effect of non-solvent additives on the structure and performance of PVDF hollow fiber membrane contactor for CO2 stripping," *J. Membr. Sci.*, vol. 423, pp. 503–513, Dec. 2012.

[37] S. Li, D. J. Rocha, S. James Zhou, H. S. Meyer, B. Bikson, and Y. Ding, "Post-combustion CO2 capture using super-hydrophobic, polyether ether ketone, hollow fiber membrane contactors," *J. Membr. Sci.*, vol. 430, pp. 79–86, Mar. 2013.

[38] S. Mosadegh-Sedghi, D. Rodrigue, J. Brisson, and M. C. Iliuta, "Wetting phenomenon in membrane contactors – Causes and prevention," *J. Membr. Sci.*, vol. 452, pp. 332–353, Feb. 2014.

[39] R. B. Saffarini, B. Mansoor, R. Thomas, and H. A. Arafat, "Effect of temperature-dependent microstructure evolution on pore wetting in PTFE membranes under membrane distillation conditions," *J. Membr. Sci.*, vol. 429, pp. 282–294, Feb. 2013.

[40] S. Rajabzadeh, S. Yoshimoto, M. Teramoto, M. Al-Marzouqi, Y. Ohmukai, T. Maruyama, and H. Matsuyama, "Effect of membrane structure on gas absorption performance and long-term stability of membrane contactors," *Sep. Purif. Technol.*, vol. 108, pp. 65–73, avril 2013.

[41] I. Brovchenko and A. Oleinikova, "4 - Phase diagram of confined water," in *Interfacial and Confined Water*, I. Brovchenko and A. Oleinikova, Eds. Amsterdam: Elsevier, 2008, pp. 91–119.

[42] R. Klaassen, P. H. M. Feron, and A. E. Jansen, "Membrane Contactors in Industrial Applications," *Chem. Eng. Res. Des.*, vol. 83, no. 3, pp. 234–246, Mar. 2005.

[43] Y. Lv, X. Yu, S.-T. Tu, J. Yan, and E. Dahlquist, "Wetting of polypropylene hollow fiber membrane contactors," *J. Membr. Sci.*, vol. 362, no. 1–2, pp. 444–452, Oct. 2010.

[44] E. Chabanon, D. Roizard, and E. Favre, "Membrane Contactors for Postcombustion Carbon Dioxide Capture: A Comparative Study of Wetting Resistance on Long Time Scales," *Ind. Eng. Chem. Res.*, vol. 50, no. 13, pp. 8237–8244, Jul. 2011.

[45] V. Y. Dindore, D. W. F. Brilman, P. H. M. Feron, and G. F. Versteeg, "CO2 absorption at elevated pressures using a hollow fiber membrane contactor," *J. Membr. Sci.*, vol. 235, no. 1–2, pp. 99–109, juin 2004.

[46] H.-Y. Zhang, R. Wang, D. T. Liang, and J. H. Tay, "Theoretical and experimental studies of membrane wetting in the membrane gas–liquid contacting process for CO2 absorption," *J. Membr. Sci.*, vol. 308, no. 1–2, pp. 162–170, 2008.

[47] W. Rongwong, R. Jiraratananon, and S. Atchariyawut, "Experimental study on membrane wetting in gas–liquid membrane contacting process for CO2 absorption by single and mixed absorbents," *Sep. Purif. Technol.*, vol. 69, no. 1, pp. 118–125, Sep. 2009.

[48] S. Rode, P. T. Nguyen, D. Roizard, R. Bounaceur, C. Castel, and E. Favre, "Evaluating the intensification potential of membrane contactors for gas absorption in a

chemical solvent: A generic one-dimensional methodology and its application to CO2 absorption in monoethanolamine," *J. Membr. Sci.*, vol. 389, pp. 1–16, 2012.

[49] W. Rongwong, S. Assabumrungrat, and R. Jiraratananon, "Rate based modeling for CO2 absorption using monoethanolamine solution in a hollow fiber membrane contactor," *J. Membr. Sci.*, vol. 429, pp. 396–408, Feb. 2013.

[50] K. A. Hoff, O. Juliussen, O. Falk-Pedersen, and H. F. Svendsen, "Modeling and Experimental Study of Carbon Dioxide Absorption in Aqueous Alkanolamine Solutions Using a Membrane Contactor," *Ind. Eng. Chem. Res.*, vol. 43, no. 16, pp. 4908–4921, 2004.

[51] R. Wang, H. Y. Zhang, P. H. M. Feron, and D. T. Liang, "Influence of membrane wetting on CO2 capture in microporous hollow fiber membrane contactors," *Sep. Purif. Technol.*, vol. 46, no. 1–2, pp. 33–40, Nov. 2005.

[52] H.-Y. Zhang, R. Wang, D. T. Liang, and J. H. Tay, "Modeling and experimental study of CO2 absorption in a hollow fiber membrane contactor," *J. Membr. Sci.*, vol. 279, no. 1–2, pp. 301–310, 2006.

[53] P. Keshavarz, J. Fathikalajahi, and S. Ayatollahi, "Analysis of CO2 separation and simulation of a partially wetted hollow fiber membrane contactor," *J. Hazard. Mater.*, vol. 152, no. 3, pp. 1237–1247, avril 2008.

[54] N. Boucif, E. Favre, and D. Roizard, "capture in HFMM contactor with typical amine solutions: A numerical analysis," *Chem. Eng. Sci.*, vol. 63, no. 22, pp. 5375–5385, Nov. 2008.

[55] S. Eslami, S. M. Mousavi, S. Danesh, and H. Banazadeh, "Modeling and simulation of CO2 removal from power plant flue gas by PG solution in a hollow fiber membrane contactor," *Adv. Eng. Softw.*, vol. 42, no. 8, pp. 612–620, août 2011.

[56] R. Faiz, M. H. El-Naas, and M. Al-Marzouqi, "Significance of gas velocity change during the transport of CO2 through hollow fiber membrane contactors," *Chem. Eng. J.*, vol. 168, no. 2, pp. 593–603, 2011.

[57] N. Boucif, J. P. Corriou, D. Roizard, and E. Favre, "Carbon dioxide absorption by monoethanolamine in hollow fiber membrane contactors: A parametric investigation," *AIChE J.*, vol. 58, no. 9, pp. 2843–2855, 2012.

[58] E. Chabanon, D. Roizard, and E. Favre, "Modeling strategies of membrane contactors for post-combustion carbon capture: A critical comparative study," *Chem. Eng. Sci.*, vol. 87, pp. 393–407, Jan. 2013.

[59] S. Khaisri, D. deMontigny, P. Tontiwachwuthikul, and R. Jiraratananon, "CO2 stripping from monoethanolamine using a membrane contactor," *J. Membr. Sci.*, vol. 376, no. 1–2, pp. 110–118, Jul. 2011.

[60] A. Mansourizadeh, "Experimental study of CO2 absorption/stripping via PVDF hollow fiber membrane contactor," *Chem. Eng. Res. Des.*, vol. 90, no. 4, pp. 555–562, Apr. 2012.

[61] M. Rahbari-Sisakht, A. F. Ismail, D. Rana, and T. Matsuura, "Carbon dioxide stripping from diethanolamine solution through porous surface modified PVDF hollow fiber membrane contactor," *J. Membr. Sci.*, vol. 427, pp. 270–275, Jan. 2013.

[62] Z. Wang, M. Fang, H. Yu, Q. Ma, and Z. Luo, "Modeling of CO2 Stripping in a Hollow Fiber Membrane Contactor for CO2 Capture," *Energy Fuels*, vol. 27, no. 11, pp. 6887–6898, Nov. 2013.

[63] E. Chabanon, E. Kimball, E. Favre, O. Lorain, E. Goetheer, D. Ferre, A. Gomez, and P. Broutin, "Hollow Fiber Membrane Contactors for Post-Combustion CO $_2$ Capture: A Scale-Up Study from Laboratory to Pilot Plant," *Oil Gas Sci. Technol. – Rev. D'IFP Energ. Nouv.*, vol. 69, no. 6, pp. 1035–1045, 2014.

[64] F. A. Tobiesen, H. F. Svendsen, and O. Juliussen, "Experimental validation of a rigorous absorber model for CO2 postcombustion capture," *AIChE J.*, vol. 53, no. 4, pp. 846–865, 2007.

[65] S.-H. Yeon, K.-S. Lee, B. Sea, Y.-I. Park, and K.-H. Lee, "Application of pilot-scale membrane contactor hybrid system for removal of carbon dioxide from flue gas," *J. Membr. Sci.*, vol. 257, no. 1–2, pp. 156–160, Jul. 2005.

[66] S. Yan, M. Fang, W. Zhang, W. Zhong, Z. Luo, and K. Cen, "Comparative analysis of CO2 separation from flue gas by membrane gas absorption technology and chemical absorption technology in China," *Energy Convers. Manag.*, vol. 49, no. 11, pp. 3188–3197, Nov. 2008.

[67] D. Albarracin Zaidiza, B. Belaissaoui, S. Rode, T. Neveux, C. Makhloufi, C. Castel, D. Roizard, and E. Favre, "Adiabatic modelling of CO2 capture by amine solvents using membrane contactors," *J. Membr. Sci.*, vol. 493, pp. 106–119, Nov. 2015.

[68] Q. Xu and G. Rochelle, "Total pressure and CO2 solubility at high temperature in aqueous amines," *Energy Procedia*, vol. 4, pp. 117–124, 2011.

[69] A. Aboudheir, P. Tontiwachwuthikul, A. Chakma, and R. Idem, "Kinetics of the reactive absorption of carbon dioxide in high CO2-loaded, concentrated aqueous monoethanolamine solutions," *Chem. Eng. Sci.*, vol. 58, no. 23–24, pp. 5195–5210, Dec. 2003.

[70] J. M. Smith, H. V. Ness, and M. M. Abbott, *Introduction to Chemical Engineering Thermodynamics*. McGraw-Hill Education, 2005.

[71] D. M. Austgen, G. T. Rochelle, X. Peng, and C. C. Chen, "Model of vapor-liquid equilibria for aqueous acid gas-alkanolamine systems using the electrolyte-NRTL equation," *Ind. Eng. Chem. Res.*, vol. 28, no. 7, pp. 1060–1073, Jul. 1989.

[72] T. Neveux, *Modélisation et optimisation des procédés de captage de CO2 par absorption chimique*. Université de Lorraine, 2013.

[73] G. Puxty and M. Maeder, "A simple chemical model to represent CO2–amine–H2O vapour–liquid-equilibria," *Int. J. Greenh. Gas Control*, vol. 17, pp. 215–224, Sep. 2013.

[74] M. Wagner, I. von Harbou, J. Kim, I. Ermatchkova, G. Maurer, and H. Hasse, "Solubility of Carbon Dioxide in Aqueous Solutions of Monoethanolamine in the Low and High Gas Loading Regions," *J. Chem. Eng. Data*, vol. 58, no. 4, pp. 883–895, Apr. 2013.

[75] M. D. Hilliard, "A predictive thermodynamic model for an aqueous blend of potassium carbonate, piperazine, and monoethanolamine for carbon dioxide capture from flue gas," Aug. 2008.

[76] T. Neveux, Y. Le Moullec, J.-P. Corriou, and E. Favre, "Modeling CO2 Capture in Amine Solvents: Prediction of Performance and Insights on Limiting Phenomena," *Ind. Eng. Chem. Res.*, vol. 52, no. 11, pp. 4266–4279, Mar. 2013.

[77] I. von Harbou, M. Imle, and H. Hasse, "Modeling and simulation of reactive absorption of CO2 with MEA: Results for four different packings on two different scales," *Chem. Eng. Sci.*, vol. 105, pp. 179–190, Feb. 2014.

[78] K. A. Hoff and H. F. Svendsen, "Membrane contactors for CO2 absorption – Application, modeling and mass transfer effects," *Chem. Eng. Sci.*, vol. 116, pp. 331–341, Sep. 2014.

[79] F. A. Tobiesen, O. Juliussen, and H. F. Svendsen, "Experimental validation of a rigorous desorber model for post-combustion capture," *Chem. Eng. Sci.*, vol. 63, no. 10, pp. 2641–2656, May 2008.

[80] R. Crovetto, "Evaluation of Solubility Data of the System CO2–H2O from 273 K to the Critical Point of Water," *J. Phys. Chem. Ref. Data*, vol. 20, no. 3, pp. 575–589, May 1991.

[81] G. Astarita, D. W. Savage, and A. Bisio, *Gas treating with chemical solvents*. John Wiley, 1983.

[82] J. Gabrielsen, M. L. Michelsen, E. H. Stenby, and G. M. Kontogeorgis, "A Model for Estimating CO2 Solubility in Aqueous Alkanolamines," *Ind. Eng. Chem. Res.*, vol. 44, no. 9, pp. 3348–3354, Apr. 2005.

[83] U. E. Aronu, S. Gondal, E. T. Hessen, T. Haug-Warberg, A. Hartono, K. A. Hoff, and H. F. Svendsen, "Solubility of CO2 in 15, 30, 45 and 60 mass% MEA from 40 to 120 °C and model representation using the extended UNIQUAC framework," *Chem. Eng. Sci.*, vol. 66, no. 24, pp. 6393–6406, Dec. 2011.

[84] I. Kim, K. A. Hoff, E. T. Hessen, T. Haug-Warberg, and H. F. Svendsen, "Enthalpy of absorption of CO2 with alkanolamine solutions predicted from reaction equilibrium constants," *Chem. Eng. Sci.*, vol. 64, no. 9, pp. 2027–2038, May 2009.

[85] D. Albarracin Zaidiza, B. Belaissaoui, S. Rode, T. Neveux, C. Makhloufi, C. Castel, D. Roizard, and E. Favre, "Adiabatic modelling of CO2 capture by amine solvents using membrane contactors," *J. Membr. Sci.*

[86] S. Ma'mun, R. Nilsen, H. F. Svendsen, and O. Juliussen, "Solubility of Carbon Dioxide in 30 mass % Monoethanolamine and 50 mass % Methyldiethanolamine Solutions," *J. Chem. Eng. Data*, vol. 50, no. 2, pp. 630–634, Mar. 2005.

[87] D. Tong, J. P. M. Trusler, G. C. Maitland, J. Gibbins, and P. S. Fennell, "Solubility of carbon dioxide in aqueous solution of monoethanolamine or 2-amino-2-methyl-1-propanol: Experimental measurements and modelling," *Int. J. Greenh. Gas Control*, vol. 6, pp. 37–47, Jan. 2012.

[88] I. Kim and H. F. Svendsen, "Heat of Absorption of Carbon Dioxide (CO2) in Monoethanolamine (MEA) and 2-(Aminoethyl)ethanolamine (AEEA) Solutions," *Ind. Eng. Chem. Res.*, vol. 46, no. 17, pp. 5803–5809, 2007.

[89] P. V. Danckwerts, "The reaction of CO2 with ethanolamines," *Chem. Eng. Sci.*, vol. 34, no. 4, pp. 443–446, 1979.

[90] J. E. Crooks and J. P. Donnellan, "Kinetics and mechanism of the reaction between carbon dioxide and amines in aqueous solution," *J. Chem. Soc. Perkin Trans. 2*, no. 4, pp. 331–333, Jan. 1989.

[91] W. J. DeCoursey, "Enhancement factors for gas absorption with reversible reaction," *Chem. Eng. Sci.*, vol. 37, no. 10, pp. 1483–1489, 1982.

[92] P. . Kumar, J. . Hogendoorn, P. H. . Feron, and G. . Versteeg, "Approximate solution to predict the enhancement factor for the reactive absorption of a gas in a liquid flowing through a microporous membrane hollow fiber," *J. Membr. Sci.*, vol. 213, no. 1–2, pp. 231–245, Mar. 2003.

[93] S. Wilson, "Modelling of CO2 post-combustion capture by membrane contactors; comparison between one- and two-dimensional adiabatic approaches & study of the influence of the diffusion of the complex-product and the reversibility of the absorption reaction on overall CO2 capture," Université de Lorraine, ENSIC, Master's Dissertation, Jun. 2015.

[94] R. E. Treybal, *Mass-transfer operations*, vol. 2. McGraw-Hill, 1956.

[95] N. Ghasem, M. Al-Marzouqi, and N. Abdul Rahim, "Modeling of CO2 absorption in a membrane contactor considering solvent evaporation," *Sep. Purif. Technol.*, vol. 110, pp. 1–10, juin 2013.

[96] L.-Z. Zhang and S.-M. Huang, "Coupled heat and mass transfer in a counter flow hollow fiber membrane module for air humidification," *Int. J. Heat Mass Transf.*, vol. 54, no. 5–6, pp. 1055–1063, Feb. 2011.

[97] K. Villeneuve, Zhang, D. Albarracin Zaidiza, E. Favre, S. Rode, and D. Roizard, "Study of water vapor transport in HFMC: evaluation of its impact on gas-liquid treatmentof flue gas," presented at the Euromembrane 2015, Aachen, Germany, 07-Sep-2015.

[98] S. Boributh, S. Assabumrungrat, N. Laosiripojana, and R. Jiraratananon, "A modeling study on the effects of membrane characteristics and operating parameters on physical absorption of CO2 by hollow fiber membrane contactor," *J. Membr. Sci.*, vol. 380, no. 1–2, pp. 21–33, Sep. 2011.

[99] S. Boributh, W. Rongwong, S. Assabumrungrat, N. Laosiripojana, and R. Jiraratananon, "Mathematical modeling and cascade design of hollow fiber membrane contactor for CO2 absorption by monoethanolamine," *J. Membr. Sci.*, vol. 401–402, pp. 175–189, mai 2012.

[100] W. Rongwong, S. Assabumrungrat, and R. Jiraratananon, "Rate based modeling for CO2 absorption using monoethanolamine solution in a hollow fiber membrane contactor," *J. Membr. Sci.*, vol. 429, pp. 396–408, février 2013.

[101] M. H. El-Naas, M. Al-Marzouqi, S. A. Marzouk, and N. Abdullatif, "Evaluation of the removal of CO2 using membrane contactors: Membrane wettability," *J. Membr. Sci.*, vol. 350, no. 1–2, pp. 410–416, Mar. 2010.

[102] B. Hanley and C.-C. Chen, "New mass-transfer correlations for packed towers," *AIChE J.*, vol. 58, no. 1, pp. 132–152, Jan. 2012.

[103] R. Dugas, P. Alix, E. Lemaire, P. Broutin, and G. Rochelle, "Absorber model for CO(2) capture by monoethanolamine - application to CASTOR pilot results," in *Greenhouse Gas Control Technologies 9*, vol. 1, J. Gale, H. Herzog, and J. Braitsch, Eds. Amsterdam: Elsevier Science Bv, 2009, pp. 103–107.

[104] S. Khaisri, D. deMontigny, P. Tontiwachwuthikul, and R. Jiraratananon, "Comparing membrane resistance and absorption performance of three different membranes in a gas absorption membrane contactor," *Sep. Purif. Technol.*, vol. 65, no. 3, pp. 290–297, Mar. 2009.

[105] C. S. Chang and G. T. Rochelle, "Mass transfer enhanced by equilibrium reactions," *Ind. Eng. Chem. Fundam.*, vol. 21, no. 4, pp. 379–385, Nov. 1982.

[106] P. Keshavarz, J. Fathikalajahi, and S. Ayatollahi, "Mathematical modeling of the simultaneous absorption of carbon dioxide and hydrogen sulfide in a hollow fiber membrane contactor," *Sep. Purif. Technol.*, vol. 63, no. 1, pp. 145–155, Oct. 2008.

[107] R. Faiz and M. Al-Marzouqi, "Mathematical modeling for the simultaneous absorption of CO2 and H2S using MEA in hollow fiber membrane contactors," *J. Membr. Sci.*, vol. 342, no. 1–2, pp. 269–278, Oct. 2009.

[108] W. J. Beek, K. M. K. Muttzall, and J. W. Heuven, *Transport phenomena*. Wiley, 1999.

[109] D. Albarracin Zaidiza, J. Billaud, B. Belaissaoui, S. Rode, D. Roizard, and E. Favre, "Modeling of CO2 post-combustion capture using membrane contactors, comparison between one- and two-dimensional approaches," *J. Membr. Sci.*, vol. 455, pp. 64–74, Apr. 2014.

[110] P. Khakharia, L. Brachert, J. Mertens, A. Huizinga, B. Schallert, K. Schaber, T. J. H. Vlugt, and E. Goetheer, "Investigation of aerosol based emission of MEA due to sulphuric acid aerosol and soot in a Post Combustion CO2 Capture process," *Int. J. Greenh. Gas Control*, vol. 19, pp. 138–144, Nov. 2013.

[111] G. A. Dibrov, V. V. Volkov, V. P. Vasilevsky, A. A. Shutova, S. D. Bazhenov, V. S. Khotimsky, A. van de Runstraat, E. L. V. Goetheer, and A. V. Volkov, "Robust high-permeance PTMSP composite membranes for CO2 membrane gas desorption at elevated temperatures and pressures," *J. Membr. Sci.*, vol. 470, pp. 439–450, Nov. 2014.

[112] R. Jiang, M. Yang, S. Chen, S.-M. Huang, and X. Yang, "Fluid flow and heat transfer across an elliptical hollow fiber membrane tube bank with randomly distributed features," *Int. J. Heat Mass Transf.*, vol. 76, pp. 559–567, Sep. 2014.

[113] S.-M. Huang and M. Yang, "Heat and mass transfer enhancement in a cross-flow elliptical hollow fiber membrane contactor used for liquid desiccant air dehumidification," *J. Membr. Sci.*, vol. 449, pp. 184–192, Jan. 2014.

[114] T. H. Chilton and A. P. Colburn, "Mass Transfer (Absorption) Coefficients Prediction from Data on Heat Transfer and Fluid Friction," *Ind. Eng. Chem.*, vol. 26, no. 11, pp. 1183–1187, Nov. 1934.

[115] S. Wickramasinghe, M. Semmens, and E. Cussler, "Mass-Transfer in Various Hollow Fiber Geometries," *J. Membr. Sci.*, vol. 69, no. 3, pp. 235–250, May 1992.

[116] O. Miyatake and H. Iwashita, "Laminar-flow heat transfer to a fluid flowing axially between cylinders with a uniform surface temperature," *Int. J. Heat Mass Transf.*, vol. 33, no. 3, pp. 417–425, Mar. 1990.

[117] O. Miyatake and H. Iwashita, "Laminar-flow heat transfer to a fluid flowing axially between cylinders with a uniform wall heat flux," *Int. J. Heat Mass Transf.*, vol. 34, no. 1, pp. 322–327, Jan. 1991.

[118] L. Bao, B. Liu, and G. G. Lipscomb, "Entry mass transfer in axial flows through randomly packed fiber bundles," *AIChE J.*, vol. 45, no. 11, pp. 2346–2356, Nov. 1999.

[119] L. Bao and G. G. Lipscomb, "Well-developed mass transfer in axial flows through randomly packed fiber bundles with constant wall flux," *Chem. Eng. Sci.*, vol. 57, no. 1, pp. 125–132, Jan. 2002.

[120] L. Bao and G. Glenn Lipscomb, "Mass transfer in axial flows through randomly packed fiber bundles with constant wall concentration," *J. Membr. Sci.*, vol. 204, no. 1–2, pp. 207–220, Jul. 2002.

[121] E. Drioli, A. Criscuoli, and E. Curcio, *Membrane Contactors: Fundamentals, Applications and Potentialities: Fundamentals, Applications and Potentialities*. Elsevier, 2011.

[122] M. J. Costello, A. G. Fane, P. A. Hogan, and R. W. Schofield, "The effect of shell side hydrodynamics on the performance of axial flow hollow fibre modules," *J. Membr. Sci.*, vol. 80, no. 1, pp. 1–11, Jun. 1993.

[123] J. Wu and V. Chen, "Shell-side mass transfer performance of randomly packed hollow fiber modules," *J. Membr. Sci.*, vol. 172, no. 1–2, pp. 59–74, Jul. 2000.

[124] L. Bao and G. G. Lipscomb, "Effect of random fiber packing on the performance of shell-fed hollow-fiber gas separation modules," *Desalination*, vol. 146, no. 1–3, pp. 243–248, Sep. 2002.

Appendix

A. Shell and Tube Mass-transfer Coefficients

In the 1D modelling of mass and heat transfer in HFMC, both local and overall mass transfer coefficient are referred to in literature. The local mass-transfer coefficients depend on the local flow configuration, velocity and concentration gradient, whereas the global mass-transfer coefficients are estimated using the overall flux, transfer area and an average driving force (e.g. for plug flow the logarithmic mean concentration difference).

Mass and heat transfer coefficients in fluids are commonly related using the Chilton-Colburn analogy (see Table 4-1) which has been verified by various investigations of HFMC [96], [112]–[114]. Therefore only mass transfer is discussed hereunder for the lumen-side and shell-side transfer. Moreover, as is the case for the velocity profiles, the temperature profiles can be considered to be fully developed.

A.1 Lumen-side Transfer

Due to the important ratio between the fibre length and the fibre inner diameter, the flow through the lumen of a fibre can be considered as plug flow. In fully developed laminar pipe flow, the local Sherwood number is given by Leveque's equation:

$$Sh_{i,f} = (a^3 + b^3 Gz_{i,f})^{1/3} \qquad \text{(A.1)}$$

With the material Graetz number defined as:

$$Gz_{i,f} = Re_f Sc_{i,f}\left(\frac{d_{h-int}}{z}\right)$$

Boundary conditions:

Uniform wall flux:

a = 4.36 and b =1.30

Uniform wall concentration:

a = 3.66 and b =1.08

For low Graetz numbers ($Gz < 3\text{x}10^{-2}$), the mass transfer boundary layer is fully developed and the Sherwood number attains a minimum value, which is independent of flow hydrodynamics. This situation invariably occurs for high reactant conversions, as in this case, the major part of the reactant diffuses from the fibre centre to the interface. However, due to the small inner fibre radius, the resulting mass transfer coefficients are of the same order of magnitude as those encountered in packed columns.

The non-uniform distribution of fibre thickness leads to a non-uniform velocity distribution between the fibres and thus to axial dispersion, reducing the average driving force and thus the overall flux. The influence of the dispersion on the overall flux is commonly taken into account by adjusting an equivalent Sherwood number to an ideal plug flow

model. The resulting Sherwood numbers are lower than those obtained in non-dispersed flow.

An experimental study of the influence of polydispersity of fibre thicknesses on the averaged mass transfer rates has been proposed by Wickramasinghe et al [115]. In their study, which was performed in conditions of developing mass-transfer boundary layers (Graetz numbers comprised between 10^{-1} and 10^{3}), a polydispersity in the fibre diameters of 5% could decrease in one order of magnitude the value of the equivalent Sherwood number.

A.2 Shell-side Transfer

The mass transfer coefficient depends on the flow configuration. In parallel flow, and for high packing fractions, the shell-side geometry is generally described using a hydraulic diameter (see Section 3.2, Table 3). As mentioned earlier, in typical operating conditions the flow is laminar and fully developed. Moreover, due to the high ratio between the hydraulic diameter and the contactor length, plug flow can be considered. As for the lumen-side flow, for high reactant conversions, the Graetz numbers are low and the Sherwood numbers reach their minimum value in the major part of the contactor. Again, due to the small hydraulic diameters involved, the resulting mass transfer coefficients are comparable to those measured in packed columns.

In parallel flow, the values of the Sherwood number have been estimated using numerical approaches. For triangular and square arrays and packing fractions comprised between 0.4 and 0.6, the values of the constant α in Equation .1, corresponding to the minimum Sherwood number, are close to the values of cylindrical pipe flow [116], [117]. Furthermore, for random packing fractions varying from 0.2 to 0.7 the Sherwood numbers have been estimated to be of about 10 to 60 in the entry zone and of less than 1 in the developed boundary layer zone [118]–[120]. This is illustrated in Figure A.1, with uniform wall flux as boundary condition. In this figure, the

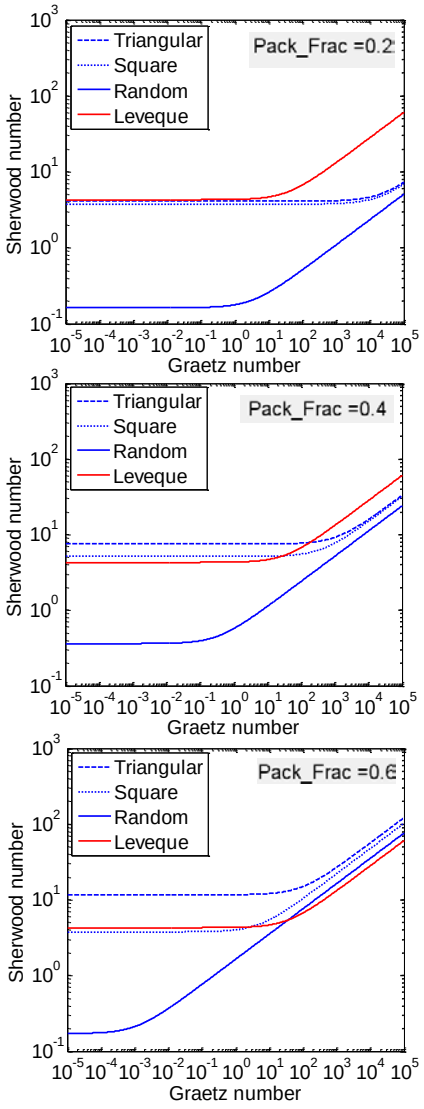

Figure A.1 Local Sherwood number as function of local Graetz number

variation of the Sherwood number with the Graetz number for the triangular, square and random arrays and for a packing fraction. The lesser is the packing fraction, the higher is the difference between the Leveque with the others approaches.
In cross flow, the concentration boundary layers are under development and thus the mass transfer coefficients depend on the fluid's velocity. Correlations of the local Sherwood number are given in [115], [121].

The random nature of the packing as well as the non-uniform distribution of the fibre external radius lead to non-uniform velocity distributions. Moreover, high packing densities are susceptible to channelling and dead zones. Accordingly, axial as well as radial dispersion are frequently encountered on the shell-side [115], [118], [122], [123]. As discussed in the previous section for the lumen-side flow, the influence of the dispersion on the overall flux in the shell-side is commonly taken into account by adjusting an equivalent Sherwood number to an ideal plug flow model [122]–[124]. The corresponding correlations are very much system-dependent, since the degree of the dispersion is a strong function of the flow arrangement.

B. Model Structure

The HFMC model structure is illustrated in Figure B.1. If other reactive system are to be studied, the information concerning the database (e.g. compounds, molar mass, Leonard-Jonnes potentials, reactivity…) must be added by the user. For the absorption step, two modes of simulation are available. The scheme of the stripping step includes the flowsheet, as described in Section 5.1. The numerical libraries are not included since the model has been built in an assisted programming software (Matlab), which has an entire series of numerical methods already included.

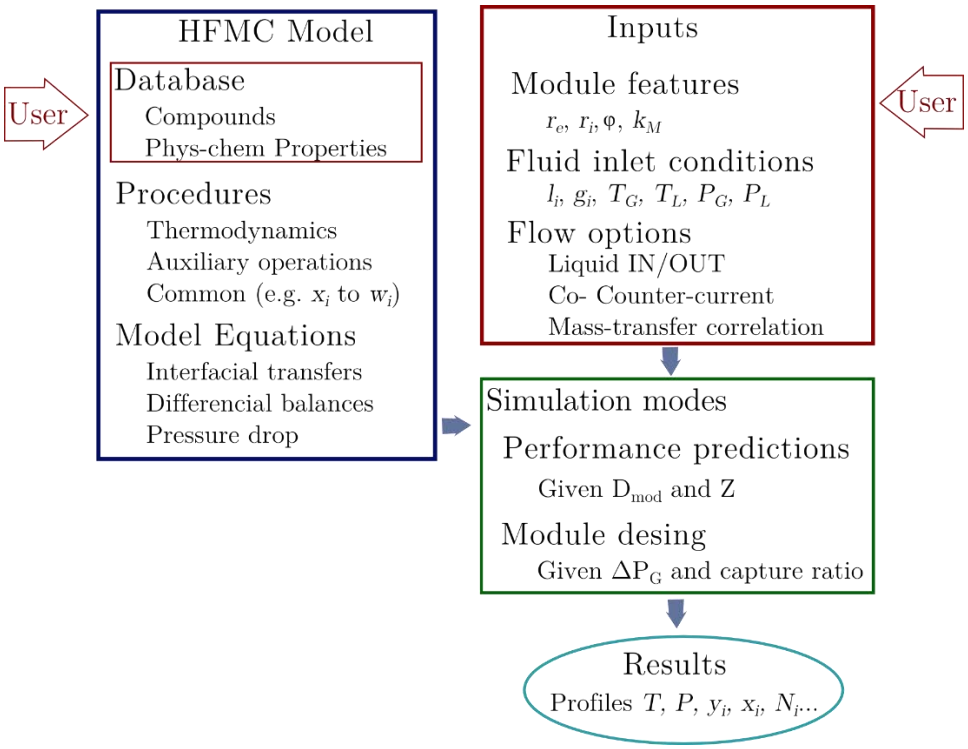

Figure B.1 Model structure

Modélisation de contacteurs membranaires à fibres creuses : application à la capture du dioxyde de carbone

Mot clés

Captage dioxyde de carbone, Contacteur membranaires à fibre creuses, Intensification de procédés, Absorption, Stripage.

Résumé

La capture du dioxyde de carbone (CO_2) en postcombustion est une stratégie importante pour la limitation de l'effet de serre. Le procédé de référence est l'absorption du CO_2 dans des solutions aqueuses aminées, suivie par une étape de stripage du solvant. La technologie mature associée à ce procédé est la colonne à garnissage. Toutefois, afin de rendre le procédé plus attractif, il convient de l'intensifier en réduisant le volume des équipements et le coût énergétique associé.

Les contacteurs membranaires à fibres creuses (CMFC) constituent une alternative aux colonnes à garnissage. Les CMFC permettent de développer d'importantes aires spécifiques conduisant potentiellement à une intensification des transferts gaz-liquide. Ainsi, l'utilisation des CMFC réduirait la taille des installations, mais aussi diminuerait la consommation énergétique par la diminution de la quantité de vapeur de stripage.

Cependant, l'utilisation de CMFC dans les étapes d'absorption et de stripage dans des conditions industrielles a été peu étudiée. Afin de combler cette lacune, des modèles à différents niveaux de complexité : monodimensionnel, bidimensionnel, isotherme et adiabatique ont été développés, comparés et validés. Ceci afin d'identifier le niveau de complexité approprié. Les résultats de simulation ont mis en évidence le potentiel d'intensification des CMFC dans l'étape d'absorption et aussi de stripage, se traduisant par une réduction en volume de 4 à 10 fois par rapport aux colonnes à garnissage. Néanmoins, les CMFC peuvent difficilement réduire le coût énergétique du procédé étant donné que l'étape de stripage fonctionne dans des conditions très proches de la limite thermodynamique.

Modelling of Hollow Fibre Membrane Contactors: Application to Post-combustion Carbon Dioxide Capture

Keywords

Carbon Dioxide Capture, Hollow Fiber Membrane Contactors, Process Intensification, Absorption, Stripping.

Abstract

Post-combustion CO_2 capture (PCC) is an important strategy in mitigating greenhouse effect. The reference process in PCC is the CO_2 absorption into amine aqueous solutions, followed by the regeneration (or stripping) of the solvent. The robustness of packed columns makes it the standard technology for both absorption and stripping steps. However, the treatment of large quantities of flue gases requires itself equipment of a large size.

Hollow fibre membrane contactors (HFMC) are considered as one of the most promising strategies for intensified CO_2 absorption process, due to their significantly higher interfacial area than that of packed columns, allowing to reduce the equipment size. In addition, this would reduce the energy penalty of the process by reducing the required amount of stripping steam.

However, despite the potential advantages of HFMC, very few investigations have studied implementing this technology for PCC within an industrial framework. To fill this lack, the performances of both absorption and stripping steps using HFMC under industrial conditions were estimated by modelling and simulation. To identify the optimal modelling strategy, transfer models with different levels of complexity were developed ranging from one-dimensional isothermal single-component to two-dimensional adiabatic multi-component. Simulation results of both absorption and stripping steps revealed that, compared to traditional packed columns, contactor volume reduction factors comprised between 4 and 10 might be achieved using HFMC. However, since the stripping operating conditions are very close to thermodynamic equilibrium, HFMC can hardly reduce the energy consumption of the process.